Northumbria Research Link

Citation: Cherianlukose, Cecil (2018) An investigative study of Manganese-based Antiperovskite structures as a thin film resistive material system. Doctoral thesis, Northumbria University.

This version was downloaded from Northumbria Research Link: http://nrl.northumbria.ac.uk/id/eprint/44502/

Northumbria University has developed Northumbria Research Link (NRL) to enable users to access the University's research output. Copyright © and moral rights for items on NRL are retained by the individual author(s) and/or other copyright owners. Single copies of full items can be reproduced, displayed or performed, and given to third parties in any format or medium for personal research or study, educational, or not-for-profit purposes without prior permission or charge, provided the authors, title and full bibliographic details are given, as well as a hyperlink and/or URL to the original metadata page. The content must not be changed in any way. Full items must not be sold commercially in any format or medium without formal permission of the copyright holder. The full policy is available online: http://nrl.northumbria.ac.uk/policies.html

Northumbria University
NEWCASTLE

UniversityLibrary

An investigative study of Manganese-based Antiperovskite structures as a thin film resistive material system

Cecil Cherian Lukose

Ph. D.

2018

An investigative study of Manganese-based Antiperovskite structures as a thin film resistive material system

Cecil Cherian Lukose

A thesis submitted in partial fulfilment
of the requirements of
The University of Northumbria at Newcastle
for the award of
Doctor of Philosophy

Research Undertaken at
Department of Mechanical and Construction engineering,
Northumbria University
and in Collaboration with
TT Electronics, Bedlington UK.

April 2018

Abstract

Novel manganese (Mn) based antiperovskite material systems have been reported to have Temperature Coefficient of Resistance (TCR) in the range of +0.09 to +46 ppm/˚C. Such extremely low values of TCR make these materials an ideal choice to replace existing thin film resistor systems like NiCr and TaN, which are reaching their current limit at ±5 ppm/˚C. These ultra-precise passive components find use in applications such as medical diagnostics, industrial automation and military systems, where they must maintain a stable resistance value across an extreme temperature range of -55 to +155 ˚C throughout their lifetime.

Based on previous literature, Mn based antiperovskites: Mn_3AgN, Mn_3CuN and $Mn_3Ag_{(x)}Cu_{(1-X)}N$ were selected to be sputter deposited as thin films on alumina and glass substrates using industrial standard fabrication processes to enable future scale up of the developed material.

The experiments within this project focus on fine-tuning key deposition parameters of nitrogen flow rate, temperature and pressure to investigate their effect on electrical properties of TCR and stability of Mn based antiperovskite thin films. The as-grown values of electrical properties are stabilised by finely tuning heat treatment temperature, time and environment. To assess the scope of improvement in electrical properties, Ag was partially substituted by Cu in the $Mn_3Ag_{(X)}Cu_{(1-X)}N$ structure. Sputter deposition parameters, heat treatment parameters and chemical composition were tuned to target resistive films with TCR values lower than ±5ppm/ºC and stability values closer to industry standard of 0.05%.

The lowest TCR value achieved for binary Mn_3CuN films was +14.25ppm/˚C and this was improved to -4.66ppm/˚C by partially substituting Cu with Ag in the films to a composition of $Mn_3Ag_{(0.4)}Cu_{(0.6)}N$. The best stability value of 0.57% was achieved for Mn_3CuN and this value deteriorated with increasing content of Ag in the film. The Mn_3CuN films also performed extremely well through the industrial fabrication stages, yielding a stable variation in TCR value of <±3ppm/˚C. This research is an important step in establishing the low TCR nature of Mn based antiperovskite materials suitable for industrial scale fabrication of thin film resistors.

“You never change things by fighting the existing reality. To change something, build a new model that makes the existing model obsolete.”

— Buckminster Fuller

Table of Contents

Abstract .... **II**

List of Figures .... **VII**

List of Tables .... **XII**

Declaration .... **XIV**

Acknowledgement .... **XV**

CHAPTER 1 Introduction **1-1**

1.1 Introduction 1-2

1.2 Background: A historical development of precision 1-3

1.3 Aims and Objectives 1-6

1.4 Thesis outline 1-7

1.5 Original contribution 1-9

1.6 Thin Film Resistors 1-9

1.7 Summary 1-22

CHAPTER 2 Literature review **2-1**

2.1 Introduction 2-2

2.2 Manganese: A starting point in the search 2-2

2.3 Introduction to the Perovskite structure: 2-3

2.4 Antiperovskites and their unique properties: 2-8

2.4.1 Unique properties of the antiperovskite structure: 2-8

2.4.2 Low TCR properties of the antiperovskite structure: 2-9

2.4.3 Existing TFR material systems with Mn based AP structures 2-15

2.5 Methodology 2-17

2.6 Summary 2-20

CHAPTER 3 Thin film deposition and characterization system **3-1**

3.1 Introduction 3-2

3.1.1 Deposition system: 3-4

3.1.2 Target Materials: 3-5

3.1.3 Substrate material: 3-6

3.1.4 Characterization equipment 3-7

3.2 Setting up the deposition and characterization equipment:.................3-16

3.2.1 Setting up the deposition plant to run individual targets: 3-17

3.2.2 Setting up the plant to run in co-sputtering mode:........................3-21

3.2.3 Reactive sputtering in Nitrogen: 3-23

3.2.4 Setting up the tube furnace for heat treatment: 3-24

3.3 Results and Discussion..3-25

3.3.1 Thickness and magnetron power level calibration:........................3-25

3.3.2 Initial electrical measurement:...3-27

3.3.3 Basic effects of introducing reactive Nitrogen: 3-30

3.3.4 Basic effects of heat treating TFR films..3-31

3.4 Summary 3-34

CHAPTER 4 Study of Mn_3AgN and Mn_3CuN thin films 4-1

4.1 Introduction 4-2

4.2 Design of Experiment:..4-5

4.3 Results and Discussion...4-7

4.3.1 Effect of Nitrogen flow rate on as grown films: 4-8

4.3.2 Effect of substrate temperature on as-grown film:........................4-18

4.3.3 Effect of annealing temperature on film properties.......................4-23

4.3.4 Effect of annealing time on properties of film 4-44

4.3.5 Electrical resistance stability of antiperovskite films 4-45

4.4 Summary 4-48

CHAPTER 5 Partial substitution of Cu in Mn_3AgN 5-1

5.1 Introduction 5-2

5.2 Experimental 5-4

5.2.1 As grown ternary films of $Mn_3Ag_{(1-X)}Cu_{(X)}N$: 5-4

5.2.2 Two stage heat treatment of ternary films: 5-6

5.3 Results and Discussion 5-7

5.3.1 As grown ternary films of $Mn_3Ag_{(1-X)}Cu_{(X)}N$ 5-7

5.3.2 Two stage heat treatment of ternary films 5-10

5.4 Summary 5-28

CHAPTER 6 Process Tuning and Commercial fabrication feasibility 6-1

6.1 Introduction 6-2

6.2 Experimental 6-4

6.2.1 Effect of varying working pressure 6-4

6.2.2 Heat treatment optimisation 6-5

6.2.3 Commercial fabrication cycle feasibility study 6-6

6.3 Result and discussion 6-8

6.3.1 Effect of varying working pressure 6-8

6.3.2 Heat treatment optimisation 6-22

6.3.3 Commercial fabrication cycle feasibility study 6-28

6.4 Summary 6-31

CHAPTER 7 Conclusions and Recommendations for Future Work 7-1

7.1 Conclusions 7-1

7.2 Recommendations for future work 7-3

References: I

Appendix 1- Substrate Dimension Diagrams XI

Appendix 2: Result comparison from isolated and sequential process run XIII

List of Figures

FIG 1-1 A TYPICAL POWER DERATING CURVE OF A THIN FILM RESISTOR. [22]....................................1-13

FIG 1-2 (A) GENERAL PROCESS FLOW OF TFR FABRICATION [2] (B) PHOTOLITHOGRAPHIC DEPOSITION OF RESISTIVE AND CONDUCTIVE LAYERS ON THE SUBSTRATE [27]..1-15

FIG 1-3 (A) STABILIZING EFFECT OF HEAT TREATMENT ON 50 AND 100 Ω TAN RESISTORS ON AS-FIRED AND POLISHED ALUMINA SUBSTRATES [30] (B) GRAPH SHOWING AGGLOMERATION RESULTING IN IRREVERSIBLE INCREASE OF RESISTANCE AT HIGHER TEMPERATURE (REDRAWN FROM SOURCE) [19]..1-16

FIG 1-4 (A) RELATIONSHIP BETWEEN SPOT SIZE, BITE SIZE, AND OVERLAP (B) DIFFERENT TRIMMING GEOMETRIES INTRODUCED BY LASER ON RESISTIVE FILM [31]...1-17

FIG 1-5 (A) SAMPLES OF PFC SERIES SMD TYPE RESISTORS (B) CAR SERIES THROUGH HOLE PRECISION METAL FILM RESISTOR (IMAGE COURTESY OF TT ELECTRONICS LTD.). 1-18

FIG 1-6 SCHEMATIC DIAGRAM SHOWING PARTS OF A CHIP TYPE THIN FILM RESISTOR [33]..................1-18

FIG 1-7 MICROSCOPE IMAGE OF FILM RESISTOR SHOWING DEGRADATION OF TRACKS [23].................1-21

FIG 2-1 SIMPLIFIED REPRESENTATION OF CUBIC UNIT CELL (A) PEROVSKITE STRUCTURE (B) ANTIPEROVSKITE STRUCTURE [54]. 2-6

FIG 2-2 GRAPH SHOWING NO OF ARTICLES PUBLISHED ON PEROVSKITE RESEARCH SINCE 1920 ON YEARLY BASIS. [SOURCE SCOPUS]...2-6

FIG 2-3 GRAPH SHOWING THE NO OF PUBLICATION RELATED TO ANTIPEROVSKITE STRUCTURE SINCE 1920 ON YEARLY BASIS [SOURCE SCOPUS]...2-7

FIG 2-4 GRAPH SHOWING THE LOW TCR NATURE OF MEMBERS FROM MN BASED ANTIPEROVSKITE FAMILY [79]..2-9

FIG 2-5 GRAPH OF TEMPERATURE DEPENDENT VARIATION OF RESISTIVITY FOR (A) MN_3CUN [80] (B) $MN_3AG_{(1-X)}SN_{(X)}N$, X REPRESENTING THE CONTENT OF SN IN THE FILM [81]. 2-10

FIG 2-6 GRAPH SHOWING EFFECT OF TERNARY DOPING ON TCR VALUES OF (A) $MN_3AG_{(1-X)}CU_{(X)}N$ [79] (B) $MN_3NI_{0.7}CU_{0.3}N$ [89]. 2-13

FIG 2-7 TYPICAL PROCESS FLOW FOR CHIP RESISTOR FABRICATION [COURTESY TT ELECTRONICS, UK].2-17

FIG 2-8 FLOWCHART SHOWING THE STAGES AS PER PERFORMED IN FURTHER CHAPTERS..................2-19

FIG 3-1 SCHEMATIC DIAGRAM OF TOP VIEW OF UDP 350 PLANT AND SUBSYSTEMS............................3-3

FIG 3-2 CROSS-SECTION DIAGRAM OF INNER ARRANGEMENT OF THE UDP 350 PLANT SHOWING VERTICALLY LOADED SUBSTRATE. 3-5

FIG 3-3 TARGETS MANUFACTURED BY TESTBOURNE LTD (A) CIRCULAR MN (B) CIRCULAR AG AND (C) RECTANGULAR CU IN THEIR MAGNETRONS 3-6

Fig 3-4 (a) Image of university designed alumina substrate plate (b) Individual chip showing areas of film deposited on individual chip. 3-7

Fig 3-5 Two wire measurement technique showing the flow of source current through both R_{LEADS} and R_{DUT} [101]. 3-8

Fig 3-6 Four - wire Kelvin measurement technique showing the flow of source current through Source R_{LEADS} and R_{DUT}, and V_R measured by Sense leads [101]. 3-9

Fig 3-7 Schematic diagram of electron beam interaction with sample [107]. 3-13

Fig 3-8 XRD pattern for Mn_3AgN and Mn_3CuN antiperovskite structure [116]. 3-15

Fig 3-9 Process flow showing deposition and heat treatment system setup. 3-16

Fig 3-10 Graph showing thickness variation for Mn with varying time and power 3-18

Fig 3-11 Graph showing thickness variation for Ag with varying time and power 3-19

Fig 3-12 Graph showing thickness variation for Cu with varying time and power. 3-20

Fig 3-13 Graph comparing the deposition rates of Mn, Ag and Cu 3-21

Fig 3-14 Graph of resistivity for Mn:Ag films with at% of Mn in films 3-27

Fig 3-15 Graph of resistivity and TCR variation for Mn:Ag 3:1 film with film thickness 3-29

Fig 3-16 Graph of varying resistivity and TCR of Mn:Ag films with N_2 flow rate. 3-31

Fig 3-17 Graph of resistivity and TCR variation with film thickness for Mn-Ag films heat treatment. 3-32

Fig 3-18 Graph of resistivity and TCR variation with N_2 flow rate for Mn-Ag film. 3-33

Fig 4-1 Process flow to deposit Mn based Ag or Cu binary thin films. 4-5

Fig 4-2 Cross section images of (a) Mn_3AgN films (sample no 2: deposited at 3 sccm and without Tsub) (b) Mn_3CuN films (sample no 12: deposited at 5 sccm and without Tsub). 4-10

Fig 4-3 Graph of sheet resistance values of as-grown films with increasing substrate temperature for 4 varying N_2 flow rates (a) Mn-AgN films (b) Mn-CuN films 4-12

Fig 4-4 Graphs of TCR values of as grown films with increasing substrate temperature for 4 varying N_2 flow rates (a) Mn-AgN films (b) Mn-CuN films. 4-14

Fig 4-5 XRD spectrum (a) Mn-AgN films (b) Mn-CuN films at increasing N_2 flow rates and without Tsub. 4-15

Fig 4-6 Surface images of Mn-CuN film grown at (a) 2, (b) 3 and (c) 5 sccm of N_2 flow rate(without Tsub). (d) Published images of Mn_3CuN antiperovskite shows deteriorating of antiperovskite structure (from inset a to d) with increasing Ge content [75]. 4-17

Fig 4-7 Graph of sheet resistance values of as-grown (a) Mn-AgN (b) Mn-CuN films plotted against increasing N_2 flow 4-19

Fig 4-8 Graph of TCR values of as-grown (a) Mn-AgN (b) Mn-CuN films plotted against increasing N_2 flow 4-20

Fig 4-9 XRD spectrum of (a) Mn_3AgN antiperovskite structure (b) Mn_3CuN antiperovskite, deposited at increasing substrate temperature 4-21

Fig 4-10 Mn_3AgN films grown at Tsub (a) without Tsub, (b) 50 and (c) 100°C. 4-23

Fig 4-11 Graph of sheet resistance values of Mn-AgN film (without substrate temperature) with increasing annealing temperature. 4-25

Fig 4-12 Graph of sheet resistance of Mn_3AgN film (3 sccm N_2 flow) with increasing annealing temperature 4-26

Fig 4-13 XRD spectrums of Mn-AgN deposited at (a) 1 , (b) 2, (c) 3, and (d) 5 Sccm before and after heat treatment. 4-27

Fig 4-14 XRD spectrums before and after heat treatment for Mn_3AgN films grown (a) without Tsub (b) Tsub = 50°C (c) Tsub = 100°C. 4-29

Fig 4-15 (a) Cross section (b) top profile of Mn_3AgN, grown at 3sccm N_2 flow and without Tsub, after heat treating at 350°C 4-30

Fig 4-16 Graph of TCR values of Mn-AgN films grown (without Tsub) with increasing N_2 flow rate. 4-32

Fig 4-17 Graph of TCR values of Mn-AgN films grown (without Tsub) with increasing annealing temperature. 4-33

Fig 4-18 Graph of TCR values of Mn_3AgN antiperovskite films (3sccm N_2 flow) with increasing annealing temperature. 4-34

Fig 4-19 Graph of Rs values of Mn-CuN film with annealing temperature. 4-35

Fig 4-20 Graph of sheet resistance values of Mn_3CuN film (5 sccm N_2 flow) with increasing annealing temperature. 4-36

Fig 4-21 XRD spectrums of Mn-CuN films grown at (a)2 , (b) 3, (c) 5, and (d) 6 sccm N_2 flow rate after heat treatment. 4-37

Fig 4-22 XRD spectrums of Mn_3CuN films grown (a) without Tsub, (b) 50 and (c) 100°C after heat treatment. 4-39

Fig 4-23 (a) Cross section (b) Top profile of Mn_3CuN films grown at 5 sccm N_2 flow rate and without Tsub, after heat treating at 350°C. 4-40

Fig 4-24 Graph TCR values of Mn-CuN films (without Tsub) with N_2 flow rate. 4-42

Fig 4-25 Graph of TCR values of Mn-CuN films grown (without Tsub) with annealing temperature 4-43

Fig 4-26 Graph of TCR values of Mn_3CuN films (5 sccm N_2 flow) with annealing temperature. 4-43

Fig 4-27 Graph of R_s and TCR values of (a) Mn_3AgN films (without Tsub) (b) Mn_3CuN films (without Tsub) with annealing duration. 4-45

Fig 4-28 Graph of electrical resistance stability in $\Delta R/R\%$ after heat treatment at 350ºC for (a) Mn_3AgN films (b) Mn_3CuN films.................... 4-47

Fig 4-29 Graph of electrical resistance stability of Mn_3AgN and Mn_3CuN films after heat treatment at 350ºC.................... 4-48

Fig 5-1 Process flow for deposition and heat treatment optimization of $Mn_3Ag_{(1-x)}Cu_{(x)}N$ ternary samples 5-3

Fig 5-2 Top view of chamber showing shutter arrangement designed for magnetron 4 to lower Ag deposition rate. 5-5

Fig 5-3 Graph of sheet resistance and TCR values of as grown ternary $Mn_3Ag_{(1-x)}Cu_{(x)}N$ films with increasing Cu doping concentration in the film. 5-9

Fig 5-4 XRD spectrums of as-grown films of $Mn_3Ag_{(1-x)}Cu_{(x)}N$ with increasing value of x from 0 to 1. 5-10

Fig 5-5 Graph of sheet resistance values of $Mn_3Ag_{(1-x)}Cu_{(x)}N$ ternary films with heat treatment temperature between 300 and 350ºC. 5-11

Fig 5-6 Effect of Cu dopant concentration on TCR values of $Mn_3Ag_{(1-x)}Cu_{(x)}N$ 5-12

Fig 5-7) XRD spectrums of 6 different compositions of $Mn_3Ag_{(1-x)}Cu_{(x)}N$, x= (a) 0, (b) 0.2, (c) 0.4, (d) 0.6, (e) 0.8, and (f) 1.0 before and after heat treatment.................... 5-13

Fig 5-8 SEM images showing the topology of $Mn_3Ag_{(1-x)}Cu_{(x)}N$ with x = 0, 0.6 and 1 as grown, (a) (b) and (c) and after heat treatment at 325ºC (d) (e) and (f) respectively.................... 5-15

Fig 5-9 SEM images showing the cross section of $Mn_3Ag_{(1-x)}Cu_{(x)}N$ with x = 0, 0.6 and 1 as grown (a) (b) and (c) and after heat treatment at 325ºC (d) (e) and (f) respectively. 5-17

Fig 5-10 SEM images showing the cross section of $Mn_3Ag_{(1-x)}Cu_{(x)}N$ with x=1 after heat treatment at (a) 300ºC (b) 350ºC and (c) 375ºC 5-18

Fig 5-11 Graphs showing elemental depth profile of (a) Mn^+(b) Cu^+ (c) N^+ and (d)O^- ions in Mn_3CuN films (x=1.0) before and after heat treatment at 325ºC 5-19

Fig 5-12 Cross section image showing thin deposition of film in the valley between two alumina grain responsible for detection of O- in the SIMS 5-20

Fig 5-13 Sites at the side profile image of Mn_3CuN films for EDX analysis of (a) as-grown (b) heat treated at 325ºC 5-21

Fig 5-14 Graph of sheet resistance values before and after introducing second stage of heat treatment. 5-23

FIG 5-15 GRAPH OF PERCENTAGE CHANGE IN RESISTANCE FOR SIX COMPOSITION OF $MN_3AG_{(1-X)}CU_{(X)}N$ TERNARY FILMS WITH INCREASING CU DOPANT CONCENTRATION 5-24

FIG 5-16 GRAPH SHOWING VARIATION IN (A) SHEET RESISTANCE (B) TCR VALUES OF THREE COMPOSITION OF $MN_3AG_{(1-X)}CU_{(X)}N$ WITH X=0,0.6 AND 1, WITH EACH PROCESS STAGE 5-26

FIG 5-17 CROSS SECTION IMAGE OF UPPER LAYER AFTER TWO STAGES OF HEAT TREATMENT AND DRY HEAT STABILITY TEST ON $MN_3AG_{(1-X)}CU_{(X)}N$ WITH X= (A) 0 (B) 0.6 AND (C) 1................................ 5-27

FIG 6-1 SCHEMATIC REPRESENTATION OF THE STRUCTURE ZONE MODEL BY THRONTON DEPICTING FOUR ZONES BASED UPON TEMPERATURE [155] 6-2

FIG 6-2 (A) STANDARD 1206 INDUSTRIAL PACKAGE (B) STANDARD SERPENTINE TRIMMING PATTERN ON A SINGLE 1206 CIRCUIT.. 6-7

FIG 6-3 GRAPH SHOWING VARIATION IN R_S OF MN_3CUN SAMPLES DEPOSITED UNDER VARYING PRESSURE, WITH HEAT TREATMENT STAGES... 6-11

FIG 6-4 GRAPH FOR MN_3CUN FILMS DEPOSITED AT VARYING PRESSURE SHOWING (A) TCR VALUES (B) PERCENTAGE CHANGE IN RESISTANCE. 6-13

FIG 6-5 XRD SPECTRUM FOR MN_3CUN FILMS DEPOSITED AT VARYING PRESSURES (A) AS GROWN (B) HEAT TREATED AT 325°C (C) STABILIZATION TREATED AT 260°C. 6-15

FIG 6-6 (A) ORIGINAL AFM IMAGES OF AS GROWN MN_3CUN FILMS (B) GRAIN BOUNDARY MASK GENERATED BY SEGMENTATION ALGORITHM. 6-16

FIG 6-7 AFM IMAGE OF MN_3CUN FILMS DEPOSITED AT 2, 3 AND 5 MBAR RESPECTIVELY (A-C) AS-GROWN (D-F) HEAT TREATED AT 325°C (G-I) STABILIZATION TREATED AT 260°C. 6-18

FIG 6-8 CROSS SECTION IMAGES OF MN_3CUN FILMS (A)2 MBAR (B)3 MBAR AND (C)5 MBAR. 6-20

FIG 6-9 CROSS SECTION IMAGE OF SHOWING SITES OF EDX MEASUREMENT FOR FILMS DEPOSITED AT (A) 2 μBAR (B) 3 μBAR (C) 5 μBAR 6-21

FIG 6-10 BAR CHART OF RS VALUES FOR FOUR HEAT TREATMENT CASES. 6-24

FIG 6-11 BAR CHART OF ELECTRICAL STABILITY VALUE FOR FOUR HEAT TREATMENT CASES. 6-25

FIG 6-12 BAR CHART OF TCR VALUES FOR FOUR HEAT TREATMENT CASES 6-26

FIG 6-13 CROSS SECTION IMAGES OF UPPER OXIDE LAYER ON MN_3CUN FILM AFTER HEAT TREATMENT UNDER (A) CASE 1 (B) CASE 2 (C) CASE 3 (C) CASE 4. 6-27

FIG 6-14 GRAPH OF SHEET RESISTANCE VARIATION IN 1206 SAMPLES AT VARIOUS FABRICATION PROCESS STAGE 6-29

FIG 6-15 GRAPH OF TCR VARIATION IN 1206 SAMPLES AT VARIOUS FABRICATION STAGES................ 6-30

List of Tables

TABLE 1-1 MATERIAL SYSTEMS EMPLOYED IN A TYPICAL TFR FABRICATION..1-22

TABLE 2-1 TABLE SHOWING ELECTRICAL PROPERTIES FOR THIN TAN AND MN FILM...............................2-3

TABLE 2-2 TABLE SHOWING ELECTRICAL PROPERTIES OF ESTABLISHED TFR MATERIALS AGAINST MEMBERS OF MN BASED ANTIPEROVSKITE FAMILY 2-16

TABLE 3-1 TABLE OF TCR AND STABILITY MEASUREMENT LIMITS FOR MULTIMETER RESOLUTION. 3-10

TABLE 3-2 CALIBRATION RESULT FOR LTC GRANT OIL BATH KIT WITH GD120 THERMOSTAT AND AGILENT 3408A MULTIMETER..3-11

TABLE 3-3 DEPOSITION PARAMETERS FOR INITIAL DEPOSITION IN UDP 350 PLANT. 3-17

TABLE 3-4 TABLE OF VARYING POWER AND TIME TO DETERMINE MN SPUTTER RATE............................3-18

TABLE 3-5 TABLE OF VARYING POWER AND TIME TO DETERMINE AG SPUTTER RATE. 3-19

TABLE 3-6 TABLE OF VARYING POWER AND TIME TO DETERMINE CU SPUTTER RATE 3-20

TABLE 3-7 TABLE OF VARYING POWER ON MN AND AG TARGET IN CO-SPUTTERING MODE.....................3-22

TABLE 3-8 TABLE OF VARYING THE DEPOSITION TIME IN MN:AG CO-SPUTTERING MODE........................3-23

TABLE 3-9 TABLE OF VARYING POWER ON MN AND CU TARGET IN CO-SPUTTERING MODE.....................3-23

TABLE 3-10 TABLE OF VARYING PARTIAL NITROGEN ENVIRONMENT IN THE CHAMBER 3-24

TABLE 3-11 TABLE OF RESULTS FOR THICKNESS AND COMPOSITION WITH VARYING MN/AG POWER LEVELS 3-25

TABLE 3-12 TABLE OF MN:AG FILM RESISTIVITY WITH INCREASING CONCENTRATION OF MN 3-26

TABLE 3-13 TABLE OF THICKNESS AND COMPOSITION VARIATION WITH MN/CU POWER LEVELS 3-27

TABLE 3-14 : TABLE OF RESISTANCE CHANGE AFTER EACH 24 HOURS...3-33

TABLE 4-1 DOE FOR 2 DEPOSITION FACTORS USED TO DEPOSIT BINARY FILMS OF MN-AGN AND MN-CUN. 4-6

TABLE 4-2 TABLE OF THICKNESS AND COMPOSITION ANALYSIS FOR AS-GROWN SAMPLES OF MN-AGN AND MN-CUN FILMS...4-9

TABLE 4-3 TABLE OF FWHM AND CALCULATED MEAN GRAIN SIZE FOR MN_3AGN AND MN_3CUN FILMS DEPOSITED AT INCREASING SUBSTRATE TEMPERATURE..4-22

TABLE 4-4 TABLE OF FWHM AND CALCULATED CRYSTALLITE GRAIN SIZE FOR MN_3AGN SAMPLES BEFORE AND AFTER HEAT TREATMENT 4-29

TABLE 4-5 TABLE OF EDX COMPOSITION OF MN_3AGN SAMPLES MEASURED BEFORE AND AFTER HEAT TREATMENT. 4-31

TABLE 4-6 TABLE OF FWHM AND CALCULATED CRYSTALLITE GRAIN SIZE BEFORE AND AFTER ANNEALING TREATMENT, FOR MN_3CUN SAMPLES DEPOSITED AT INCREASING SUBSTRATE TEMPERATURE. 4-39

TABLE 4-7 TABLE SHOWING EDX COMPOSITION OF MN_3CUN SAMPLES BEFORE AND AFTER HEAT-TREATING. 4-41

TABLE 4-8 TABLE WITH SUMMARY OF ELECTRICAL PROPERTIES ACHIEVED ON MN_3AGN AND MN_3CUN FILMS HEAT TREATED AT 350°C FOR 3 HOURS. 4-49

TABLE 5-1 TABLE OF CU DOPING INCREMENT PLANNED IN THE $MN_3AG_{(1-X)}CU_{(X)}N$. 5-4

TABLE 5-2 TABLE OF DEPOSITION PARAMETERS FOR TERNARY ANTIPEROVSKITE FILMS. 5-6

TABLE 5-3 TABLE OF FILM THICKNESS AND COMPOSITION FOR $MN_3AG_{(1-X)}CU_{(X)}N$ TERNARY FILMS. 5-8

TABLE 5-4 TABLE OF FILM THICKNESS AS GROWN AND POST HEAT TREATMENT FOR VARYING COMPOSITION. 5-16

TABLE 5-5 TABLE SHOWING COMPOSITION FROM CROSS SECTION OF MN_3CUN FILMS AS-GROWN AND AFTER HEAT TREATMENT AT 325°C 5-22

TABLE 5-6 TABLE OF ELECTRICAL PERFORMANCE FROM PROCESS RUN IN ISOLATED MODE AND SEQUENTIAL MODE. 5-28

TABLE 6-1 TABLE SHOWING ARGON AND N_2 FLOW RATES FOR MN_3CUN DEPOSITIONS AT VARYING PRESSURES. 6-5

TABLE 6-2 TABLE OF HEAT TREATMENT CONDITIONS FOR TERNARY FILMS. 6-6

TABLE 6-3 TABLE OF LASER TRIMMING SPECIFICATION FOR MN_3CUN FILMS ON 1206 PLATE. 6-8

TABLE 6-4 TABLE OF THICKNESS AND COMPOSITION FOR MN_3CUN FILMS AT VARYING PRESSURES. 6-9

TABLE 6-5 TABLE OF FWHM AND CRYSTALLITE GRAIN SIZE FOR MN_3CUN SAMPLES DEPOSITED AT VARYING PRESSURE. 6-16

TABLE 6-6 TABLE COMPARING CALCULATED CRYSTALLITE GRAIN SIZE FOR AS GROWN MN_3CUN FILM USING AFM AND SEM TECHNIQUE. 6-17

TABLE 6-7 EDX ANALYSIS OF FILMS DEPOSITED AT VARYING DEPOSITION PRESSURE 6-22

TABLE 6-8 TABLE OF HEAT TREATMENT OPTIMIZATION CASES AND CASE ID FOR EACH CASE. 6-23

TABLE 6-9 TABLE OF ELEMENTAL COMPOSITION FOR UPPER OXIDE LAYER FOR EACH HEAT TREATMENT CONDITIONS. 6-28

Declaration

I confirm that this thesis represents my own work and that contribution of any supervisors and others to the research and to the thesis was consistent with normal supervisory practice. All the external contributions made to this research and to this thesis, are duly acknowledged.

I declare that no part of this work has been submitted for any other award.

The word count for this thesis is 46438

Name: Cecil Cherian Lukose

Signature:

Date: 18/10/2018

Publication of parts of this thesis:

I declare that no part of this thesis has been officially published, in advance of submission of the thesis for examination, keeping in with the confidentiality agreement between TT Electronics, Bedlington and Northumbria University, Newcastle upon Tyne.

Candidate:

Date: 18/10/2018

Acknowledgement

This work in its present form is an outcome of support and help extended to me throughout the course of this project, and here I would like to take this opportunity to express my acknowledgement of these.

I shall begin with God the almighty, for the perfect will that has lead me to find the right path and kept the inner curiosity alive in me throughout this journey. I have always found the reliance on spiritual strength to be of great comfort in times of doubt.

I want to express my sincere thanks and gratitude to my principle supervisor, Dr. Martin Birkett for believing in me and allowing me to pursue roads less travelled during this project. I appreciate all the contributions he has made in terms of his time, ideas, feedbacks and resources to make this PhD experience stimulative and immersive.

I would also like to thank my other academic supervisor, Dr. Guillaume Zoppi and industrial supervisor, Mr. David Jackson (TT Electronics, Bedlington, UK) for their training on equipment of importance and expert advice in technical matters.

I would like to acknowledge Department of Mechanical and Construction engineering together with Department of Mathematics, Physics and Electrical engineering, within Northumbria University, for the thin film deposition and characterization facilities made available to me. Especially, I would like to thank Dr. Pietro Maiello, for his countless hours and expert advice with SEM, EDX and XRD machines.

I also extend my sincere thanks to Welwyn Components Ltd, for all of their support in this project, in terms of funding, material, and resources. With special mention to Mr. Barry Peters and team (TT Electronics Bedlington) and Mr. Patrick Klersy and team (IRC TT, USA) for all of the discussions, feedbacks and test product development from industrial aspect of this project.

Finally, I would like to thank my parents and my family who always encouraged me to go beyond the visible and explore the unknown, my friends who kept me from becoming socially withdrawn and in particular my wife, Gloria who supports and encourages me to be a better person in my life.

I dedicate this work to

my Parents, Grace Cherian and Lukose Cherian,

for all their unconditional sacrifices to nurture my growth.

CHAPTER 1 Introduction

1.1 Introduction

In a survey published by the IRE (Institute of radio engineers) in May 1962, it was mentioned that:

> "The factor common to all resistors, fixed and variable, which largely determines properties and performance, is the resistor element. It has therefore been the primary subject of significant investigations which fundamentally resolve into a search for new resistive materials. The evolution of the resistor field parallels this search." (Marsten, J, 1962)[1].

And for the last six decades, the search for novel resistive materials has fuelled the research in the resistor industry and the same quest has enabled the manufacturers with expertise required to tailor make the properties of their finalised resistor product. In an age where advanced technology makes it possible to fit millions of devices in a space no greater than a fingernail, it appears too trivial to dedicate a research work to develop resistors with enhanced properties. In general perception, it appears that a resistor could be developed by following the straightforward Ohm's law. But contrary to the general perception, resistor technology has grown in a very rapid way, and the resultant products exist in various shapes, sizes and are very much application specific. Today developing a resistor product takes into consideration the similar complex physical laws that govern the functioning and fabrication of an active device. With the size of portable devices shrinking rapidly, resistor technology has also embraced the ongoing miniaturisation trend to be at pace with rest of the circuit elements. In a period between 1991 and 1996, chip resistors reported an annual production increase of 17%, from 125 billion to 230 billion per year, compared to an average annual increase of 5% for integrated circuits from 35 billion to 42 billion [2]. It is better to develop passive devices independently, rather than trying to integrate them along with active devices to compete for an already scarce real estate on the chip. Therefore, a steady demand along with the standalone nature of the resistor will be a motivation to conduct this research, to extend the properties of resistors beyond the current limits achieved.

Resistors are an integral part of every electronic circuit and the properties of resistors required are very much application specific. For example, when a resistor

is employed as a temperature sensor, it is required to have a large temperature coefficient of resistivity (TCR) so as to sense the miniscule change in temperature, but to be employed as a component of a reliable current sensing circuit, a resistor is expected to have its TCR as close to zero as possible, so that the device doesn't change its properties and results through its lifetime.

Various technologies of resistor development provide solutions for this varying need of resistors. Resistor technology can be broadly classified into four types: wirewound resistors, metal foil resistors, thick film resistors and thin film resistor technology. Each of these was developed during different time-periods in the last century, has its own strengths and weaknesses and still today specifically caters to provide a particular section of the resistor industry. Now the need for portable and ultra-precise devices for use in military, communication and scientific applications, calls for passive components with performance two or three orders of magnitude better than those used for conventional domestic and industrial applications.

1.2 Background: A historical development of precision

With the advent of radio and military requirements for World War 2, the immediate need for precise passive components was realised. With the passage of time and advancement in technology, this need became stricter in terms of precise resistance value without being affected by the ambient or device temperature. Therefore, encouraged by this, more and more research was dedicated to study the complex interactions occurring at the atomic scale, to extend the performance of resistor technologies further closer to the ideal value of zero TCR and stability.

In the late 1940`s, wire wound resistors saw the introduction of new resin materials like epoxy and Si for protection from external elements, wires made of novel alloys of Ni-Cr-Al-Cu, careful heat treatment, careful construction, all resulted in space saving, and increased temperature stability [1, 2], but these improvements in performance were not significant enough to provide a solution for very high precision seeking applications.

From the mid-1940`s to early 1970`s researchers were focussed on developing the performance of metal film resistors. Prominent among these were the works of Weber and Johnson [1945] to produce evaporated thin films of Nichrome on glass and Stein and Riseman [1954] to control TCR to any desired value very close to 0 [1]. In 1962, metal foil resistors were introduced, in which resistance change in the film, due to thermal expansion of the substrate is adjusted in such a manner so as to compensate for the TCR of the film. But these values are not the inherent properties of the material and therefore materials with low inherent TCR were of great interest to the resistor industry. Metal foil resistors have developed significantly to offer performance increases, as required for high precision electronics, but they are not able to keep pace with the shrinking size requirement, as their superior performance depends upon compensation of TCR by thermal expansion. After the 1970s, advancement in technology led to a large number of researches in the field of thin film resistors. The bulk property of a material will vary significantly when it is deposited as a thin film. Performance of thin film resistors could be improved either by improving the existing material system and optimising process parameters or by introducing a new material system.

Lots of research has been carried out to improve the existing material systems and to optimise the process parameters. Tantalum nitride or TaN is a well-established material in the thin film resistor industry and a lot of research has been conducted on studying the effect of deposition parameters and annealing conditions on the various properties of TaN films [3], including their unique property which makes them the best for protection against humidity [4]. TaN was reported to have a NTCR or negative TCR [4], and there are suggestions to use TaN combined with TiN which has a PTCR or positive TCR to compensate both TCRs and generate a NZTCR or near zero TCR material [4].

Chromium Silicon or CrSi is another well-known material, used specifically for its long life stability [5] and high sheet resistance value [6]. Air annealed CrSi gets oxidised and shows an increase of resistance and with increasing concentration of Si the sign of TCR shifts from negative to positive [7]. Extremely low TCR values

of -6 ppm/°C (parts per million change in resistance per degree change in temperature) have been observed for cermets (generic name for materials made by combining ceramic with sintered metals) made from CrB_2-Si-SiC [6] with sheet resistances as high as 1kΩ/□.

Nichrome or NiCr is the most used and most researched material for TFRs. TFR`s based on NiCr have been studied for performance at extremely low temperatures of 50mK [8, 9], effect of Chromium concentration [10][15], optimisation of sputtering parameters [11], effect of annealing on Ni-Cr thin films [12, 13], effect of depositing on various substrates such as Al_2O_3/Copper and foil/Silicone/GaAs [12-15], effect of doping with other elements like Ti/Cu/Al/Ge etc. to modify crystal structure [8, 9, 14], optimising other properties like strain sensitivity [16], developing TFR's for microwave integrated circuits [15], effect of various fabrication process parameters [15], and interdiffusion between various layers in a NiCr based TFR [17, 18]. One advantage of such an extensive study on a single alloy is that it helps to verify the rules governing the electrical resistivity [8] and acts like a reference point for material systems investigated in the future.

The implementation of some of the improvements and optimisations mentioned above has enabled the industry to set the standard it has today. Only a very few high precision thin film resistors in the range of 500Ω to 20KΩ exist in the market with TCRs as low as ±5 ppm/ºC. Some of the metal foil resistors offer better stability and TCR values, but to keep up with the miniaturisation of portable devices, it is very much necessary to develop thin film resistors to the standard of metal foil resistors.

1.3 Aims and Objectives

The Aims of this research are as follows:

1. Identify a novel thin film material system, which can be used to develop ultra-precision thin film resistors with the performance values equivalent to that of metal foil resistor technology.
2. Develop a deposition process, which could validate the reliability and repeatability of the performance values of the thin films of this material system in a laboratory environment.
3. Study the possibility of incorporation of this new material system to fabricate thin film resistors as a product on a commercial production scale.

The objectives of this work are to:

1. Conduct an extensive literature search to gain an in-depth knowledge about the potential material system, which could be used to develop ultra-precise thin film resistors and establish a relationship between the performance values and the material system.
2. Deposit thin films of the identified material and fine tune the process parameters to attain the following electrical characteristics:

Sheet resistance	0.5 to 500 Ω/□
TCR (20ºC to 70ºC)	< ± 5 ppm/ºC

3. Characterize the thin film developed under varying process parameters using identified techniques to develop a relationship between the observed results and the various process parameters.
4. Verify the validity and repeatability of the results by producing initial batches of fully functional thin film resistors on a laboratory set up and study the feasibility of this material for commercial production set up.

1.4 Thesis outline

Chapter 1: This chapter gives an introduction to the most important performance parameters of an ultra-precise thin film resistor followed by an overview of the fabrication process and material systems used to fabricate different components of a precision thin film resistor. It will help to understand the need and importance of developing a new material for ultra-precision requirements.

Chapter 2: The focus of this chapter is a systematic literature search conducted to identify a potential material system which is investigated further as a candidate for fabrication of ultra-precise thin film resistors. Mn based antiperovskite is identified as a material system with suitable resistivity range, extremely low TCR and stability. This literature search also reveals a potential gap in the research conducted to develop the Mn based antiperovskite thin film structure for its low TCR property.

Chapter 3: The aim of this chapter is to present in detail the capabilities of the deposition plant and heat treatment equipment present at Northumbria University. It explains the basic principles and the working of test equipment available for electrical, chemical, and morphological characterization such as Scanning Electron Microscope (SEM), Energy Dispersive X-Ray (EDX), profilometer and digital multimeter. Initial runs are performed on individual targets first followed by co-sputtering mode. Thereafter the plant is set up to introduce Nitrogen into the chamber to perform reactive sputtering. As grown samples are then heat treated in air to investigate the effect of heat treatment on electrical properties. Results from these samples help to understand the basic role of individual elements in the alloy system and also helps to focus on some deposition parameters like power levels on each target, deposition time and thickness.

Chapter 4: Design of experiment to verify the proposed extremely low TCR nature of Mn_3AgN and Mn_3CuN antiperovskite structure is the primary motive of this chapter. Design of experiment (DoE) is executed by varying substrate temperature and Nitrogen flow rate to deposit thin films of these antiperovskite binary structures.

Electrical, structural and chemical characterizations are performed on samples before and after annealing heat treatment in N_2. Samples are found to have acceptable sheet resistance and TCR values to be considered for further studies. However, stability figures are found to be no better than 11% for the thin film resistor fabrication. This could be improved with second stage of heat treatment in air

Chapter 5: This chapter investigates the potential to shift the TCR value of Mn_3AgN closer to zero by partially doping with Cu. Seven compositions are prepared ranging from 100% Ag to 100% Cu by incrementing 0.2% atomic percentage of Cu in each step. A secondary stabilization heat treatment is introduced to improve the stability value. The TCR value of Cu rich $Mn_3Ag_{(0.4)}Cu_{(0.6)}N$ is found to be the lowest, but stability is better at either end of the composition spectrum. Secondary heat treatment improves stability and Mn_3CuN is found to have the best stability while still maintaining a very low TCR value.

Chapter 6: This chapter strives to find the possibility of improving the TCR and stability figure for Mn_3CuN, studying the effect of deposition pressure condition. A set of samples for Mn_3CuN is developed at 3µbar as previously, to verify the repeatability and reliability of the data set from the previous chapters. Two more set of Mn_3CuN are deposited at 2 and 5 µbar. The results are found to be repeatable and reliable in the lower working pressure ranges for the Mn_3CuN. Thereafter, a DoE is carried out to optimize the heat treatment environment to further tune the TCR and stability value of Mn_3CuN films. A small set of samples are laser trimmed, the next stage in TFR fabrication process, to access material potential for commercial application.

Chapter 7: Finally, this chapter concludes the thesis by summarising the main findings of the research and suggests a number of recommendations which could be useful to make improvements in the future work related to this area.

1.5 Original contribution

Extremely low TCR was one among the inherent properties of the Mn based antiperovskite material system. But most of the works conducted to date were concerned with studying these properties and enhancing them in a bulk material system, and very few efforts were made to deposit them as thin films. As this material system is relatively new, no effort has ever been made to develop this as a potential material system for thin film resistor fabrication. This work has contributed towards exploring the potential of the Mn_3AgCuN material system for precision thin film resistor fabrication. It includes fine tuning of sputter deposition parameters and heat treatment conditions to fine tune the electrical properties close to the values reported in the literature review. By comparing results, correlation between the deposition parameters and heat treatment conditions are made to the structural, chemical and morphological characteristics which dictate conduction mechanisms, thereby fine tuning the electrical properties. Resistive films of suitable composition are tested to validate the data collected from the project.

1.6 Thin Film Resistors

While other resistor technologies can compete with thin films in the dimension range of 0.127 to 0.254 mm, thin film resistors become the leading choice when high precision is required along with small device sizes below 0.127 mm [19]. Suitable sheet resistance, temperature coefficient of resistance (TCR), and stability of the resistance value during the lifetime are the main performance characteristics of thin film resistors.

Performance Properties of a Thin Film resistor:

Resistance Value: the nominal resistance value of a resistor as *R*, defined by Ohm`s law, only implies that the resistor in question will deliver the same value of resistance when the value of applied voltage V, or flowing current I, is changed, provided the temperature remains constant.

$$V = I \times R \tag{1.1}$$

In other words, the resistance value of a resistor depends only upon the material and its dimensions, at a constant temperature, and is not determined by the amount of current or voltage [20].

$$R = \frac{P \times L}{A} \quad (1.2)$$

Where, P, is the resistivity of the material, L is the length of the resistor, A is the cross section of the resistor, given by $A = W \times d$ (assuming the thin film deposited bears resemblance to a thin rectangular surface), W is the width of the resistor, d is thickness of the resistor

So the ratio of length to width could be used to visualize a thin film resistor as to be made up of number of square sections, n:

$$n = \frac{L}{W} \quad (1.3)$$

Resistivity is an inherent property of the material that quantifies how strongly a given material opposes the flow of electric current [21] and hence it finds more relevance in a research domain where a new material for resistive applications needs to be developed. For the design of thin film resistors, sheet resistance is the term usually used, which relates this inherent material property to a process parameter *d*, which is the thickness of film, as follows:

$$Rs = \frac{P}{d} \quad (1.4)$$

Sheet resistance is represented as Rs *or* $R\square$ and quoted as “resistance per square”, and in effect conveys the resistance value of a thin square film of material deposited by the process. The Resistance value of the overall resistor could in a practical sense be attained by multiplying the number of squares in a resistor having this unique sheet resistance:

$$R = n \times Rs \quad (1.5)$$

In this way resistance value can be expressed in a way which is independent from the physical dimensions of the device. So resistivity and sheet resistance are the two basic performance parameters to consider while developing a new material for thin film resistance.

The specified resistance value of the resistor could change depending upon various factors like the surrounding temperature, its age, storage environments and frequency of applied voltage. Some of these changes are temporary and some are permanent in nature.

Temperature Coefficient of Resistance, TCR: is used to represent the change in the resistance value as a function of changing temperature. It is most commonly denoted by the Greek letter α, expressed as parts per million or ppm/^{o}C, over a specified temperature interval, and is given by the formula [20-22]:

$$TCR, \alpha = \frac{Rs - Rf}{Rs(Ts - Tf)} \quad (1.6)$$

Where Rs is the resistance value measured at starting temperature Ts and Rf is the resistance value measured at final temperature Tf.

When a resistor dissipates power, its temperature increases and on a crowded circuit layout with high power dissipating components, ambient temperature can easily reach 70°C. Varying temperature can result in physical, chemical and structural alteration within film of a resistor and it affects the number of electron collisions and conduction mechanisms occurring within the thin film material and in turn varies the value of resistivity [20, 21]. Additional scattering processes at the surface start to contribute to this when very thin films of material are considered. TCR tracking is another term commonly used in data sheets to specify the TCR variation of two resistors grown under identical conditions and placed under similar environmental factors. TCR tracking appears to be almost one or two orders better than TCR, and is often mistaken for a superior performance, when it is only representing the ability of one resistor to track the TCR of another resistor grown under the same conditions. For applications requiring a high standard of performance, as in military applications, the TCR of resistors are tested using MIL-STD-202 Method 304, over the full military range of operation from -55°C to 125°C [22]. Whereas, for general purpose applications TCR is generally quoted for the temperature interval of 20°C to 70°C. While the changes in resistance value introduced by variation in temperature are temporary and the resistance will return

to its original value when temperature reverts, there are a few possible scenarios, which can introduce permanent change of resistance value.

Stability: during its lifetime of operation, a resistor is subjected to varying environments like humidity, temperature, and chemical interaction in its surroundings and these interactions bring a permanent change in resistance value. In addition, more permanent changes are introduced as the resistor ages. Thin film materials like Nichrome have higher performance than Tantalum nitride but are observed to have poorer stability results, and have forced the industry to either settle with these lower performance characteristics in harsh environments or to develop expensive specialised passivation methods to protect NiCr films [23]. Stability of the film is one key performance factor, which determines if a newly developed material could find potential application in the thin film resistor industry. Stability of thin film resistors are determined by subjecting them to elevated temperatures and moisture content, varying from standard to standard, for extended durations of time to measure the change in resistance value. Stability could be expressed as parts per million changes to original value or as a percentage change in the resistance value [24]:

$$\frac{\Delta R}{R}\ (PPM) = \frac{Rf - Rs}{Rs} \tag{1.7}$$

Or as $$\frac{\Delta \mathrm{R}}{\mathrm{R}}\ (\%) = \frac{\mathrm{Rf} - \mathrm{Rs}}{\mathrm{Rs}} \times 100$$

Where $Rf$is the final resistance after subjecting the starting resistance value Rs, to the stability test.

Along with these major performance characteristics, there are other parameters which come into effect under special applications.

Other performance parameters:

Power rating is one term which is used to define the maximum power at which a resistor must be operated, to raise its temperature above an optimum temperature, commonly 70ºC to its zero power temperature. Figure 1-1 shows the zero power temperature of a thin film resistor, maximum temperature at which a resistor can be operated without excessive change in its value, generally given as 150ºC for

hermetically sealed resistors and as 125°C for non-hermitically sealed resistor products [22]. Thin film resistors are rarely put to high power application and compared to the typical design level of a precision network which can only sustain 25W/in^2 thin films can sustain power densities up to 200W/in^2 without compromising their integrity [25]. Because of this, power ratings for thin film resistors are not as critical as for general purpose networks. Power ratings are generally shown as a power derating curve showing the increase of temperature with increasing power until it reaches the zero power temperature [26].

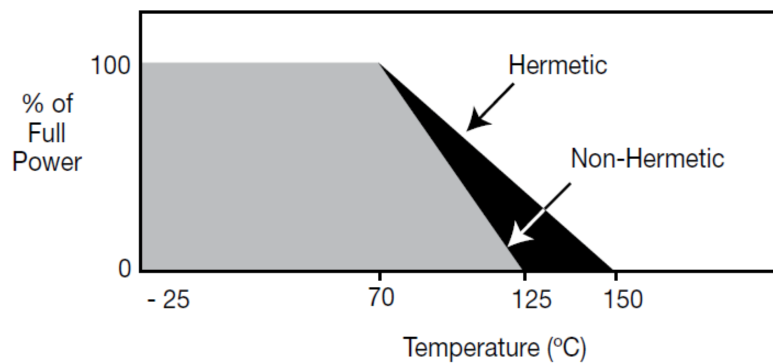

Fig 1-1 A typical power derating curve of a thin film resistor. [22].

Parasitic capacitance and inductance could be ignored for low frequency applications but for high frequency applications, greater than 100 MHz, these effects must be considered and proper care must be taken while designing and fabricating the resistor to ensure close to ideal resistor performance of the product. The size of the resistor product and trimming are the two prime factors considered to affect the parasitic impedance [22]. Another performance parameter which only comes into effect at resistance values of mega ohms range, is the voltage coefficient of resistance or VCR, it is the change of resistance value with the per unit change in voltage. At mega ohm range, this value is typically 0.1 ppm/V [22], so for medium range resistor products as concerned with this project, this performance characteristic is not identifiable. For resistors with large dimensions, thermoelectric voltages or thermoelectric potential (TEP) may be generated if their termination ends are at different temperatures, but because of the small size of thin film resistors and substrates effectively spreading out the heat, this value is typically less than 0.1 μV/°C [22] and can be neglected in this work.

Fabrication Process

In wirewound technology, different resistance values are realised by varying the physical length and width of wire and in thick film technology, the individual proportion of the components are varied to achieve varying resistivity. Now thin film technology has a limited number of successfully established material systems, hence design concepts are used to adjust the conductive tracks to realise the need for varying resistor values. The sheet resistance of a material, discussed in the previous section, becomes very useful in the design phase of thin film resistors.

From Eq 1.5

$$R = n \times Rs \qquad (1.8)$$

The maximum value of resistance which can be achieved on a substrate surface is dependent upon the maximum number of repetitive squares, *n*, of sheet resistance *Rs* that could be drawn on it, which is defined by the aspect ratio possible by the patterning technique. Therefore, from Eq: 1.3

$$n = \frac{L}{W} \qquad (1.9)$$

Now the patterning technique limits the lowest possible width of line, *w*, which could be drawn on a substrate surface, and in turn pins the upper limit of the aspect ratio which can be achieved. To achieve higher resistance values, films of higher resistivity or higher substrate area or higher aspect ratio or a combination of these options should be realised. Design of a thin film resistor covers a board range of topics other than the physical design of resistor. It decides the optimum parameters for the thin film deposition, suitable heat treatment for stabilisation of the film, and proper trimming method for tight tolerances.

As shown in figure 1-2 (a) and (b), wafers of the selected substrate are subjected to thorough cleaning by means of plasma and chemical agents. Dehydrating baking might be required to remove moisture content from the substrate surface. Removal of contamination from the substrate surface is a must to ensure the proper adhesion and integrity of the resistive film [27]. Cleaned substrates are then loaded into the deposition chamber maintained at high pressure of the order of 10^{-5} Pa. Sputtering is the most preferred vacuum deposition method employed to deposit refractory metals, and since most of the established thin film resistor material

systems are of refractory nature, sputtering is considered as the most suitable deposition method for this industry [19, 27]. The chosen material system is deposited by means of a perfectly tailored recipe to control working pressure, RF/DC power, and substrate speed. Normally deposition is carried out with non-reactive Argon ions, but in certain cases as in the deposition of Tantalum nitride, the deposition environment is deliberately made reactive by the introduction of Nitrogen or Oxygen, to deposit respective compounds [3]. Multiple cathodes are employed to deposit resistive and conductive films which are then subjected to photolithographic patterning to form resistive tracks and conductive contact pads.

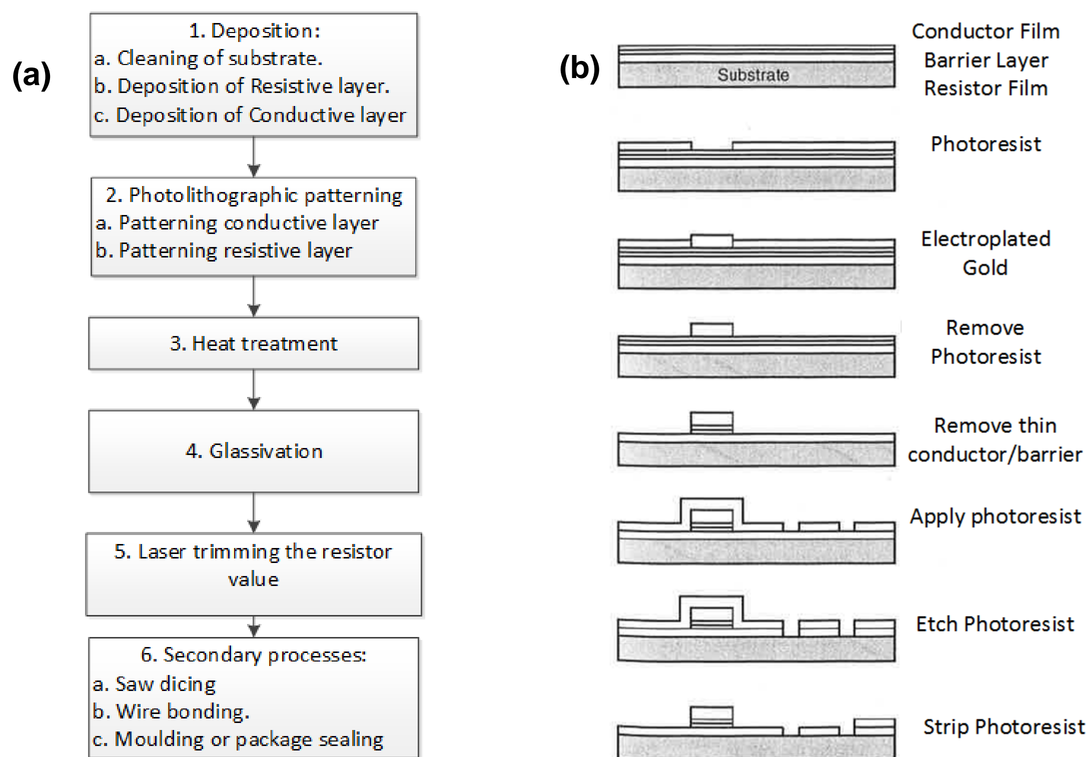

Fig 1-2 (a) General process flow of TFR fabrication [2] (b) Photolithographic deposition of resistive and conductive layers on the substrate [27].

The patterned thin film resistor structures are then subjected to heat treatment to stabilise their properties. The crystal structure of the as-grown film structure has many micro-imperfections and vacancies and subjecting them to heat treatment brings in structural, and chemical changes in the film by elimination of these vacancies and micro imperfections [28]. Stabilization in air leads to formation of an oxide layer on top of films, which leads to rapid increase of resistance during the initial duration of stabilization, and then settle to the stable resistance value, as

shown in figure 1-3 (a). Annealing temperature and time should be carefully chosen as a longer duration at a higher temperature can result in agglomeration of film islands resulting in an exponential irreversible increment in resistance value and loss of desirable properties as shown in figure 1-3 (b), [19, 29].

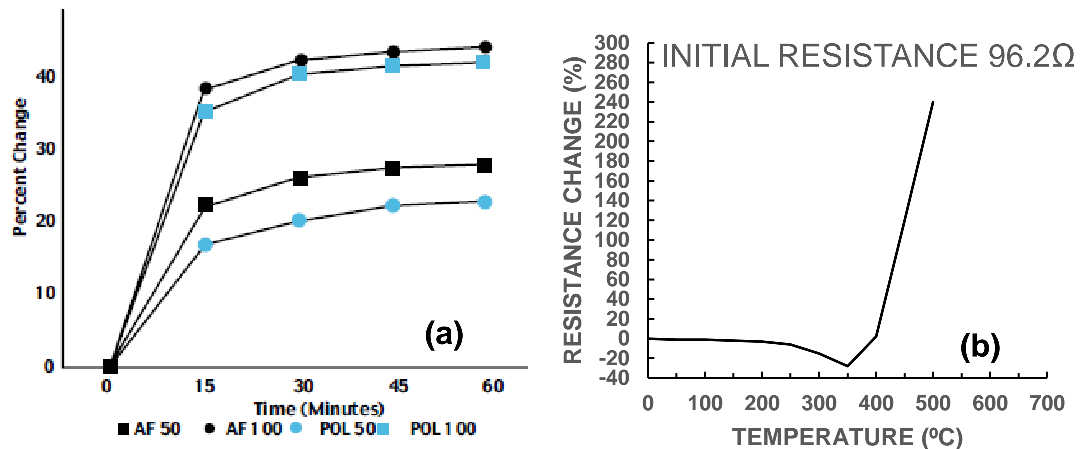

Fig 1-3 (a) Stabilizing effect of heat treatment on 50 and 100 Ω TaN resistors on as-fired and polished alumina substrates [30] (b) Graph showing agglomeration resulting in irreversible increase of resistance at higher temperature (redrawn from source) [19].

During deposition, the deposition conditions vary slightly from resistor to resistor according to its placement on the wafer, and the resulting inaccuracy and variation of the resistance value is referred to as the tolerance value of a resistor and is generally of the order of ±10% of the total resistance value [27]. Trimming is the process applied to bring the tolerance value of a resistor to a tighter value. The ratio of trimmed resistance value to untrimmed one is known as the trim factor. There are many trimming methods developed like anodization, heat trimming, electrical trimming and mechanical trimming, but laser trimming is the most widely applied trimming method [25, 27]. An Nd-YAG laser of suitable power is used to vaporise the resistive layer with minimum penetration to the substrate layer below, figure 1-4 (a) [31]. Component position is determined using a vision system and then the laser beam is focussed and moved over the resistive layer. The process can be passive, in which the required resistor value is measured to stop the laser beam or it could be active in which the laser stops and measures a specified parameter of an existing measurement system like AC/DC voltage or frequency and repeats the loop until a set value differs from the measured [31]. Laser power,

Q-rate (repetition rate), trim speed and bite size are the critical parameters of a laser used to form most common patterns of I, L, and M shape cuts on the resistor film figure 1-4 (b) [31, 32].

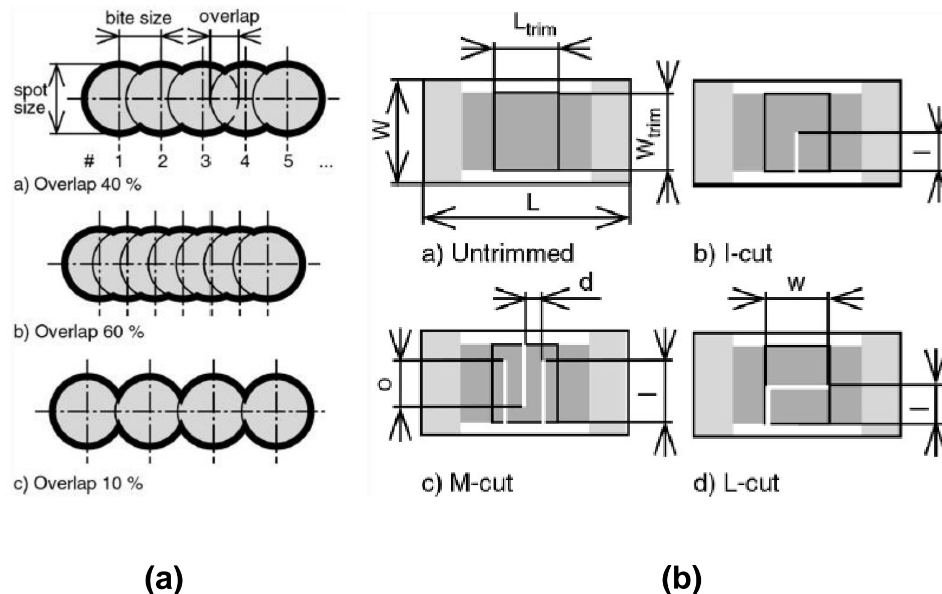

(a) **(b)**

Fig 1-4 (a) Relationship between spot size, bite size, and overlap (b) Different trimming geometries introduced by laser on resistive film [31].

The next stage of TFR fabrication involves coating the resistive film with its alumina substrate in a resin encapsulation to protect it against the environment. Materials like TaN are self-passivating, which means that the oxide layer formed during the heat treatment will safeguard them during the interaction with external elements like moisture [30] but for materials like Nichrome, a separate layer of passivating film of polyimide is deposited to protect the resistive film from environmental conditions [27]. On a wafer scale production, the final step is the singulation of the individual chips by dicing the substrate and breaking it into individual resistors and attaching the outer termination contacts. The exact sequence of TFR fabrication may vary from manufacturer to manufacturer and depends on the finished format of the products. Thin film resistors are produced as chip resistor (Surface Mount Device (SMD) format) or as axial lead resistors (through hole format) as shown in figure 1-5 (a) and (b) respectively.

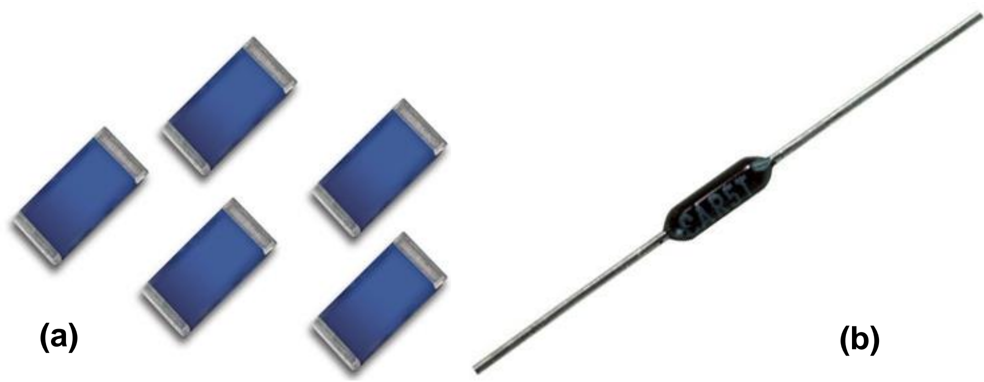

Fig 1-5 (a) Samples of PFC series SMD type resistors (b) CAR series through hole precision metal film resistor (image courtesy of TT electronics Ltd.).

Material Selection:

Performance properties can be improved by tailoring the various steps of TFR fabrication but these improvements strongly depend upon the choices made for materials systems to be used for individual components. Different components of a thin film resistor are shown in figure 1-6, and it is the combined effect of materials in all these parts which grants the final resistor product its performance levels.

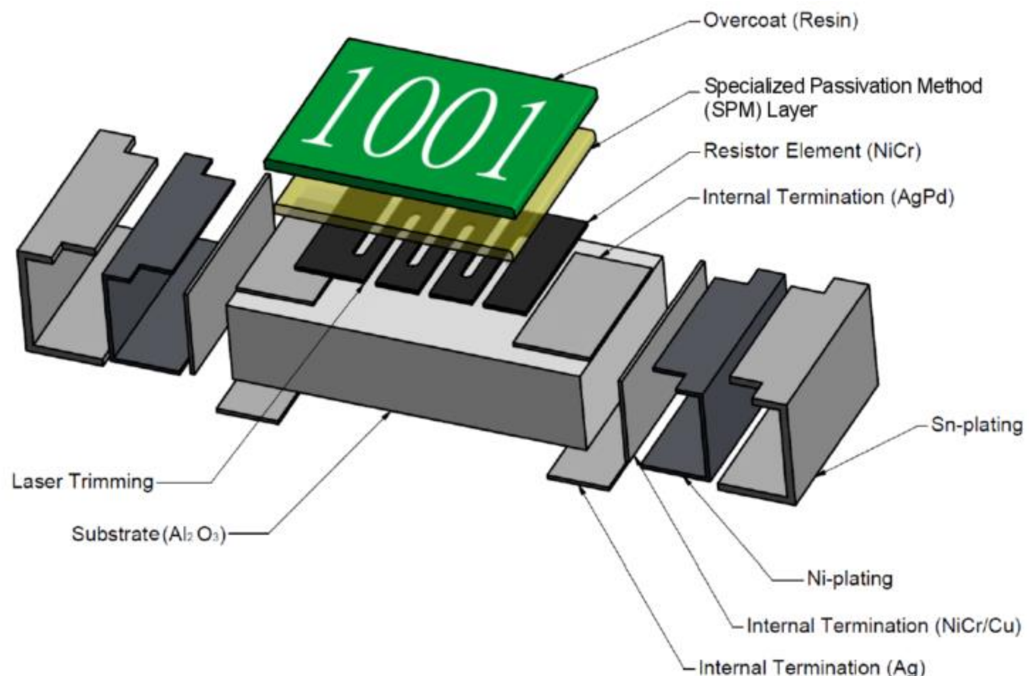

Fig 1-6 Schematic diagram showing parts of a chip type thin film resistor [33].

So care must be taken to ensure proper selection of material for each to match with the performance of others. Proper material selection is the focus of this project, hence a detailed explanation will be made in the second chapter, but to provide an overall view of the TFR fabrication process, an introduction to the importance of material selection will be presented here.

The substrate is the first material to be handled in a TFR fabrication process and it is used as a base to deposit the thin resistive film. Previously the substrate was seen only as a mechanical support to provide rigidity and surface adhesion, but to push the limits of electronic device performance it is required to consider many other factors previously overlooked. For example in metal foil resistors, substrates of comparatively smaller coefficient of thermal expansion than foil, are used to create stresses in the foil which results in negative TCR, to counter balance the positive TCR of the foil in the free state, to produce near zero TCR resistors [2]. Similarly surface roughness is reported to have an effect on sheet resistance, stability and TCR [19]. Surface smoothness, coefficient of thermal expansion, and surface uniformity, are some of the important substrate properties which bear an effect on the performance of thin film circuitry formed on them [27]. While mechanical strength, thermal conductivity, chemical inertness, electrical resistance, and cost, are some of the properties which decide if a particular substrate would be able to withstand the manufacturing process. The choice has to be made keeping in mind the effect substrate properties will have on the thin film but also on the ability of the substrate to pass through the manufacturing process. There does not exist one substrate for all thin film applications, but rather it is a choice made upon the acceptable compromise of these properties satisfying the need of the specific application. Alumina, glass, beryllia, aluminium nitride, silicon and metals are some of the commonly used substrates, and of these, alumina is the most commonly used substrate in thin film resistor fabrication.

The resistive material is the functional material system on the thin film resistor product, and hence the most important because all the other decisions from substrate material to deposition process, up to storage are made to work for the choice made for this resistive film. Most of the performance parameters discussed

in the previous sections are inherent properties of the material system chosen; they are fine tuned to the limits by strictly controlling the fabrication steps. There are many microstructure defects like dislocations, vacancies, interstitials, grain boundaries, impurities, island structures, agglomeration, etc., brought during the deposition. Material systems exhibit very different and generally preferential properties when deposited as thin films, because many of these defects which were dormant and hence ignored at bulk level, become dominant and effective when film thickness is comparable to their size.

Material systems successfully tried out in the resistor industry could be categorised under three classes: single metal system, metal alloy system and cermets [19, 34]. Tantalum nitride is the most successful example of single metal system, and is used to fabricate thin film resistors of very good stability in humid environments. Nichrome, an alloy of nickel and chromium is the most suitable and widely used example of a metal alloy system used to produce high precision TFR's. Nichrome resistors lag behind TaN resistors in stability performance in humid environments. A good example of a cermet would be the Cr-SiO system, which is observed to have very high sheet resistance and shift the TCR sign from negative to positive with annealing. A lot of research and studies are already conducted to improve the performance of these materials. An ideal ultra-precision thin film resistor material system will have sheet resistance in the range of 10 to 300Ω/□ with inherent TCR close to ±5 ppm/ºC and very high stability and be easy to incorporate into the existing fabrication process.

External environmental factors like humidity, temperature, and chemical agents affect the performance parameters of a resistor by degrading resistor tracks, as seen in figure 1-7. Hence, suitable protection must be provided to the thin film resistor to safeguard it from degrading under these conditions. Silicon monoxide is one such coating layer which is used to provide stability to Nickel-Chromium films under various atmospheric conditions. Polyimide is another material which is used to passivate Nichrome films to protect them under operating conditions involving higher load, humidity and temperature [35]. Specialised passivation techniques employed by manufacturers have the capability to drastically improve the stability

performance of Nichrome film resistors equal to or better than that of Tantalum nitride resistors [23]. Tantalum pentoxide, Ta_2O_5 is formed during anodization of tantalum films and acts as a protective layer. The most important requirement for a protective coating and its application process, is that it should not interfere with the performance of the resistive film [27, 35].

Fig 1-7 Microscope image of film resistor showing degradation of tracks [23].

Normally three different layers of material are deposited to provide external electrical contact to the resistive film. It is preferred to deposit the first or inner conductive layer after depositing the resistive layer to avoid the thinning of the resistive film at the step formed between conductive layer and substrate [19]. The Inner conductive layer ensures proper connection of external solder to the resistive thin film. Gold-platinum, palladium-gold and palladium-silver are some of the material systems commonly used to form the inner conductive layer [2, 36] where platinum or palladium ensures proper adhesion of the film, gold/silver provides the conductive nature of this layer. A thin layer of Nickel is generally used as a middle level termination or barrier layer to prevent diffusion between the contact pad and inner conductive layer [37, 38]. This layer also helps the films to withstand the wire bonding process [27]. Tin (Sn)-Lead (Pb) alloy or gold (Au) is the preferred termination finish provided by most manufacturers. Contact materials are exposed to external environments on a regular basis. This is of major concern when the external environment contains reactive agents like sulphur. Because of its greater affinity towards silver, sulphur can leach through external wrap around terminations, react with the silver present in the Pd-Ag contact layer to form silver sulphide and result in an open circuit [39]. For this reason, products like the WIN series resistors

from TT Electronics are manufactured with anti-sulphur terminations made by properly chosen material provides adequate protection.

1.7 Summary

It is evident from this introduction that performance parameters of thin film resistors depend upon the material system chosen and the fabrication process employed to bring these individual components together. Table 1-1 provides a summary of different material system used in various parts of a thin film resistor.

Table 1-1 Material systems employed in a typical TFR fabrication

Component		Material systems available
Substrates		Alumina
Resistive films		TaN, NiCr, Cr-SiO
Protective coatings		SiO, Polyimide, Ta_2O_5
Contacts	Inner	Pd-Ag, Pd-Au, Pt-Au
	Middle	Ni, Cr, Ti,
	External	Sn, Sn-Pb, Au

And choosing the right resistive material is the most important and the one which brings the revolutionising change in the performance parameters. NiCr and TaN have been in existence for a long time and are reaching their performance limits. Only limited improvement could be achieved by trying to optimise the fabrication process and choosing suitable supporting materials. There is an increase in demand for higher precision passive devices for accurate current measurement in medical (e.g. diagnostic equipment like MRI operating at high temperature), industrial (e.g. automation control circuits working under high temperature within industrial settings) and military and aerospace (e.g. precision guided Unmanned Aerial Vehicles and weapon systems). Therefore, it could be lucrative to keep researching and modifying the already existing material systems and fine tuning process parameters, but the interest to explore a new novel material system to develop thin resistive films, with better performance parameters needs to be taken further. It is therefore a big challenge to identify a novel material which could be fine-tuned beyond the limits of the already existing material systems whilst also being suitable for scale up for volume production.

CHAPTER 2 Literature review

2.1 Introduction

A basic literature search on thin film resistor returns a high volume of work published on resistive materials used in the fabrication of these devices and major developments in fine-tuning their properties, most of them on the established NiCr or TaN or CrSi systems. But there were also some notable attempts to develop low TCR property by exploring novel material compositions like co sputtered SiO_2-Pt [40], TiN_xO_y [41], CuAlO [42], Ruo_2-Tio_2 [43],Ta_3N_5-Ag [44] etc. However, most of these works were not able to extract any property better than NiCr.

2.2 Manganese: A starting point in the search

A further literature review for material with low TCR property revealed Mn based alloys like Zeranin and Manganin, which had extremely low TCR values and were in the same resistivity range as NiCr. Material data sheets published by precision material supplier Isabellenhütte shows a very low value of ±10ppm/^{0}C for Manganin (an alloy of Mn:Cu:Ni = 12:86:2) and Zeranin (an alloy of Mn:Cu:Sn =7:90:3). Another product from Isabellenhütte called Noventin (a Cu:Mn:Ni ratio of 65:35:10) is also reported to have very low TCR of ±10ppm/^{0}C [45-47]. This caused particular interest in low TCR behaviour of alloys having Manganese and Copper constituents.

Some of the earliest attempts to make thin film resistors out of Mn and its alloys were made in the late 1960s and 1970s. Hammond et al 1968 [48] and Olumekor 1977 [49] independently, make mention of achieving high resistivity and near zero TCR films by flash evaporation of mixtures containing cermets containing Manganese. It was Angadi et al (1984) who conducted a systematic study about the low TCR nature of pure Mn films and observed that they showed a near zero TCR of 30ppm/^{0}C with a fairly good stability of resistance value while having a resistivity in the range of 400 µΩ-cm [50]. Angadi`s group [51] believed that Manganese could be used as a new material system to fabricate TFR`s and claimed these to be better than the tantalum based material systems employed by industry. Their work also claimed that the TCR value and adhesion of Mn thin films

could be improved by changing the deposition parameters like substrate temperature. Their work further showed that Manganese thin films exhibit very low values of TEP (thermo-electric potential) which will contribute in the reduction of noise of junctions held at different temperatures. By adding a small layer, 50 nm, of SiO it was shown that resistance variation due to aging could also be reduced, hence improving stability. In summary Angadi et al. showed that pure Mn thin films have better resistivity, TCR and TEP, and lower cost when compared to tantalum films as shown in table 2-1. Another study performed by A.H. Ammar in 1996 [52] achieves similar results as Angadi et al. in 1984.

Table 2-1 Table showing electrical properties for thin TaN and Mn film.

Material	**Bulk Resistivity (P_b in μΩ-cm)**	**Film resistivity (P_f in μΩ-cm)**	**TCR (ppm/ºC)**	**TEP (μV/ºC)**	**Cost material (US$/g)**
Manganese	185	375	±5	0.7	0.37
Tantalum	13	180	±100	-0.9 to	1.5

Current research being carried out at Northumbria University on Manganin based shunt resistors also suggests that Manganese based resistors have good stability and tolerance of resistance [53]. While these works give really good results supporting Mn thin films as a good material for thin film resistor fabrication, because of lack of further work from these or other authors, this work could only be taken, at best, as a milestone arrow pointing in the right direction towards narrowing the search for the material system suitable for ultra-precise thin film resistors.

2.3 Introduction to the Perovskite structure:

As discussed in chapter 1, alloying different metals in suitable proportions (NiCr) or depositing metals in a reactive environment (TaN) is seen to bring resistivity and TCR in a suitable range for thin film resistor fabrication. But further literature study has revealed a recent rise of interest among researchers for a structure called antiperovskite: X_3AB [23], with repeated mention of thin films of this structure with Manganese having extremely low TCR [54]. Thus, this literature review will start

with an introduction to the much researched perovskite structure, and then develop its discussion to the antiperovskite structure that is obtained by exchanging the position of cations and anions in unit cell of the perovskite structure.

Calcium titanate ($CaTiO_3$) or Perovskite is a mineral, which was discovered in the Ural Mountains by German mineralogist Gustav Rose in 1839 and named after Count Lev Aleksevich von Perovski (1792-1856), a well-known Russian noble and mineralogist. Victor Moritz Goldschmidt, developer of Goldschmidt classification of elements, first described this structure in his work on tolerance factors in 1926 [55] and the perovskite name was given to a class of compounds with similar structure to that of calcium titanate $CaTiO_3$. The general formula of Perovskite compounds are: ABX_3, where A is a monovalent cation and B is divalent metallic cations of different sizes and the X site is occupied by a monovalent anion which bonds to both of them [56]. Goldschmidt described that stability of perovskite structures can be determined by the ionic radius of the individual species participating to form the structure by the following equation [56, 57]:

$$t = \frac{Ra+Rx}{\sqrt{2}(Rb+Rx)} \tag{2.1}$$

And axes of the unit cell can be given by:

$$a = \sqrt{2}(Ra + Rx) = 2(Rb + Rx) \tag{2.2}$$

Where *t* represents Goldschmidt's tolerance factor, and *Ra*, *Rb* and *Rx* represent the ionic radii of elements occupying A, B and X sites in the perovskite structure respectively.

The shape of the unit cell for a perovskite is determined by the value of its tolerance factor. For a value above 1 the structure will be hexagonal, while for a value between 0.9 to 1 it will shift to cubic and for those between values of 0.71 and 0.9 the shape will be orthorhombic or rhombohedral, and below a value of 0.7 another structure called Ilmenite will be formed [56-58]. Perovskites are of different types, like simple Perovskite , antiperovskite, inverse Perovskite, double Perovskite, and

double antiperovskite, according to composition and chemical interaction of the constituent elements within the compound [58].

Perovskite structures have been extensively studied because of their interesting properties like superconductivity, magnetoresistance, ionic conductivity and many others[59]. The Perovskite structure has found application in many research fields like solid oxide fuel cells, capacitors, optoelectronics devices, magnetic field detectors and sensors, and many more. However, photovoltaics is the subject for which perovskite structures have been extensively studied. Perovskite solar cells first made an appearance around 2009 with an efficiency of just 3.9% [60] but because of very high levels of interest in this material structure much progress has been made. One such example is Prof. Charles Chee Surya, of The Hong Kong Polytechnic University who, in 2016 developed a perovskite-Silicone tandem solar cell with the world's highest efficiency of 25.5% [61].

As the name suggests the antiperovskite structure is realised by exchanging the positions of cations and anions in the unit cell of a perovskite structure. For antiperovskite, the X is an electropositive cation situated at the face of the unit cell cube with a coordination number of 6. While B represents a divalent anion at the octahedral positions at the unit cell corners and A is a small interstitial element forming a monovalent anion sitting at the centre of unit cell cube. Figures in 2-1(a) and 2-1(b) show this exchange of ions within unit cell between both the structures. Roughly a decade after perovskites were described by Goldschmidt, F.R Morral, in 1934 [62] described a cubic cell structure having heavy iron atoms at the cubic face and aluminium at the cubic corners with a trapped C atom in its cubic centre which is an antiperovskite structure. The same formula for tolerance factor and unit cell size from perovskites applies to antiperovskite as well, and just like perovskites, the properties of antiperovskite depend greatly upon the individual elements of the structure and it can be fine-tuned by varying the concentration of constituent elements in the structure.

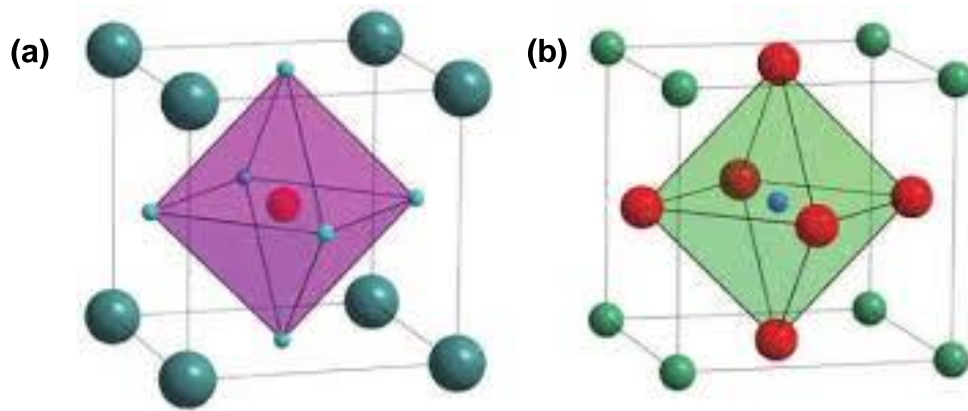

Fig 2-1 Simplified representation of cubic unit cell (a) perovskite structure (b) antiperovskite structure [54].

Despite having all these common factors and being introduced around the same time, research interest gathered very quickly for the perovskite structure while antiperovskites didn't catch attention until late 1980`s. As of March 2018, a basic search on databases of peer reviewed literatures, like Scopus website, with the word "perovskite" returned a total of 1,80,006 documents with the earliest document recorded in 1934 (yearly rise represented in figure 2-2) and on a similar database from web of science website returned 62,501 documents with the earliest one recorded in 1970.

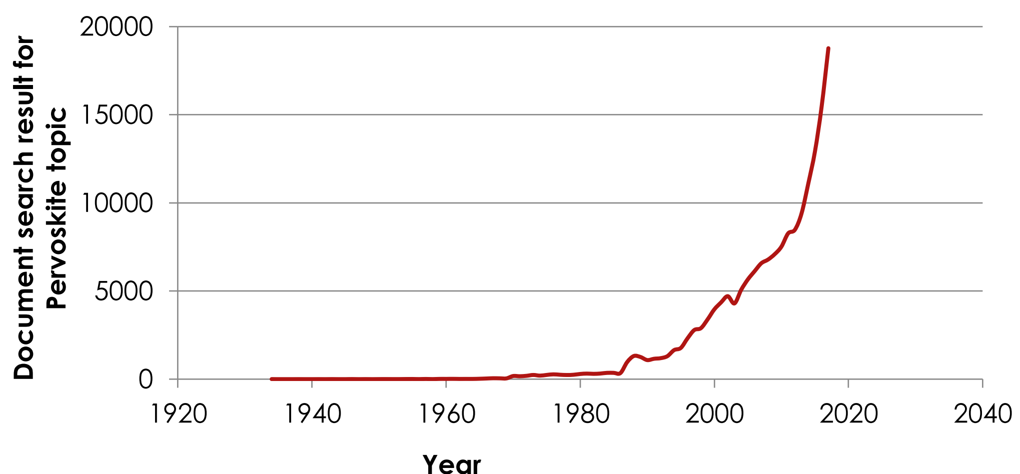

Fig 2-2 Graph showing no of articles published on perovskite research since 1920 on yearly basis. [Source Scopus]

The late rise of interest is evident from the number of documents found for the antiperovskite structure which is comparatively very low with 1411 documents from Scopus with the earliest recorded in 1989 (yearly rise represented in figure 2-3) and web of sciences with 390 documents with the earliest record in 1992. This gives a strong indication that study related to the antiperovskite structure is still in its infancy and this indication will be strengthened in further sections below. This will also form the basis for the original contribution to knowledge by supporting the fact that the antiperovskite structure has not been scientifically explored for its unique properties.

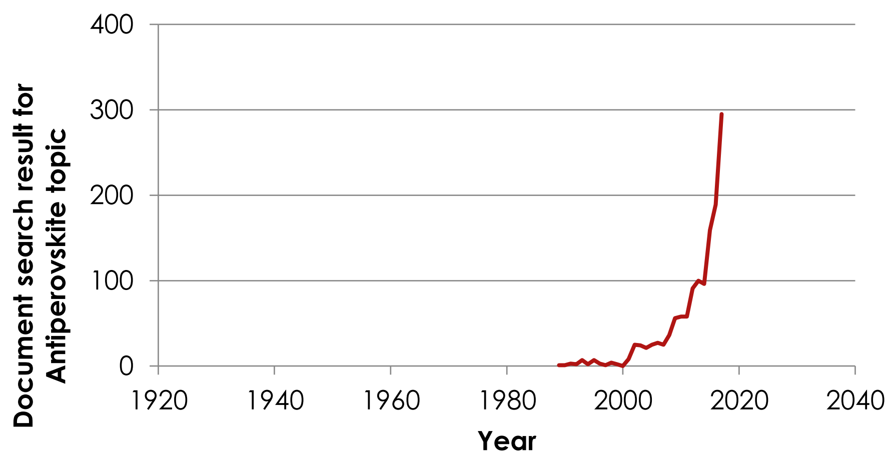

Fig 2-3 Graph showing the no of publication related to antiperovskite structure since 1920 on yearly basis [source Scopus].

2.4 Antiperovskites and their unique properties:

According to Bilal et al. [58] there are two types of antiperovskites: group II- A based antiperovskites where the A site at the unit cell face centres are occupied by metals from group II, but these are mostly insulators or semiconductors. There is a second group of antiperovskite known as transition metal based antiperovskites in which a transitional metal occupies the face centre, and cubic corners are occupied by a metal or semiconductor element and the cubic corner by interstitial like C or N.

2.4.1 Unique properties of the antiperovskite structure:

These antiperovskite structures are reported to have functionalities such as: superconductivity (SC), giant magnetostriction (MS), large magnetocaloric effect (MCE), negative or zero thermal expansion (N or ZTE), giant magneto resistance (GMR), piezo magnetic effect, and near zero temperature coefficient of resistance (NZTCR) [54, 63]. Discovery of superconductivity in Ni_3MgC by He et al [64] in 2001 led to renewed interest in the properties of the antiperovskite structure. Since then many other antiperovskites have shown superconductivity like Ni_3CuN [65], and Ni_3CdC [66]. Giant magnetostriction is a property by which a material can change its shape when subjected to a changing magnetic field by realigning the micro magnetic domains without changing the actual volume of material. Because of this exchange between magnetic field and mechanical form, these materials are of importance for actuator and sensor application [67]. Giant magnetostriction is observed in Mn_3CuN (up to 2000ppm) [68] and Mn_3SbN (up to 1000 ppm) [69]. The magnetocaloric effect is the thermal response of a material when subjected to a magnetic field. Developing a refrigeration system based upon magneto-caloric effect will help get rid of current refrigeration system which uses ozone depleting chemicals [70]. Mn_3GaC antiperovskite structures have shown very large magnetocaloric effect [71] and continued research in this field has led to the development of $Fe_3Sn_{1-x}Ga_xC$ [72], (antiperovskite structure of Fe and Sn with Ga partially replacing Sn) with relative cooling power or RCP of 3.22J/cm^3 which is comparable to the RCP of Gadolinium (Gd) a naturally occurring element having high magnetocaloric effect. Most of the material expands upon heating, but materials which contract upon heating or those having negative thermal expansion

coefficient, would find a wide range of application from dental fillings to high precision optics [73]. antiperovskite structures like Mn_3CuN, Mn_3GaN and Mn_3ZnN [74, 75] have shown very high NTE around -30ppm/K which is better than other well-known NTE materials like ZrW_2O_8. Giant magnetic resistance is a property by which the electrical resistance of a material changes depending upon the magnetic field which realigns the magnetic domains in a parallel or antiparallel manner and can find application in magnetic field sensors and hard drive read heads etc. [76]. Mn_3GaC and Zn doped Mn_3GaC are reported to exhibit enhanced giant magneto resistance [77, 78].

2.4.2 <u>Low TCR properties of the antiperovskite structure:</u>

Therefore, we can see that transitional metal based antiperovskite structures have many interesting and highly sought after properties. Manganese based antiperovskites are a member of this family and have unique properties for which this particular structure is well known. Near zero TCR experiments reported so far are based upon this family of antiperovskites. Low TCR behaviour is reported by the Mn_3AN structure with Ni, Ag, Co, Zn, and Cu at the cubic corners represented by the flat nature of curves after magnetic reordering temperature T_c, in the figure 2.4, [79]. Most of these experiments use Kelvin scale to represent lower temperature ranges as well, the dotted line represents the region of interest in Celsius scale lying between 0˚C and 70˚C required for this project.

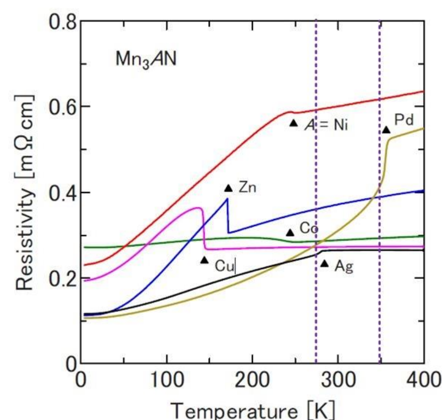

Fig 2-4 Graph showing the low TCR nature of members from Mn based antiperovskite family [79].

Manganese –Copper antiperovskite structure:

In 2001 Chi et al., reported a very low value of TCR for Mn_3CuN, of around 46 ppm/^oC which is two orders of magnitude less than their constituent elements and with a high value of resistivity between 2000-3000 μΩ-cm [80]. This work opened a new scope for antiperovskite material to be developed into standard and precision resistive applications. Chi et al observed a sharp drop of resistivity value around a transition temperature T_c, at which the magnetization data also showed a transition from a paramagnetic to ferrimagnetic phase. In addition, at this temperature the shape of the unit cell is seen to change from tetragonal to cubic. Moreover, after these transitions, the resistivity curve is seen to be independent of change in temperature see figure 2-5 (a). Another point observed by Chi et al. is that even though it looks like the low TCR nature coincides with rearranged magnetic alignment, the nature of TCR after realignment is independent of the surrounding magnetic field, and becomes an inherent nature of this material above its transition temperature Tc as seen in figure 2-5 (a).

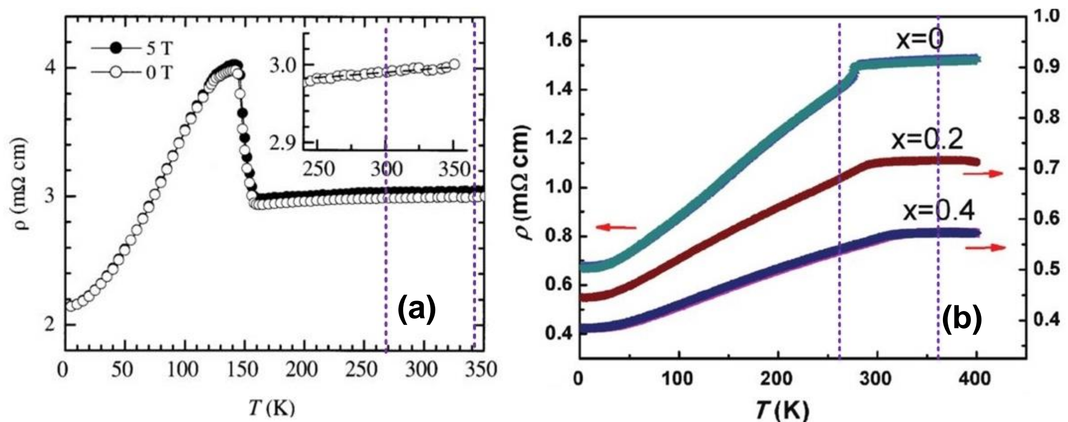

Fig 2-5 Graph of temperature dependent variation of resistivity for (a) Mn_3CuN [80] (b) $Mn_3Ag_{(1-X)}Sn_{(X)}N$, x representing the content of Sn in the film [81].

But when experiments were conducted by Ying Sun et al [82, 83], thin films of Mn_3CuN exhibited a resistivity curve similar to a semiconductor material in which the resistivity was found to decrease with increasing temperature, unlike the bulk sample prepared by Chi et al., which exhibited the metallic property of increasing resistivity with temperature. A similar kind of magnetic transition from paramagnetic to ferromagnetic was observed by Ying sun et al (2011) in one of their films. Both

of these studies agree on the transition temperature for Mn_3CuN structure (bulk or thin film) to be around 143K at which the structure starts showing low TCR nature, thereby making it suitable for room temperature applications. Deposition parameters like substrate temperature, target to substrate distance, partial Nitrogen pressure and total pressure can be used to fine tune the electrical and magnetic properties of these structures [83, 84].

Manganese –silver antiperovskite Structure:

Similar low TCR values are observed in Mn_3AgN [81] with a TCR value of 102 ppm/^oC and a resistivity value of 154 μΩ-cm in bulk samples prepared by solid state sintering. Mn_3AgN also shows metallic behaviour and increases its resistivity with temperature and its resistivity value shows a sudden independence above the transition temperature of 274K. The Magnetic transition from paramagnetic to antiferromagnetic phase is observed around 260K. By doping this system with Sn or Zn it was possible to reduce the TCR value to 31 and 36 ppm/^oC respectively. The lowest value of 23ppm/^oC was observed in $Mn_3Ag_{(1-x)}S_{(x)}N$ with a value of X=0.4. These values were observed to be stable and reproducible as seen in figure 2-5(b).

Manganese-nickel antiperovskite structure:

Mn_3NiN is another member of the Mn based antiperovskite family which exhibit the metallic nature in bulk with resistivity in the region of 500μΩ-cm and very low TCR of 123ppm/^oC [85]. Magnetic transition for this material system occurs above 250K from ferromagnetic to paramagnetic phase. In thin films of Mn_3NiN semiconducting nature was observed [86] unlike its bulk counterpart . A High level of MR effect (up to 31%) was observed in these thin films, which was also not found in their bulk counterpart. Similar differences in nature of resistivity change and MR effect were observed between thin films and bulk samples of Mn_3CuN samples. Thin film characteristics of Mn based antiperovskite differ to a great extent from their bulk counterpart but most of the experiments conducted in this family of material system are mainly done on bulk samples [82, 86].

Ternary Manganese antiperovskite structures:

The TCR results from binary antiperovskite films are still much higher than the required TCR of 5ppm/ºC to find application in the fabrication of ultra-high precision thin film resistors. Partial substitution of the transition metal by a third metal is seen to provide better control to fine tune these properties. For example by varying the partial concentration of Cu in the Mn_3AgN system, K. Takenaka et al (2011) were able to achieve TCR values as low as 6ppm/ºC in a temperature range of 280K to 322K having a resistivity value between 200 to 300μΩ-cm [79], see figure 2.6(a). It was observed that the Mn_3AgN structure undergoes a transition from the paramagnetic phase to the antiferromagnetic phase at 280K whereas Mn_3CuN exhibits a transition from paramagnetic to ferromagnetic phase at 143 K [87]. Moreover, since TCR also suddenly drops closer to zero at this point, it is expected that rearrangement of magnetic domains cause the extremely low TCR nature of this solid solution.

Takenaka et al. were successful is achieving extremely low TCR values of 0.42ppm/ºC for a resistive block of $Mn_3Ag_{0.6}Cu_{0.4}N$ having a resistance value of 0.88Ω [87]. T.Oe. et al. (2013) were able to supress the drift rate of $Mn_3Ag_{0.7}Cu_{0.3}N$ samples to low values of 9.1μΩ/Ω/year by annealing at high temperatures and by use of proper contact materials [88]. Lei Ding et al in 2011 did the same experiment by partially substituting Ni in Mn_3NiN by Cu thereby making $Mn_3Ni_{(1-x)}Cu_{(X)}N$ [89]. For a value of X=0.3 i.e. $Mn_3Ni_{0.7}Cu_{0.3}N$ a resistivity value close to 800 μΩ-cm and a TCR value of 22 ppm/ºC was obtained for a very broad temperature range of 260K to 360K, figure 2.6(b). And for X= 0.5 i.e. $Mn_3Ni_{0.5}Cu_{0.5}N$ a TCR value of 0.09 ppm/ºC is obtained within a temperature range of 300 to 330K for a resistivity value of 280μΩ-cm [89].

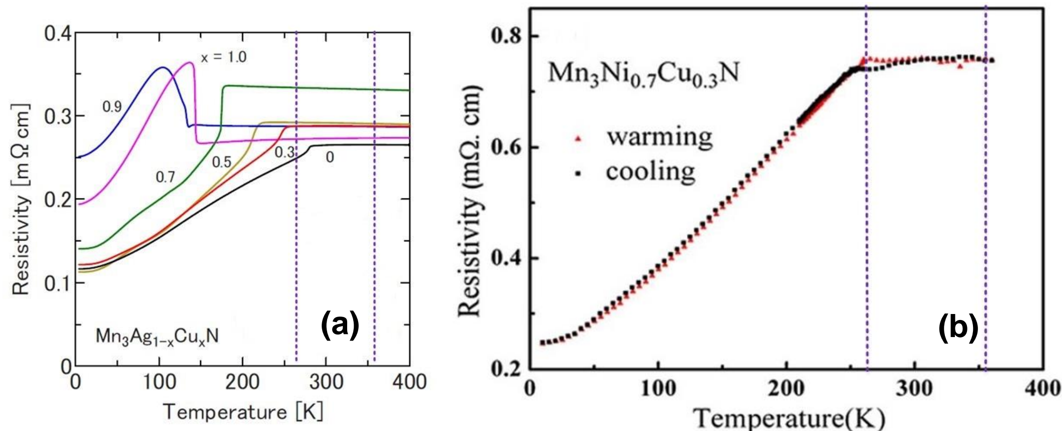

Fig 2-6 Graph showing effect of ternary doping on TCR values of (a) $Mn_3Ag_{(1-X)}Cu_{(X)}N$ [79] (b) $Mn_3Ni_{0.7}Cu_{0.3}N$ [89].

While some experiments and results were available on thin film deposition of binary Mn_3AN structures like Mn_3AgN and Mn_3CuN, no publications were found which contained experiments of ternary metal introduced into the Mn_3AN system. All of the ternary depositions were performed on bulk samples made by solid state sintering [79, 87, 88]. In 2016, N.P.Lu et al., for the first time achieved a low TCR value of 20ppm/ºC in ternary thin films of $Mn_3Ag_{(1-X)}Mn_XN$, for a resistivity value of 250-350µΩ-cm. Mn_4N can be seen as an antiperovskite structure of Mn_3NMn, with Mn on both face centre and cubic corners. The Ternary film of Lu et al is achieved by replacing Mn atoms at the cubic corner which are weakly bonded with Ag atoms [90]. According to Lu et al., with increasing concentration of Ag, the conductive behaviour of Mn_4N changes from metallic to semiconductor. For $Mn_3Ag_{(1-X)}Mn_{(X)}N$ this border between metallic and semiconductor state is observed at X= 0.81 and it is at this border where lowest TCR is also observed [90].

Despite all these previous experiments there are no unified and widely accepted theories explaining the low TCR nature of the Mn based antiperovskite structure. Most of the experiments performed on antiperovskite structure makes use of magnetic property measurement system (MPMS) to correlate the effect of changing magnetic domains orders with changing temperature on the electrical properties of these materials. It is obvious to believe that underlying physics change slightly with each element varying at the cubic corner or with partial substitution of elements at cubic corners. However, the presence of a low TCR

nature in so many Mn based antiperovskite structure stands for the fact that a there should be a very basic underlying principle which governs its existence irrespective of the changing element at the cubic corner. Some of the proposed theories for Low TCR behaviour of antiperovskite structures are:

1. Temperature dependence of Carrier density and carrier mobility: Chi et al believed that a low resistivity slope (dρ(T)/dT) in combination with a large resistivity (ρ0) is considered to be the reason for the low TCR of Mn_3CuN [80]. For Mn_3NiN, it is explained as a delicate balance between carrier mobility and carrier density, (which are both temperature dependent) at the transition temperature being responsible for its low TCR [85]. And because of this dependence on carrier mobility and carrier density, Y.Sun et al believes that the low TCR nature relates to the outer electronic structure of the metals at the X sites (cubic corners) [85]. This relationship looks possible because all the three metals Ni, Cu and Ag lie adjacent to each other in the periodic table and hence have similar electron configuration.

2. Restructuring of magnetic domains above the transition temperature: For all antiperovskite structures a sharp transition in physical and electrical properties is observed at the magnetic transition temperature, above which magnetic domain orders re arrange [54]. Lei Ding et al (2011) explains that in the Mn_3NiCuN structure, resistance keeps increasing with increasing temperature because of long range order, and above the transition temperature this increasing magnetic domain disorder destroys the long range order, making the short range domain orders more effective [89]. This is understood that for long range orders, band structure are arranged so that transfer of electron from valance band to conduction band becomes easier and upon increase of temperature, these electrons collide with each other and increases resistance thereby showing PTCR effect. De Gennes and Friedel explained that the short range magnetic orders exhibit negative TCR [91] and thereby balance the positive TCR produced by the vibrating electrons, making the net effective TCR value of the overall structure closer to zero.

3. Resistivity saturation effect: In the resistivity saturation effect the mean free path of conduction electrons becomes shorter than the interatomic distances because of a collapse of quasi particles, and thereby inhibits further increases in resistivity with increasing temperature [92, 93]. For Mn_3AgN, TCR is observed to reach its lowest value when resistivity is seen to approach its maximum value after its transition temperature, so the resistivity saturation effect can be related to the low TCR nature [81]. This same phenomenon is believed to be at play in Mn_3AgCuN, but the improvement of TCR value from 102 ppm/ºC in Mn_3AgN to just 6 ppm/ºC in Mn_3AgCuN was ascribed to the partial substitution of silver atoms at the cubic corner by Copper atoms thereby optimizing the electronic structure close to the fermi level [79].

2.4.3 Existing TFR material systems with Mn based AP structures

Table 2-2 shows the comparisons of the electrical properties of established thin film resistor material systems like NiCr against members of the Mn based antiperovskite family. From the table one can observe that partially substituted Mn based antiperovskite structures have electrical properties suitable for high precision thin film resistors. Comparing the values of NiCr to Mn_3AgCuN, one can clearly see the potential of the latter for resistive applications: similar resistivity range and better or similar TCR values. Since the primary motive of experiments conducted on the antiperovskite structure were not to develop a material suitable for the resistor industry, the stability figures are absent for most of them. However, the drift rate value for Mn_3AgCuN is shown to be 9.1μΩ/Ω/year, which can be used as a very good indicator of stability during shelf life for a resistor product. Though the certain composition (X =0.5) of Mn_3NiCuN has shown TCR values as low as 0.09ppm/ºC [89], the inherent magneto-resistive nature of Mn_3NiN will result in a resistive product made out of it to change its resistance value if a magnetic field is produced within an electric circuit and hence discourages its use in thin film resistor production [86].

Table 2-2 Table showing electrical properties of established TFR materials against members of Mn based antiperovskite family

Material systems	**Nature of material**	**Resistivity (µΩ-cm)**	**TCR (ppm/ºC)**
NiCr[94, 95]	Thin film	200-500	±5
TaN[96, 97]	Thin film	242-1126	±15
Mn[49, 50]	Thin film	375	±5
Manganin[46]	Bulk	43	±10
Mn_3CuN[80]	Thin film	2000-3000	+46
Mn_3AgN[81]	Thin film	140-200	+102
Mn_3NiN[85]	Thin film	500	+123
Mn_3AgCuN[87, 88]	Bulk	200-300	0.42-6
Mn_3NiCuN[89]	Bulk	800	0.09-22

As discussed in chapter one, NiCr, TaN, and Ru containing compounds are the industries favourite material systems for high precision thin film resistor fabrication. However, they have their own shortcomings. Virtually every chromium ore contains hexavalent ion Cr^{+6} and compounds containing this ion are regarded to be a genotoxic carcinogen [54, 98]. Chronic inhaling of this ion in the work environment can substantially increase the risk of lung cancer. Ruthenium is a rare earth element and hence increases the cost of production significantly. Hence, successful implementation of Mn based antiperovskite structure for production of ultra-precise thin film resistors will be a benefit in both an economic and environmental sense.

Because of the relatively uncharacterized nature of the antiperovskite structure, much less information is available about the preparation and analysis of its thin film form. In addition, the information pertaining to its underlying physics that gives these unique properties is also not well known. This will be a new approach in the field of TFRs, to move away from the established material system and to experiment with a new one. Hence, it will be a challenge to narrow down the proper deposition parameters, data analysis and feasibility studies for its commercial application.

2.5 Methodology

TT Electronics PLC, Bedlington, UK, is an innovative global electronics company, supplying passive components to world leading manufacturers in transportation, industrial, aerospace, defence and medical markets. TT Electronics PLC has joined in this project as a collaborative partner along with Northumbria University, Newcastle upon Tyne, UK, to develop a material system suitable to fabricate thin film resistors with very high precision and stability. The flowchart in figure 2-7 shows a generalised version of the process flow followed by TT Electronics in their Bedlington facility to fabricate high precision chip resistors.

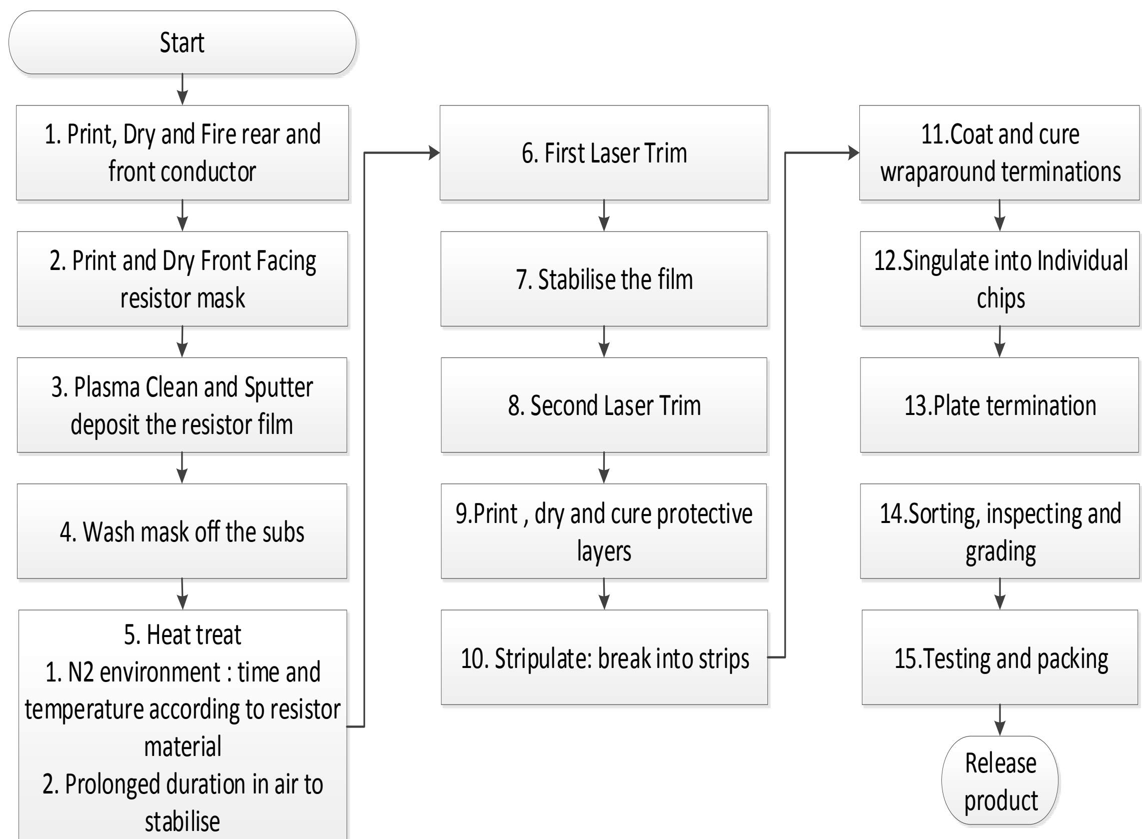

Fig 2-7 Typical process flow for chip resistor fabrication [courtesy TT Electronics, UK].

The project is designed to be carried out on a small scale in Northumbria University facilities and in a way to stay as close to the original process flow engaged in the industry. This project aims to cover from step 1 up to step 8 of the commercial TFR fabrication process in Figure 2-7 to determine the most suitable composition of the

novel antiperovskite material system. This will make it easier to transfer the developed process on to a commercial scale later on. Figure 2-8 shows the methodology (colour coded according to the chapters of this thesis) designed to tie in the three main stages of the project with its aim as discussed in chapter 1:

1. Deposition and characterization of Mn_3AgN and Mn_3CuN binary thin film antiperovskite structure to investigate the low TCR nature of these structures. In this stage, it is aimed to identify proper deposition parameters to achieve results as mentioned in the literature search.

2. Deposition and characterization of $Mn_3Ag_{(1-x)}Cu_{(X)}N$ ternary thin film antiperovskite structure by substituting Cu in Mn_3AgN under the deposition parameters identified in first stage, to explore the possibility of pushing TCR values closer to zero, as found in literature search.

3. Test the response of the most suitable university developed thin film composition towards the commercial laser trimming process using the facilities at TT Electronics Bedlington, UK; to anticipate the expected final performance of the fabricated thin film resistors made with Mn based ternary antiperovskite thin film.

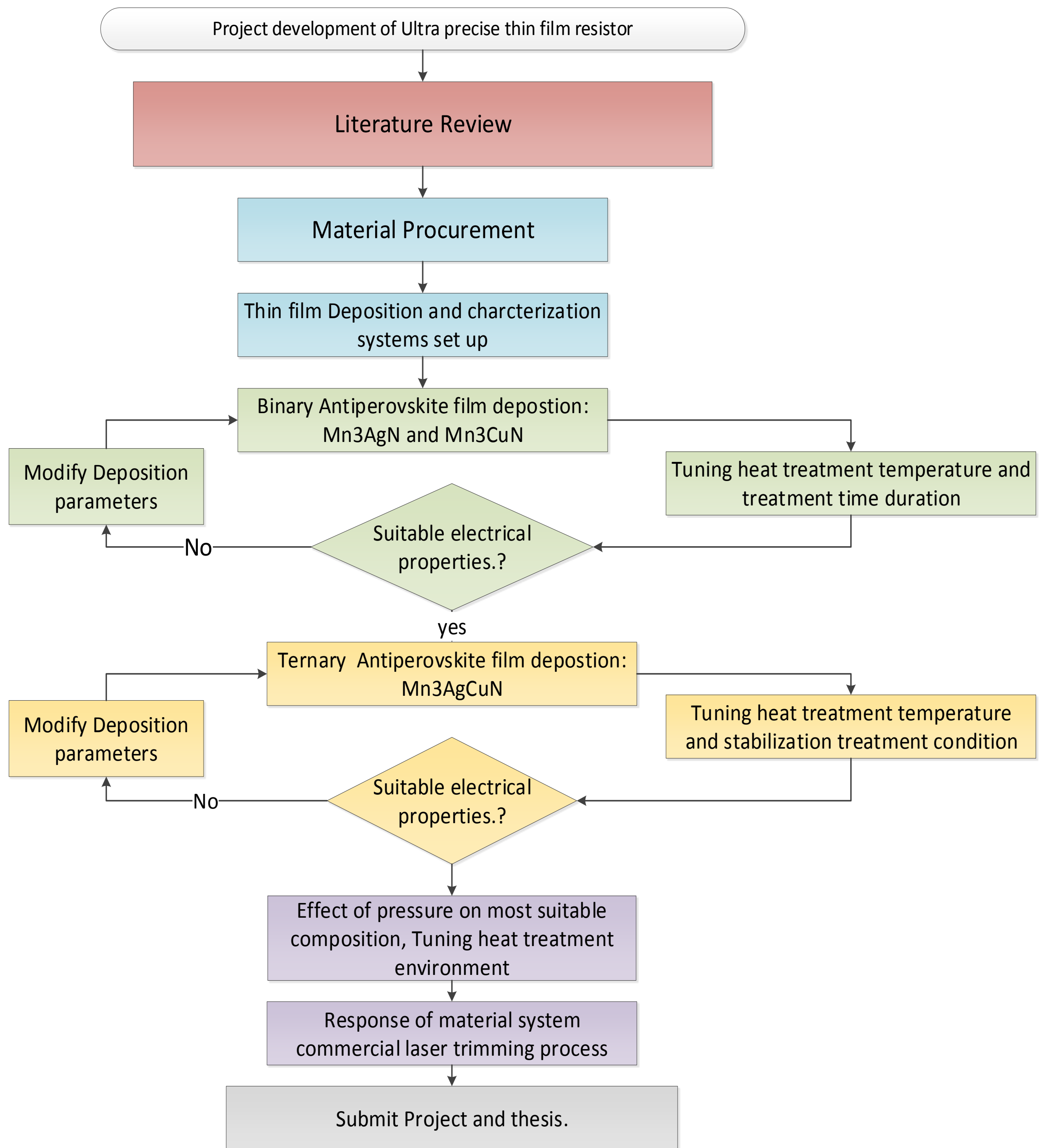

Fig 2-8 Flowchart showing the stages as per performed in further chapters.

2.6 Summary

The literature review conducted in this chapter has explained that the family of Mn based antiperovskite structures exhibit many interesting properties and extremely low TCR is one among them. The outcome of this review strongly favours a study of a Mn based antiperovskite structure, with Cu partially replacing Ag as a potential candidate for this project. This material system has a resistivity range similar to current material systems like NiCr and TaN, with better promise of TCR values. It is also evident from this literature search that very few works exist which deal with the development of these structures for thin film resistor applications. Therefore, this will be a new approach for TFRs, to move away from the established material systems and to experiment with new ones. Binary films of Mn_3AgN and Mn_3CuN will help to narrow down to suitable deposition parameters. Ternary films of $Mn_3Ag_XCu_{(1-X)}N$ developed from these results could be used to develop test samples helping to analyse the feasibility of this material system in the TFR industry. This new approach will potentially have rewards and risks of its own.

CHAPTER 3 Thin film deposition and characterization system

3.1 Introduction

As explained in chapter 1, the main objective of this work was to identify a novel material system with electrical performance values comparable to metal foil resistor technology, and study the deposition process suitable to produce repeatable and reliable results, which could later be incorporated into industrial scale production. In addition, from chapter 2, Mn based ternary antiperovskite thin film structures were identified to hold favourable electrical properties for use in precise thin film resistor fabrication.

Bulk samples used in most of the above mentioned literature review were produced by solid state sintering, mixing precisely calculated amounts of constituent materials (Mn_2N, Ag/Cu) in the presence of a plasma or high pressure [79, 88, 99, 100], thereby creating the stoichiometric composition required for the antiperovskite structure. Whereas, to deposit thin films of antiperovskite structure, most of the groups have preferred physical vapour deposition like sputtering. Both RF [90] and DC [75, 82-84] sputtering have been used by various groups to produce thin film antiperovskite structures.

A sputtering system is made up of many subsystems as shown in figure 3-1, of which primary importance are: vacuum system, target biasing system, substrate stage, gas inlet system and target cooling system. A vacuum system creates a vacuum environment inside the chamber in which controlled amounts of inert (Argon) or reactive ($Ar+N_2/O_2$ etc.) gas species are introduced by the gas inlet system. When biased, Argon is stripped of its outer electron creating Ar^+ ions. The target biasing system biases the targets made out of the required material to be deposited. This accelerates the Ar^+ ions towards targets and these ions on impact knocks out target material into the chamber environment and deposits them onto the substrate held by the substrate stage. The target gets heated up in this process and is cooled by the target cooling system. In addition, there could be other systems in place to perform additional functions like substrate rotation, substrate heating, in-situ measurements, etc. Understanding the capabilities and limitations

of the in house deposition system helps in better design of the experiments for further stages.

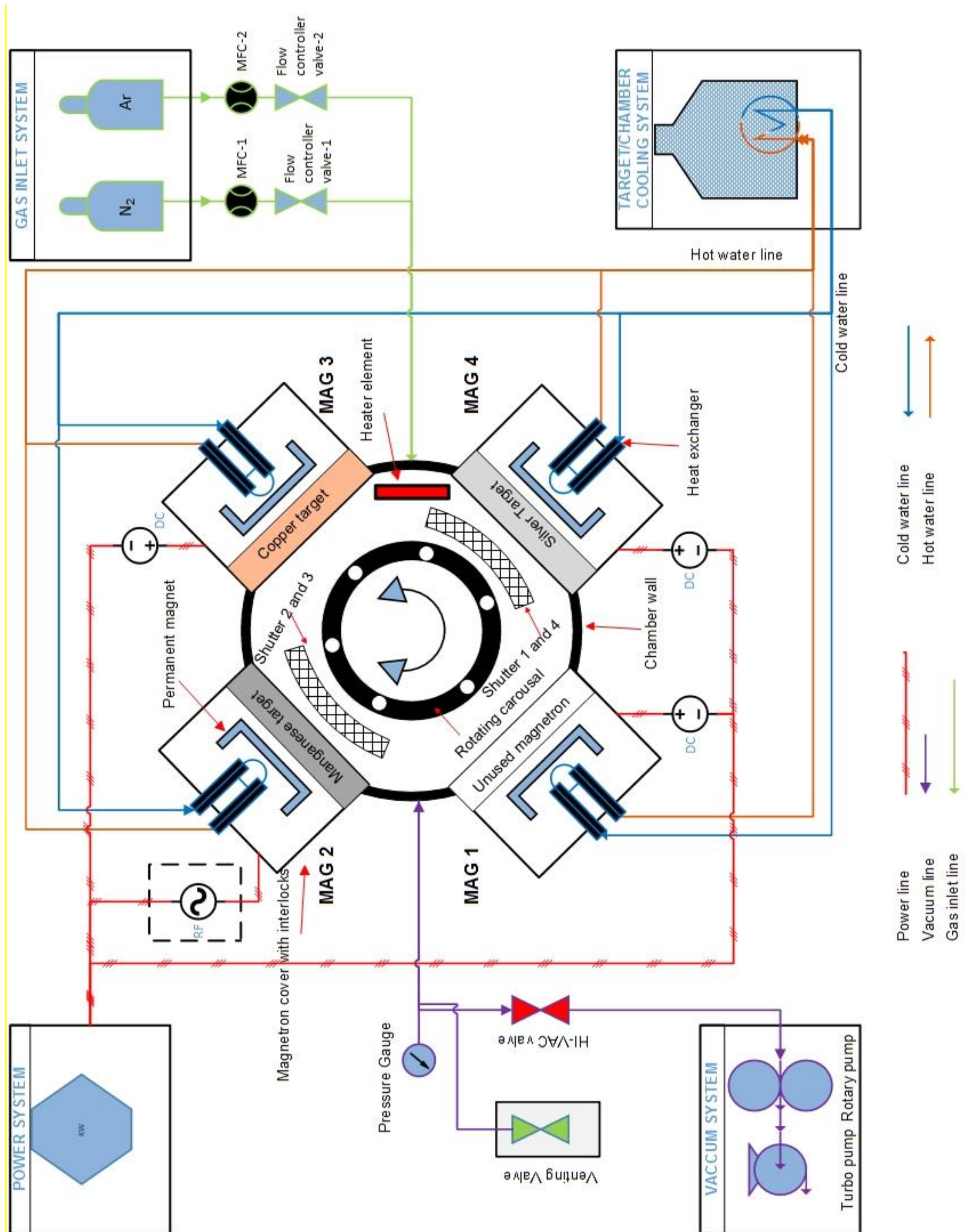

Fig 3-1 Schematic diagram of top view of UDP 350 plant and subsystems

3.1.1 Deposition system:

The depositions of binary and ternary samples were carried out in a Teer Coating UDP 350 multi-cathode sputtering plant. This deposition system had 4 magnetrons: two rectangular and two circular, with a target in each, see figure 3-1. Three of these magnetrons were configured for DC sputtering mode and one in RF or DC mode. The Teer Coatings UDP 350 lacks a load lock system, and multiple pressure gauges were connected to the main chamber using feedthrough valves. The pumping speed of the system was very slow and took approximately 24 hours to reach an acceptable base pressure range of 1×10^{-5} mbar allowing only one deposition per day.

The substrates were loaded onto a substrate holder, as shown in figure 3-2, which were then attached to vertical poles of a circular carousal. The carousel was free to rotate on its axis, and in one rotation, the carousel exposed the substrate to plasma plumes from each of the four magnetron targets. The substrate to target distance using this carousel is 130mm.

There were four gas inlets to the chamber to allow reactive sputtering. Mass flow controllers attached to each inlet provided precise control over the flow rate of each gas. Argon was connected to gas line 1 and was the primary gas used for the non-reactive sputtering. A supply of Oxygen or Nitrogen could be given to the second and third gas inlets, controlled by mass flow controller 2 as shown in figure 3-1, to allow for reactive environment in the chamber. The fourth inlet provides Nitrogen to vent the chamber to atmospheric pressure after deposition.

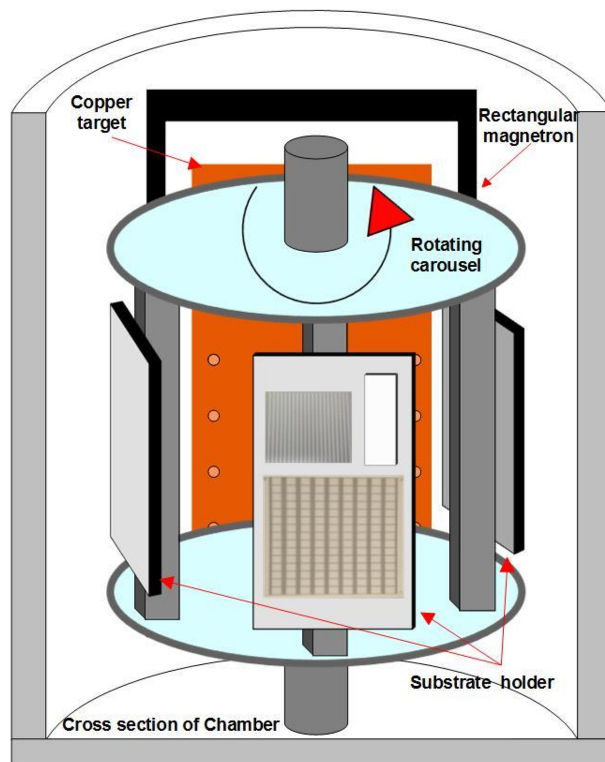

Fig 3-2 Cross-section diagram of inner arrangement of the UDP 350 plant showing vertically loaded substrate.

3.1.2 Target Materials:

In the publications related to thin films of the antiperovskite structure, it was found that the authors have used a Manganese disk as the primary target and then placed calculated amounts of Copper on top of this target to achieve the required atomic ratio of 3:1. However, for an investigative approach it was deemed better to explore a wider composition and then narrow down to the most suitable. For this purpose, having an individual target for each element provides room for flexibility and more control to fine tune the deposition rate of each target by varying its power setting. To manage the cost, it was decided to order smaller circular targets of Manganese and silver, and have a larger rectangular target of Copper. Testbourne Ltd were commissioned to manufacture a circular Manganese target of 100 mm diameter and 2 mm thickness with 99.95% purity (figure 3-3-(a)), a circular silver target of 100 mm diameter and 3 mm thickness and 99.99% purity (figure 3-3-(b)). Copper was made as a rectangular target of 248mm by 133mm by 10 mm thickness with 99.99% purity and positioning holes machined in pre-specified positions, (figure 3-

3-(c)). The targets were loaded onto their respective magnetrons and then the water flow system was attached to the backing plates of each target, to maintain a steady flow of cold water to cool down the targets during operation. A tightly clamped magnetron with an O-ring between the target and magnetron ensures that a proper seal is maintained and no water vapour escapes into the chamber during deposition.

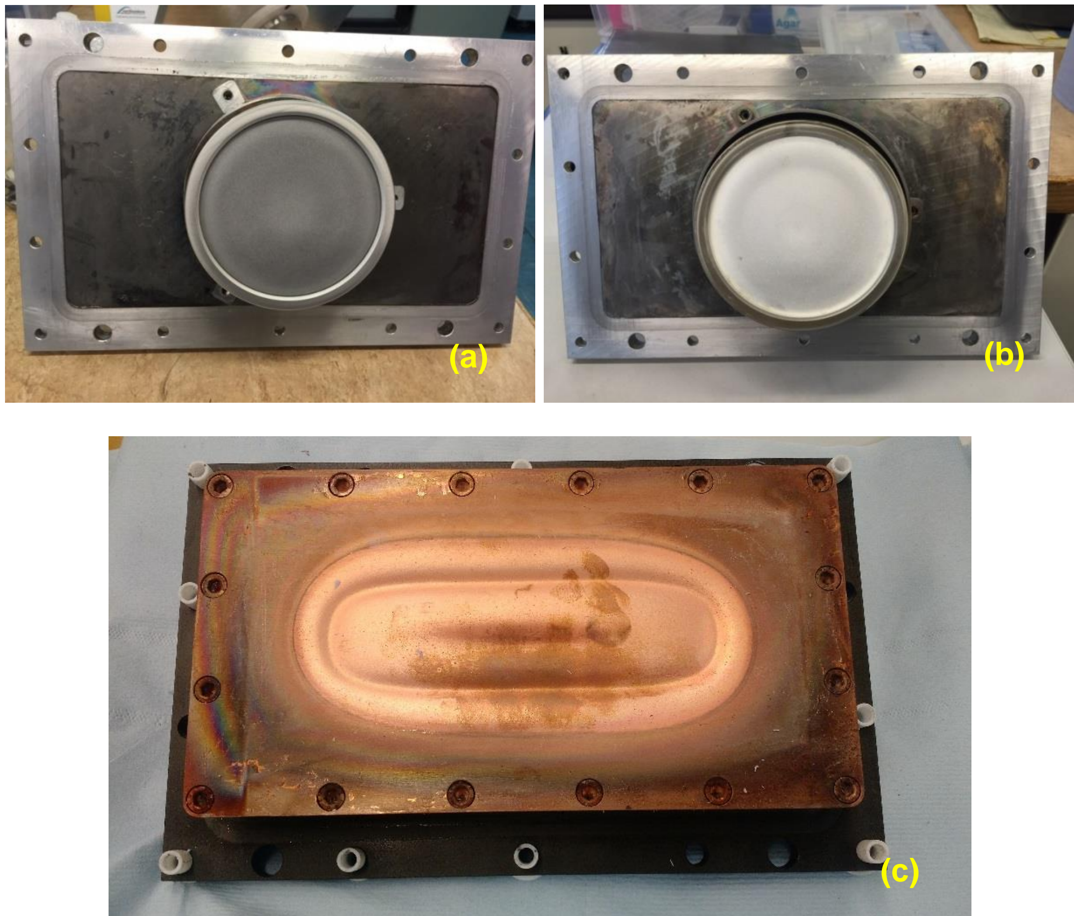

Fig 3-3 Targets manufactured by Testbourne Ltd (a) circular Mn (b) circular Ag and (c) rectangular Cu in their magnetrons

3.1.3 Substrate material:

Soda lime glass (SLG) slides and pre scribed 96% alumina (Al_2O_3) wafers with screen-printed Ag conductor pads were used as substrates. Part of the conductor pads on the alumina substrates were screen-printed with an over glaze mask, which could be washed off with Isopropyl Alcohol (IPA) solution after deposition of

the resistive thin film, as shown in figure 3-4 (a). The over glaze mask applied in this case is Okuno G1-1178 mask, which primarily consists of quartz sand mixed in a binder and colouring pigment. This mask ensures proper overlap of the deposited film with the conductor pad while leaving sufficient space for manual soldering of lead frames for electrical measurements after deposition. The alumina substrate was specifically designed for use within the university with larger individual chip size of 0.4 inch by 0.25 inch (10.16 mm by 6.35 mm, as seen in figure 3-4 (b), detailed dimension diagrams attached in appendix 1). The larger sized design was used in the University where soldering and TCR testing is carried out manually. Films deposited on soda lime glass were used for structural and chemical analysis. The glass slides were thoroughly cleaned in 1:5 ratio of DECON90 solution to water for 60 seconds, rinsed in deionised water and dried off with a Nitrogen blast to clean off residues and particles.

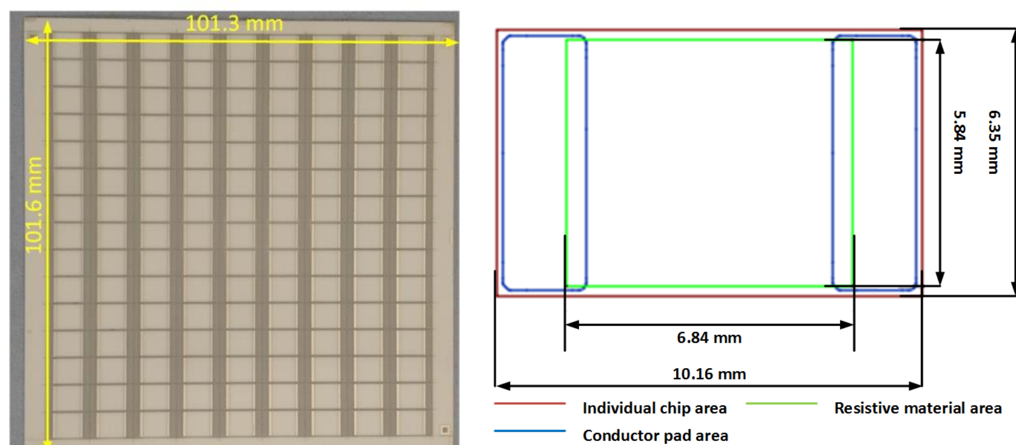

Fig 3-4 (a) Image of university designed alumina substrate plate (b) Individual chip showing areas of film deposited on individual chip.

3.1.4 Characterization equipment

a. Electrical Characterization:

Electrical properties like TCR and electrical stability are calculated from the resistance value; hence, precise measurement of resistance is very important. Generally, resistance values are measured by connecting the device across two probes of a multimeter. This is known as the Two-wire method. Most of the portable

digital multimeter (DMMs) employ this model, wherein the device under test (DUT) is connected to two probes of the meter as shown in figure 3-5. Because of the high impedance of the voltmeter, almost all of the source current goes through the probe and passes through the DUT completing the circuit [101]. Though the disadvantage of this technique is that the voltage V_m measured by voltmeter is the summation of resistance of the R_{DUT} as well as the two lead probes (R_{lead}). Even though the R_{lead} values are small and considered negligible for high resistance devices or for most general purposes. Lead resistance value can range from 1Ω to 10Ω. But for applications requiring measurement of accurate value of resistance or for resistance values smaller than 10Ω, this adds up-to a large error [101]. For example, two probes of 1Ω each when measuring a 10Ω device will give the result in total as 12Ω (R DUT plus 2 R leads), which equals to 20% error in the measurement.

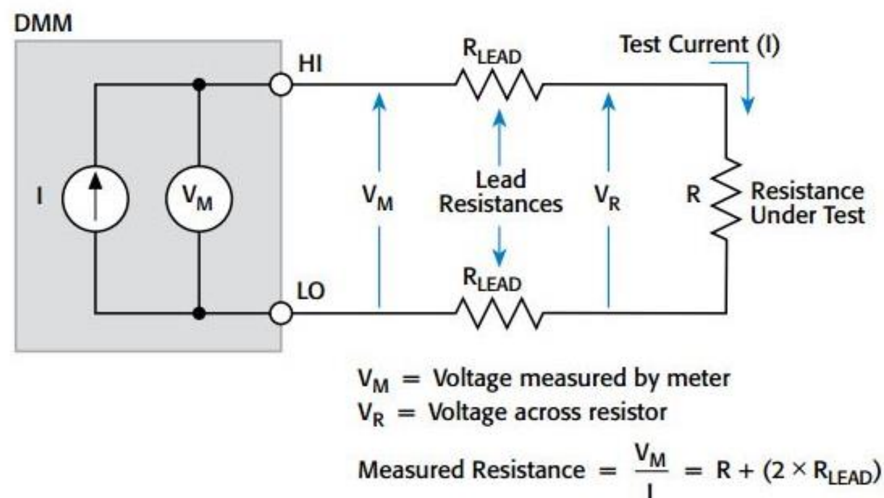

Fig 3-5 Two wire measurement technique showing the flow of source current through both R_{leads} and R_{DUT} [101].

To avoid this limitation for precision applications or for low resistance devices, the four-wire method is preferred (see figure 3-6). It is also known as the 4-wire Kelvin method. As the name suggests, this technique employs 4 wires to measure the resistance value instead of 2. Two wires known as source leads are used to feed the current through the DUT, and two leads known as sense leads are used to measure the voltage drop across the device. And because of the high impedance of the voltmeter only a very small source current (of the order of 100pA) passes

through R_{leads} of the sense wires [101]. Therefore, for all practical sense the *Vm* measured by the voltmeter is equal to *Vr*.

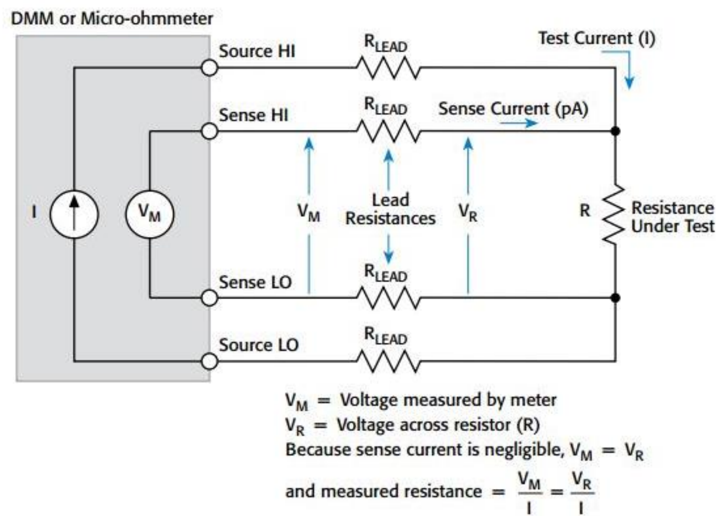

Fig 3-6 Four - wire Kelvin measurement technique showing the flow of source current through Source R_{leads} and R_{DUT}, and V_r measured by Sense leads [101].

Using a four-wire measurement technique can improve the accuracy of measurement but equally important is the resolution of the meter used to measure the resistance values. For a DMM the resolution is the smallest unit of resistance that can be measured by the DMM. This is very important when it comes to TCR and stability calculations as a meter with an insufficient number of decimal places hinders the accurate calculation of these parameters. As shown in table 3-1, for a 20Ω resistor as an example, one unit change on a DMM with 0.1Ω resolution will only give the ability to measure TCR values above 100ppm/^{o}C whereas on a DMM displaying up to a 4th decimal (100μΩ) can be used to calculate TCR as small as 0.1 ppm/^{o}C. Industrial standard for stability on the other hand, is in the range of 0.05% change in the resistance value, so a multimeter with 2 decimal places could be safely used to measure the resistance variation for stability purposes, but for precise TCR measurement a multimeter with capability to display more than 4 decimal places is required. In this work, the resistance values are measured using an Agilent 3458A digital multimeter. The multimeter is able to display 7 digits excluding the decimal and can switch between 2 wire and 4 wire measurement mode.

Table 3-1 Table of TCR and stability measurement limits for multimeter resolution.

No. of places after decimal	1 unit change in resistance	Lowest TCR measurable (ppm/ºC)	Lowest Stability figure (ΔR%)
1	20.0 to 20.1	100	0.5
2	20.00 to 20.01	10	0.05
3	20.000 to 20.001	1	0.005
4	20.0000 to 20.0001	0.1	0.0005

To measure TCR, it is required to have a suitable medium in which the resistor circuits could be subjected to accurate temperature changes. In real life, test circuits are encapsulated inside a resin protective coating and therefore, when the resistor is heated up during its operational lifetime, its resistive element is not subjected to the external environment. It is required that the medium in which the TCR test is conducted should uniformly heat the resistor surface and should not react with the resistive film itself. Mineral oil is an excellent choice to mimic the increase in the temperature around the resistor while exposing it to minimal external elements during testing.

To determine TCR, thin films deposited on alumina substrates are subjected to varying temperatures in a Grant LTC1 oil bath kit with GD120 thermostat. The Grant LTC1 kit has a 5-litre tank capacity. The GD120 is a general-purpose stirred thermostat that can uniformly maintain the temperature of the liquid (generally oil or low temperature liquid) anywhere between -30ºC and 120ºC. The thermostat has the capability to control and maintain temperature at 0.1ºC resolution. For the purpose of TCR measurement, the value is varied between 20ºC to 70ºC to mimic the real life circuit temperature and the real temperature measured with an externally calibrated thermocouple was within ±0.5ºC. The device was calibrated with 6 pre-tested standard resistors supplied by TT Electronics. Resistors from the MAR series of resistance value 1197Ω and 250Ω with very low TCR values (below 5ppm/ºC) are used to test the capacity of the Grant LTC1/GD120 oil bath along with the Agilent 3458A multimeter, (see table 3-2).

Table 3-2 Calibration result for LTC Grant oil bath Kit with GD120 Thermostat and Agilent 3408A multimeter.

Resistance Value (kΩ)	Sample no.	R_{Tstart} 20ºC	R_{Tfinal} 70ºC	TCR (ppm/ºC)	TCR from TT (ppm/ºC)
1.197	1	1196.966	1197.268	5.14	5
	2	1197.554	1197.620	1.12	1
	3	1196.771	1196.903	2.25	2
0.250	1	249.9967	249.9578	-3.2	-3
	2	249.9939	249.9513	-3.5	-3
	3	249.9965	249.9439	-4.3	-4

It is seen from the calibration table that the Grant LTC1/GD120 with Agilent 3458A is able to successfully measure the low TCR value and can record resistance values with high precision up to 7 digits, irrespective of the decimal point. To measure the resistance value of thin films deposited on glass substrates, a Jandel 4 probe head with Keithly 2602 multimeter is used. This is identical to a 4-wire measurement system but instead of two wires, 4 micro probes are lowered onto the surface of the thin films and used as a 2 source, 2 sense set up as previously described. To measure the stability, samples are loaded into the tube furnace set at 155ºC, in open-air environment. Resistance measurements are made every 24 hours until 168 hours (7 days). The percentage change in resistance after every 24 hour gives an indication of the stability of the resistance.

b. Film Thickness:

A profilometer is a device used to measure the variation in the Z-axis or thickness (d) of a thin film in the range of 50nm to 150µm. In simple terms, the profilometer is made up of two main parts: a sample stage and a detector, and the sample stage moves to slide the sample across the detector to make a Z-axis profile of the surface. The detection of Z-axis height could either be made by using a physical probe like a stylus tip as a detector of height or by a using light to make an optical profilometry of the surface [102]. In a stylus profilometer, a physical probe is run

along the surface of the film to determine the surface height. A continuous feedback loop monitors the force by which the film surface pushes against the probe as it moves along [103]. This feedback is used to keep a constant torque on the probe thereby moving the probe arm as the height of the sample changes. This recreates the surface Z profile. While this method is extremely sensitive and gives excellent resolution of the Z value, the relatively hard probe can scratch the sample surface if it is soft [102-104].

The Dekatak XTL stylus type profilometer is set up with a 12.5μm tip. Because of its high Z-resolution, high sensitivity, ease of use and immunity to surface vibration the Dekatak XTL stylus profilometer was used for most of the experiments to measure the film thickness. A step is created by sticking a strip of kapton tape on the substrate, prior to deposition that is peeled away later. This creates a step of the exact thickness of the deposited film and which is then measured using the Dekatak XTL probe based profilometer.

c. Surface topology:

Optical microscopy struggles to reproduce images of structures smaller than 500nm, because of white light reaching its diffraction limits. A scanning electron microscope (SEM) employs a beam of electrons, which has a much lower wavelength to capture images of nanoscale features [105]. In a SEM an electron gun produces a steady beam of electrons from a cathode in a column, which is accelerated and shape modified by a series of electromagnetic lenses [106], On interaction with samples this beam can either transmit through the samples without interaction or collide with the sample and be reflected back (as seen in figure 3-7). If the incident electrons collide with loosely bound electrons in the conduction band, then they will emit secondary electrons and this emission rate is highly sensitive to the height difference in the surface [105, 106].

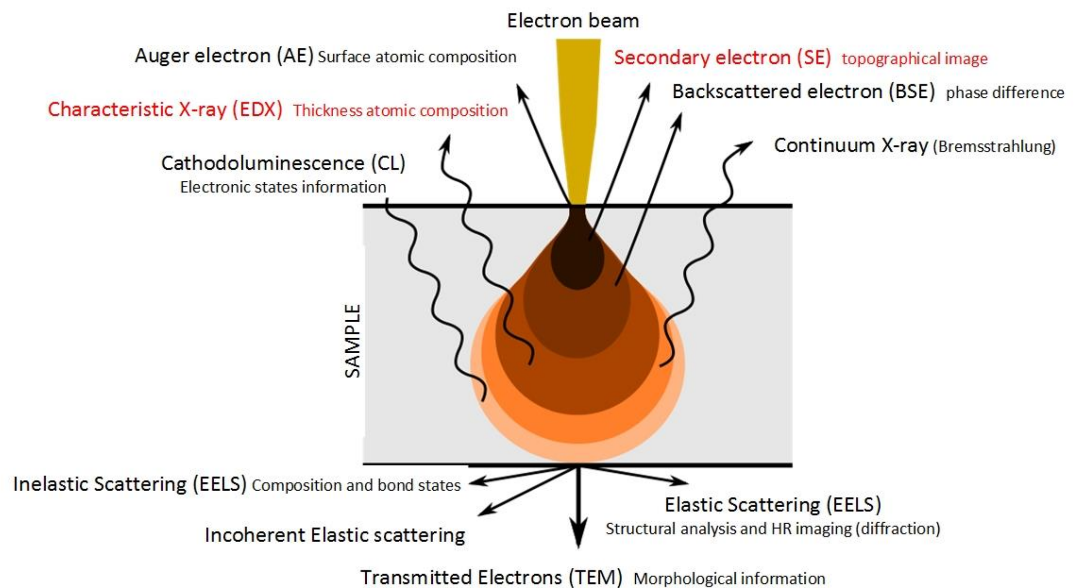

Fig 3-7 Schematic diagram of electron beam interaction with sample [107].

Older generation of SEM`s used an Everhart-Thornley detector which converted the collected secondary electrons into flashes of photons, then multiplied them in a photomultiplier tube to create a 2-D image on a screen [106, 108]. Newer versions of SEMs employ a Si-Drift Detector (SDD) which measures the amount of ionization produced by the incoming charged species on a high purity Si screen, resulting in very high count rates and raster speed, thereby achieving high resolution images at higher speeds [109].

d. Chemical composition:

In 1968, Fitzgerald, Keil and Heinrich developed the idea of Energy Dispersive X-ray analysis to study the element composition [105]. As seen in figure 3-7, element specific X-Rays are produced in an SEM if the incident e-beam knocks out an electron in the inner shell and an electron from outer shells has to fall down to fill this newly created vacancy [106]. The emitted X-ray is studied for its energy in a technique known as Energy Dispersive X-ray system or EDX. The energy of this X-Ray is measured by a specially arranged Si-Li drifted detector [105, 106]. Imaging of the samples was done by using a Mira Tescan system, equipped with an Oxford instruments X- Max 150 EDX detector.

SIMS or Secondary Ion Mass Spectroscopy is another instrumental technique used to analyse the elemental composition of solid thin films. It is one of the destructive analysis techniques in which an energised ion species (several KeV), commonly O_2^+ or Ar^+ is fired from an ion gun onto the sample surface, which on impact blasts out surface atoms and molecules from the thin film [110]. The ejected particles are detected using a mass spectrometer, which measures the mass of the secondary ions ejected. The most important advantage of SIMS is that it has very high sensitivity to most of the elements in the periodic table and hence can detect even the smallest amount of concentration. But the major disadvantage of SIMS is that the quantification of the SIMS result to get exact composition is not very reliable, hence SIMS is more suitable to develop a depth profile of elemental concentration across film thickness [110]. SIMS system assembled by Hidden Analytical equipped with IG20 type gun, and quadruple system based detector with 1-1000 atomic mass unit (a.m.u) range is used for this work.

e. Surface roughness:

Different techniques are applied to measure the roughness value of substrates, which is usually in the range of 100s of nanometres compared to that of thin films, which are generally under 10 nanometres. For substrates with higher roughness values, non-contact optical focus variation techniques can be used to create a 3-dimensional image of the substrate surface from which surface roughness values can then be calculated [111]. This technique is suitable for non-reflective surfaces like alumina and transparent glass substrates. For this work, the Alicona Infinity focus with 10X lens is used to measure the surface roughness of the substrates.

For thin film surfaces, atomic force microscopy (AFM) is a more suitable technique for measuring surface roughness. AFM makes use of a Silicon cantilever equipped with an ultra-sharp probe of 5-15 nm at its tip. The tip raster's the sample surface, either in continuous contact or intermittently tapped. A laser reflecting from the cantilever onto a photodetector, measures the vertical tip movements and records them as a 3-D image of the surface [112]. AFM has very high resolution because of its small tip dimension and can be used to support the topology of film surfaces generated from SEM techniques. In this work, a Digital instrument Dimensions™

3100 AFM system manufactured by Veeco Metrology group is used to measure and generate the surface 3D plots.

f. <u>Structural analysis:</u>

The same order magnitude of wavelength of X-rays as with the lattice parameters of crystalline structure causes the x-rays to diffract at the crystal planes. X-rays generated by the source material are made incident upon the samples surface, which after incidence get diffracted and form constructive and destructive interferences as per Bragg`s Law [113]. These interferences produce a diffraction pattern and each material has its own standard diffraction pattern. The diffraction pattern generated in the system can be compared to the diffraction patterns saved for the same material in an international database by a committee known as the Inorganic Crystal Structure Database (ICSD) [114]. By comparing diffraction patterns, important information about the material can be developed like: preferred orientation of the crystals, grain size, internal strain and the lattice parameters [115]. In this work, the diffraction patterns for materials are generated using a Siemens Diffraktometer D5000 system employing a Cu Kα radiation of wavelength, λ = 1.54184 Å. The XRD measurements were made for a 2θ range of 20° to 90° in steps of 0.02^o. The Patterns were analysed using Origin 8.1, graphing and analysis software from Origin lab and Fityk data processing and nonlinear curve fitting software. Figure 3-8 below shows the main diffraction peaks for Mn_3AgN and Mn_3CuN antiperovskite structures with corresponding miller indices.

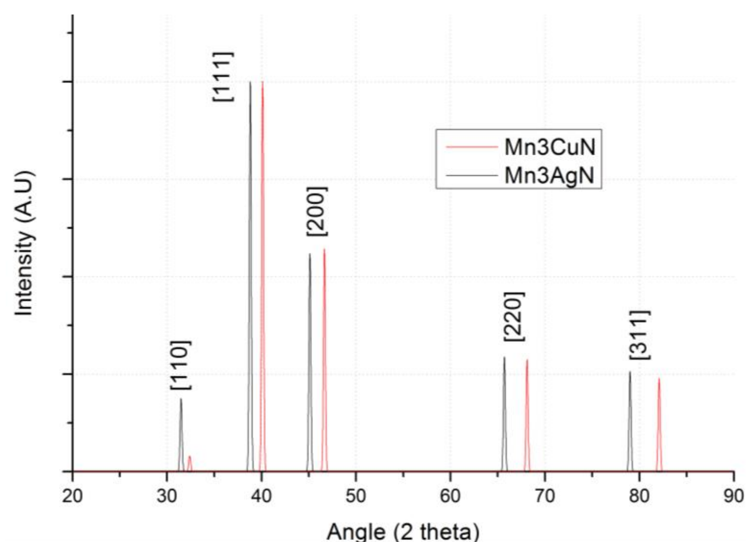

Fig 3-8 XRD pattern for Mn_3AgN and Mn_3CuN antiperovskite structure [116].

3.2 Setting up the deposition and characterization equipment:

The next section will explain the procedures undertaken to understand the capabilities of the deposition system, Nitrogen inlet system, heat treatment furnace and characterization equipment. The flowchart in figure 3-9 shows the sequential set up of the Teer coating deposition chamber for individual target sputtering, co-sputtering of two targets, co-sputtering in reactive environment and then setting up of the tube furnace for heat treatment of as grown films. The expected outcome from each stage is mentioned in the blue hexagon alongside.

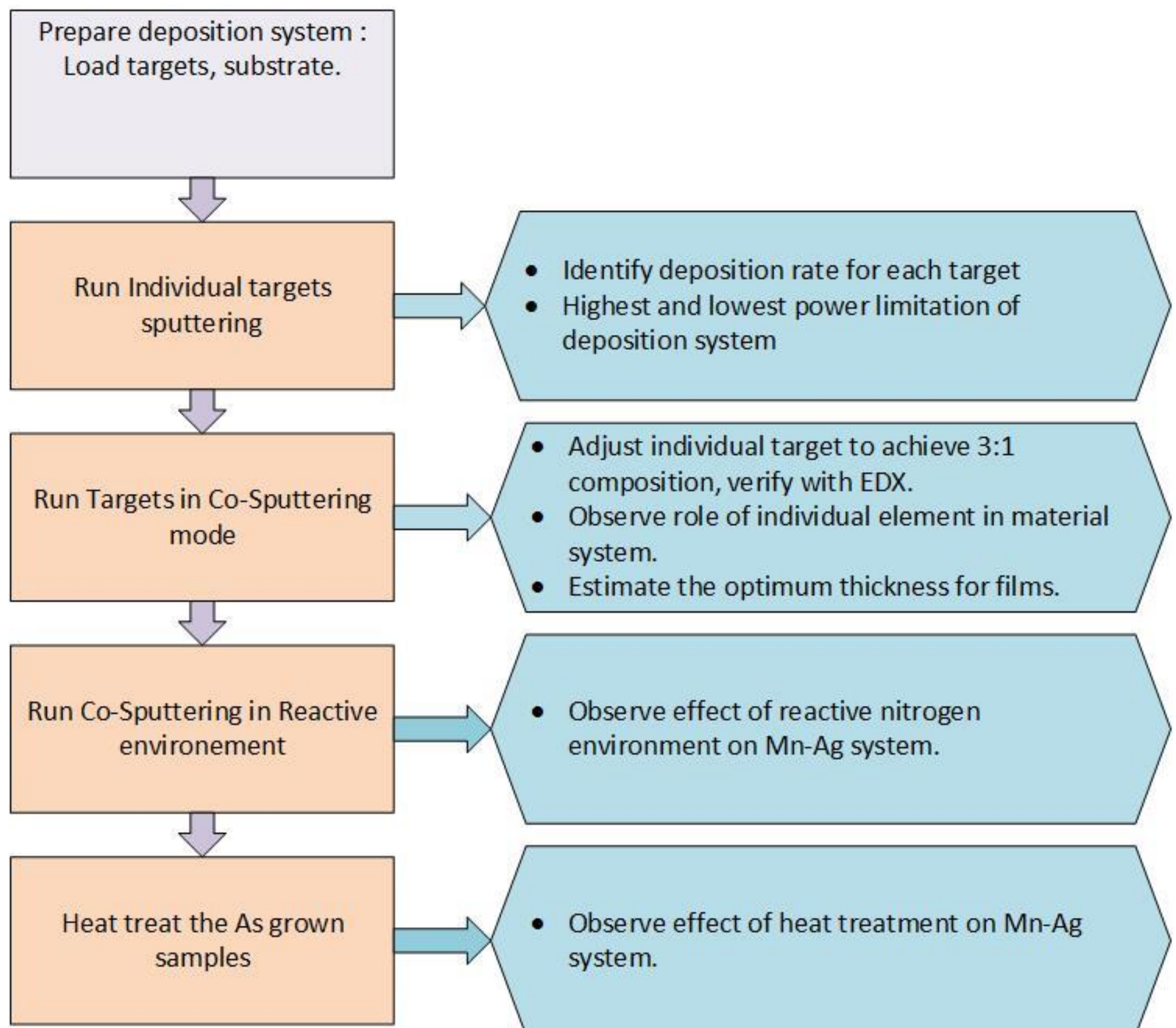

Fig 3-9 Process flow showing deposition and heat treatment system setup.

3.2.1 Setting up the deposition plant to run individual targets:

Firstly, it is necessary to establish the deposition rate of individual elements by sputtering them at varying powers and for varying times. This will help to understand the limitations of the deposition plant and to know the relationship between the power levels on the target to the deposition rate of each element. Thin films of individual elements were deposited on SLG substrates that were loaded on the carousel, set to rotate at a constant speed of 5rpm, and at a target to substrate distance of 130 mm. With 24 hours of pumping, a base pressure of $1.1e^{-5}$ mbar was achieved. A working pressure of 3 μbar was reached by setting the flow of Argon to 30 sccm. The deposition parameters which were kept constant are listed in table 3-3 below. Mn was sputtered using RF power on magnetron 2, because of its reduced efficiency on DC sputtering mode as a result of its magnetic nature. DC power was used to sputter Ag and Cu on magnetron 3 and magnetron 4 respectively. Substrates were masked with high temperature kapton tape to create a step feature, which could be used to measure the film thickness later with a profilometer.

Table 3-3 Deposition parameters for initial deposition in UDP 350 plant.

Deposition parameter	Value
Base pressure	1.1 e-5 mbar
Working pressure	3 e-3 mbar
Target to substrate distance	130mm
Argon flow rate	30 sccm
Carousel rotation speed	5 rpm
Substrate temperature	none

Twelve sets of depositions at four power levels of: 150W, 200W, 250W and 300W, in combination with three time durations of 30, 60 and 90 min as shown in table 3-4, were performed to determine the sputter rate of the Mn target. Plotting the thickness of the film against the time duration for each power setting revealed that

the deposition rate of Mn is linear, see figure 3-10. Calculated deposition rates were 2.66, 3.39, 4.09 and 5.06 nm/min for 150, 200, 250, and 300W respectively.

Table 3-4 Table of varying power and time to determine Mn sputter rate.

Sample No	Power in W	Time in mins	Thickness (nm)
TC 278	150	30	81
TC 277		60	160
TC 279		90	238
TC 282	200	30	102
TC 272		60	206
TC 273		90	308
TC 281	250	30	120
TC 276		60	248
TC 280		90	375
TC 294	300	30	150
TC 293		60	306
TC 295		90	453

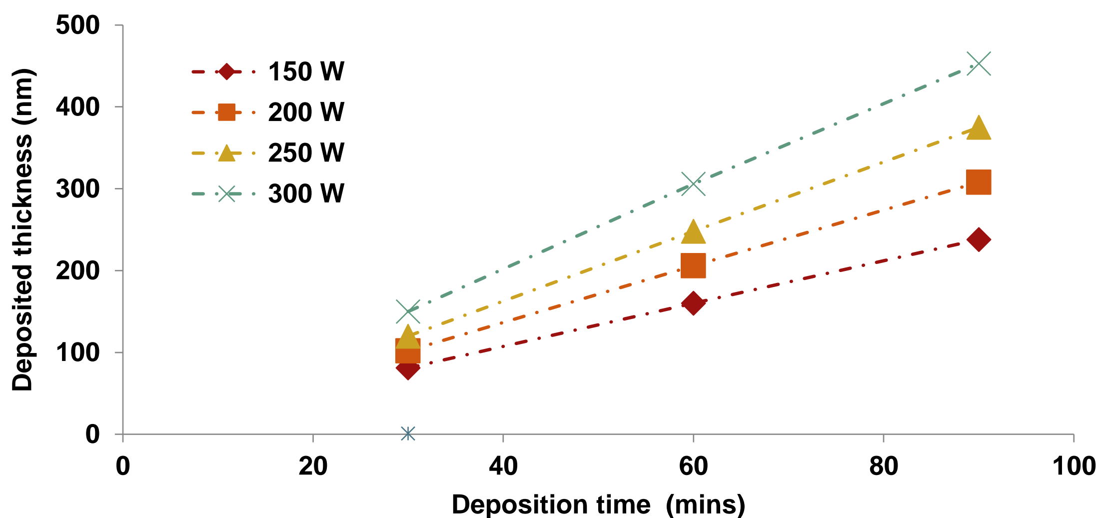

Fig 3-10 Graph showing thickness variation for Mn with varying time and power

DC sputtering of Ag and Cu only allows the current to the magnetron to be controlled and calculates the corresponding power according to the target resistance. Nine sets of depositions were carried out for Ag (table 3.5), with three power levels of 50, 30 and 23 W with three time durations of 30, 60 and 90 mins. It was not possible to strike and sustain a plasma below 0.05 A. So the minimum power was restricted to 23 W. Plots of time versus thickness for Ag were also linear as seen in figure 3-11 and sputter rates were determined to be: 1.79, 2.35, and 3.95 nm/min for 23, 30 and 50W power settings.

Table 3-5 Table of varying power and time to determine Ag sputter rate.

Sample No.	Power in W (current in A)	Time (minutes)	Thickness (nm)
TC 290	23 (0.05 A)	30	55
TC 291		60	107
TC 292		90	160
TC 287	30 (0.06 A)	30	73
TC 288		60	138
TC 289		90	211
TC 284	50 (0.09 A)	30	125
TC 285		60	231
TC 286		90	348

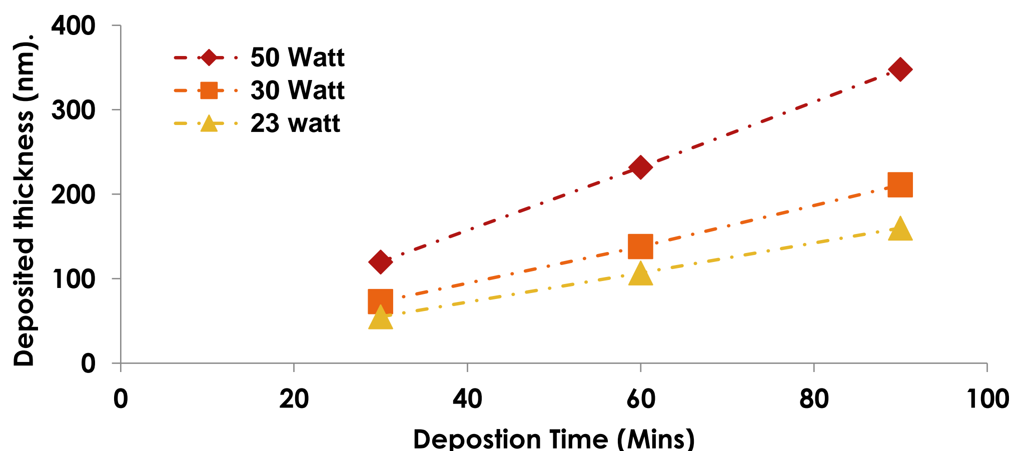

Fig 3-11 Graph showing thickness variation for Ag with varying time and power

Twelve sets of depositions (table 3.6) with four power levels of 15, 55, 99 and160 W and the same time durations of 30, 60 and 90 minutes were carried out for Cu. Plots of time vs thickness for Cu are also linear (see figure 3-12) and sputter rates were determined to be 0.60, 1.99, 4.73 and 6.95 nm/min for 15, 45, 99 and 160 W power settings.

Table 3-6 Table of varying power and time to determine Cu sputter rate

Sample	Power in	Time in	Thickness
Tc 354	15	30	15
Tc 353		60	35
Tc 352		90	67
Tc 351	45	30	56
Tc 343		60	126
Tc 350		90	183
Tc 349	99	30	154
Tc 344		60	283
Tc 348		90	392
Tc 347	160	30	205
Tc 345		60	422
Tc 346		90	630

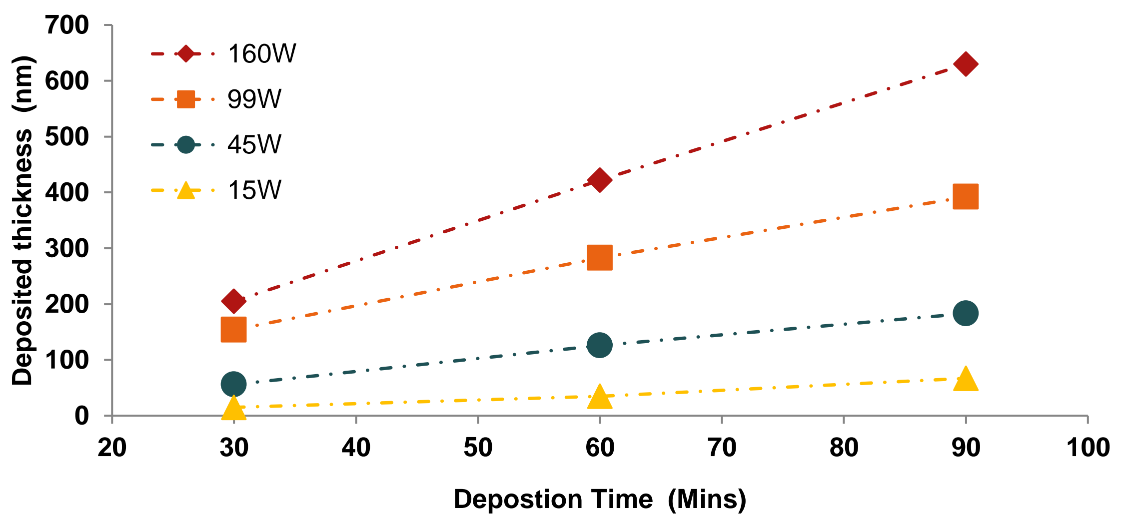

Fig 3-12 Graph showing thickness variation for Cu with varying time and power.

It is evident from the figure 3-13, that the individual deposition rate of Mn is very slow when compared to Ag and Cu. Because of this difference in the sputter rates of the materials, to achieve the required 3 times atomic ratio of Mn to Ag or Cu, it becomes very necessary that the deposition system should be used at the extremes of its capabilities. The highest possible power (~300W) for magnetron 2 having Mn target while operating Ag and Cu at lower power settings (around 23 W and 28 W for Ag and Cu respectively) required to achieve lower Ag/Cu concentration in the film.

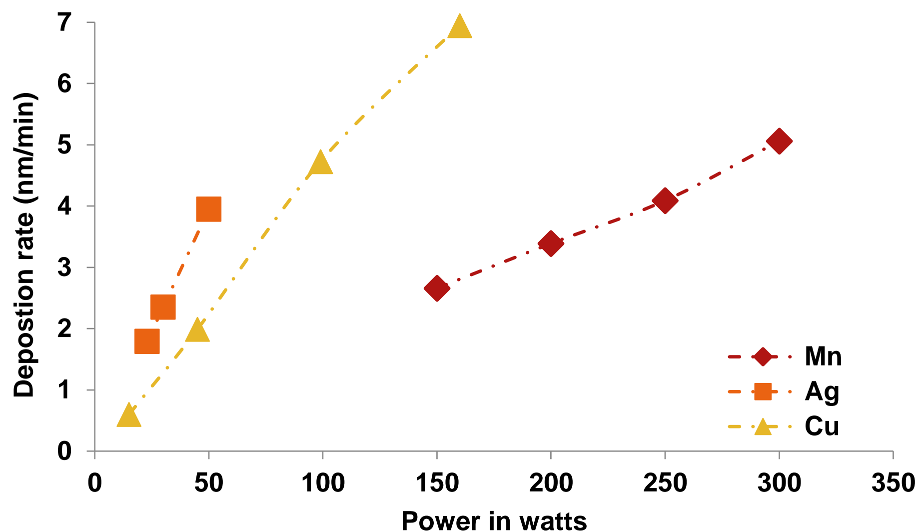

Fig 3-13 Graph comparing the deposition rates of Mn, Ag and Cu

3.2.2 <u>Setting up the plant to run in co-sputtering mode:</u>

Now with the sputter rate for individual elements established, two targets could be co-sputtered in a non-reactive environment to find out the power levels required to achieve stoichiometric ratios of elements in the film. Firstly, Mn and Ag targets were sputtered simultaneously onto the same substrate. This step helped to calculate the power levels required to achieve 3:1 stoichiometric ratio of Mn:Ag needed to make the antiperovskite structure in chapter 4 and 5. Secondly, electrical measurements from these samples will also provide an outlook of the role of individual elements in the binary system. RF power on the Mn target was varied from 250W to 350W and DC power on Ag target was varied from 48W to 22W to deposit films having an increasing concentration of Manganese, see table 3-7.

Table 3-7 Table of varying power on Mn and Ag target in co-sputtering mode

Sample No.	RF Power on Mn (W)	DC Power on Ag (W)	Time duration (minutes)
TC 296	250	48	120
TC 297	300	28	120
TC 298	300	22	120
TC 299	350	22	120

Once the power levels are established for the required stoichiometric ratio, it is important to find out the suitable thickness of films to deposit in the subsequent runs. The deposition system has a shutter that is closed during the pre-sputter cleaning of target step and swings open to reveal the target plasma plume during the coating step. During this coating time the plume deposits on the substrate surface loaded onto the rotating carousel, as well as onto the entire carousal surface and the chamber walls. The Teer coating UDP 350 is a huge industrial type deposition system to be used primarily for coating of surfaces with metal thin films and hence has limited capacity to control the plume direction, spread or carousal to target distance. Moreover, because of this limited control and industrial nature of the deposition plant, running the process recipe for 120 minutes for each individual deposition, to achieve a film thickness of 1µm on the substrate, will lead to huge wastage of precious target material deposited on the rotating carousal and chamber walls. Hence, it is important to find a film thickness that is thick enough for characterization while minimizing wastage for each deposition cycle. Once the power setting required to achieve a 3:1 ratio was determined, the deposition time was varied from 120 minutes to 100 seconds to achieve films of varying thickness, see table 3-8. These films were then analyzed under EDX to determine the chemical composition of films of varying thickness.

Table 3-8 Table of varying the deposition time in Mn:Ag co-sputtering mode

Sample No.	RF power on Mn (W)	DC power on Ag (W)	Deposition time in (minutes)
TC 298	300	22	120
TC 300	300	22	60
TC 301	300	22	30
TC 302	300	22	7
TC 303	300	22	100 sec

Similar to co-sputtering of Mn-Ag, Mn and Cu targets were also co-sputtered at varying power levels to establish the settings required to achieve the 3:1 stoichiometric ratio in Mn-Cu binary films. The RF power on the Mn target was varied from 250W to 300W and DC power on Cu was varied from 90-10W, see table 3-9.

Table 3-9 Table of varying power on Mn and Cu target in co-sputtering mode

Sample No.	RF power on Mn (W)	DC power on Ag (W)	Time in (minutes)
TC 355	250/90	90	90
TC 356	250/43	43	90
TC 357	300/37	37	90
TC 358	300/28	28	90
TC 359	300/16	16	90
TC 360	300/10	10	90

3.2.3 Reactive sputtering in Nitrogen:

To make the deposition environment reactive, reactive gas species is introduced into the chamber along with the inert argon. Mass flow controllers (MFC) control the gas inlet into the chamber. There are two MFCs; MFC 1 controls the argon flow into the chamber and MFC 2 is used to let in the reactive gases like Nitrogen or Oxygen into the chamber. Three initial depositions were performed using Mn and

Ag held at constant power levels and partial Nitrogen percentage in argon varying from 0-16.66%, see table 3-10. This will help to decide the design of experiments for the next cycle based upon the atomic percentage of Nitrogen included in the film from the reactive environment.

Table 3-10 Table of varying partial Nitrogen environment in the chamber

Sample No.	RF power /DC power (Watts)	Ar flow (Sccm)	Nitrogen flow (Sccm)	Partial Nitrogen in chamber (%)	Time (mins)
TC301	300/22	30	0	0	30
Tc 311	300/21	29	1	3.33	30
Tc 310	300/22	27	3	10	30
Tc 309	300/22	25	5	16.66	30

3.2.4 Setting up the tube furnace for heat treatment:

The production line procedures followed by the TFR industry performs a heat treatment on the deposited samples to tune the TCR closer to zero. Mn-Ag samples were subjected to heat treatment in a Carbolite tube furnace TZF 12/75/700e with a quartz tube of 75 mm external diameter. The tube furnace has a horizontal quartz tube, which could be sealed off at each end with a cap to isolate the internal environment from Oxygen and contamination particles from the external surroundings. This furnace could reach up to a maximum temperature of 1200°C and has a heated zone 700mm long of which 540mm is uniformly heated to ±5°C. This is a three-zone heater set up; the 540 mm of uniform heated zone is heated up by three independent heating elements with individual PID heat controllers. A Eurotherm 2132 is used to control the side zones while the heating element in the main zone is controlled by a Eurotherm 210 controller. This means that the entire length of 540 mm could be set at one required temperature with a temperature variation of ±5°C. The Mn-Ag samples deposited at various thicknesses were heat treated at 300°C to study the effect of heat treatment on the TCR and resistance values.

3.3 Results and Discussion

3.3.1 Thickness and magnetron power level calibration:

After deposition, the kapton tape was peeled and thickness measurements were taken using the Dekatak profilometer at 6 different regions of the exposed strip. Thereafter the average thickness was calculated for each film and the difference in uniformity of film thickness was expressed. Table 3-11 below shows the measured average thickness of each of the Mn-Ag films. The films were then loaded into the SEM chamber and the EDX measurement verified the composition ratio of individual constituents, see table 3-11.

Table 3-11 Table of results for thickness and composition with varying Mn/Ag power levels

Sample No.	RF Power on Mn (W)	DC Power on Ag (W)	Time (minutes)	Thickness (nm)	Atomic % of Mn: Ag
TC 296	250	48	120	984 ± 10	52:48 (1.08:1)
TC 297	300	28	120	878 ± 10	68:32 (2.1:1)
TC 298	300	22	120	812± 10	76:24 (3.16:1)
TC 299	350	22	120	826± 10	79:21 (3.96:1)

Overall, the film thickness is observed to decrease with decreasing DC power on the silver target, even though the RF power is increased considerably on the Mn target. With lower power on the Ag target, less silver is deposited in the film. The sputter yield of Mn is reported to be 1.3 while that for Ag is almost three times higher at 3.4 and for Copper is almost twice that of Mn at 2.4 atoms/ion (calculated for a bombarding Ar^+ ion of 600ev) [19]. Because of the low sputter yield of Mn, the increase in RF power on Mn is not sufficient to overcome the reduction of film thickness caused by lowering the power on the Ag target, which has very high sputter yield. 300W of RF power on Mn and 22W of DC power on Ag results in Mn:Ag composition ratio of close to 3:1.

By comparing the EDX spectrum of films at various thicknesses (samples from table 3-12), it was observed that for films below 400-500 nm thickness that composition of film varies even though power is kept constant. It is because, the interaction volume for incident electron beams goes up to a depth of 500 nm and for films thinner than this thickness, the electron beam generates a considerable amount of X-rays specific to other elements related to common elements of SLG. Therefore, the counts of elements like Si, Mg, Ca, K, and Na increases dramatically. This leads to an error in the composition estimation of the film itself. Even though the power is kept constant the Mn:Ag ratio is observed to deviate much more for thinner films. While films deposited for 120 mins having thickness ~900nm are good for EDX measurements, these will also lead to more wastage of target material and increase deposition time. Therefore, a deposition time of 90 mins is more suitable giving a thickness of 500nm, which is just at the same value as the electron beam interaction volume.

Table 3-12 Table of Mn:Ag film resistivity with increasing concentration of Mn

Sample No.	Thickness (nm)	Atomic % of Mn:Ag
TC 298	812± 10	76:24 (3.16:1)
TC 300	382± 10	76:24(3.16:1)
TC 301	195± 10	77:23(3.5:1)
TC 302	41± 10	79:21(3.76:1)
TC 303	14± 10	80:20 (4:1)

Similarly, in the case of Mn-Cu films, it was observed (see table 3-13) that reducing the DC power level of the Cu target had a significant effect on the thickness of the film. A 300W of RF power on Mn and 28W of DC power on Cu was observed to produce a near 3:1 stoichiometric ratio of Mn: Cu.

Table 3-13 Table of thickness and composition variation with Mn/Cu power levels

Sample No.	RF power on Mn (W)	DC power on Cu (W)	Thickness (nm)	Ratio of Mn:Cu (at %)
TC 355	250	90	748	22:78 (1:3.54)
TC 356	250	43	518	58:42 (1.38:1)
TC 357	300	37	575	66:34 (1.94:1)
TC 358	300	28	529	73:27 (2.7:1)
TC 359	300	16	477	83:17 (4.88:1)
TC 360	300	10	442	88:12 (7.33:1)

3.3.2 Initial electrical measurement:

While overall film thickness is heavily affected by the sputter power on secondary targets like Ag and Cu, electrical resistivity of the film is affected largely by the Mn concentration in the film. By taking the general electrical resistivity values of Mn, Ag and Cu elements at room temperature, it is seen that Mn has almost 2 orders of magnitude higher electrical resistivity of 1.5μΩ-m, while that of Cu is 0.02μΩ-m, and that of Ag is only 0.015 μΩ-m [117]. The films deposited on glass were measured using the Jandel 4 probe head attached to a Keithly 2602 digital multimeter. By measuring the resistivity of Mn-Ag films deposited on glass, it can be clearly seen that resistivity increases with the increasing concentration of Mn. The resistivity of the Mn-Ag films deposited on glass was observed to increase from 110 to 158 μΩ-cm with increase Mn: Ag ratio, see figure 3-14.

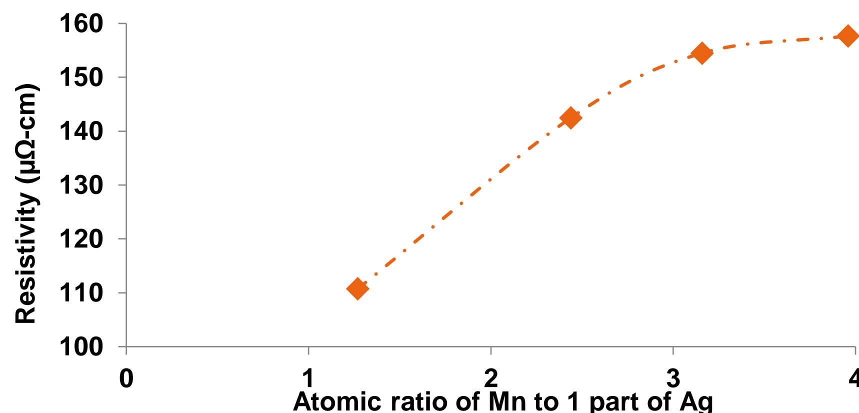

Fig 3-14 Graph of resistivity for Mn:Ag films with at% of Mn in films .

Films deposited on alumina substrates along with their glass counterparts, exhibited significantly higher resistivity values. For the Mn:Ag ratio of 4:1, resistivity was noted to be 250 μΩ-cm, which is 60% higher than that for the same composition on glass. This increase can be explained by the relatively high surface roughness of the alumina substrate, which plays a dominating role in scattering of electrons and thereby reduces their mean free path leading to increased resistivity [118]. The Average roughness value (Ra) derived for blank alumina substrates by studying three substrates under an Alicona Infinity Focus roughness measurement system, gives a Ra of 390 ±15nm. After coating with Mn-Ag binary composition, this roughness decreases to 347±10nm. However, this surface roughness is still 3 times the average roughness of their glass counterparts, which had a surface roughness of only 100±10nm increasing to 120±10nm when deposited with Mn-Ag film.

For a constant Mn:Ag ratio of 3:1, decreasing the thickness of the binary thin film from 800 to 14 nm resulted in increases in resistivity from 155 to 205 μΩ-cm on glass substrates and 250 to 613 μΩ-cm on alumina substrates, see Figure 3-15. This can be explained as a result of the discontinuous nature of the film increasing with the decrease in its thickness, which results in an increase in resistivity [28]. Shivprasad [51] and Ammar [52] reported resistivity above 300 μΩ-cm for a 160 nm thick Mn film deposited on glass, higher than the bulk resistivity of Mn (185μΩ-cm). It is evident by comparison that the introduction of the Ag conductive element into the Mn thin film has reduced the overall resistivity of the film significantly. Resistivity values of binary Mn-Ag films deposited on alumina substrates are comparable to those of NiCr (200-400 μΩ-cm) and TaN (250-300 μΩ-cm), materials which are at present used by the thin film resistor industry [2].

The TCR value of bulk material varies greatly in the literature, but by comparing various sources on TCR values for individual elements, we can see that bulk silver and Copper registers very high TCR values of 4000 ppm/^{o}C. The figure for Manganese is lower by more than one order and is in the range of 100 ppm/^{o}C. Figure 3-15 shows that the TCR of the binary Mn-Ag 3:1 ratio film, is observed to fluctuate between -98 to -154 ppm/^{o}C with the decrease in film thickness. Another

point to be noticed from these results is that even though the individual constituent materials in bulk registered a positive TCR, when deposited as thin films they show a negative TCR.

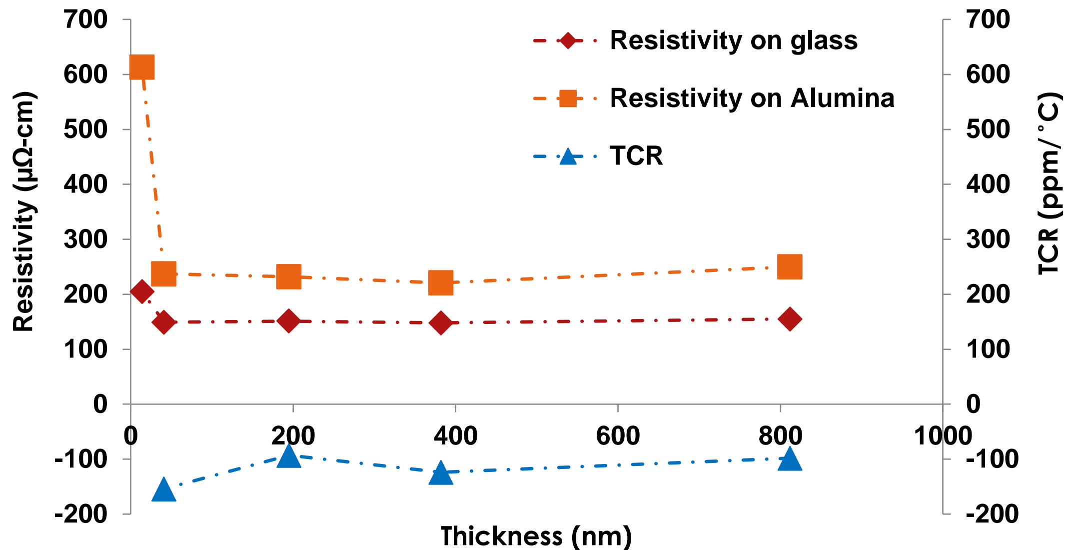

Fig 3-15 Graph of resistivity and TCR variation for Mn:Ag 3:1 film with film thickness

Shivprasad and Angadi [28, 50] summed up that when metal is in its bulk form, it contains a large number of free electrons which are the main charge carriers and with the increasing energy, the random collisions between neighbouring electrons increases, resulting in an increased electrical resistance for the given same shape. But in thin film form, as the thickness of the film decreases, island structures take shape, and voids between these islands are dominated more by thermally activated conduction mechanisms which are known to exhibit negative TCR [28]. Now the island structure of a thin film is affected by various deposition parameters such as substrate temperature, film thickness, and the nature of target materials [119].

The literature review also suggests that variation in TCR can be related to the difference in the values of coefficient of thermal expansion (CTE parts per million change in length per degree Celsius or ppm/^{o}C) for the substrate and film that leads to changes in the distance between the island structures of the thin film. Published

work from many other authors [19, 28] have also supported this. A progressively positive nature of TCR is seen on gold [with low CTE ~14 ppm/°C] films deposited on Teflon substrates [with large CTE ~80 ppm/°C] with increasing film thickness because of the increasing distance between the island structures of the gold film as the Teflon substrate expands [19]. By this reasoning, Mn and Ag with higher CTE values [~19 and 22 ppm/°C respectively] than alumina [~6.4 ppm/°C] are expected to show a positive nature of TCR with decreasing thickness. The TCR value of the thin film is therefore a combined outcome of multiple phenomenon, and the direction of its final value is steered by the phenomena, which is most dominating out of all these. Difference between CTE for substrate and thin film are known to create adhesion issues, but for all the samples in this project when tested with high strength masking tape no flaking or peeling off was ever observed. Therefore assuring proper adhesion of film to substrate.

3.3.3 <u>Basic effects of introducing reactive Nitrogen:</u>

Now with the introduction of N_2 in the film, it was observed that, for a constant film thickness of 200 nm and Mn:Ag ratio of 3:1, the resistivity of binary films of Mn:Ag increased linearly from 231.9 to 551.2 μΩ-cm with increase in Nitrogen flow rate from 0 to 5 sccm (0-16% partial Nitrogen concentration in the chamber), see figure 3-16. For each percentage increase in Nitrogen concentration in the deposition chamber, the resistivity of the resulting film increased by ~20 μΩ-cm and the TCR became increasingly negative, varying from -93 ppm/°C at 0% Nitrogen to -300 ppm/°C at 16% Nitrogen.

These distinct variations in electrical properties of the thin films can be related to the Nitrogen introduced from the reactive environment, which becomes trapped inside the film and eventually migrates to and diffuses along grain boundaries much faster than in bulk materials. Hence the increased resistivity could be explained as the result of grain boundaries which are electrically discontinuous even if physically continuous [28].

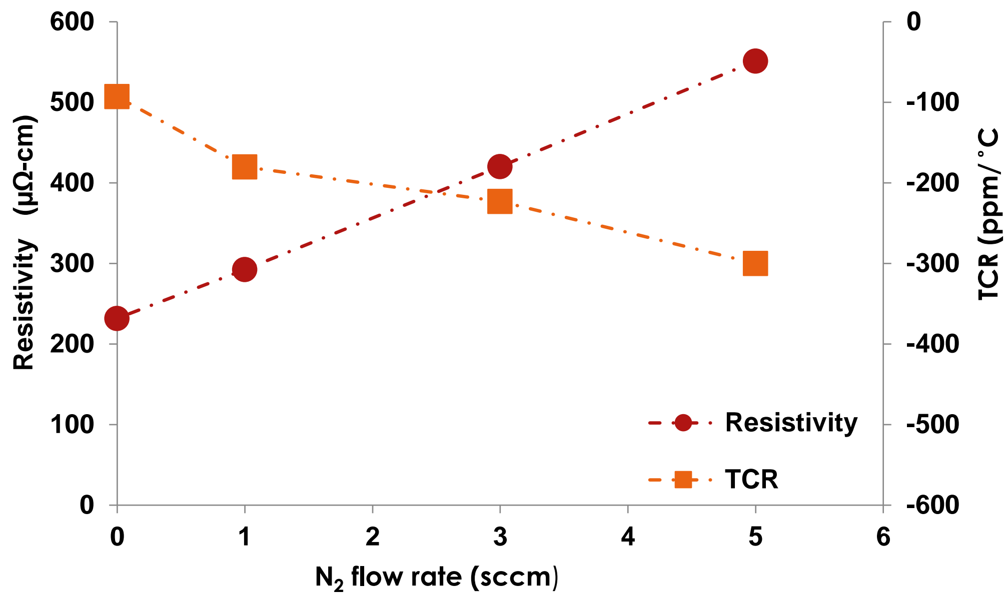

Fig 3-16 Graph of varying resistivity and TCR of Mn:Ag films with N_2 flow rate.

This could also explain the increased negativity of TCR, as the electrically insulated grain boundaries can effectively be viewed as the voids between islands structures. Matthiessens rule supports that deliberate introduction of external defects like oxiding, nitriding corrosion effects etc., will increase the resistivity of a material system, not only because it distorts the crystal lattice structure leading to more scattering, but the introduction of such species also removes one or more conduction electrons and thereby effectively reduces carrier concentration per unit volume [2].

3.3.4 <u>Basic effects of heat treating TFR films</u>

Figure 3:17 shows the resistivity and TCR values before and after heat treatment for binary films of Mn:Ag in 3:1 ratio, deposited in pure argon for 1 hour at 300°C in air environment resulted in a small decrease in resistivity value with increasing film thickness. However, for films thinner than 200nm, the resistivity is observed to increase, this increase is very large for 41 nm thick TC 302 where its resistivity value increased significantly from 237 to 2028 μΩ-cm.

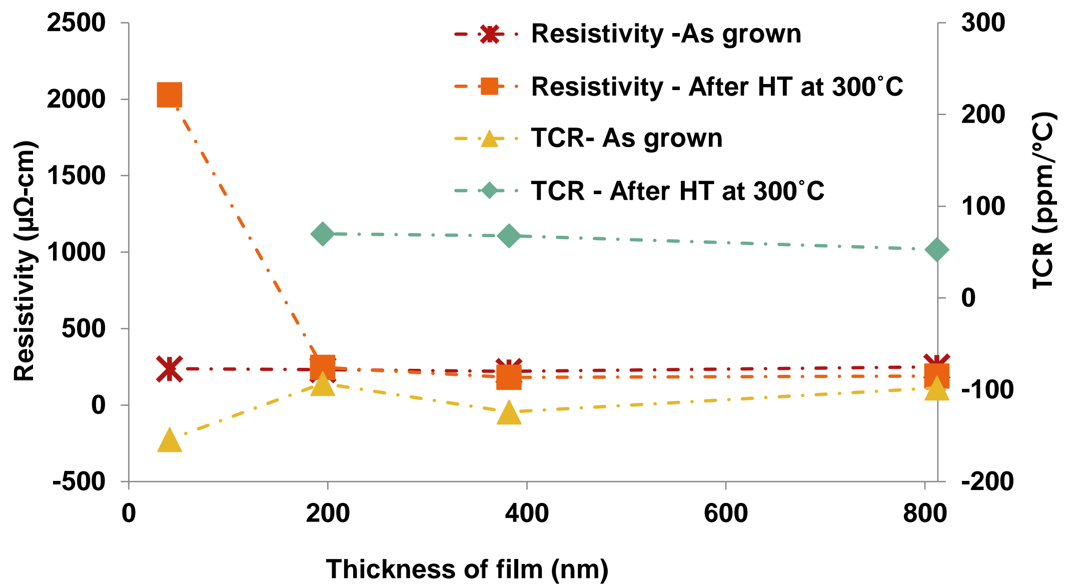

Fig 3-17 Graph of resistivity and TCR variation with film thickness for Mn-Ag films heat treatment.

A literature search reveals two main effects which heat treatment in air has on resistivity of thin films: healing of defects which reduces material resistivity according to Matthiessen rule [2] and surface oxidation with the potential to increase film resistance [12, 120]. At higher thicknesses above 200 nm, healing of defects appears to be dominant, slightly reducing the resistivity of the Mn-Ag films. These effects compensate each other for thickness of ~200 nm while as the films continue to get thinner, the effect of surface oxidations is dominant, increasing resistivity drastically. The secondary Y-axis of Figure 3-17 shows that the TCR of the Mn-Ag films has shifted from negative to positive for all film thicknesses following heat treatment. The trend line developed by TCR points becomes progressively positive with decreasing thickness and is in agreement with earlier explained effect of the CTE making the TCR positive.

Figure 3-18 shows that heat treatment of Mn-Ag films of thickness ~200nm, deposited in Nitrogen environment, results in an increase in resistivity value with increasing concentration of Nitrogen. This result could be explained by the enhancement of diffusion of Nitrogen around grain boundaries during heat treatment, which makes them more electrically isolated [121]. Films deposited in a Nitrogen environment also show a migration of TCR towards the zero TCR line following the heat treatment, as seen on the secondary Y- axis of Figure 3-18.

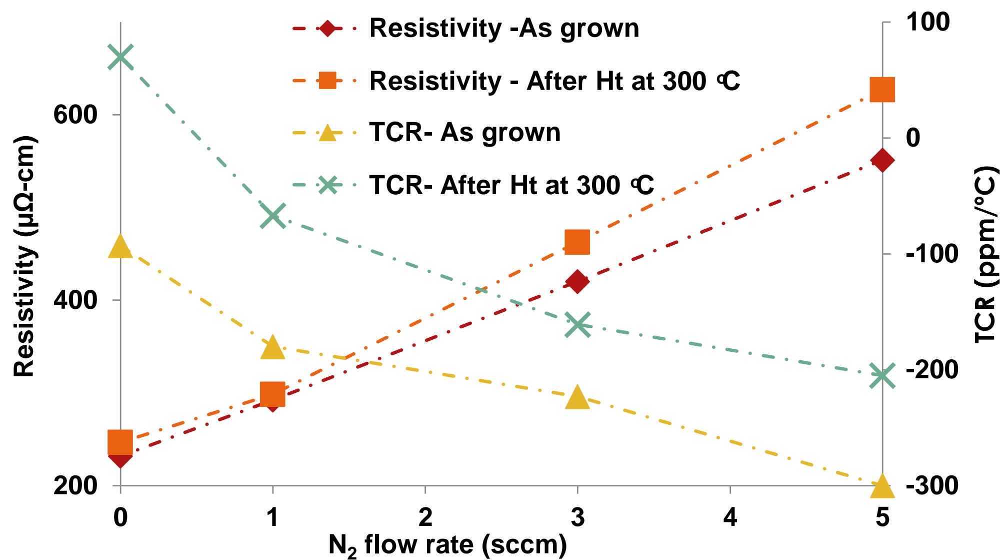

Fig 3-18 Graph of resistivity and TCR variation with N_2 flow rate for Mn-Ag film.

Another important property of TFRs is stability. From table 3.14, the final percentage change in the resistance value for films without Nitrogen, after subjecting to heat treatment, is seen to be around 6% for TC301 sample. For films deposited in reactive Nitrogen, the stability figure is seen to improve with 2% change in resistance for TC311. Similar to the TaN material system, it is observed that introduction of Nitrogen results in an improvement of stability, but these values are still extremely high to be of any use for practical TFR fabrication purposes [122]. Stability values could be improved by heat treating samples in Nitrogen/vacuum [123] environment instead of open air. This will minimize the oxidation of the film surface at higher temperature. Therefore, by optimizing the heat treatment process, stability figures could be improved.

Table 3-14 : Table of resistance change after each 24 hours.

Sample No.	N_2 Flow (Sccm)	Film Thickness (nm)	Resistance value each 24 hour (Ω)				ΔΩ/Ω% each 24 hour		
			0	24	48	72	24	48	72
Tc 309	5	201	78.01	81.102	82.086	82.197	3.96	5.22	5.37
Tc 310	3	198	58.44	59.223	60.012	60.173	1.34	2.69	2.97
Tc 311	1	195	38.3	38.748	38.926	39.182	1.17	1.63	2.30
Tc 301	0	195	31.63	32.229	33.048	33.62	1.89	4.48	6.29

3.4 Summary

To summarise, this chapter explains the setup and functioning of the deposition system, heat treatment furnaces and functioning of characterization equipment. From deposition of individual elements, it is observed that Ag has the highest deposition rate followed by Copper and Manganese is observed to have the slowest deposition rate. Through co-sputtering it is seen that 300W RF/22W DC power is required on Mn/Ag combination to achieve a 3:1 ratio, while for Mn/Cu it required 300W RF/28W DC. A deposition time of 90 minutes is more suitable to minimise the target wastage while giving sufficient thickness for EDX measurements. The resistivity of the as deposited films was observed to increase from 220 to 613 μΩ-cm with decreasing film thickness, which is suitable for midrange resistive applications, with TCR in the range of -98 to -154 ppm/^{o}C. Increasing the concentration of Mn, increasing the concentration of Nitrogen in the film or decreasing film thickness are cases in which the film resistance is observed to increase. In further chapters, the concentration of Mn is required to be fixed at 60 atomic % (3:1:1 ratio of Mn:Ag/Cu:N) and film thickness is fixed to ~500nm. Films with Nitrogen exhibited resistance in the range of 231 μΩ-cm to 551 μΩ-cm with TCR values from -180 ppm/^{o}C to -300 ppm/^{o}C. After heat treatment, resistance values increased slightly while TCR values had a positive shift closer to the zero line, at -67 ppm/^{o}C. Now, in the further chapters the optimum Nitrogen concentration in the film needs to be identified, which is set by the optimum partial Nitrogen pressure inside the chamber. The best stability figure of 2% change in resistance was observed, while this value is very large to be used as a TFR, these films were heat treated in air, and with heat treatment in Nitrogen, the stability figure could be further reduced. These initial results show that bulk Mn or Ag or Cu when deposited as a Mn-Ag/Cu-N thin film structure, exhibits a negative TCR which can be positive shifted by right process parameters. Mn based antiperovskites developed by optimising N_2 content, deposition parameters and heat treatment can be expected to be fit for ultra-precise thin film resistors.

CHAPTER 4 Study of Mn_3AgN and Mn_3CuN thin films

4.1 Introduction

In Chapter 3, thin films from preliminary runs on Mn and Ag/Cu targets in reactive nitrogen environment, were shown to exhibit negative TCR, which on subsequent heat treatment showed migration towards the positive direction. Sputter deposition and subsequent heat treatment consist of a very wide range of process variables, and studying the effects of each process variable simultaneously will increase the number of experiments considerably. The focus of this chapter was to identify the key deposition and heat treatment process variables and study their effect in achieving desirable electrical properties in Mn based antiperovskite structures.

Sputtering power in Watts, applied on individual targets is one of the most important variables in deciding the electrical properties of thin films. M. Yoshitake et al (1991) in their work to develop a thermally stable resistor from Zr-N, used RF power as a parameter to control electrical resistivity of films [124]. Similarly, H.Toku et al (2010), showed that varying target power leads to a change in the phase structure of the material system thereby altering its properties [125]. But between the lowest power required to ignite the plasma and highest power to keep the Teer coating plant within a safe usage limit, the sputter power level combinations to achieve the required 3:1 ratio of Mn:Ag and Mn:Cu is fixed to be 300W-RF/ 23W-DC and 300W-RF/28W-DC respectively.

There are three process parameters related to the vacuum and gas inlet systems: Base pressure, Working pressure and Reactive species partial pressure. There is less information about the effects of base pressure on electrical properties of thin films; A Asthana et al (2008), suggested that a lower base pressure is helpful to lower the kinetic ordering temperature which in turn lowers the annealing temperatures in FePt thin films [126]. On the Teer coatings plant, a lack of load lock, lack of better pumping system, multiple external attachment ports etc. limits the lowest possible base pressure to $1.0e^{-5}$ mbar. Adding 30 sccm of gas into the chamber raises its pressure from base pressure to working pressure of 3μbar. If the sputtering is performed in non-reacting (inert) environment, then the working pressure is dependent only on the volume of inert Ar introduced, but if a reactive

N_2 is introduced, the working pressure is expressed as the partial N_2 /Ar+N_2 % pressure. There is lot of research conducted on thin film resistors, that has concluded that the working pressure or partial N_2 pressure has the most significant impact on the morphology, and crystal structure of the film, thereby changing its electrical properties [29, 127-131]. Setting the correct amount of partial Nitrogen is important to ensure the right amount of Nitrogen in the thin film as well. Experiments in this chapter will be planned to deposit Mn-AgN and Mn-CuN thin films with varying Nitrogen content in them.

J. Mashaiekhy et al (2012) in their work found that electrical resistivity of thin silver films varies with varying substrate temperature they are deposited at. They observed a growth in grain size in direct relation to increasing substrate temperature and correlated it to the varying electrical resistivity [132]. From various literature sources, substrate temperature is seen to be an important process parameter when depositing thin film resistive films [133, 134]. The Teer coating UDP has a heating element situated along its chamber wall, which was used to heat the substrates rotating on the centre carousal (see figure 3-1). Substrate temperature is known to have effects on the resistivity of Mn_3CuN antiperovskite structures also [83, 84]. Substrate temperature will be the second parameter varied in correlation with partial N_2 pressure to deposit thin films of Mn-AgN and Mn-CuN.

Film thickness is another important variable which leads to changes in electrical properties, by changing the internal strain within the films and by affecting the conduction mechanism [132]. This is also shown in chapter 2, where the thickness of the Mn-Ag film affects the resistivity of the film. However, film thickness is resultant of varying power level and deposition duration, hence is less of a process variable and more of a film property. To satisfy the EDX requirements and to avoid wastage of precious target material, (as explained in chapter 2) the thickness of the film is kept constant at around 500 nm. With both power level and required thickness fixed, the duration of deposition is automatically fixed to 90 min.

The distance between the target to substrate is a process variable which affects the deposition rate and therefore influences the thickness of the film formed. H.B. Nie et al (2001) observed that even under constant gas pressure, the growth mechanism of TaN films were greatly affected by the target to substrate distance [128]. In a work published by H.Toku et al (2010), TiO_2 films are seen to change from a well crystallised anatase phase to low crystalline structure, with the increasing distance between substrate and target [125]. The Teer coating UDP 350 system has one single circular carousel with 6 substrate holders set at equal constant distance of 130mm from all of the targets and cannot be changed.

From chapter 3, the as-grown TCR values are observed to be negative and resistance values to be unstable. Heat treatment at higher temperature heals the defects and increases the crystalline nature of TaN films thereby shifting their as grown negative TCRs in a positive direction [135]. The duration of heat treatment time is seen to affect the resistivity of NiCr thin film resistors [136]. Therefore, temperature and duration of post deposition heat treatment is very important to tune the TCR values closer to zero and impart resistance stability.

The figure 4-1 below shows the process flow for the first stage in which binary films of Mn-CuN and Mn-AgN will be deposited under varying partial Nitrogen pressures and substrate temperatures. As-grown films will be heat treated under varying temperatures, from 200 to 400ºC in steps of 100ºC, and for varying time durations from 1 hour to 5 hours, to tune the electrical properties of as grown thin films close to the desired values. The combination of deposition parameters, which yield the closest value, will be narrowed down and electrical properties of these films will be analysed to validate results from the literature search. Results from the binary films will be used to proceed to ternary deposition in the second stage.

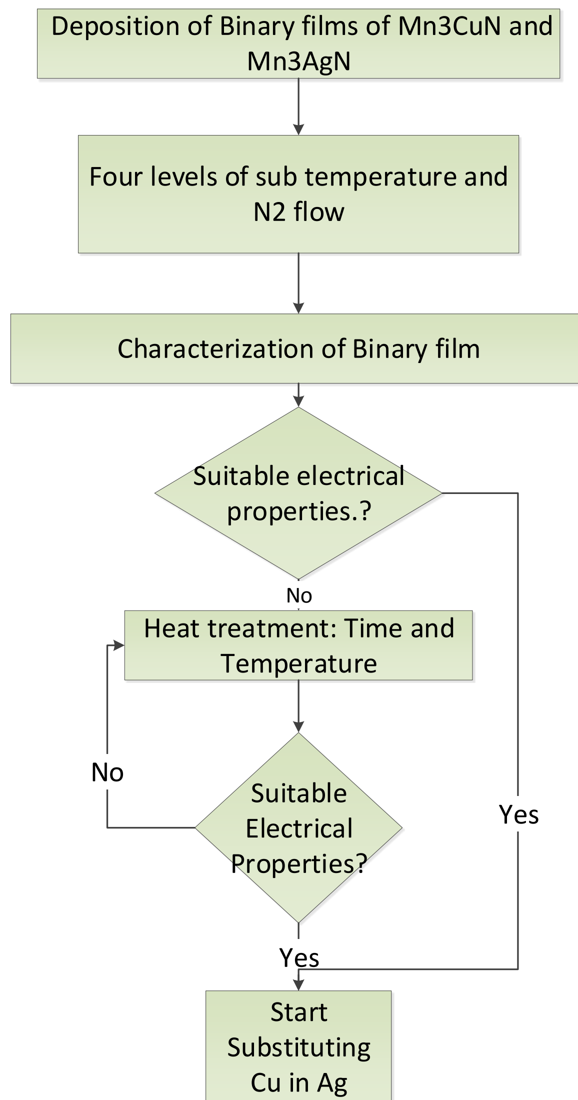

Fig 4-1 Process flow to deposit Mn based Ag or Cu binary thin films.

4.2 Design of Experiment:

From the previous section, four of the process parameters were selected to study their effect on the material system. Two of them were sputter deposition parameters: N_2 partial pressure and substrate temperature, and the other two were post deposition heat treatment parameters: temperature and duration.

N_2 partial pressure percentage for deposition was calculated by taking the ratio of N_2 flow per minute over the combined flow of N_2 and Ar into the chamber per minute, as given by:

$$N_2\ Partial\ pressure\ \% = \frac{N2\ flow\ in\ sccm}{N2\ flow\ (in\ sccm) + Ar\ flow\ (in\ sccm)} \times 100 \quad (4.1)$$

The total amount of gas flow (N_2+Ar) into the chamber was kept at a constant value of 30 sccm. Four levels of N_2 flow rates were achieved by increasing the N_2 flow as 1, 2, 3 and 5 sccm for Mn-AgN films and 2, 3, 5, and 6 sccm for Mn-CuN films. For each increase in N_2 flow, Ar flow was adjusted accordingly, to keep the total gas flow constant at 30 sccm. By using the eq. 5.1, the N_2 flow rates could then be converted to the following N_2 partial pressure percentages of: 3.33, 6.66, 10, 16.66 and 20% for N2 flow rates of 1, 2,3,5,and 6 Sccm.

Substrate heating was achieved by a heating plate situated inside the deposition chamber. Y.Na et al (2011) have deposited Mn_3CuN antiperovskite structures at higher T_S of 180ºC, and Aoyama et al (2013) have also observed very flat temperature dependence of resistivity at intermediate T_S levels of 75 and 100ºC [83, 84]. The highest temperature possible on a substrate kept inside the Teer coating plant was 130ºC. Three levels of substrate temperature were used: film deposition without substrate heating, at 50, and 100ºC.

DoE to deposit Mn-AgN and Mn-CuN films, by varying two of the sputter deposition parameters: Substrate temperature and N_2 partial pressure over different levels are as detailed in table 4-1

Table 4-1 DoE for 2 deposition factors used to deposit binary films of Mn-AgN and Mn-CuN.

Factors	Material system	No of levels	Level values
Factor 1: N_2 flow rate (sccm)	**Mn-Ag-N films**	4	1,2,3,5 sccm
	Mn-Cu-N films	4	2,3,5,6 sccm
Factor 2: Substrate Temperature (˚C)	**Mn-Ag-N films**	3	Without Tsub, 50ºC,100ºC
	Mn-Cu-N films	3	Without Tsub, 50ºC,100ºC

For each material system, the number of deposition conditions generated is given as

No. of deposition conditions = No. of level factor 1 X No of levels factor 2 (5.2)

Using this,

No of deposition conditions for Mn-AgN + No of deposition conditions for Mn-CuN = (4x3) + (4X3) = 24

The 24 sets of depositions along with their material type, process parameters, and levels of process parameters are as shown in table 4-2. After as grown measurements, samples from these sets were subjected to heat treatment. Heat treatment was carried out in closed tube furnace and in flowing Nitrogen environment, with constant flowing rate of 2l/min. Three separate batches of samples from as grown film plates were subjected to three levels of heat treatment: 200ºC, 300ºC and 400ºC, incrementing in steps of 100ºC. The lowest temperature was chosen as 200ºC to keep it above the dry heat stability test temperature of 155ºC. One more batch was heat treated later at 350ºC when it was noticed that crossing of the zero TCR line takes place between 300 and 400ºC. The film samples showing the lowest TCR values were chosen to experiment for the time duration of heat treatment. Time duration was varied from 1 hour to 5 hours with one-hour increments.

4.3 Results and Discussion

The following three main electrical properties were measured for each batch of samples: Electrical sheet resistance at room temperature, Rs (Ω/□), $TCR_{avg.}$ between 20ºC and 70ºC (ppm/ºC), and Resistance Stability ΔΩ/Ω, (%). Resistance measurement and TCR measurement was made both on as-grown and heat treated samples. Dry heat stability tests were only made on the heat-treated samples that showed lowest TCR values.

4.3.1 Effect of Nitrogen flow rate on as grown films:

Chemical composition and thickness analysis:

Chemical compositions of as-grown films were measured using the EDX system, for five sites across the length of the glass slide for each sample. The average values for each sample were calculated as atomic percentage ratio of each constituent material and then rounded off to the next closest whole digit. Thickness for each sample was measured using the DEKATAK profilometer. Six measurements were made across the artificial step created by the kapton tape during deposition. The average thickness values in nm and atomic percentage ratio for deposition sample set are presented in table 4-2.

As can be seen, the N_2 flow rate is a more significant factor in deciding the atomic composition of the films as compared to the substrate temperature. The Mn:Ag:N ratio of 3:1:1 required for formation of Mn_3AgN antiperovskite composition is obtained at the 3 sccm flow rate of N_2 or at 10% partial N_2 percentage in the chamber. For the formation of Mn_3CuN antiperovskite composition, it requires a higher N_2 flow rate of 5 sccm or 16.66% of partial N_2 pressure. Previous work done has experimented with varying Nitrogen partial pressure to successfully fabricate these structures, for example, Y. Sun et al (2010) [82] and Y. Na et al (2011) [75] were able to realize the Mn_3CuN structure at 10% N_2 partial percentage, whereas work done by M. Aoyama et al (2013) [84] required this parameter to be 50%. So the N_2 flow rate required to form the structure will be related to the individual sputter machine dimensions and other working recipe parameters like working pressure, which will decide the amount of Nitrogen species available in the plasma plume for the sputtered atoms to react with.

From table 4-2 it can be seen that Mn-AgN films are deposited with a higher thickness of~600 nm, compared to Mn-CuN films which are deposited in the range of~500 nm. With the same deposition time and almost same deposition power, it can be concluded that the reason for increased thickness for Mn-AgN films is the higher deposition rate of Ag compared to Cu. Figure 4-2 (a) shows the side profile images of Mn-AgN deposited at 3 sccm N_2 flow and without any substrate

temperature (Tsub), and figure 4-2 (b) shows the side profile for Mn-CuN deposited at 5 sccm N_2 flow rate and without Tsub. The thickness values achieved from the profilometer measurements are strongly supported by the side profile images of these films taken on the SEM. Neither N_2 flow rate or substrate temperatures seems to have any major effect on the thickness variation.

Table 4-2 Table of thickness and composition analysis for as-grown samples of Mn-AgN and Mn-CuN films.

Material	**Tsub (ºC)**	**N_2 Flow rate (sccm)**	**EDX ratio of Mn:Ag:N (at %)**	**Thickness (nm)**	**Sample No**
Mn-AgN	Without Substrate heating	1	64:31:5	586	1
		2	58:28:14	612	2
		3	59:21:20	617	3
		5	39:20:39	614	4
	50	1	68:32:0	604	5
		2	59:29:12	629	6
		3	54:21:25	635	7
		5	36:20:44	628	8
	100	1	69:31:0	548	9
		2	60:26:14	605	10
		3	58:20:22	635	11
		5	31:20:49	621	12
Mn-CuN	Without Substrate heating	2	77:23:0	498	13
		3	70:20:10	493	14
		5	60:21:19	488	15
		6	54:20:26	497	16
	50	2	75:24:1	504	17
		3	69:22:9	496	18
		5	62:20:18	486	19
		6	56:20:24	490	20
	100	2	76:24:0	517	21
		3	69:22:9	505	22
		5	60:20:20	499	23
		6	53:19:28	511	24

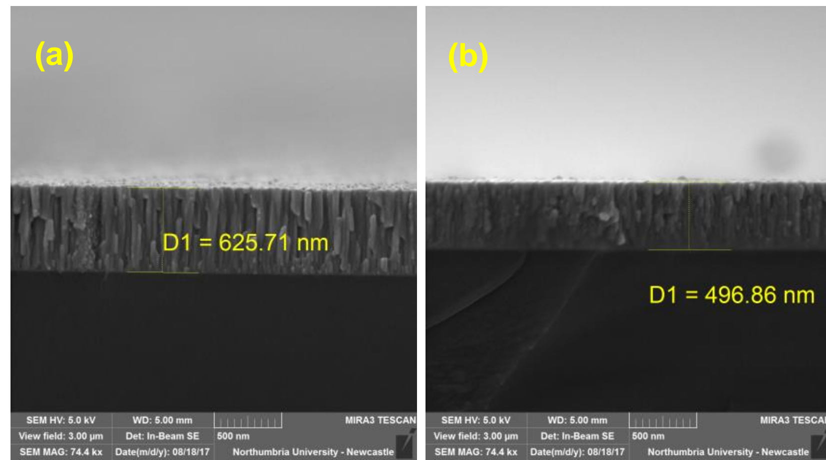

Fig 4-2 Cross section images of (a) Mn_3AgN films (sample no 2: deposited at 3 sccm and without Tsub) (b) Mn_3CuN films (sample no 12: deposited at 5 sccm and without Tsub).

<u>Electrical analysis of as grown film:</u>

Figures 4-3 (a) and (b) show the as-grown average electrical sheet resistance of the Mn-AgN and Mn-CuN films respectively, with increasing substrate temperature for the three varying N_2 flow rates discussed above. The average value of sheet resistance is calculated from a sample of 6 resistors taken from the central region of the alumina plate.

The lowest value of sheet resistance for Mn-AgN is seen to be 4.28 Ω/□ for films grown at 1 sccm of N_2 and without any Tsub whereas the highest value is recorded to be 8.54 Ω/□ for films grown at 5 sccm and a Tsub of 50°C. For Mn-AgN films, the sheet resistance is seen to increase with increasing N_2 flow rate, as more Nitrogen atoms become available in the film to migrate towards grain boundaries making them more resistive [137]. At lower N_2 flow rates the substrate temperature is not as effective in increasing the sheet resistance value, but for higher N_2 flow rates the resistance increases with the increased substrate temperature. Similar increases in sheet resistance observed at increased Tsub are explained by the migration of N_2 species to grain boundaries at higher Tsubs, which reduces the hole mobility leading to an increase in sheet resistance [138-141]. The sheet resistance value of Mn_3AgN structure formed at 3 sccm of N_2 flow rate lies in between the other two flow rates.

For Mn-CuN films, the lowest value of 12.42 Ω/□ is obtained for the films grown at 2 sccm of N_2 flow with a substrate temperature of 100ºC and the highest value of 27.90 Ω/□ is obtained for the films grown at 6 sccm of N_2 flow at 100ºC. Sheet resistance is seen to be comparatively higher than Mn-AgN films by a factor of 2 to 3. This could be a combined effect of the higher resistivity of Cu than Ag and the comparatively thinner films of Mn-CuN samples. It is seen that with each increasing N_2 flow rate there is a 20-30% increase in the sheet resistance of the film. So again similar to Mn-AgN films, increase in N_2 flow rate results in a significant increase in sheet resistance values. For lower N_2 flow rates, sheet resistance values decrease with increasing substrate temperature, which could be seen as the result of defect healing, caused from the increased energy from the substrate temperature, which leads to better conductivity in the film. However, for the Mn_3CuN films deposited at 5 and 6 sccm of N_2 flow rate, the higher Nitrogen content in the film migrates easily to grain boundaries with increasing substrate temperature. This make the films more resistive as it overcomes the decrease in the resistance caused by the defect healing caused by higher temperature [142].

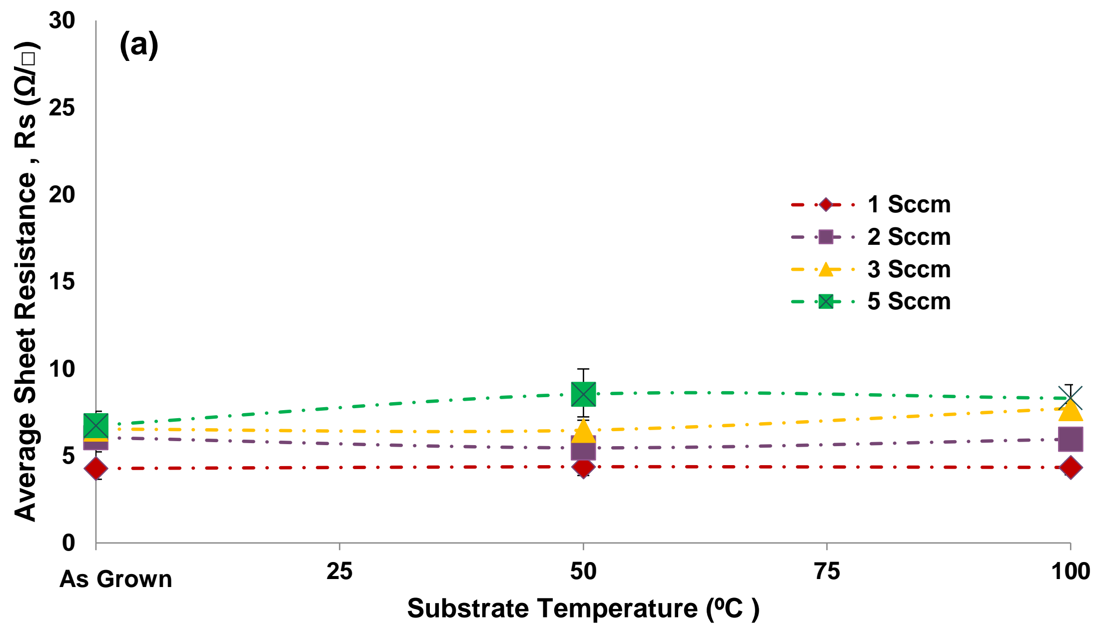

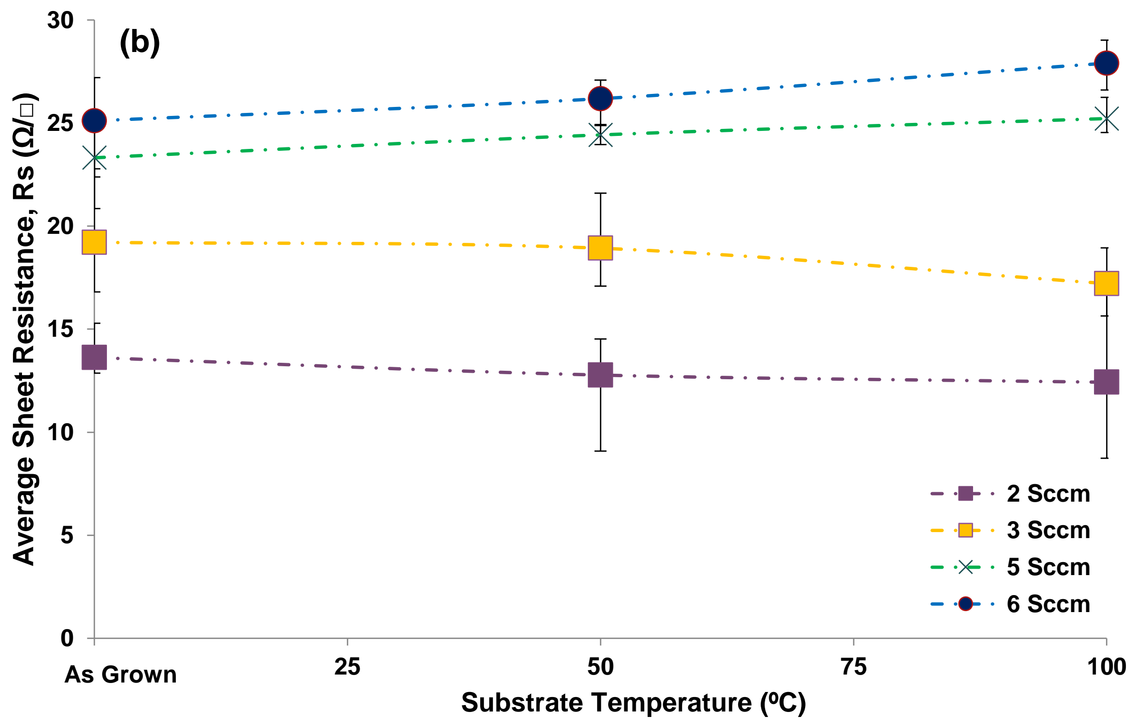

Fig 4-3 Graph of sheet resistance values of as-grown films with increasing substrate temperature for 4 varying N_2 flow rates (a) Mn-AgN films (b) Mn-CuN films

Figures 4-4 (a) and (b) show the as-grown TCR of the Mn-AgN and Mn-CuN films respectively, with increasing substrate temperature for the three varying Nitrogen flow rates discussed above. The average resistance values are calculated from the same 6 resistor circuits used for the sheet resistance measurement.

The as-grown TCR values of all the Mn-AgN and Mn-CuN films are as presented in figure 4-4 (a) and (b). For Mn-AgN films, as shown in figure 4-4-(a), the most negative TCR of -235 ppm/^{o}C is obtained for films grown at 3 sccm of N_2 flow rate grown without Tsub. Whereas for the films grown at 5 sccm and 100°C Tsub the TCR value moves much closer to 0 at -87ppm/^{o}C. There is a negative shift in the TCR value for an increase in N_2 flow rate from 1 to 3 sccm, but from 3 to 5 sccm there is a massive positive shift in the TCR closer to zero. It is expected for a material system to exhibit negative TCR with incrementing concentration of dopants like O and N in the TFR material systems, but the behaviour of films grown at 5 sccm is deviating from the trend. For a constant N_2 flow rate, TCR is observed to shift in a positive direction with increasing substrate temperature. Voids and defects which commonly acts as a source of negative TCR get healed with the increasing substrate temperature which results in a positive shift of TCR [143, 144] . The Mn_3AgN antiperovskite structure formed at 3 sccm is seen to exhibit the lowest TCR for all the substrate temperatures.

The as-grown TCR values of Mn-CuN films are more negative than Mn-AgN films. The lowest TCR of -363 ppm/^{o}C is observed for Mn-CuN films grown at 6 sccm and without Tsub and the highest value for TCR is observed to be -287 ppm/^{o}C for films grown at 2 sccm and 100°C. Unlike Mn-AgN films, the TCR values of Mn-CuN films show a consistently negative shift with increasing N_2 flow rate, though the shift between 3 and 5 sccm line is barely visible. The positive shift in TCR with increasing substrate temperature for each N_2 flow rate is present, possibly because of defect and void healing at higher temperature, but its effect is not very strong as seen in TCR lines of the Mn-AgN samples.

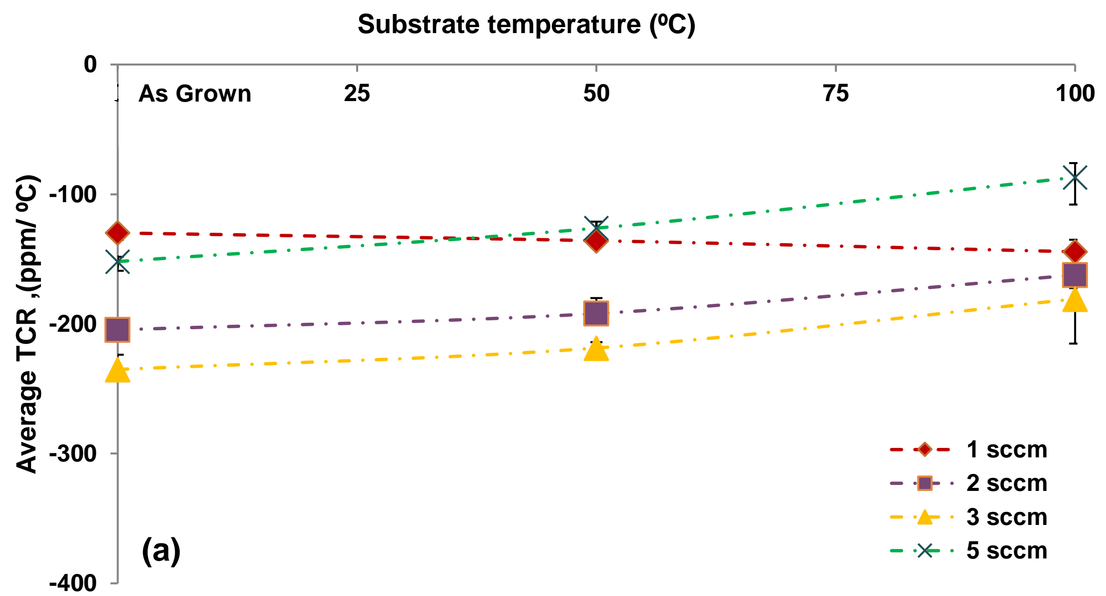

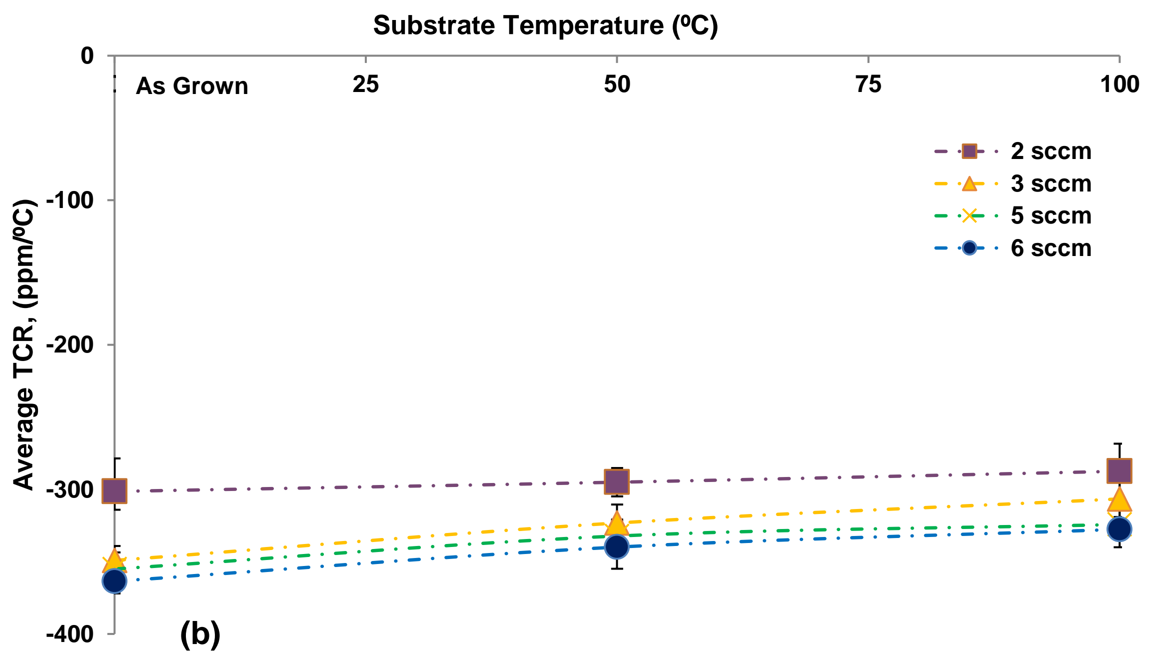

Fig 4-4 Graphs of TCR values of as grown films with increasing substrate temperature for 4 varying N_2 flow rates (a) Mn-AgN films (b) Mn-CuN films

Structural and topographical analysis of as-grown films at varying N_2 flow rates:

As-grown samples were analyzed in a Siemens D5000 X-Ray diffractometer to identify the nature of crystal structure formed under these varying deposition parameters. Samples were measured at room temperature for 2θ values from 20 to 90 ° with a step increment of 0.02 °. Figure 4-5 (a) and (b) shows the XRD peaks for Mn-AgN and Mn-CuN films deposited at increasing N_2 flow rate.

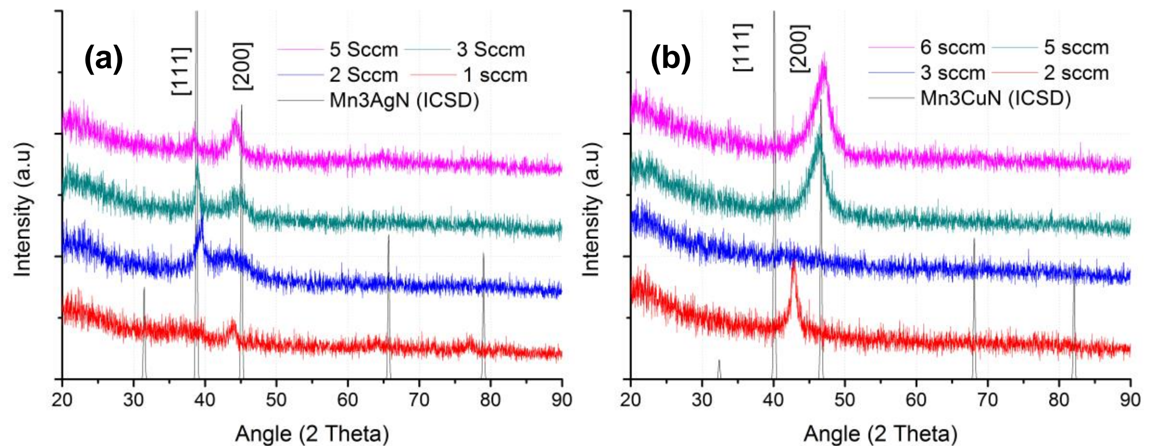

Fig 4-5 XRD spectrum (a) Mn-AgN films (b) Mn-CuN films at increasing N_2 flow rates and without Tsub.

According to the Inorganic crystal structure database (ICSD) the most distinctive peaks for Mn_3AgN antiperovskite occurs at 38.8 and 45.11 ° and represents planes with miller indices of (111) and (200) respectively. These are represented as black sharp peaks in figure 4-5 (a) along with the other less dominant peaks for the material system as shown in fig-3-18. By comparing these peaks to the XRD spectrums of films of Mn-AgN, it can be seen that the films have a preferential orientation along these two planes compared to other planes reported for the material structure. At the lowest N_2 flow rate of 1 sccm, one small peak exists in the spectrum to suggest presence of some kind of crystalline structure but the curve is far away from the expected position for antiperovskite structures. At 2 sccm, the peak previously observed appears to grow and two peaks are visible with a broad shoulder between them both. With the further increase in N_2 flow rate to 3 sccm, both the peaks become separate and align with the central peak position for the Mn_3AgN structure, indicating the structure formation at this flow rate. At a still higher N_2 flow rate of 5 sccm, the (111) plane reduce in intensity while (200)

plane undergoes a shift from the original position, indicating internal strain in the film because of higher Nitrogen content in the film. Introduction of dopants with varying radii can initiate strain in the crystal lattice of cubic antiperovskite which are then manifested in XRD spectrums as a shift of the central peak [81].

Peak positions for Mn_3CuN are recorded to be 40.11 and 46.65° representing (111) and (200) crystal lattice planes and are shown as black peaks in figure 4-5(b). As opposed to Mn_3AgN, no distinctive antiperovskite peaks are formed at lower N_2 flow rates for Mn_3CuN. However, a very clear peak at 46.6° is seen for XRD spectrums of samples deposited with 5 sccm of N_2 flow rate, indicating preferential growth only along (200) crystal lattice planes. For this flow rate it can be seen that no other peaks exist to suggest existence of Manganese or Copper in any other form, either pure or as an oxide and it can be stated that the film is in a pure antiperovskite phase [82]. Most of the work done on thin film deposition of Mn_3CuN have achieved single phase Mn_3CuN with crystal orientation in the (200) plane [75, 82-84, 89]. The peaks achieved in the films in this work are considerably broader, for both Mn_3AgN and Mn_3CuN films, when compared to the XRD spectrums of recorded specimens. In XRD analysis, the grain size decreases with the increasing width of the peak. So the sharp peaks suggest a crystalline nature of film, the width of the peaks suggest a very small crystallite size therefore it can be concluded that the films exists in a nano - crystallized state [82].

Figure 4-6 (a) - (c) shows the effect on the shape and size of grains of Mn-CuN films grown with increasing Nitrogen flow rate. The triangular structure of Mn_3CuN films developed at 5 sccm of N_2 flow rate (figure 4-6(c)) is very similar to the grain shape achieved by Y.Na et al [75] in their work with Mn_3CuN thin films, figure 4-6 (d) (inset a). The figures in 4-6 (d) (inset b-d) show the degradation of Mn_3CuN grain shape after introduction of Ge in their work and these images bear resemblance to the Mn-CuN attempts at lower N_2 flow rates, figure 4-5 (a) and (b).

From EDX composition, XRD spectrums and SEM imaging it can be seen that N_2 flow rate plays an important role in determining the antiperovskite structure for the

Mn based group. So after annealing heat treatment (in section 4.3.3) if the samples grown at these N_2 flow rates (3 sccm Mn-AgN and 5 sccm for Mn-CuN films) lead to stable near zero TCR values, the potential of antiperovskite for the TFR industry could be justified, and N_2 flow rates for experiments in further chapters could be fixed.

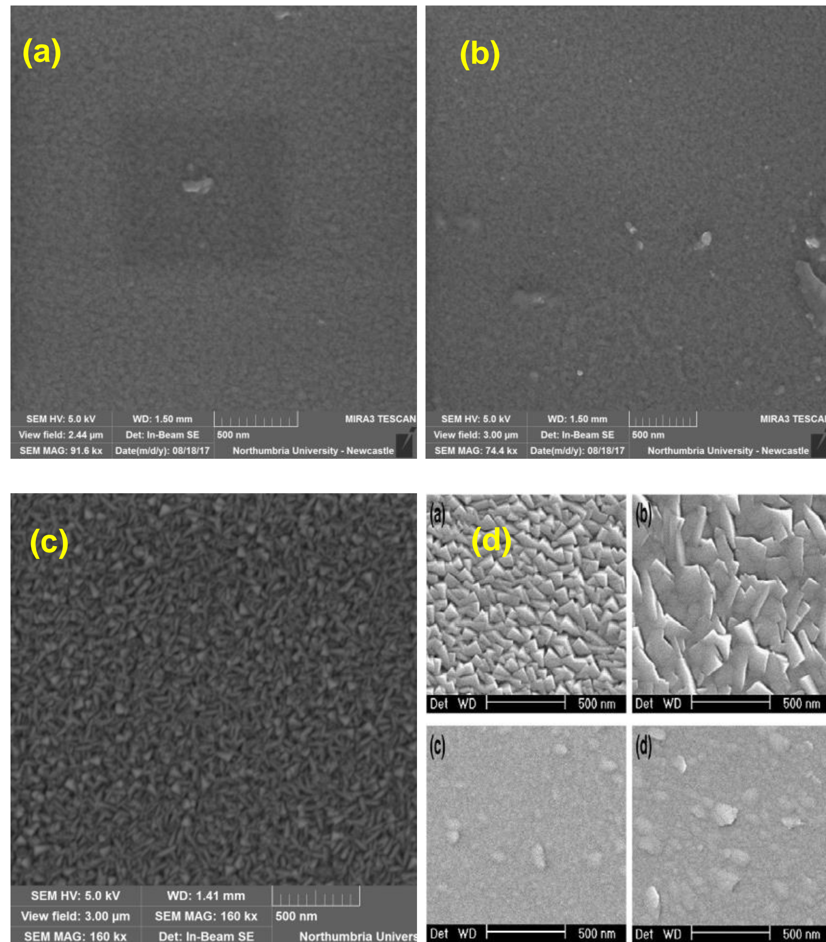

Fig 4-6 Surface images of Mn-CuN film grown at (a) 2, (b) 3 and (c) 5 sccm of N_2 flow rate(without Tsub). (d) Published images of Mn_3CuN antiperovskite shows deteriorating of antiperovskite structure (from inset a to d) with increasing Ge content [75].

4.3.2 Effect of substrate temperature on as-grown film:

Figure 4-7 (a) and (b) gives another perspective of the results described in the previous section, to emphasize the role of substrate temperature on the as-grown sheet resistance of the Mn-AgN and Mn-CuN films being studied. Each line in their respective plots represents as-grown sheet resistance values of Mn-AgN and Mn-CuN films deposited at increasing substrate temperature, plotted for their sheet resistance against N_2 flow rate. In both cases, the lines deposited on increasing substrate temperature are spaced much closed to each other. Substrate temperature has more effect on sheet resistance of Mn-AgN films than on Mn-CuN films, but for a constant N_2 flow rate, no combination of substrate temperature could produce a change in sheet resistance greater than +/- 2.79 Ω/□ (15>20%), in either set of Mn-AgN and Mn-CuN films. Lower N_2 flow rates show decreasing sheet resistance with increasing substrate temperatures possibly due to increasing crystallization. At higher N_2 flow rates, substrate temperatures aid more outflow of N_2 to grain boundaries, which begins to overcome the reduction in Rs from crystallization and starts increasing sheet resistance.

Figure 4-8 (a) and (b) shows a similar effect of increasing substrate temperature on TCR of Mn-AgN and Mn-CuN films respectively, plotted against increasing N_2 flow rate. Each line of TCR plotted for increasing substrate temperature shows a clear shift in the positive direction, irrespective of N_2 flow rate. One major reason to experiment with the substrate temperature during deposition stage was to see if near zero TCR values could be achieved by this step alone, thereby avoiding an additional annealing step currently used to tune TCR value closer to zero. While the shift for Mn-AgN is more pronounced than for Mn-CuN, the effect of substrate temperature is not pronounced enough, on either of the material systems, to shift the TCR values to a near zero value without additional annealing treatment. Near-zero as-grown TCR values might be possible with still higher substrate temperature, especially for Mn-AgN films, but the effect of such a deposition technique on electrical stability would then have to be further studied.

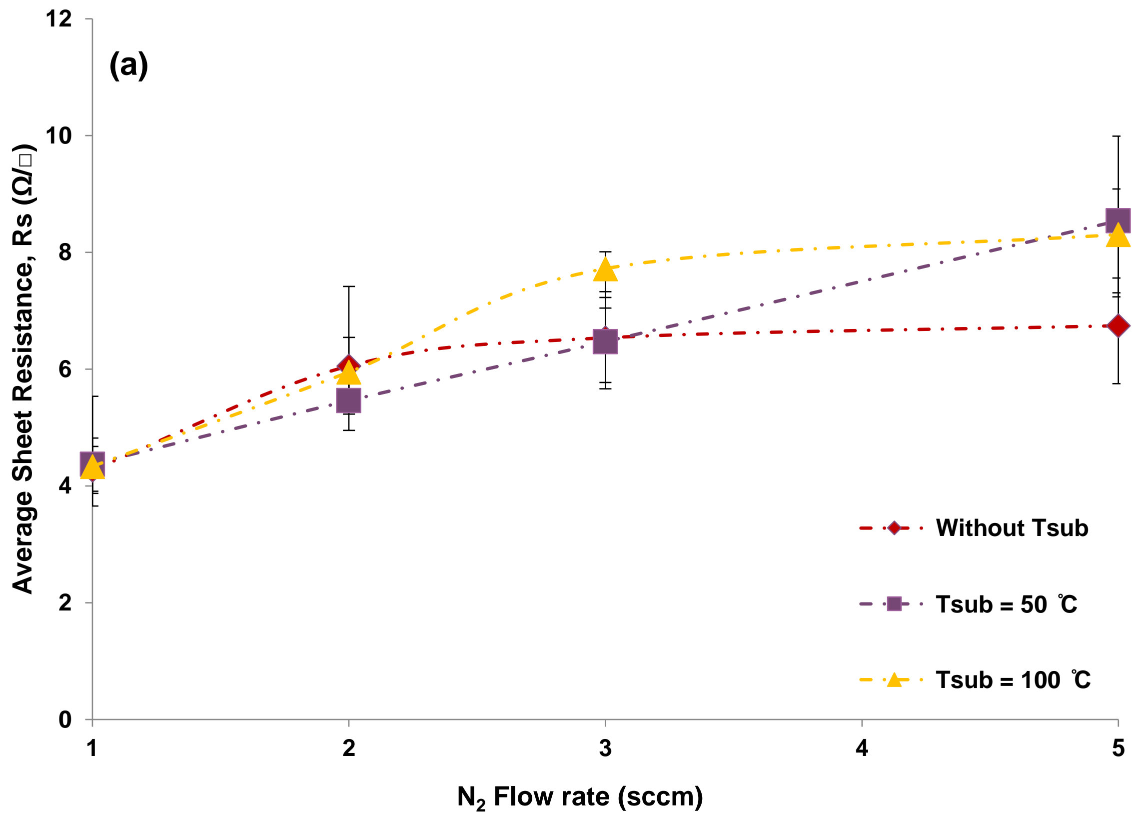

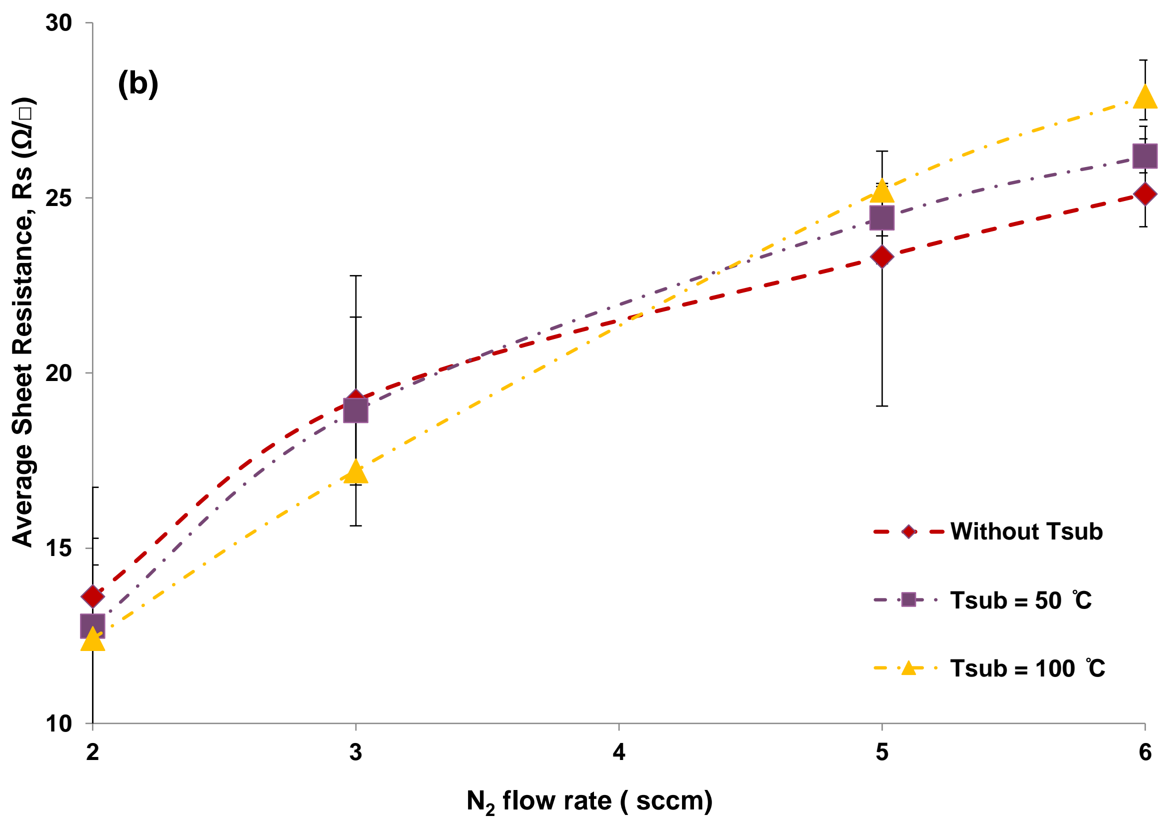

Fig 4-7 Graph of sheet resistance values of as-grown (a) Mn-AgN (b) Mn-CuN films plotted against increasing N_2 flow

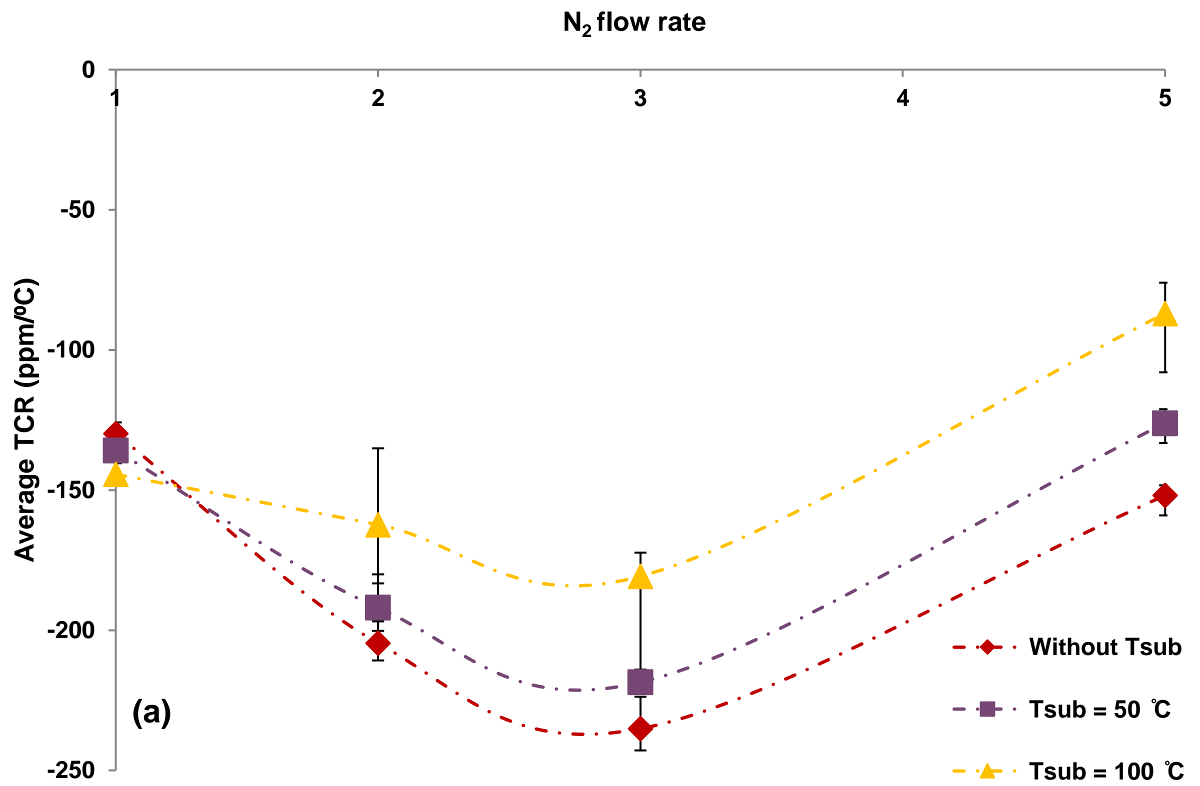

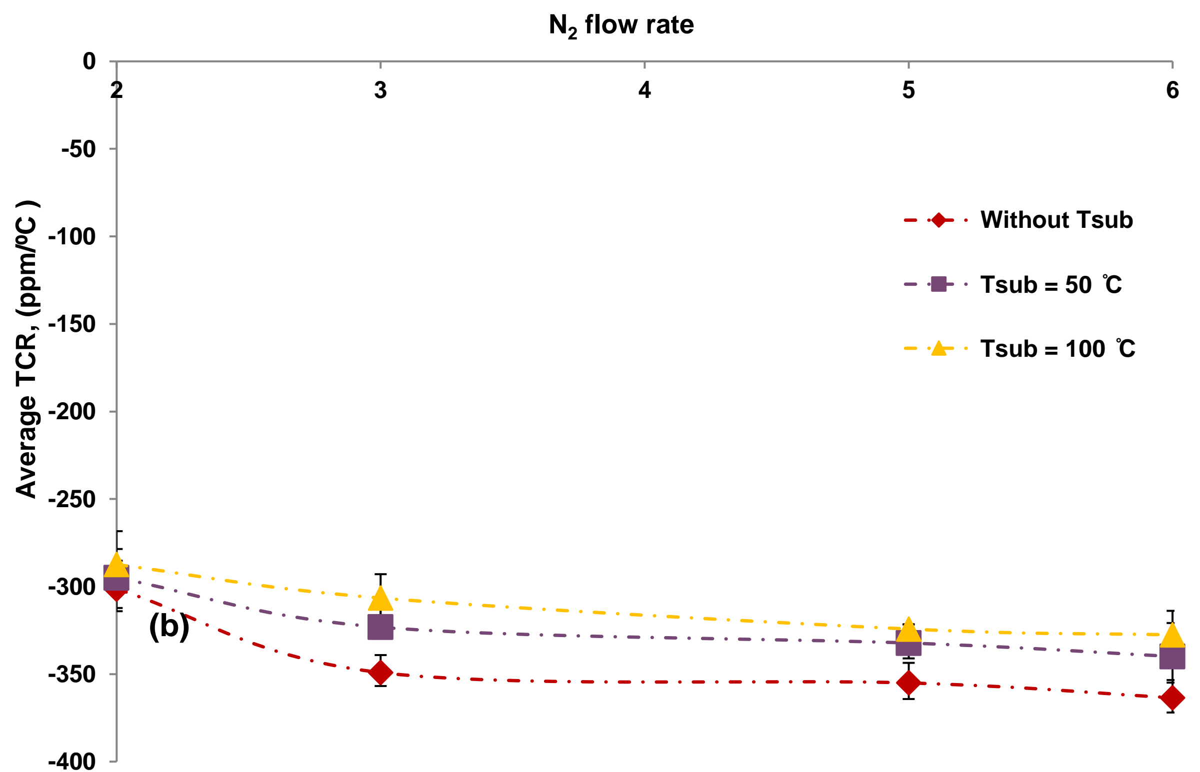

Fig 4-8 Graph of TCR values of as-grown (a) Mn-AgN (b) Mn-CuN films plotted against increasing N_2 flow

Structural and topographical analysis of films grown at varying Tsub:

Comparison between XRD spectrums of Mn_3AgN and Mn_3CuN (constant Nitrogen flow rate of 3 sccm for Mn-AgN and 5 sccm for Mn-CuN) films grown at varying substrate temperatures are shown in figure 4-9 (a) and (b). It is very hard to see the small increase in crystallization of Mn_3AgN films when grown at different substrate temperatures. The noticeable change occurs for the (200) planeof Mn_3CuN, which is seen to have become more developed when grown at Tsub of 100ºC.

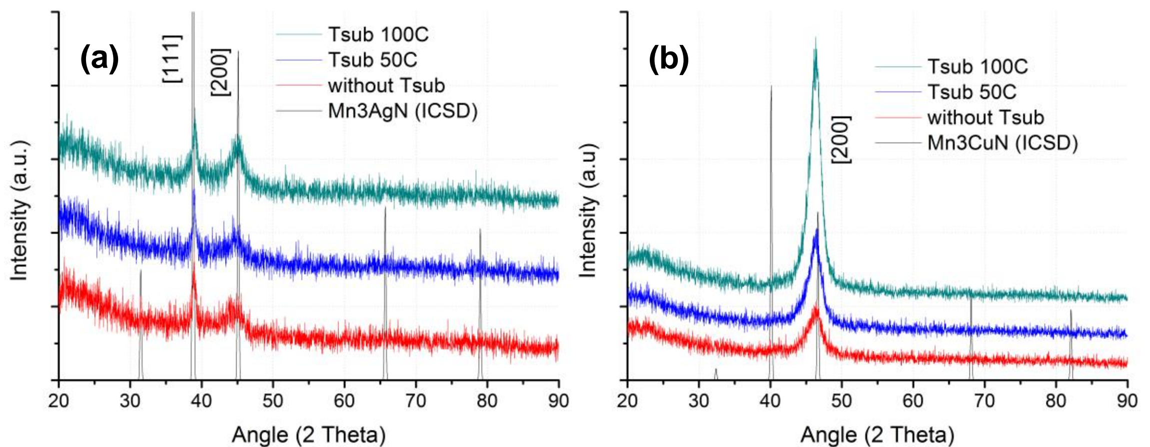

Fig 4-9 XRD spectrum of (a) Mn_3AgN antiperovskite structure (b) Mn_3CuN antiperovskite, deposited at increasing substrate temperature

The XRD plot can be used to calculate the average crystallite size by using the Scherrer formula and could be used to verify the increasing crystallinity of the film. The Scherrer formula is given as

$$\tau = \frac{K\,\lambda}{\beta\,\cos(\theta)} \qquad (4.3)$$

Where τ is the crystallite size of the film, K is is the Scherrer's constant with a value of 0.9, λ is the wavelength of incident Cu (Kα) radiation (1.5418 Å), β is the Full Width Half Maximum (FWHM) of the peak, and θ is Bragg's angle of the peak. Because of the high level of background noise, it is very hard to establish the FWHM of the peaks and therefore calculating the grain sizes for Mn_3AgN peaks. The table 4-3 presents the observed FWHM and calculated mean grain sizes for

the (111) peak of Mn_3AgN samples deposited at increasing substrate temperature and suggests that the higher substrate temperature does lead to a small increase in crystallization of the Mn_3AgN antiperovskite structure formed.

Table 4-3 Table of FWHM and calculated mean grain size for Mn_3Agn and Mn_3Cun films deposited at increasing substrate temperature.

Material	Substrate temperature (˚C)	FWHM (˚)	Mean grain size (nm)
Mn_3AgN	0	0.68	14.58
	50	0.68	14.47
	100	0.66	15.50
Mn_3CuN	0	2.62	9.89
	50	2.42	11.05
	100	2.00	12.95

On the other hand, for Mn_3CuN films a very clear distinction could be seen for films grown at different substrate temperature, from figure 4-9 (b). The Table 4-3 presents the value for crystallite size in the (200) plane for the Mn_3CuN structure and a difference of ~3 nm in crystal size is calculated between films grown without Tsub and those grown at 100ºC. Work done by Tan et al (2015) reports crystallite sizes of 12 nm for Mn_3CuN samples developed by the spark plasma sintering method which employs high preparation temperatures and supports that higher preparation temperatures are beneficial for development of larger crystallite size [145]. The increasing crystallization from Tsub decreases sheet resistance and adjust TCR closer to 0, but the effect itself is small and could be realized better by an additional process of annealing treatment.

SEM images showing the grains of the Mn_3AgN films deposited at various substrate temperatures are shown in figure 4-10 (a), (b) and (c), and appear to be very similar in size. SEM shows presence of larger grain sizes but the majority of the grain sizes appear to be very close to the size figures calculated by the Scherrer equation above. The SEM analysis along with the XRD results, strongly suggests

that substrate temperature leads only to a minor increase in the crystalline nature of the film. So after annealing heat treatment (section 4.3.3), if samples deposited at elevated substrate temperature do not lead to a clear improvement in electrical values when compared to ones grown without Tsub, it would be reasonable to continue the further experiments without Tsub.

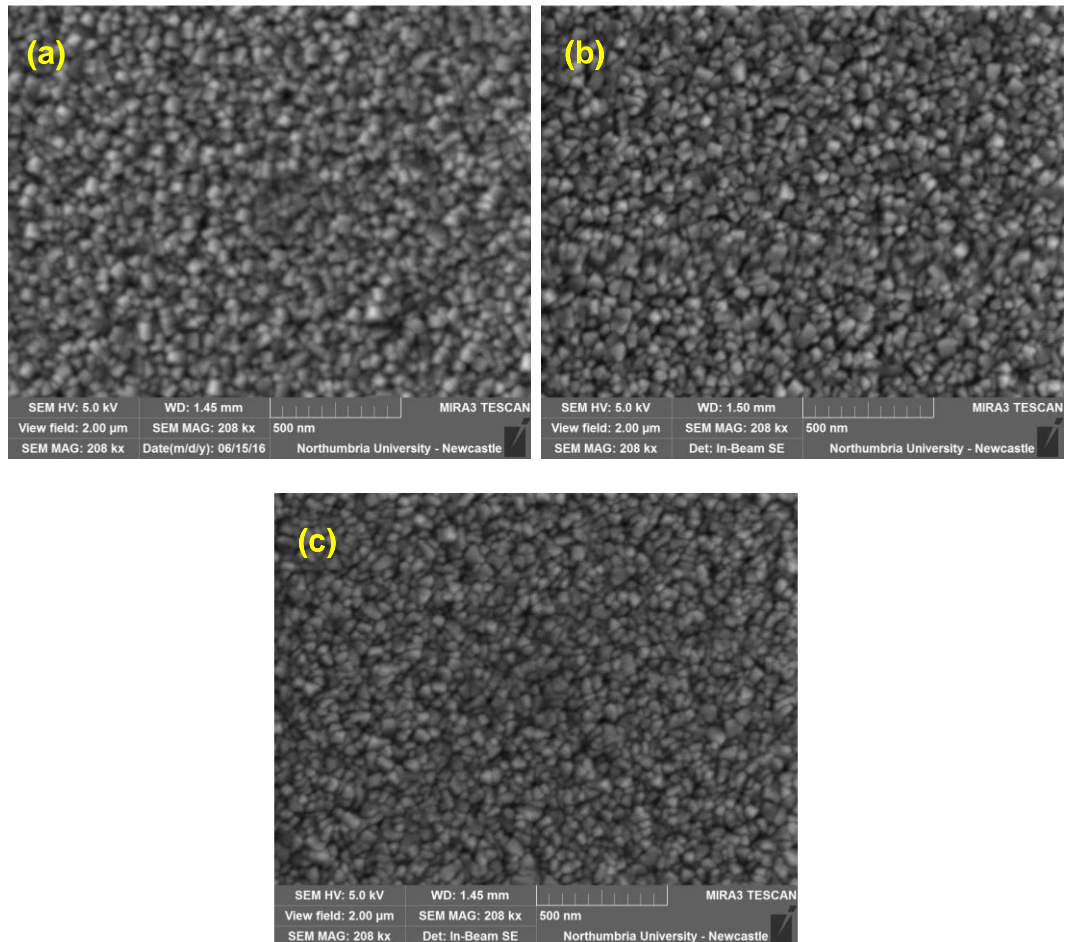

Fig 4-10 Mn_3AgN films grown at Tsub (a) without Tsub, (b) 50 and (c) 100ºC.

4.3.3 Effect of annealing temperature on film properties

The sheet resistance and TCR of Mn-AgN and Mn-CuN films deposited at four levels of Nitrogen flow and three levels of substrate temperature were measured after heat treating them at 200, 300, and 400ºC, in a flowing Nitrogen environment. An additional treatment temperature of 350ºC was added later when TCR was observed to cross over the zero line between 300 and 400ºC. From results on as-

grown films, it is observed that, the substrate temperature produces only a small effect on the electrical properties due to crystallization resulting from increased Tsub. However, N_2 flow rate on the other hand is seen to affect chemical composition, structure, and electrical properties significantly. Therefore, in the proceeding sections, sheet resistance and TCR measured after heat treatment will be studied primarily for films grown without Tsub, at various N_2 flow rates. Later, comparison of results for films grown at increasing Tsub and fixed N_2 flow rate will aim to clarify if Tsub is in fact able to produce any favorable effect on the electrical properties of antiperovskite films after annealing heat treatment.

Mn-AgN Sheet Resistance

Figure 4-11 shows the effect of various annealing temperatures on the sheet resistance of Mn-AgN films grown with increasing N_2 flow rate. Each line in the graph represents one N_2 flow rate. It can be seen that for heat treatment temperatures up to 300ºC, the sheet resistance is slightly decreasing for lower flow rates of 1, 2 and 3 sccm. For the lowest flow rate of 1 sccm, the resistance decreases at every step of increasing annealing temperature from 4.20 to 2.96 Ω/□. Sheet resistance, for the films deposited at 2 sccm decreases from 6.05 to 4.66 Ω/□, for heat treatment temperatures up to 300ºC and thereafter gradually increases with further increase in temperature up to 7.61Ω/□. A similar trend is shown by films deposited at 3 sccm of N_2 flow, Rs decreases from 6.53Ω/□ to 5.98Ω/□ for heat treatment up to 300ºC, but for temperatures above 300ºC shows an increasing trend ending at 11.87Ω/□ after heat treatment at 400ºC. For the highest flow rate of 5 sccm, the resistance shows an increasing trend even for the lowest of the heat treatment temperatures, and becomes very steep for higher heat treatment temperature up to a maximum of 30.36 Ω/□ following treatment at 400ºC.

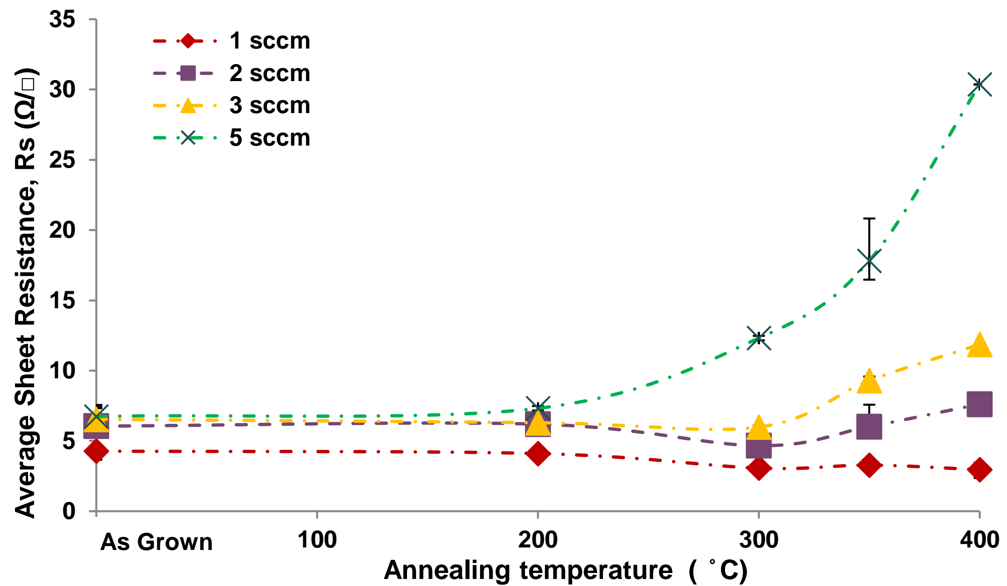

Fig 4-11 Graph of sheet resistance values of Mn-AgN film (without substrate temperature) with increasing annealing temperature.

To analyses the effect of substrate temperature after heat treatment, figure 4-12 compares the sheet resistance value of Mn_3AgN formed at 3 sccm of N_2 flow rate. Visible difference in the sheet resistance values for films grown at varying substrate temperatures only occurs at temperatures above 300⁰C. One common trend between Figure 4-11 and figure 4-12 is that, irrespective of deposition parameters, the resistance values are observed to increase very steeply for films heat treated at 300⁰C and above. While decrease in resistance at lower heat treatment temperature could be a result of defect healing and increased crystallization, the steep increase in sheet resistance at higher heat treatment temperature could be explained by increased oxidation of the top layer, which starts to compensate and overcome the decrease by the other two phenomena, (shown later in the EDX measurements).

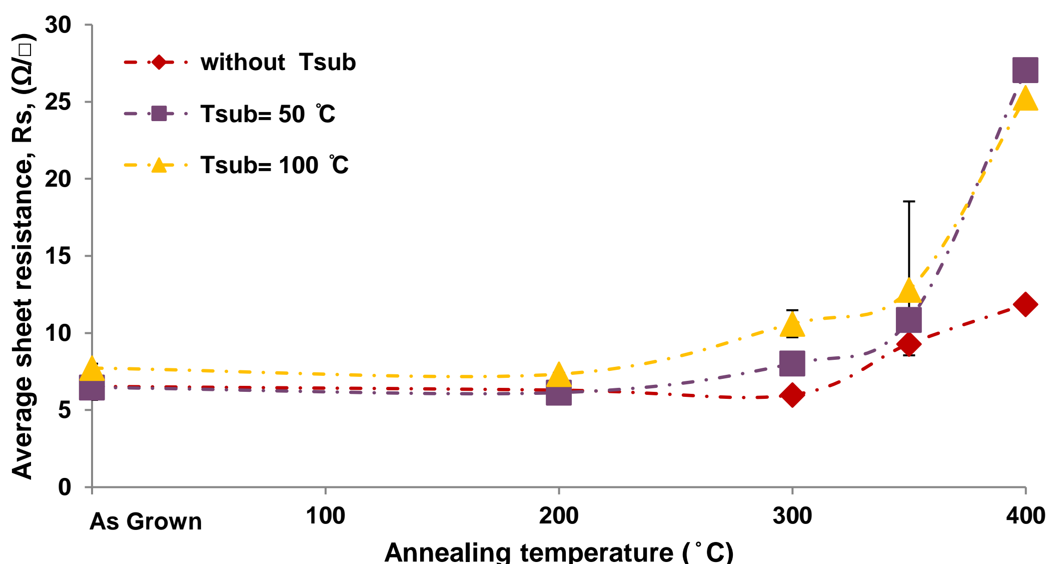

Fig 4-12 Graph of sheet resistance of Mn_3AgN film (3 sccm N_2 flow) with increasing annealing temperature.

Structural and topographical changes after annealing treatment:

After heat treatment at four different temperatures, the size of the sample set increased four times. The time consuming nature of XRD limited the analysis of the entire sample set. XRD spectra were developed only for heat treatment temperatures of 300 and 350°C. These temperatures were chosen as TCR values were observed to be closest to zero between these two values of heat treatment and they could subsequently be compared against the spectra for the as-grown samples. XRD spectra in figure 4-13 (a) to (d) show the effect of heat treatment temperature on the crystal structure of Mn-AgN films deposited with increasing N_2 flow rate.

The protrusion observed for the as-grown 1 sccm film (fig 4-13 (a) red line), becomes more pronounced with increasing heat treatment temperatures, and at 350 °C of heat treatment could be seen to shift closer to the (200) central peak than in the as grown state. A secondary peak very close to [111] appears after heat treatment at 300 C. It can be concluded that energy provided by heat treatment aids in rearrangement of elements into some form of crystalline formation with similarity to a strained antiperovskite structure. The as-grown sample at 2 sccm of N_2 flow rate has a peak very close to the (111) crystal peak position, and after heat

treatment at 300ºC appears to align more towards the 38.8° central position. But it is joined by a very broad shoulder passing well beyond the (200) plane position at 45.1°. While the strong peaks after 300ºC could suggest a structure under formation, the absence of a similar strength of peak after heat treatment at 350ºC, along with spectra of those at 1 sccm, indicates that the structure formation is not very reliable when films are deposited in a N_2 deficient environment. The films deposited at 3 sccm show consistent development of the antiperovskite structure when treated at increasing annealing temperature.

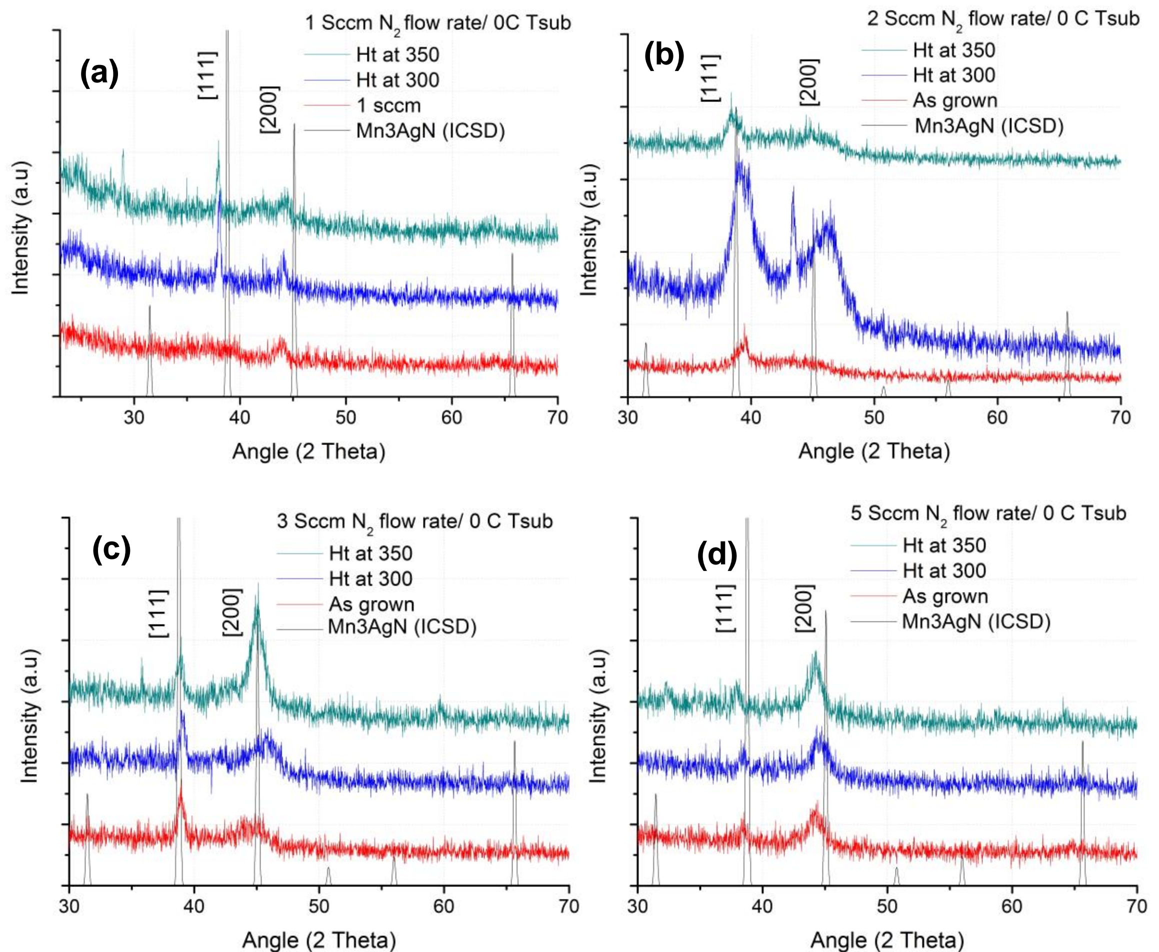

Fig 4-13 XRD spectrums of Mn-AgN deposited at (a) 1 , (b) 2, (c) 3, and (d) 5 Sccm before and after heat treatment.

After heat treatment at 350ºC the (200) plane becomes the dominant phase compared to, the (111) plane up to 300ºC. The films deposited at 5 sccm of N_2 flow rate also show presence of a dominant (200) phase but the shift from the central

peak position indicates a strain in the film [114]. With the increasing heat treatment temperature, the shift increases towards a lower angle indicating an increasing strain within the film. It can be concluded that the right amount of N_2 flow rate dictates the amount of Nitrogen in the film, which governs the formation and stability of the antiperovskite structure during the heat treatment process.

The effect of substrate temperature on the crystal structure of Mn_3AgN thin films before and after annealing heat treatment is presented in figure 4-14 (a) to (c). These three images compare three Mn_3AgN films (at 3 Sccm of N_2 flow rate) deposited at increasing Tsub, as they are heat treated at increasing annealing temperatures. For films grown without Tsub, after annealing at 350ºC the (200) peak gets sharp and dominant, but no clear difference is observed for the (111) peak. For films deposited at 50ºC of Tsub, the dominative nature of the (200) plane starts early after annealing at 300ºC, compared to films without Tsub. For the films deposited at 100ºC of Tsub, both the (111) and (200) peaks get sharper from 300ºC onwards, with the intensity of the (200) plane marginally higher than that of the (111).

The observed FWHM and crystallite size for the (200) peak is presented in table 4-4. It can be seen that there is an increase of 3.5 nm in grain size after heat treatment for samples grown without substrate temperature. Whereas samples deposited at 50 and 100ºC of Tsub only showed an increase of 1.63 and 0.9 nm respectively. Therefore, the rate of growth of crystal size after heat treatment appears to reduce for films deposited at higher substrate temperatures.

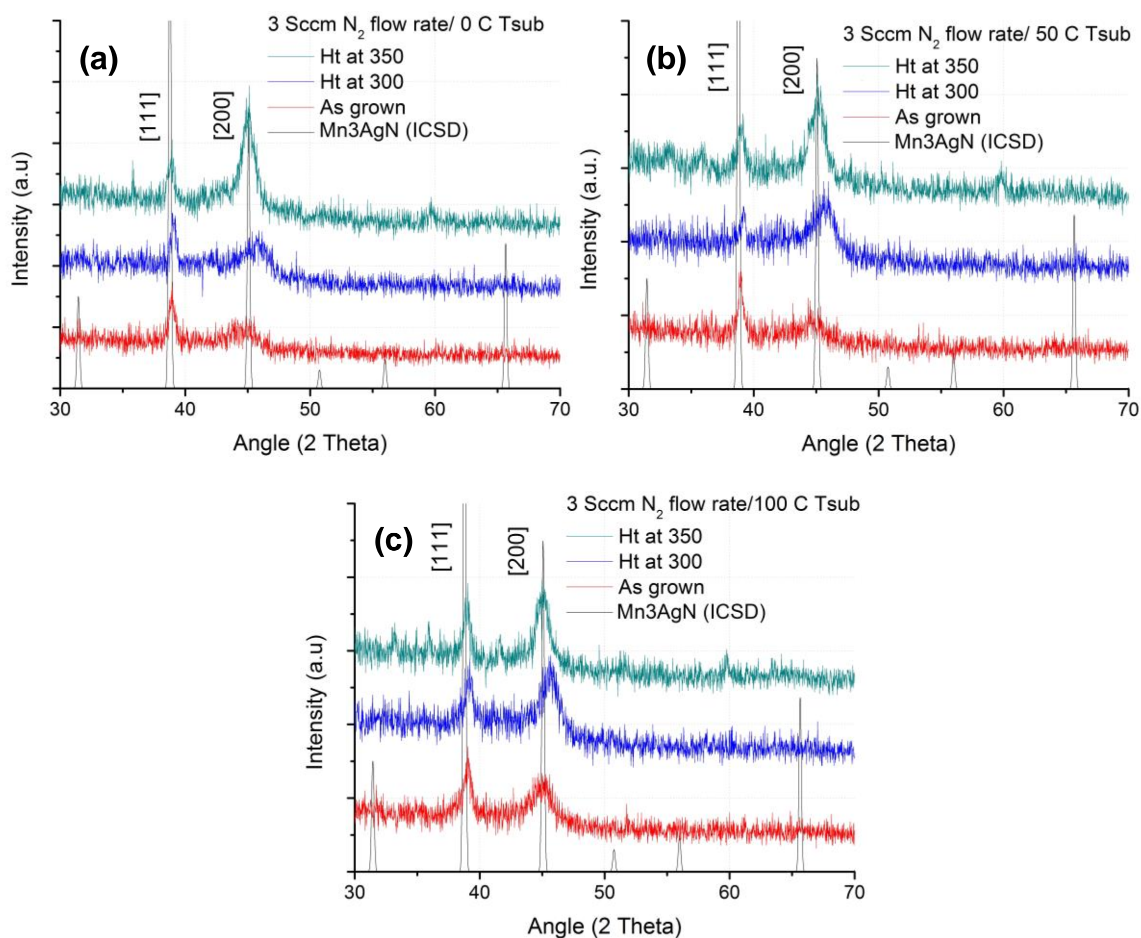

Fig 4-14 XRD spectrums before and after heat treatment for Mn_3AgN films grown (a) without Tsub (b) Tsub = 50ºC (c) Tsub = 100ºC.

Table 4-4 Table of FWHM and calculated crystallite grain size for Mn_3AgN samples before and after heat treatment

Material	**Tsub (˚C)**	**Annealing temperature (˚C)**	**FWHM (˚)**	**Mean Grain Size (nm)**
Mn_3AgN	Without Tsub	As-Grown	2.38	3.69
		300	2.26	4.15
		350	1.3	7.17
	50	As-Grown	2.72	3.79
		300	2.56	4.50
		350	1.72	5.42
	100	As-Grown	1.96	5.09
		300	2.04	5.90
		350	1.52	5.99

Side profile imaging of the samples after heat treatment, in figure 4-15, reveals that a secondary layer is formed on the top of the thin films. The Mn_3AgN film (3 sccm and at room temperature) had an as-grown thickness of 625 nm when analyzed, but after heat treatment at 350ºC the thickness of film increased to 748 nm, with the newly formed top layer having a thickness of 196 nm. The new layer on top could be an oxide layer formed during the heat treatment. There are cases of material systems in TFRs where oxide layers formed on top are known to protect the underlying layers from further degradation thereby making the thin film resistor stable [34]. Analyzing the heat-treated samples under the SEM verified the presence of larger structures on the top surface of the film but the grain boundaries are not very well defined like seen in as-grown films.

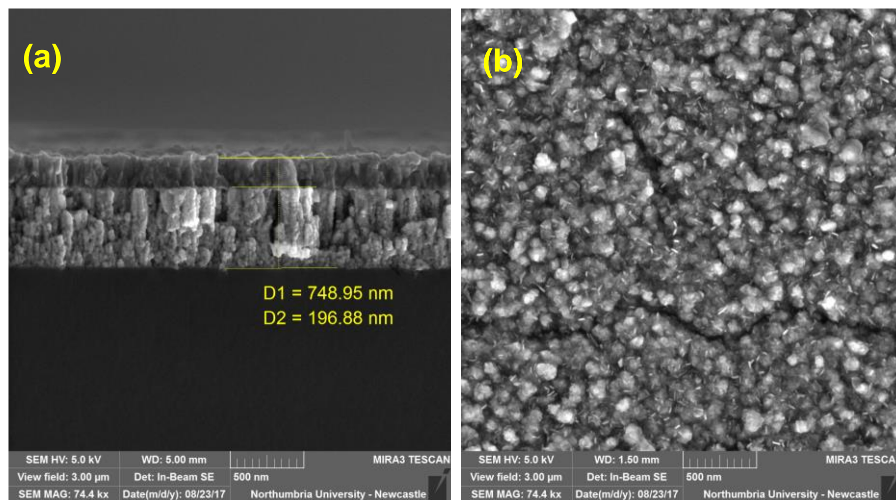

Fig 4-15 (a) Cross section (b) top profile of Mn_3AgN, grown at 3sccm N_2 flow and without Tsub, after heat treating at 350ºC .

EDX analysis performed on the Mn_3AgN shows rapid oxidation of the film, table 4-5. The films were annealed in a closed tube furnace with flowing Nitrogen environment. So the presence of Oxygen to this level is not expected. The tube furnace lacked an externally controlled stage movement, hence after 1 hour at elevated temperature, a small opening is created to move the samples to a colder region to cool down and then it is sealed again in a flowing Nitrogen environment. This would introduce a considerable amount of Oxygen into the tube, which could be oxidizing the upper layers of film. The effects of heat treatment environment are further explored in section 6.3.2. After heat treatment at 300°C, 9% of Oxygen is

observed in the film, while heat treatment at 350°C accelerates this value to 23%. Comparing with SEM images it could be expected for the upper layer to be Oxygen rich. Therefore, major trend changes observed in both the sheet resistance and the TCR for Mn_3AgN film between 300 and 350ºC, could be very reasonably related to the combined effect of increased oxidation along with defect healing and crystallization of the film.

Table 4-5 Table of EDX composition of Mn_3AgN samples measured before and after heat treatment.

Mn_3AgN samples (3 sccm/0 Tsub)	**As-grown (Mn:Ag:N:O)**	**Heat treated (ºC)**	
		300 (Mn:Ag:N:O ratio)	**350 (Mn:Ag:N:O ratio)**
Composition (at %)	59:21:20:0	55:19:17:9	61:9:7:23

Mn-AgN TCR

Figure 4-16 shows the effect of various increasing annealing temperatures on the TCR of Mn-AgN films grown with increasing N_2 flow rate. Each line in the graph represents increasing heat treatment temperature. The as-grown film is seen to have the most negative TCR and with each successive increase in heat treatment temperature, the TCR shifts in the positive direction, irrespective of the N_2 flow rate. The rate of positive shift is highest for films deposited at 1 sccm. But contrary to expectations, the films deposited at 5 sccm is the next set to show a higher degree of positive shift compared to films grown at 2 or 3 sccm. This behavior forms a depression in the TCR curve attaining its lowest TCR at 3 sccm and this trend is maintained for all the steps of heat treatment. The zero TCR line lies in between the 300 and 350ºC regime of heat treatment for films grown at 2 and 3 sccm but films grown at 1 and 5 sccm attains positive value of TCR at 300ºC itself.

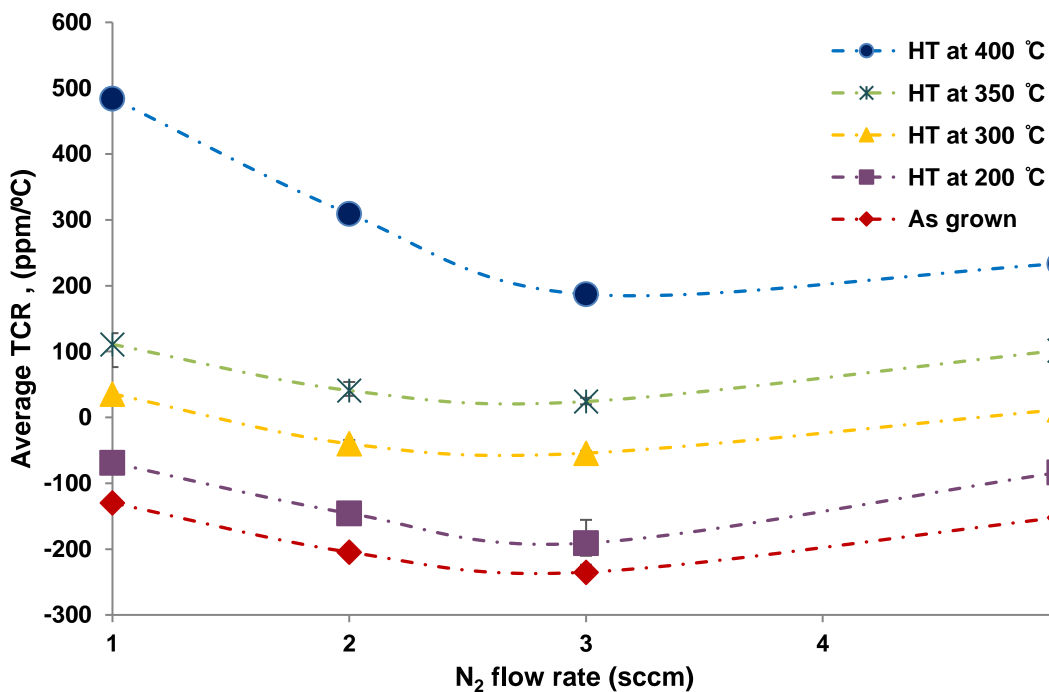

Fig 4-16 Graph of TCR values of Mn-AgN films grown (without Tsub) with increasing N_2 flow rate.

To better compare the relative TCR values between each N_2 flow rate, the same values of TCR are plotted against increasing annealing temperature for each N_2 flow rate in figure 4-17. It can be clearly seen that the films deposited at the higher N_2 flow rate of 5 sccm demonstrate a positive TCR when compared with the TCR values of lines representing 2 and 3 sccm. The 5 sccm line is only lower than the line representing 1 sccm. The 1 sccm and 5 sccm lines cross over the 0 TCR before 300ºC and the 2 sccm and 3 sccm lines crosses over the 0 TCR line in between 300 and 350ºC. From the previous sections, it is expected that the Mn_3AgN antiperovskite structures are formed at an N_2 flow rate of 3 sccm. The TCR value for Mn_3AgN films (3 sccm line) remains the least negative and after heat treatment at 300ºC attains -54 ppm/ºC and after heat treating at 350ºC a closer to zero value of 24 ppm/ºC is achieved. It could be possible to attain a closer to zero TCR by heat-treating these films at a treatment temperature between 300 and 350ºC.

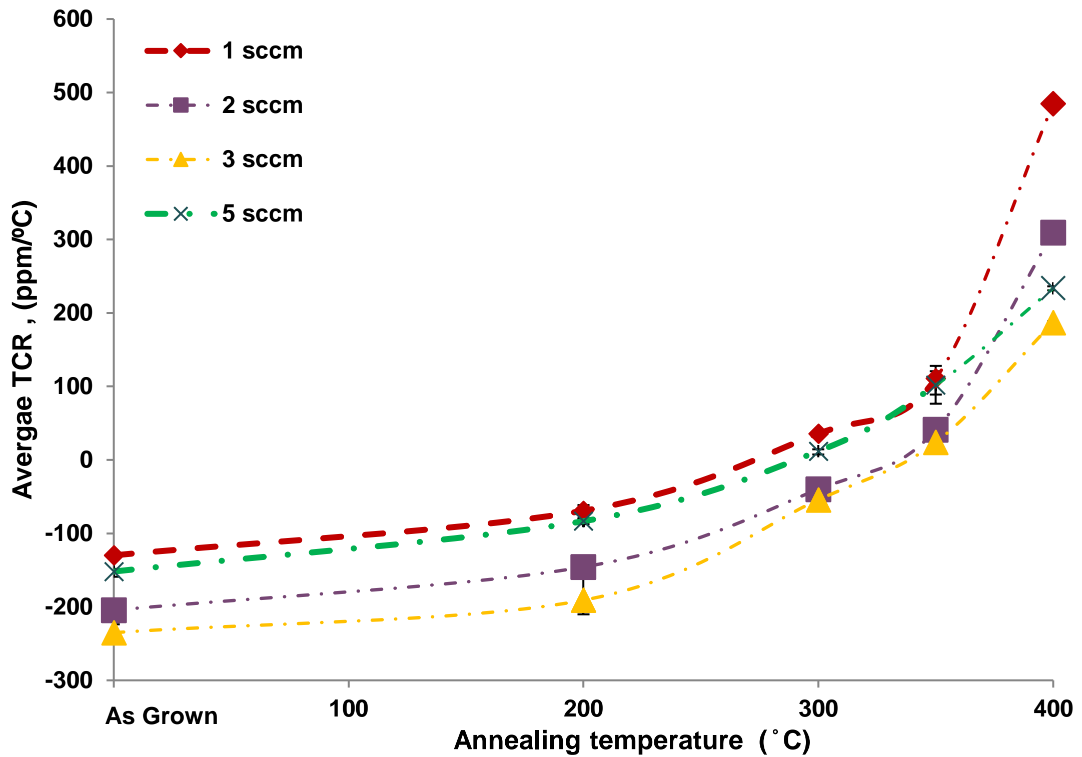

Fig 4-17 Graph of TCR values of Mn-AgN films grown (without Tsub) with increasing annealing temperature.

In the section 4.3.2, for as-grown films, it was seen that the substrate temperature shifts the TCR values of the as-grown Mn-AgN films in the positive direction (irrespective of N_2 flow rate). In figure 4-18, the TCR values of Mn_3AgN films deposited at varying substrate temperature are plotted against increasing heat treatment temperature. It can be observed that up to 350ºC, the lines depicting successive increments in substrate temperature remain shifted higher in the positive direction, and thereafter the TCR value becomes independent of the effect of substrate temperature. It is reasonable to conclude that the increment in TCR value registered at the time of deposition, because of substrate temperature is carried forward for lower regimes of heat treatment temperature. However, the effect of substrate temperature is not strong enough to produce any visible difference in TCR values of films grown at different Tsub values when heat-treated at temperatures above 350ºC.

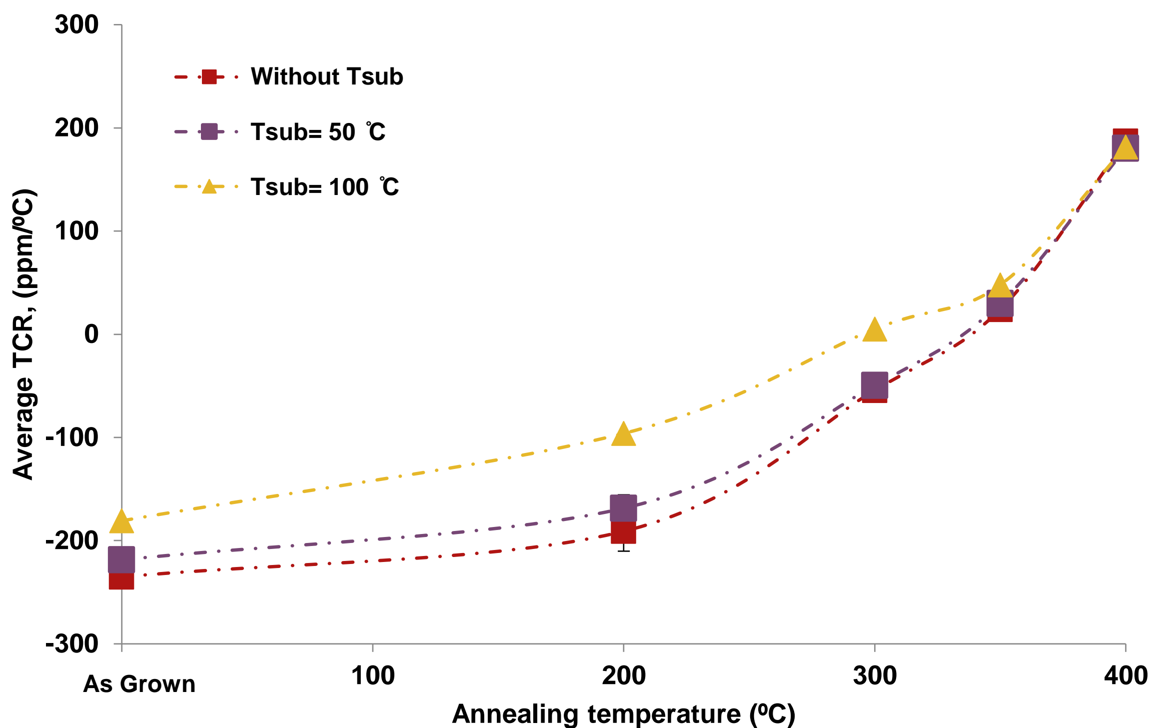

Fig 4-18 Graph of TCR values of Mn_3AgN antiperovskite films (3sccm N_2 flow) with increasing annealing temperature.

Mn-CuN Sheet Resistance

Mn-CuN films also show trends similar to those observed after annealing heat treatment of Mn-AgN films. Figure 4-19 shows the effect of increasing annealing temperatures on the sheet resistance of Mn-CuN films grown with increasing N_2 flow rate. It can be seen that for each successive increase in N_2 flow rate, the sheet resistance value is higher than the previous N_2 flow rate and this is maintained at every point of annealing heat treatment. Similar to Mn-AgN films, for heat treatment temperatures up to 300ºC, Mn-CuN films show a decrease in the sheet resistance value and are consistent for all three N_2 flow rates. Moreover, for heat treatment at 350ºC and 400ºC, a sharp rise in sheet resistance is observed for all Mn-CuN films. Films deposited at 1 sccm had the lowest mean value for as-grown sheet resistance at 13.62 Ω/□ and after heat treatment at 300ºC decreased to the lowest value at 10.38 Ω/□ before rising again to 20.92 Ω/□ when heat treated at 400ºC. For films deposited at 2-sccm flow rate, the sheet resistance decreased to 10.38 Ω/□ from their as-grown value of 13.62 Ω/□. For films deposited at 3-sccm this

decrease was from 19.21 Ω/□ to 16.82 Ω/□ and for films deposited at 5 sccm, the value dropped from 23.31 Ω/□ to 18.27 Ω/□. Maximum sheet resistance value for 3, 5 and 6-sccm N_2 flow rate appears to level off around 26.57, 28.82, and 29.09 Ω/□ respectively after heat treatment temperatures above 350°C. However, this levelling off cannot be confirmed without further heat treatment at higher temperatures going beyond 500˚C.

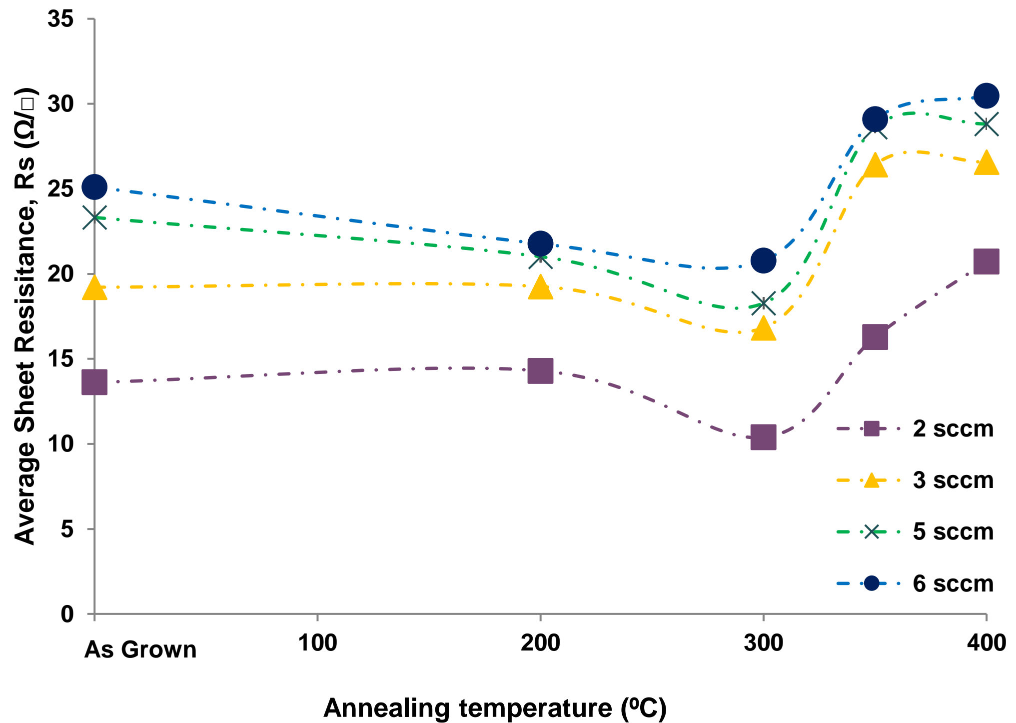

Fig 4-19 Graph of Rs values of Mn-CuN film with annealing temperature.

In order to study the effect of substrate temperature, samples deposited at 5 sccm of N_2 flow rate are selected, because it is at this flow rate that Mn_3CuN antiperovskite structures are realized. Figure 4-20 compares the effect of annealing temperature on the Mn_3CuN films grown at varying initial substrate temperature. The general trend of initial decrease in sheet resistance for lower annealing temperatures followed by a steep rise in sheet resistance for higher annealing temperatures is observed for all the films irrespective of substrate temperatures. However, it is expected that the onset of this steep rise is effected to some degree by the initial substrate temperature. The films deposited without substrate temperature show the rising Rs values for heat treatment temperatures above

300ºC. Whereas for films deposited at Tsub of 50ºC and 100ºC, the Rs value starts reversing the direction of change from 200ºC. However, other than the early onset of resistance reversal, there is no major difference observed as result of introducing substrate temperature.

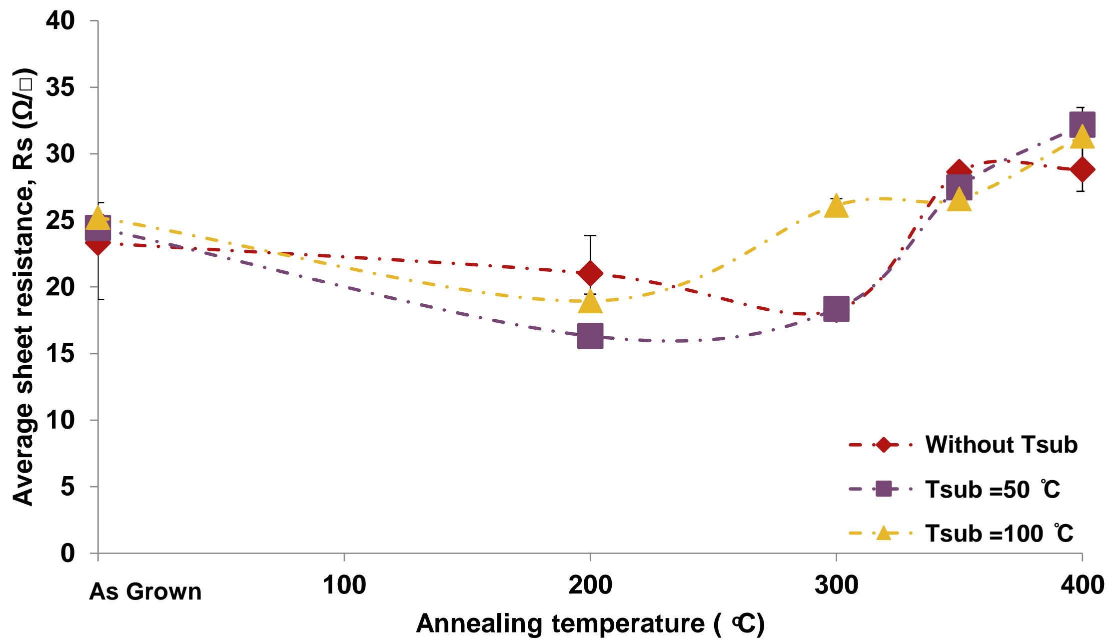

Fig 4-20 Graph of sheet resistance values of Mn_3CuN film (5 sccm N_2 flow) with increasing annealing temperature.

<u>Structural and topographical changes after annealing treatment:</u>

Mn-CuN samples heat-treated at 300 and 350ºC were chosen to study the crystal structure and then compared with respect to the as-grown films to measure the changes happening in XRD spectrums as a result of annealing heat treatment. Figure 4-21 shows the XRD spectrums achieved from Mn-CuN films deposited at different N_2 flow rates stacked together to compare the varying crystalline nature when heat treated.

For samples deposited at the lowest N_2 flow rate of 2 sccm a very sharp peak occurs at 42.44˚. With each successive heat treatment, this peak is observed to get more and more crystallized with a shift towards higher angles. A central peak

of 42.2 exist for the (131) phase of $Mn_2N_{0.86}$, which indicates a Manganese structure developed in a Nitrogen deficient condition [ICSD database]. This peak is not visible for samples deposited at a higher N_2 flow rate of 3 sccm, although a considerable swell is observed around 41.88˚ for films heat treated at 300ºC, but this does not repeat itself when heat treated at a higher temperature of 350ºC. No antiperovskite peaks are observed for as-grown films for either of the flow rates, though a small bump starts to appear around 46.42˚ when the sample deposited at 3 sccm is heat treated at 350ºC.

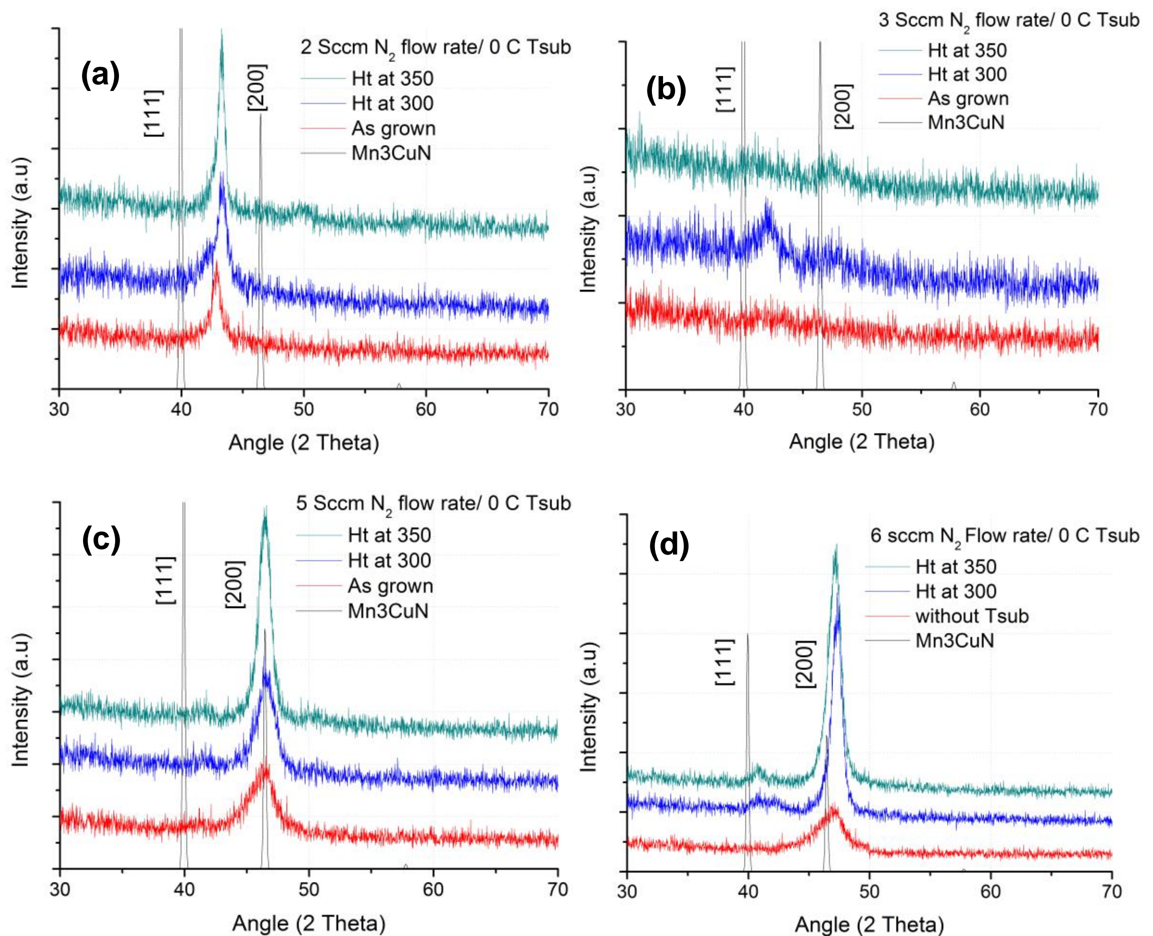

Fig 4-21 XRD spectrums of Mn-CuN films grown at (a)2 , (b) 3, (c) 5, and (d) 6 sccm N_2 flow rate after heat treatment.

For samples deposited at 5 sccm there is a very clear peak formed at 46.5˚ representing a (200) preferential orientation. Upon increasing the heat treatment to 300 and 350ºC the peak at (200) continues to become sharper indicating growth of single phase antiperovskite Mn_3CuN thin films. Absence of any other peaks or

shifts in the existing peak indicates that the Mn_3CuN antiperovskite structure formed with (200) phase remains stable throughout the heat treatment regime. Absence of other peaks along with increasing crystallization of a single-phase structure also supports that, with increasing heat treatment, inter-planar defects and irregularities are healed which leads to a reduction in the sheet resistance as seen before. This absence of defects also supports shifts of TCR in the positive direction as defects and irregularities in the film are factors contributing towards negative TCR. For the as grown samples at 6 sccm of N_2 flow rate, peaks were observed to shift towards higher angles. It is reasonable because the increment of N_2 species in the film, which has smaller atomic radius compared to Cu atoms, the films experience contraction, which is observed as a shift in the higher angle. In figure 4-21 (d) it can be seen that this shift increases with increasing heat treatment temperature.

To further explore the role of substrate temperature on the physical structure of the films, XRD spectrums are taken from Mn_3CuN films (deposited at 5 sccm) deposited at increasing Tsub before and after annealing heat treatment, see figure 4-22 (a)-(c). No other peaks except that for (200) were found, even when Mn_3CuN films are deposited at higher substrate temperature. One thing which is very clear and which was also explained previously along with the as-grown films, is that with increasing substrate temperature, the as-grown Mn_3CuN film increases in crystallization, indicated by the peak for (200) phase getting sharper. This first stage of crystallization as a result of substrate temperature affects the further rapid crystallization when an annealing heat treatment is introduced later. This can be seen in figure 4-22 below as well as in the mean grain size calculated for each case as presented in the table 4-6 below. The average grain size for films deposited without substrate temperature increases from 9 nm to 26 nm whereas films deposited at 100ºC Tsub shows an increment from 12 nm to 29 nm. It can be seen that antiperovskite structure formation is determined by the partial pressure of reactive N_2 in the chamber, which is related to N_2 flow rate. The substrate temperature helps in early crystallization of the film, which can also be achieved by annealing later. This is correlated to the observation that increased crystallization as a result of substrate temperature shifts the TCR of Mn_3CuN early in a positive

direction, which can also be achieved by a dedicated annealing stage later in the process.

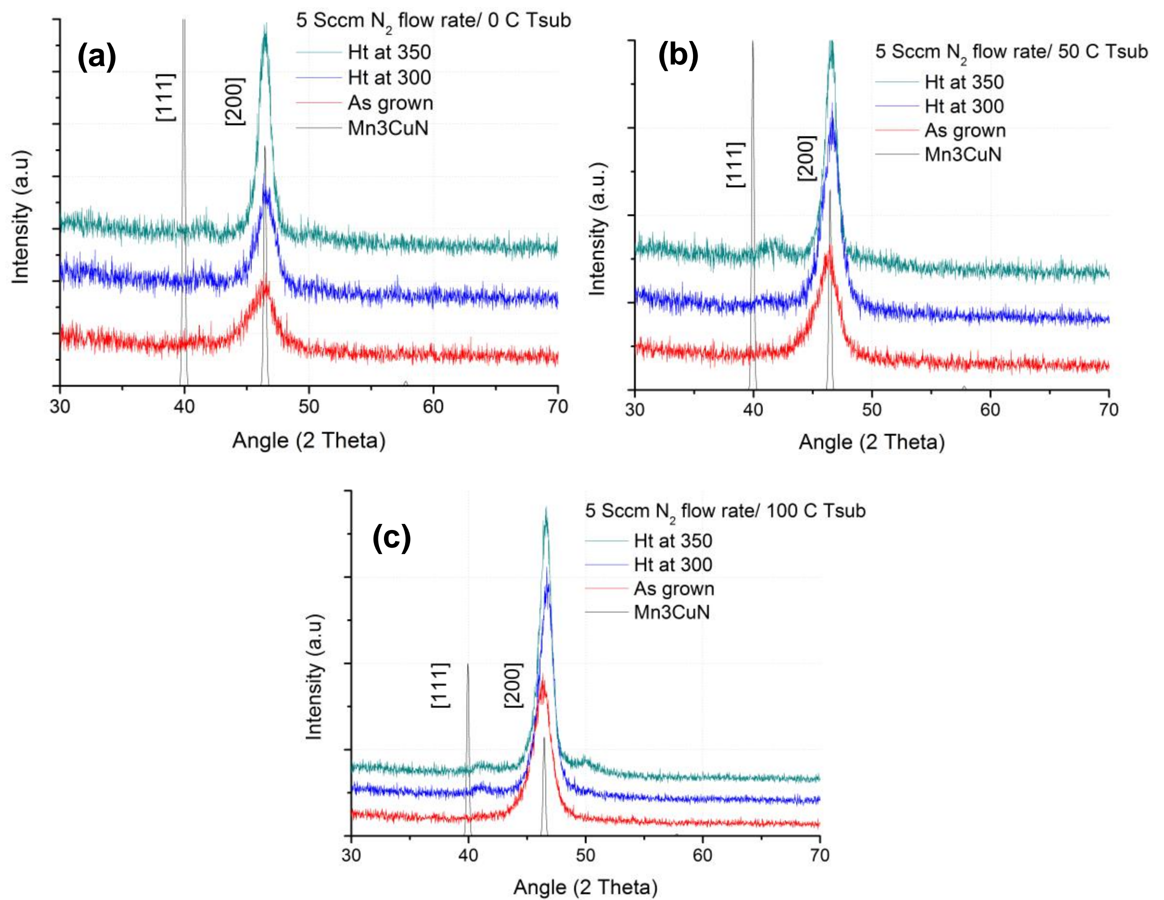

Fig 4-22 XRD spectrums of Mn_3CuN films grown (a) without Tsub, (b) 50 and (c) 100°C after heat treatment.

Table 4-6 Table of FWHM and calculated crystallite grain size before and after heat treatment, for Mn_3CuN samples deposited at increasing Tsub.

Material	Tsub (°C)	Annealing temperature (°C)	FWHM (°)	Mean Grain Size (nm)
Mn_3CuN	Without Tsub	As-Grown	2.62	9.88
		300	2.12	13.03
		350	1.16	26.46
	50	As-Grown	2.42	11.04
		300	1.72	18.54
		350	1.22	26.14
	100	As-Grown	2	12.95
		300	1.24	29.12
		350	1.12	29.62

Analyzing the side profile of a Mn_3CuN film showed the presence of secondary layer on top of the thin film similar to that observed on Mn_3AgN films. In the case of Mn_3CuN films, the thickness only registered a minor increase of 25 nm going from 496 nm for the as grown film to 521 nm after heat treatment at 350ºC as seen in figure 4-23(a). The thickness of the top layer formed is also less at 86 nm compared to the Mn_3AgN film at 196 nm. In comparison to Mn_3AgN, the layer on top of Mn_3CunN looks denser and well adhered to antiperovskite film at the bottom layer. The top layer could be assumed to be an oxide layer formed by the residue Oxygen within the annealing tube at high temperature but will have to confirmed by SIMS or low voltage EDX in further chapters. The top profile analysis of the film shows a definite increment in the grain size when compared to the as grown Mn_3CuN films validating the structural analysis from the XRD results.

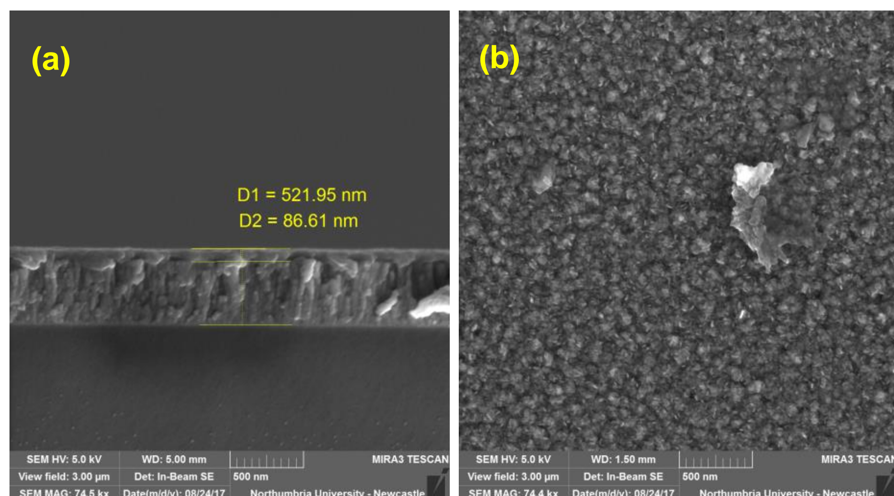

Fig 4-23 (a) Cross section (b) Top profile of Mn_3CuN films grown at 5 sccm N_2 flow rate and without Tsub, after heat treating at 350ºC.

EDX analysis performed on the heat-treated sample revealed increased Oxygen content in the film, presented in table 4-7. As explained with heat treatment of Mn_3AgN before, the source of Oxygen could be identified as the opening created within the tube to allow movement of samples to a colder region. However, unlike Mn_3AgN films, Mn_3CuN films registered much lower content of Oxygen in the film after heat treatment. After 300ºC only 5% of Oxygen is detected in the film which increases to 16% after heat treatment at 350ºC. This data correlates with the SEM

images where the upper protective oxide layer formed is much thinner when compared to upper layer seen in Mn_3AgN films.

Table 4-7 Table showing EDX composition of Mn_3CuN samples before and after heat-treating.

Mn_3CuN samples (5 sccm/No Tsub)	**As-grown (Mn:Cu:N:O)**	**Heat treated (ºC)**	
		300 (Mn:Cu:N:O)	**350 (Mn:Cu:N:O)**
Composition	60:21:19:0	58:20:17:5	50:19:15:16

Therefore, the correlation between upper layer thickness and Oxygen content detected in film, lends credibility that the concentration of Oxygen is mainly in the upper layer and not throughout the film depth. Moreover, if found to be true it could be acting as a protective layer for the underlying antiperovskite structure. EDX analysis of the cross section is performed for films tested under different heat treatment conditions in section 5.3.3 to further prove this point.

Mn-CuN TCR

Figure 4-24 plots the shift in the TCR values for Mn-CuN films grown at varying N_2 flow rate as they are heat treated at 4 different temperatures after deposition. One point very clear from the figure is that with each successive increment in heat treatment temperature, the TCR values shift in a positive direction. This is as expected and similar to the previously seen results after heat treatment of Mn-AgN films. The zero TCR line for the most part, again lies in between the 300 and 350ºC heat treatment limits. But in comparison to the Mn-AgN films, where some results were already positive at 300ºC if not close to zero in the negative TCR region, for Mn-CuN films the heat treatment temperature of 350ºC is not sufficient to shift the entire line of films deposited at 5 sccm to the positive TCR region. This means that Mn-CuN can withstand higher temperature before shifting NTCR to PTCR values. Mn-CuN films continuously become negative in TCR with N_2 flow rate and this trend remains throughout the heat treatment regime, though the difference between the TCR values for 3, 5 and 6 sccm films are significantly less. From previous results,

the films grown at 5 sccm of flow rate are known to form the Mn_3CuN antiperovskite structure and these samples are still negative after heat treatment at 350ºC.

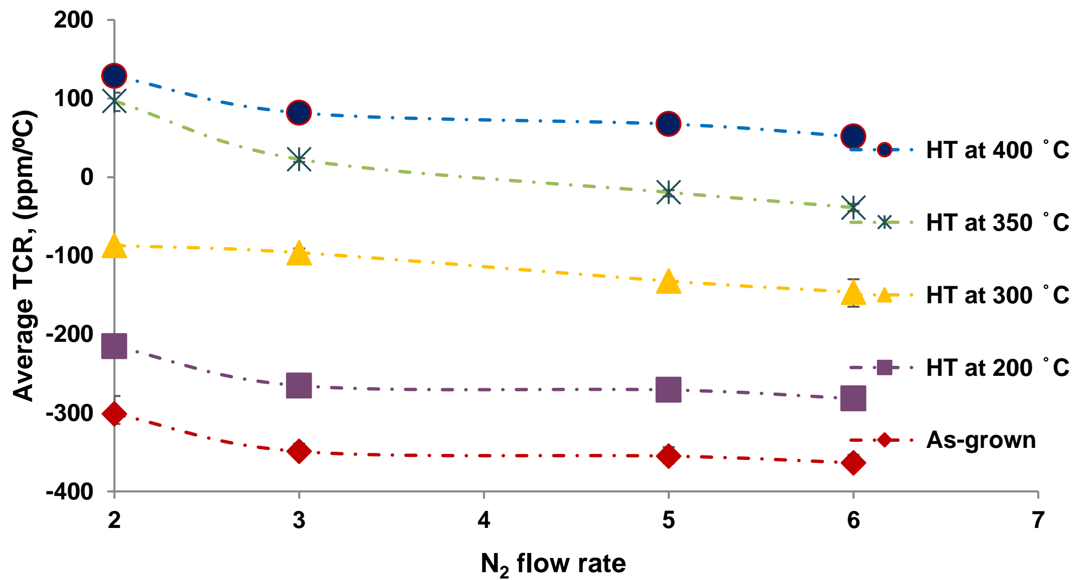

Fig 4-24 Graph TCR values of Mn-CuN films (without Tsub) with N_2 flow rate.

Mn_3CuN films exhibit the lowest TCR value of -19 ppm/ºC for the sample set after heat treatment at 350ºC. Figure 4-25 presents the data set for individual N_2 flow rates when heat-treated. As expected, the TCR continues to grow negative with each increment in N_2 flow rate and this relationship is maintained throughout the entire heat treatment regime. The lowest value of TCR is observed for Mn_3CuN films. While the effect of N_2 flow rates on TCR of Mn-CuN films is very clear to observe, the same cannot be said about the effect of substrate temperature. Figure 4-26 shows the effect of substrate temperature on the TCR values of Mn_3CuN films (5-sccm flow rate). The lines for films deposited without Tsub barely separates from the TCR lines of films grown at 50 and 100ºC of substrate temperature. After heat treatment at 350ºC, films grown without Tsub register a negative TCR of -19 ppm/ºC, whereas films grown at 50 and 100ºC are shifted into the positive TCR region and register values of +20 ppm /ºC and +42 ppm/ºC respectively. Similar to earlier films of Mn_3AgN, it can be seen that the effect of substrate temperature on the TCR of Mn_3CuN films is to provide an initial shift to the TCR in the positive direction but is not sufficient enough to push the TCR value closer to the zero TCR

line. Additional heat treatment will need to be provided to fine tune TCR values closer to zero.

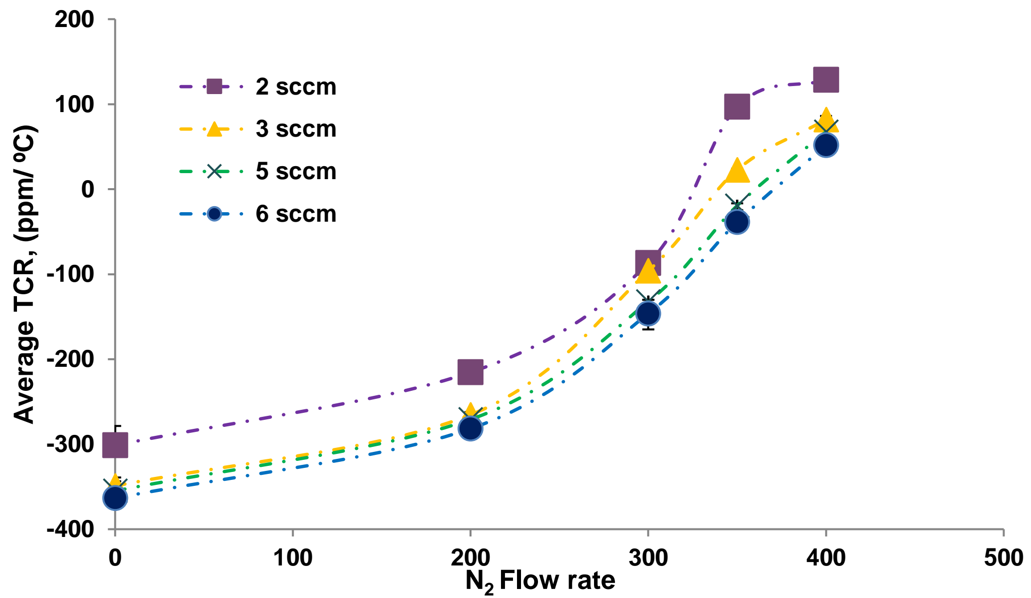

Fig 4-25 Graph of TCR values of Mn-CuN films grown (without Tsub) with annealing temperature.

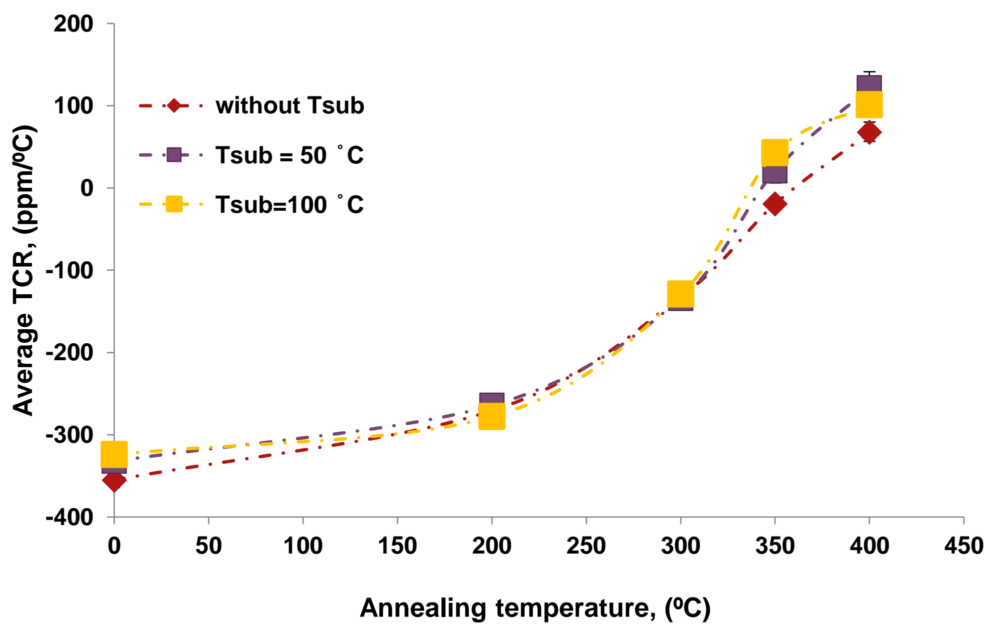

Fig 4-26 Graph of TCR values of Mn_3CuN films (5 sccm N_2 flow) with annealing temperature.

4.3.4 Effect of annealing time on properties of film

From previous results, N_2 flow rate, substrate temperature and annealing temperature are narrowed down to achieve the lowest TCR possible. In experiments so far heat treatment is performed for 1 hour. To determine the effect of annealing treatment time on properties of Mn_3AgN and Mn_3CuN films, samples are heat treated at 350ºC for 1, 2, 3, 4 and 5 hours in the same tube furnace with flowing Nitrogen environment.

From figure 4-27 (a) and (b) it can be seen that increasing the time duration doesn't change the sheet resistance of film more than 1 Ω/□ for both Mn_3AgN and Mn_3CuN films. They appear to reach a stable sheet resistance after 3 hours of heat treatment. Increasing the time duration of heat treatment is seen to shift the TCR values in the positive direction for both Mn_3AgN and Mn_3CuN films. For Mn_3AgN the value shifts from +28 ppm/ºC and begins to settle around +47 ppm/ºC after 3 hours of heat treatment. For Mn_3CuN films also the TCR value settles around 20 ppm/ºC after 3 hours at 350ºC.

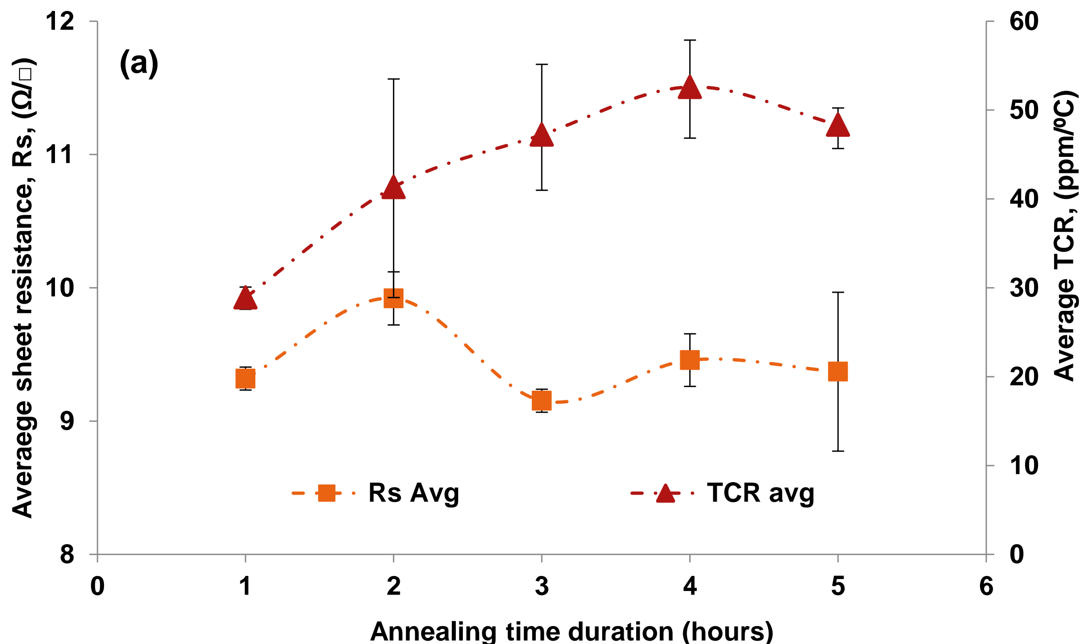

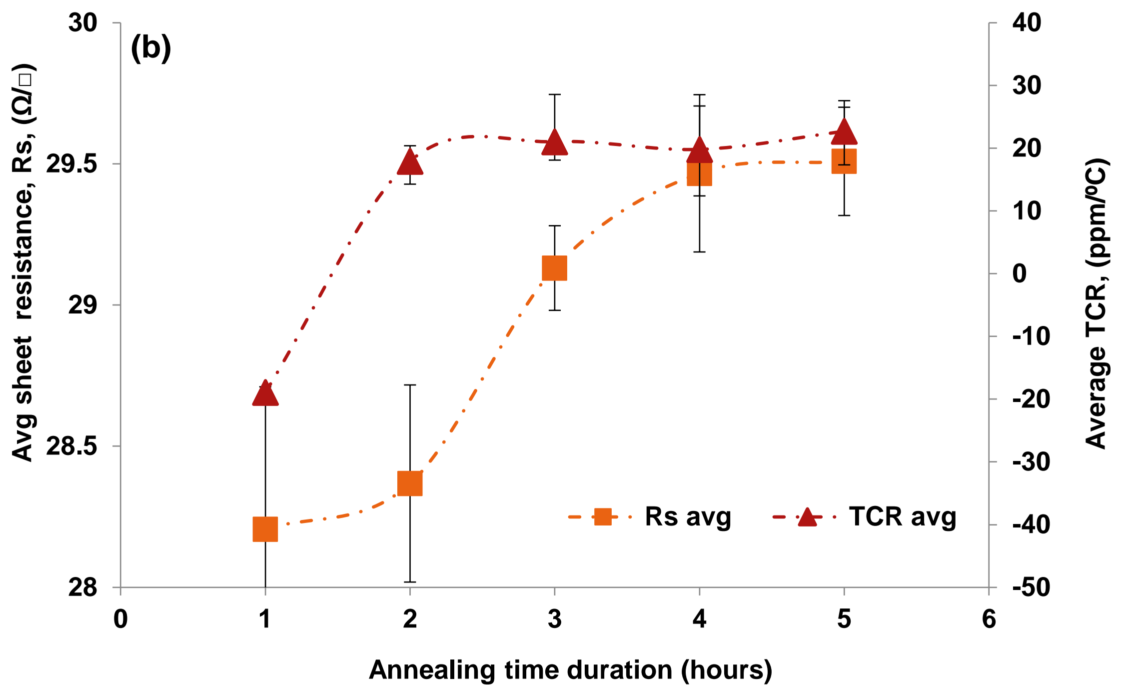

Fig 4-27 Graph of R_s and TCR values of (a) Mn_3AgN films (without Tsub) (b) Mn_3CuN films (without Tsub) with annealing duration.

4.3.5 Electrical resistance stability of antiperovskite films

The stability of the resistance value was measured by subjecting the samples to open air at elevated temperature of 155ºC for 1 week (168 hours). This is based on Mil-PRF 55342 standard for military grade resistor products and mimics the worst-case scenario that an encapsulated resistor product can face in a printed circuit and measures the resistance change during this time[146].

Mn_3AgN and Mn_3CuN samples deposited at three varying substrate temperature levels are subjected to dry heat stability test to check if the elevated substrate temperatures have any effect on improving the stability figures for these films. In the previous sections, no commercially favourable improvements are observed in TCR or sheet resistance values as a result of increased substrate temperature. A favourable effect of substrate temperature on electrical stability can justify the use of elevated substrate temperature for the experiments in the further chapters. As grown samples were heat treated at 350ºC for 3 hours in flowing Nitrogen

environment and then after cooling kept at 155ºC for 1 week in open air environment with 4-wire resistance measurement made every 24 hours. Figure 4-28 (a) and (b) shows the percentage change in resistance value in every 24 hours for Mn_3AgN and Mn_3CuN samples deposited at varying substrate temperatures.

The data shows that antiperovskite film structures are not stable after the first annealing treatment. In the Mn_3AgN set of films shown in figure 4-28 (a), the best stability figure achieved was for the films grown without substrate temperature, and it was not better than 15% after 1 week at 155ºC. With increasing substrate temperature, the stability figure worsened to 21% for the films grown at 100ºC Tsub after 1 week. Comparatively, the Mn_3CuN set of films showed better stability values in figure 4-28 (b), but that was also no better than 11% for the best case for films grown without Tsub. For films grown at elevated substrate temperature of 100ºC the resistance values of films changes more than 15% after 1 week. As compared to Cu, Ag was seen to be more susceptible to oxidation when subjected to elevated temperature therefore the relatively higher degree of instability in Mn_3AgN films when subjected to 155ºC for 168 hours is expected. Further, for Mn_3AgN films the graphs are observed to have extremely large error bars faring the worst value of 8% on each side of average value for films grown at Tsub of 100ºC. While for Mn_3CuN this the error bars never gets wider than 1.3% on either side of average value for any of the Tsub condition. However, these values are excessively high to be considered for a commercial application in thin film resistor fabrication. Typical industrial standards require thin film resistors to show figures better than 0.5% [147] for the dry heat stability test and high stability products like WIN series resistors have stability values better than 0.03% after 100 hours at 150ºC [96].

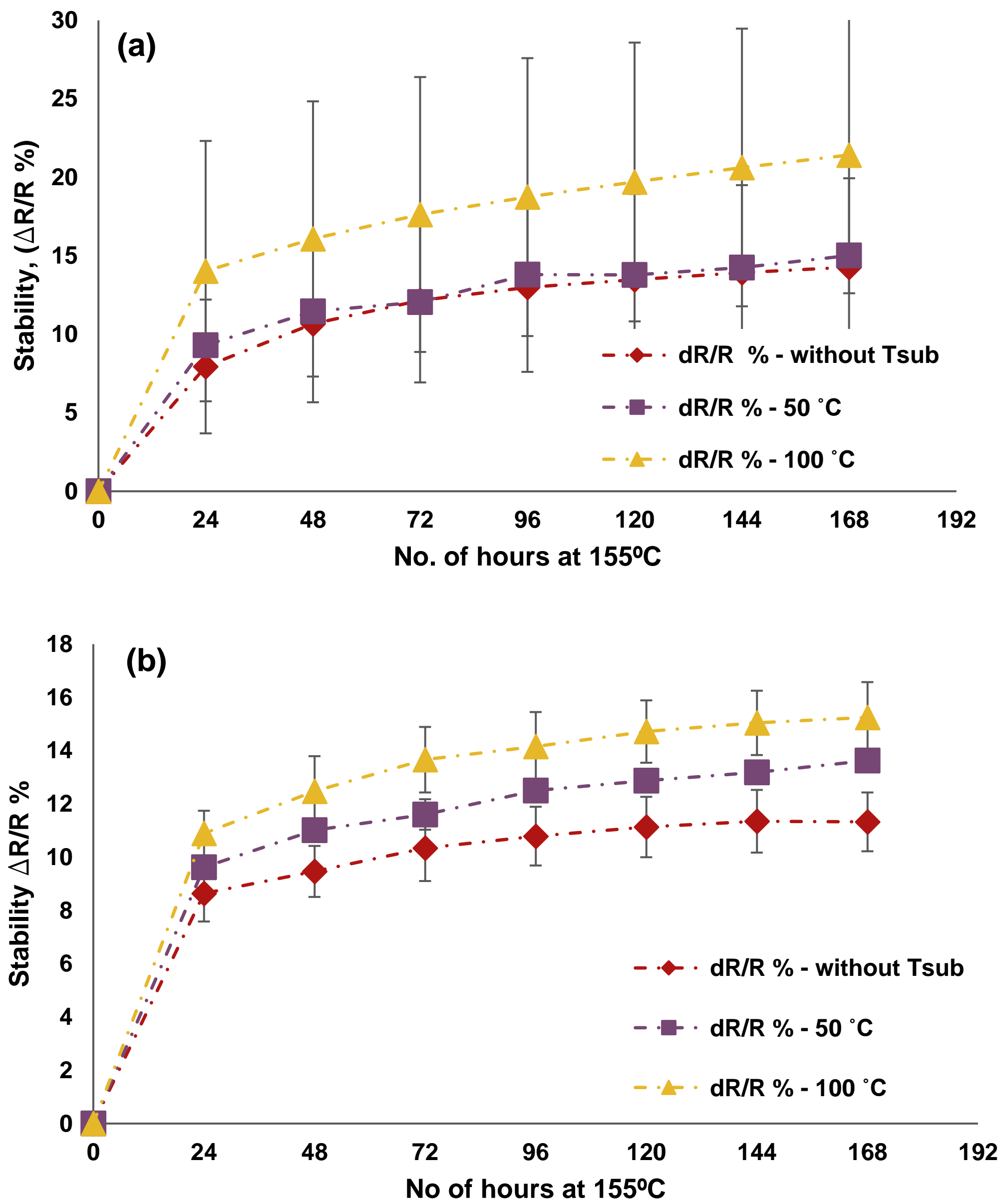

Fig 4-28 Graph of electrical resistance stability in ΔR/R% after heat treatment at 350ºC for (a) Mn_3AgN films (b) Mn_3CuN films

Having said that, in figure 4-29, the curves having the best stability figures from both set of materials can be seen together and a sharp bend can be observed at 24-hour mark, for both sets of films. This suggest that the films have a tendency to settle down to a stable resistance value as the dry heat test progresses. In addition, the key difference in the industry measurements for stability and measurements performed in the university, is that the industry standards are derived by testing resistor films after they are subjected to a second stage of stabilization treatment

and resin encapsulation. Therefore, a stabilization stage of heat treatment could be further explored to investigate the possibility of improving stability values by performing a secondary stage of stabilization heat treatment and if found suitable could be further tested with an encapsulation process in industry.

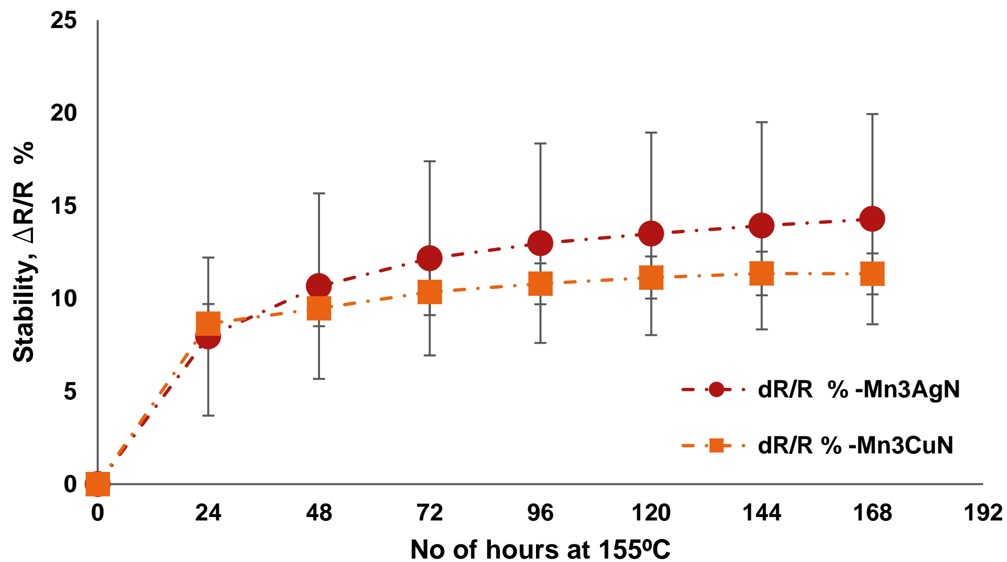

Fig 4-29 Graph of electrical resistance stability of Mn_3AgN and Mn_3CuN films after heat treatment at 350ºC.

4.4 Summary

The results presented in this chapter support the findings of the literature review that the Mn based antiperovskites: Mn_3AgN and Mn_3CuN, have very low TCR values and could be taken further for studies to be developed into a potential material system for thin film resistor fabrication.

The films deposited at varying N_2 flow rate showed that the amount of Nitrogen present in the chamber plays a major role in deciding the electrical, structural, chemical and morphological characteristics of the films. 3 sccm of N_2 flow rate (10% partial Nitrogen pressure) is required to realise Mn_3AgN antiperovskite structure which bears structural, chemical and morphological resemblance to the previously published works, whereas for Mn-CuN films, 5 sccm of N_2 flow rate or 16.66% of partial Nitrogen pressure is required to grow Mn_3CuN antiperovskite structures similar to those published in the previous work. Substrate temperature is seen to

play a role in in-situ crystallization of the as-grown samples, which in turn affects the as grown electrical properties. Although, this is not something exclusive to substrate temperature and could be realised later with a separate annealing treatment to a greater extent.

The as-grown TCR value is seen to be negative: between -180 and -235 ppm/ºC for Mn_3AgN and -324 and -355 ppm/ºC for Mn_3CuN films. This as-grown negative TCR showed a shift in the positive direction with increasing heat treatment in flowing Nitrogen environment. For 1-hour heat treatment, both sets of films crossed the zero TCR line between 300ºC and 350ºC. 3 hours of heat treatment at 350ºC was found to be sufficient to stabilize the TCR value of Mn_3AgN to +47 ppm/ºC and that of Mn_3CuN to +21 ppm/ºC. Table 4-8 provides a summary of the best results achieved for the Mn based system and shows that for similar process conditions, Mn_3AgN has more positive TCR values than Mn_3CuN structure. Therefore, it is possible for a ternary antiperovskite structure formed by partial substitution of Cu into the Mn_3AgN system to achieve TCR values closer to zero by heat-treating at a temperature lower than 350ºC. The dry heat stability test showed stability figures no better than 11% for either set of films, which is not acceptable for industry standards by a far margin. The rapid attack from Oxygen in the environment might be leading to the degradation of resistance values in these films. It is expected that by introducing a secondary stage of heat treatment in an optimum environment, a good improvement in stability can be achieved.

Table 4-8 Table with summary of electrical properties achieved on Mn_3AgN and Mn_3CuN films heat treated at 350ºC for 3 hours.

Material	**Process setting**				**Sheet resistance, R_S (Ω/□)**	**TCR (ppm/ºC)**	**Stability figure (ΔR/R%)**
	Tsub (ºC)	**N_2 flow rate (sccm)**	**Heat Treatment Temperature (ºC)**	**Heat treatment Time (hours)**			
Mn_3AgN	Without	3	350	3	9.15	47.2	14
Mn_3CuN	Without	5	350	3	29.13	21.0	11

CHAPTER 5 Partial substitution of Cu in Mn_3AgN

5.1 Introduction

The low TCR values of binary depositions of Mn_3AgN and Mn_3CuN antiperovskite structures achieved in chapter 4 are in agreement with the literature review conducted in chapter 2. After heat treating at 350ºC, low TCR values of +47 and +21 ppm/ºC are seen for Mn_3AgN and Mn_3CuN samples respectively. With increasing stages of heat treatment, the TCR value crosses over the 0 ppm/ºC line somewhere in between 300 and 350ºC. It should therefore be possible to achieve a closer to zero value of TCR by investigating this region of heat treatment. Another interesting trend observed in the TCR curves is that Mn_3AgN samples are consistently more positive than Mn_3CuN samples for the same level of heat treatment. It should also be possible to explore an option to partially substitute Cu in Mn_3AgN to form a ternary structure with an intermediate TCR value.

Intermixing thin film material systems with positive and negative TCR values is one of the researched techniques to achieve close to zero TCR values by compensating TCR values of each other [148]. This technique has been successfully researched on all of the TFR industry favorites like TaN [4, 44, 149], NiCr [14], and Ru based materials [43]. J.C.Lin et al (2011) explored the doping of the existing antiperovskites having low TCR with a ternary element as an effective way to further reduce their TCR value closer to zero [150]. They were able to reduce the TCR value of Mn_3CuN antiperovskite from 25 ppm/ºC to 1.29 ppm/ºC by partially substituting Carbon (C) at N positions to form $Mn_3CuN_{(X)}C_{(1-X)}$. Similarly, work done by Y. Sun et al (2014) noticed that partial doping of Mn_3AgN with Sn and Zn effectively reduced the TCR value from 102 ppm/ºC to 31 and 36 ppm/ºC respectively [81]. Another work done by N.P. Lu et al (2015) achieved a low TCR value of 20 ppm/ºC by doping Ag into Mn_4N to create $Mn_3Ag_{(0.81)}Mn_{(0.19)}N$ [90]. But it is the detailed work published by K. Takenaka and group [79, 87, 88, 99, 100] on the extremely low TCR values observed by partial substitution of Cu into Mn_3AgN which is the main encouragement for further research with these material systems. Depending upon the dopant concentration of Cu in $Mn_3Ag_{(1-X)}Cu_{(X)}N$, Takenaka

and group were able to observe low TCR values between 0.42 ppm/^{0}C [87] to 9.77 ppm/^{0}C [99].

Based upon the literature review in chapter 2 and the results from chapter 4, the following flowchart is drawn for the incremental doping of Cu by increasing the value of X from X=0 to X=1 in steps of 0.2 in $Mn_3Ag_{(1-X)}Cu_{(X)}N$ as shown in figure 5-1 below.

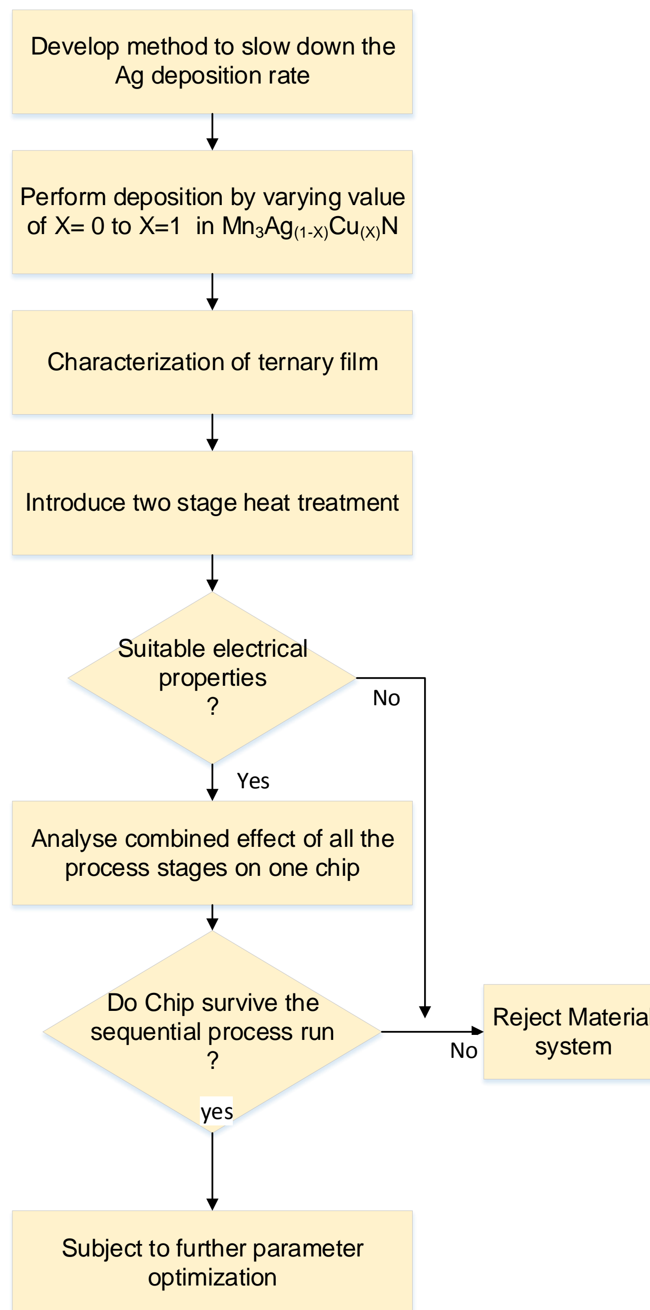

Fig 5-1 Process flow for deposition and heat treatment optimization of $Mn_3Ag_{(1-X)}Cu_{(X)}N$ ternary samples

5.2 Experimental

Two main objectives are realized by the experiments carried out in this chapter: doping of Mn_3AgN with Cu to explore the possibility of further reduction of TCR values, and to study the combined effect of the heat treatment stage on the thin films.

5.2.1 As grown ternary films of $Mn_3Ag_{(1-X)}Cu_{(X)}N$:

In order to realize the ternary antiperovskite structure $Mn_3Ag_{(1-X)}Cu_{(X)}N$, it is considered to increase the Cu dopant concentration by 0.2 atomic % in the Mn_3AgN structure, thereby realizing 6 different compositions, ranging from pure Mn_3AgN to pure Mn_3CuN, as shown in table 5-1.

Table 5-1 Table of Cu doping increment planned in the $Mn_3Ag_{(1-X)}Cu_{(X)}N$.

Sample No.	Value of X in $Mn_3Ag_{(1-X)}Cu_{(X)}N$	Ternary composition
1	0	Mn_3AgN
2	0.2	$Mn_3Ag_{0.8}Cu_{0.2}N$
3	0.4	$Mn_3Ag_{0.6}Cu_{0.4}N$
4	0.6	$Mn_3Ag_{0.4}Cu_{0.6}N$
5	0.8	$Mn_3Ag_{0.2}Cu_{0.8}N$
6	1.0	Mn_3CuN

The Copper target employed for this project was able to maintain plasma at very low power and therefore able to contribute a small dopant concentration of Cu (as in sample no 2 and 3), in the film. However, the main problem with this plan is to achieve the smaller concentration level of Ag as required in sample No 4 and 5. The Ag target is running at its lowest possible power of 23 W in order to realize sample no 1, with a 3:1 ratio between Mn and Ag, because of its higher sputtering

rate compared to Mn. Any further reduction in DC power to sputter a smaller concentration of Ag in the film will lead to plasma failure on Ag target.

To reduce the silver concentration in the film a new shutter was designed, as shown in figure 5-2. By varying the shutter along three positions, it was possible to partially shadow the plasma plume from magnetron 4 on which the Ag target was loaded. This allowed more control over the portion of Ag plume exposed on the rotating carousel and therefore controlling the amount of Ag in the film.

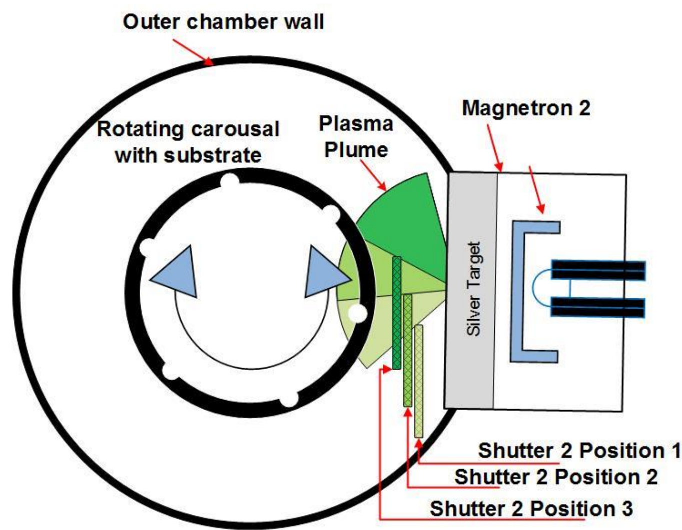

Fig 5-2 Top view of chamber showing shutter arrangement designed for magnetron 4 to lower Ag deposition rate.

By adjusting power levels of Ag in accordance with power levels of Cu and shutter position it was possible to realize the 6 required compositions of ternary $Mn_3Ag_{(1-X)}Cu_{(X)}N$. In the previous chapter, it was seen that N_2 flow rate is critical for the formation of antiperovskite structures. With increasing power on the Cu target, N_2 flow rate was also increased to cater for the increased amount of Cu in the film. The N_2 flow rate was increased at 1 sccm for every 0.4 ratio increment in Cu concentration. From the previous chapter it was also seen that the substrate temperature brings no additional benefit that cannot be achieved by a heat treatment stage later on, hence no substrate heating was introduced for depositions of ternary antiperovskite films. The final deposition matrix explaining

the power level on the Ag, Cu and Mn targets along with N_2 flow rate and substrate temperature is as shown in table 5-2.

Table 5-2 Table of deposition parameters for ternary antiperovskite films.

Sample No.	X (at. ratio)	Required composition ratio	Power on Target (W)			Shutter position	N_2 flow rate (Sccm)
			Mn	Ag	Cu		
1	0	Mn_3AgN	300	23	0	Open	3
2	0.2	$Mn_3Ag_{0.8}Cu_{0.2}N$	300	31	6	Pos 1	3
3	0.4	$Mn_3Ag_{0.6}Cu_{0.4}N$	300	37	11	Pos 2	4
4	0.6	$Mn_3Ag_{0.4}Cu_{0.6}N$	300	23	19	Pos 2	4
5	0.8	$Mn_3Ag_{0.2}Cu_{0.8}N$	300	23	20	Pos 3	5
6	1.0	Mn_3CuN	300	0	28	closed	5

5.2.2 Two stage heat treatment of ternary films:

In a typical TFR fabrication line, the deposited thin films are subjected to two stages of heat treatment: the first stage is carried out at a higher temperature within a closed oven in vacuum with inert gas or dopant gas species like N_2, to tune the TCR value close to zero. This is followed by a second stage of stabilization heat treatment in open air. The temperature for stabilization heat treatment is set lower than at the first stage but higher than any temperature encountered in all the further fabrication process stages. This way the stabilization heat treatment stage ensures that no resistance drift will take place in further fabrication process stages, by curing the resistor circuits at higher temperature compared to all the further process stages. In chapter 4, the secondary stage of stabilization heat treatment was not applied to samples. This could be considered as a primary reason for the unstable nature of the films, when subjected to 1 week of dry heat test at 155°C.

To verify the effectiveness of this secondary stage of heat treatment in improving the stability figure of sheet resistance, the as-grown ternary films were subjected to two stages of heat treatment. In the first stage, 10 samples from substrate plates are subjected to four levels of heat treatment temperature starting from 300°C and

increasing in steps of 25ºC up to 375ºC. This stage of treatment was performed for 3 hours in a sealed tube furnace with a 2 l/min flowing Nitrogen source connected. After three hours, the seal is broken to shift the samples to a cooler region and then cooled to room temperature. After this, five samples are removed to perform TCR measurements while the remaining 5 samples were subjected to a secondary stage of stabilization heat treatment. The stabilization heat treatment was performed in an open-air environment in the same tube furnace at an elevated temperature of 260ºC for 16 hours. At the end of 16 hours' the samples were moved to a cooler region to cool down to room temperature. After this, the samples were measured for their TCR values. The dry heat stability test was then performed on the samples that were subjected to the second stage of heat treatment for 168 hours at 155ºC.

5.3 Results and Discussion

As in previous chapters, three main electrical properties were studied for the samples:

1. Electrical sheet resistance at room temperature, Rs (Ω/□)
2. TCR $_{avg.}$ between 20˚C and 70˚C (ppm/˚C)
3. Resistance Stability ΔΩ/Ω, (%)

Sheet resistance and TCR measurements were made before and after heat treatment of samples, for the six resistor circuits from each of the varying compositions. Dry heat stability tests were conducted after films were subjected to stabilization heat treatment at 260ºC for 16 hours.

5.3.1 As grown ternary films of $Mn_3Ag_{(1-X)}Cu_{(X)}N$

Chemical composition and thickness:

EDX analysis was performed on five sites across the glass substrate deposited with ternary thin films. The expected film composition and the film composition achieved after deposition is as shown in table 5-3. The atomic composition achieved for ternary films are very close to the required value set in table 5-2.

Sample no. 1 is seen to deviate from the expected value with an Mn:Ag:N ratio of 2.47:1.53 as opposed to the required ratio of 3:1. Mn_3AgN films deposited using the ternary deposition plan registered a thickness value of 560 nm using the profilometer, which is also lower when compared to the thickness of 617 nm for Mn_3AgN films achieved in section 4.3.1. Sample no. 6, Mn_3CuN films also show higher deviation from the expected Mn:Cu ratio of 3:1 to the achieved value of 2.85:1.15, though the thickness value of 498 nm is comparable to that achieved in section 4.3.1. As the targets are used repeatedly, more and more of the material is removed from their surface and this gradually changes their electrical resistance, leading to changes in the corresponding current and power values. This slowly changes the sputtering calibration set between the targets as in section 3.2.2. The rest of the compositions are much closer to the expected atomic composition.

Table 5-3 Table of film thickness and composition for $Mn_3Ag_{(1-X)}Cu_{(X)}N$ films.

Sample No	Value of X	Expected Ternary composition	Atomic % of Mn:Ag:Cu:N	Ternary composition achieved	Film Thickness (nm)
1	0	Mn_3AgN	57:20:0:23	$Mn_{2.85}AgN_{1.15}$	560
2	0.2	$Mn_3Ag_{0.8}Cu_{0.2}N$	59:15:5:21	$Mn_{2.95}Ag_{0.75}Cu_{0.25}N_{1.05}$	545
3	0.4	$Mn_3Ag_{0.6}Cu_{0.4}N$	61:14:6:19	$Mn_{3.05}Ag_{0.7}Cu_{0.3}N_{0.95}$	523
4	0.6	$Mn_3Ag_{0.4}Cu_{0.6}N$	60:9:11:20	$Mn_3Ag_{0.45}Cu_{0.55}N_1$	529
5	0.8	$Mn_3Ag_{0.2}Cu_{0.8}N$	60:4:17:19	$Mn_3Ag_{0.2}Cu_{0.85}N_{0.95}$	532
6	1.0	Mn_3CuN	56:0:23:20	$Mn_{2.8}Cu_{1.20}N$	498

Electrical Analysis of as-grown ternary films:

Average values of electrical sheet resistance and TCR values observed for 6 different compositions of $Mn_3Ag_{(1-X)}Cu_{(X)}N$ with increasing concentration of X from 0 to 1 in steps of 0.2 are plotted in figure 5-3. The average sheet resistance is observed to increase from 7 Ω/□ to 21.9 Ω/□ for X=0 to X=1. Bulk Cu has higher sheet resistivity than bulk Ag, therefore this increment in sheet resistance is

reasonable [151]. At the same time the TCR value drops from -233 ppm/^{0}C for X=0 to -351 ppm/^{0}C for X=1. These values of TCRs are in agreement with the TCR values achieved in section 4.3.2 for Mn_3AgN and Mn_3CuN samples deposited without any substrate temperature.

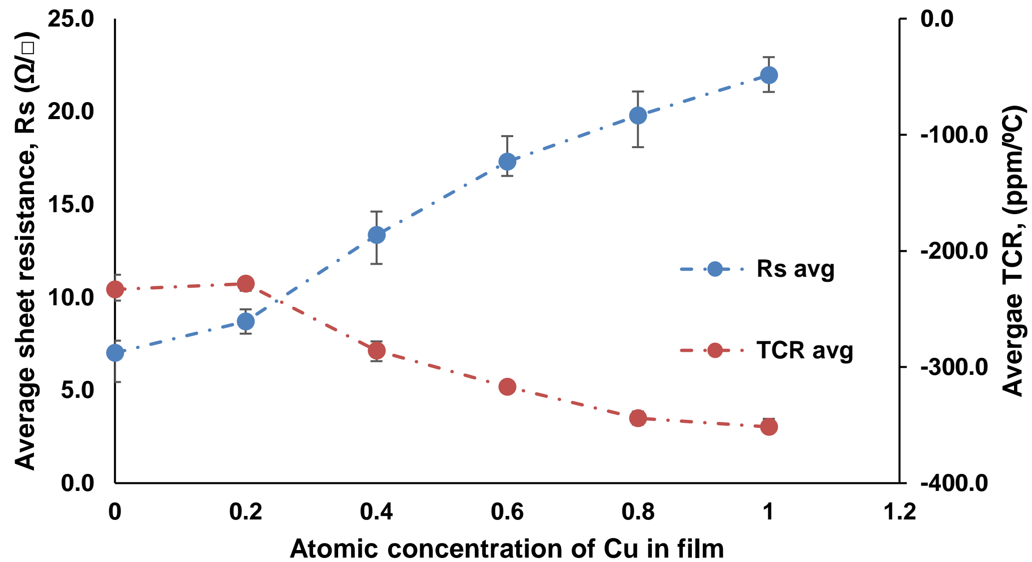

Fig 5-3 Graph of sheet resistance and TCR values of as grown ternary $Mn_3Ag_{(1-X)}Cu_{(X)}N$ films with increasing Cu doping concentration in the film.

Figure 5-4 shows the XRD spectrums developed for each of the ternary compositions. For X=0, a very faint protrusion is visible close to the (111) peak position expected for Mn_3AgN films. It is very hard to call this a definite peak, as it is not prominent enough. From section 4.3.2 it is known that Mn_3AgN peaks are not as prominent as for Mn_3CuN films. The reason for the shift from the central (111) position could be explained by the presence of a higher than required ratio of N_2 in the film, as observed in the EDX analysis. Therefore, there exists a higher probability that some kind of antiperovskite structure with (111) phase does exist for sample 1 with X=0. For the sample with an X value of 0.2, two peaks are visible, corresponding to the (111) and (200) phases. The peaks for (111) and (200) phase are expected at 38.8^0 and 45.12^0 for Mn_3AgN, and at 40.10^0 and 46.64^0 in the case of Mn_3CuN. However, because of the presence of Cu in the film, the (111) and (200) peaks, observed for samples with an X value of 0.2, shifts to a position in between both the pure phases. Further, for samples with X values of 0.4 and 0.6,

only a single peak corresponding to the (200) phase is clearly visible, and with increasing concentration for Cu dopant, the peak shifts towards higher angles. The temperature within the deposition chamber increases when three targets plasma plumes are simultaneously depositing and this rise in temperature could assist in defect healing and better crystallization of the film. Surprisingly no peaks are observed for X=0.8 and 1. It is explored further if heat treatment would enable the crystallization of Cu rich $Mn_3Ag_{0.2}Cu_{0.85}N_{0.95}$ and $Mn_{2.85}Cu_{1.15}N$ and if any peaks would appear.

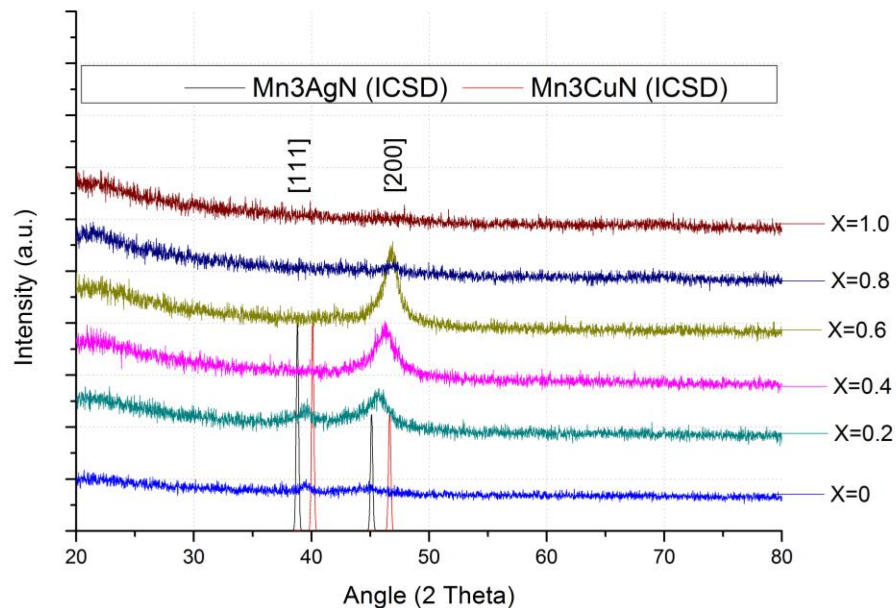

Fig 5-4 XRD spectrums of as-grown films of $Mn_3Ag_{(1-X)}Cu_{(X)}N$ with increasing value of X from 0 to 1.

5.3.2 <u>Two stage heat treatment of ternary films</u>

The as-grown samples were heat treated for 3 hours in a flowing N_2 environment at a narrowed temperature range between 300 and 375^{0}C. The effect of heat treatment on sheet resistance of $Mn_3Ag_{(1-X)}Cu_{(X)}N$ films for each increasing concentration of Cu is plotted in figure 5-5. The progressive shift of each line towards higher values shows that the mean value of sheet resistance increases with increasing concentration of Cu in the film and this remains true throughout the heat treatment regime as all the lines stay independent of each other in direction.

In the X direction, all of the compositions show a decreasing trend for the sheet resistance value up to 325ºC and thereafter start increasing. This increase becomes steeper at 375ºC.

As-grown samples with X=0, show the lowest mean value of sheet resistance of 7.01Ω/□ which further decreases to 6.60 Ω/□ after heat treating up to 325ºC and thereafter increases to 12.03 Ω/□ at 375ºC. The highest mean sheet resistance value is observed for as grown Mn_3CuN films (X=1) at 21.95 Ω/□, which decreases to 18.90 Ω/□ after heat treatment at 325ºC and with further increment in heat treatment temperature to 375 ºC the value increases to 27.97 Ω/□. These trends are in agreement with sheet resistance trends previously observed for Mn_3AgN and Mn_3CuN films in section 4.3.3.

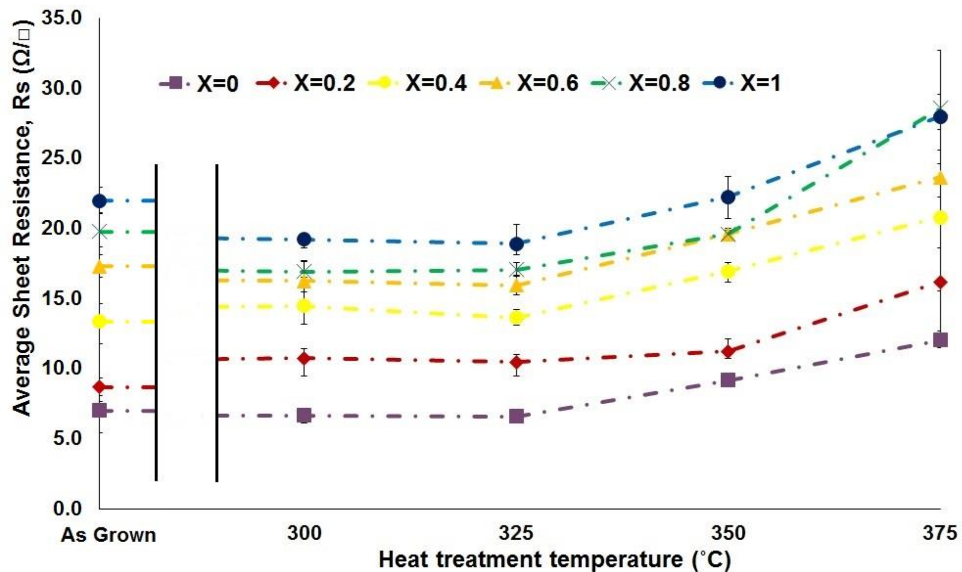

Fig 5-5 Graph of sheet resistance values of $Mn_3Ag_{(1-X)}Cu_{(X)}N$ ternary films with heat treatment temperature between 300 and 350ºC.

The samples from each of the ternary compositions registered a negative as grown TCR value. TCR values achieved after heat treatment between 300 and 375ºC are plotted in figure 5-6 to precisely locate the zero TCR line cross over temperature. TCR remains negative for all the compositions for heat treatment up to 325ºC. The lowest value of TCR is observed to be -4.66 ppm/ºC for $Mn_3Ag_{0.45}Cu_{0.55}N$ (X=0.6) films after heat-treating at 350ºC. The lowest average TCR value achieved for

Mn_3AgN and Mn_3CuN films is -18 and -25 ppm/^{o}C respectively, after heat-treating at 325°C.

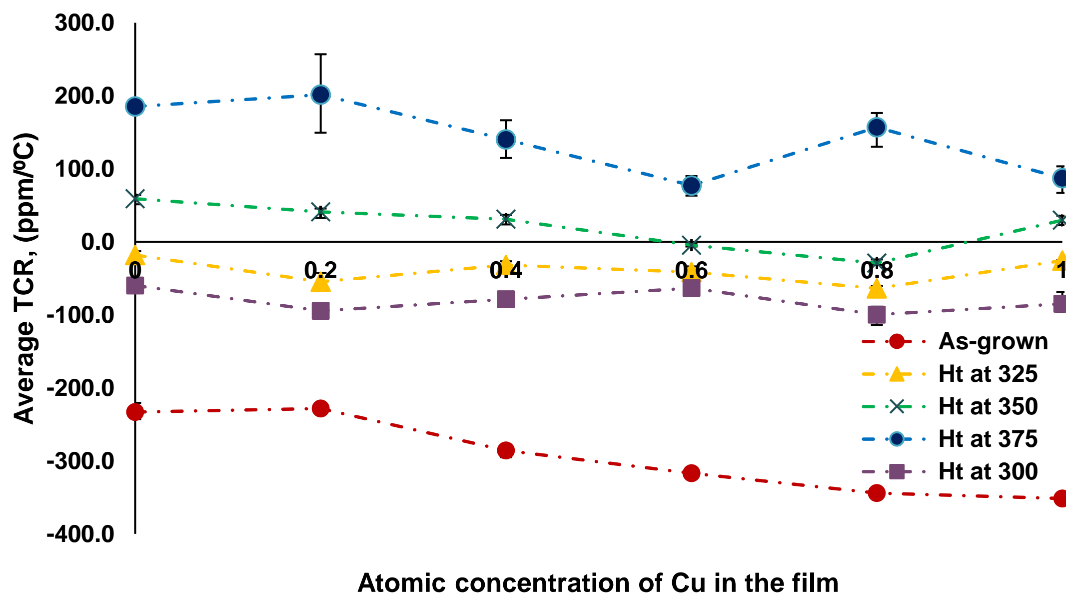

Fig 5-6 Effect of Cu dopant concentration on TCR values of $Mn_3Ag_{(1-X)}Cu_{(X)}N$ ternary films with increasing heat treatment temperature.

Figures 5-7 (a) – (f) show the XRD spectrums of the 6 compositions of $Mn_3Ag_{(1-X)}Cu_{(X)}N$ in increasing value of X from 0 to 1 in steps of 0.2, as-grown and after heat treatment at 4 different temperatures from 300 to 375°C. It can be observed that all of the samples develop sharp peaks when heat treated at higher temperature. Not all of the compositions show the very clear XRD peaks in their as grown state, like Mn_3AgN films (X=0), but as seen in figure 5-7 (a), with increasing heat treating this composition starts to show growing peaks representing (111) and (200) planes. With increasing heat treatment temperature, the peak at 45.1^{o} becomes stronger than the peak at 38.8^{o}, indicating a preferential arrangement along the (200) crystal plane with increasing temperature. With the increasing value of X, the peak representing the (200) plane gradually shifts its position from 45 to 46°, indicating formation of more Mn_3CuN structure within film [151]. For films with X values of 0.4 and 0.6, a clear shoulder exists along with the main peak at 46.6^{o}. The merged nature of the peaks suggests that the antiperovskite phase of both Mn_3AgN and Mn_3CuN exists in the film. The peak for Mn_3AgN gradually starts to disappear from the main (200) peak, while increasing concentration of Cu causes the Mn_3CuN

peak to rise, see figure 5-7 (c) and (d). For films with X values of 0.8 and 1.0, the XRD spectrums suggest that the films exist in a pure Mn_3CuN antiperovskite phase with preferential arrangement along the (200) plane. Heat treating Cu rich samples (X=0.8 and 1.0) also begins to show a growing peak at 68.1^{o} which is representative of the (220) plane of the Mn_3CuN antiperovskite structure.

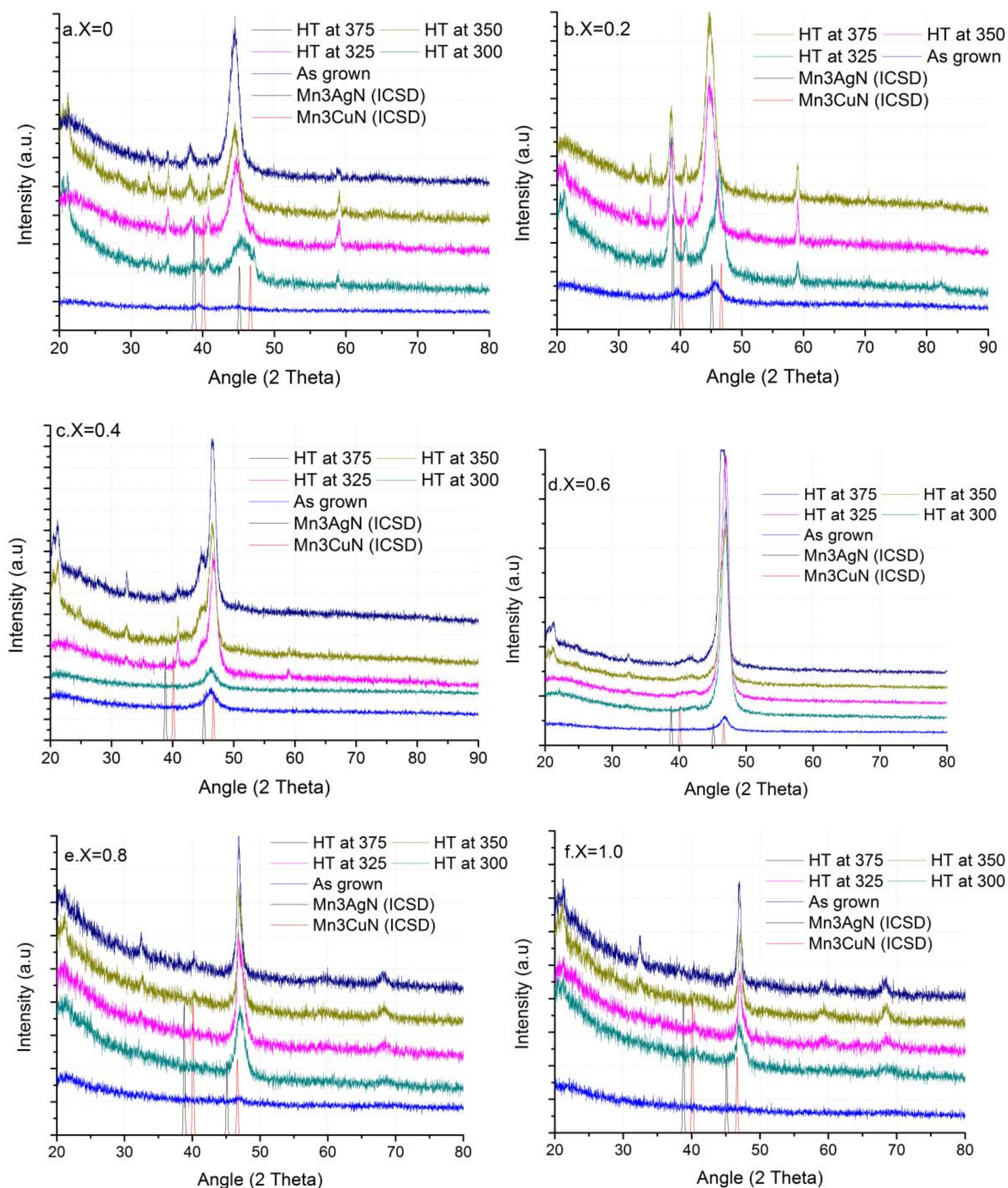

Fig 5-7) XRD spectrums of 6 different compositions of $Mn_3Ag_{(1-X)}Cu_{(X)}N$, X= (a) 0, (b) 0.2, (c) 0.4, (d) 0.6, (e) 0.8, and (f) 1.0 before and after heat treatment.

Four peaks of lower intensities at 32.4, 35.2, 40.8 and 58.9° are very clearly visible for films with X values of 0 and 0.2. These peaks could easily be related to planes of Manganese oxide, MnO [152]. It is interesting to note that with increasing concentration of Cu in the film, most of the peaks representing oxides of Manganese start to disappear. This suggests that while all compositions do undergo oxidation, films richer in Ag are more prone to oxidation. Only the peak at 32.4° is observed consistently for all of the films irrespective of Cu concentration. It is also observed that peaks representing oxides become sharper above 325°C. This observation supports the reduction in sheet resistance up to 325°C because of increasing crystallinity but higher Oxygen content in film starts to occur above this temperature, which increases the sheet resistance again.

Topographical images of sample no's 1, 4 and 6 with X values 0, 0.6 and 1, before and after heat treatment at 325˚C are shown in figure 5-8 (a) to (f), and further support the XRD results. The as grown crystals of Mn_3AgN samples are spherical in shape but have grains of varying sizes, figure 5-8 (a). With inclusion of Cu dopant, the grains appear to elongate and become more elliptical as shown in the SEM images of films with an X value of 0.6, in figure 5-8 (b). The grains appear to be bigger in size and uniform across the film surface compared to the Mn_3AgN topology. For the Mn_3CuN (X=1) films in figure 5-8 (c), a higher number of grains appear triangular with sizes smaller than those of $Mn_3Ag_{0.45}Cu_{0.55}N$ films. The bigger size justifies the presence of a sharper (200) peak for the as grown $Mn_3Ag_{0.45}Cu_{0.55}N$ compared to Mn_3AgN and Mn_3CuN films in figure 5-7 (a) (d) and (f). After heat treatment, the topology of the Mn_3AgN film in figure 5-8 (d) appears to be more porous with increased grain boundaries. Whereas the grains in the films rich in Cu (X=0.6 and 1) appear to merge with each other to form a more continuous upper layer, figure 5-8 (e) and (f).

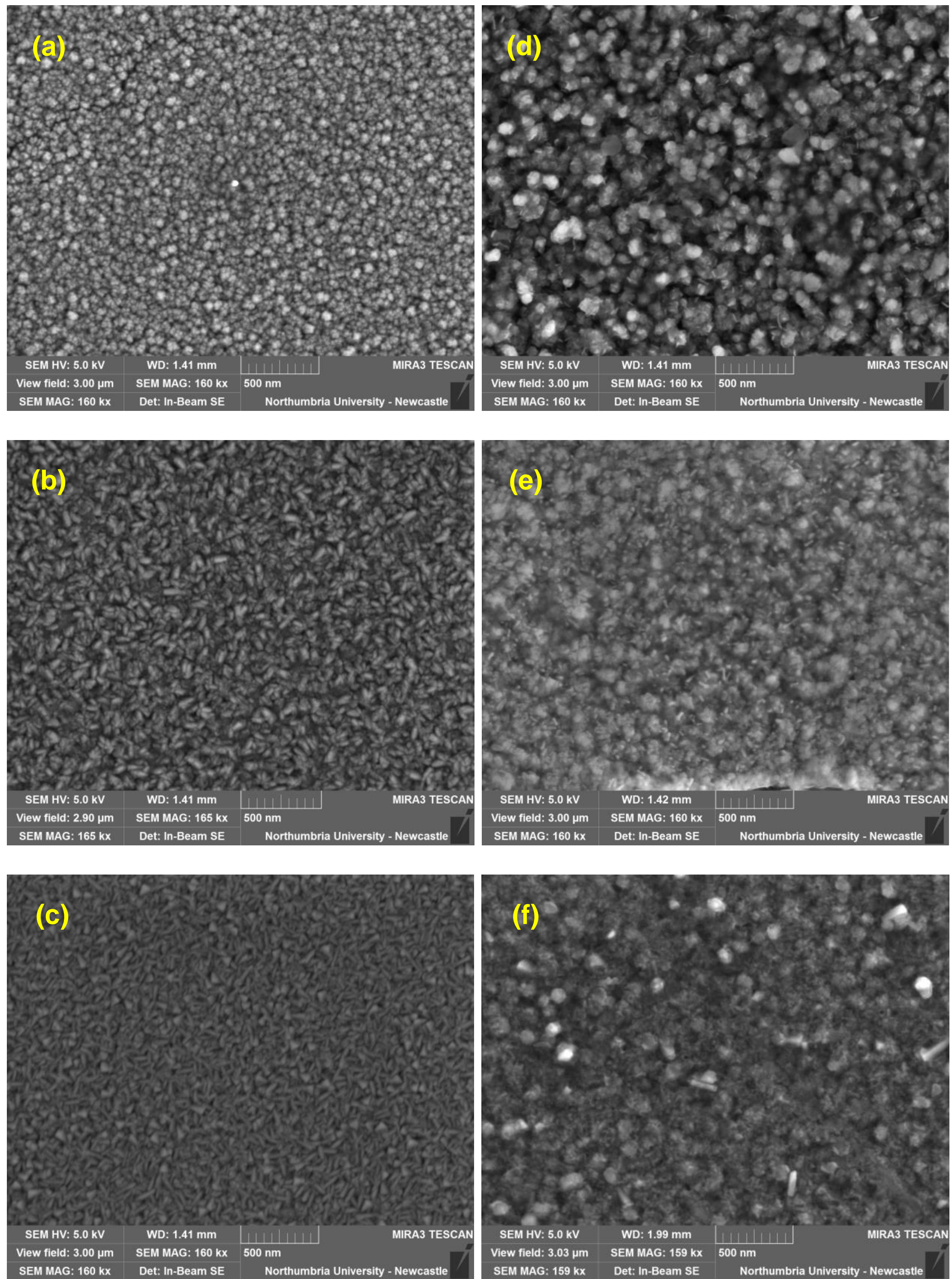

Fig 5-8 SEM images showing the topology of $Mn_3Ag_{(1-X)}Cu_{(X)}N$ with X = 0, 0.6 and 1 as grown, (a) (b) and (c) and after heat treatment at 325°C (d) (e) and (f) respectively.

Figure 5-9 (a) to (f) shows the side profile imaging of sample no's 1, 4 and 6 with X values of 0, 0.6 and 1 respectively. The thickness values of as grown films measured in the SEM side profiles match very well with the profilometer readings

presented in table 5-4. The as grown films have a columnar structure for all values of X, with Mn_3AgN having really good uniformity of column width in 5-9 (a) but column width becomes more random from figure 5-9(a) to (b) and then to (c). After heat treatment at 325˚C, the side profile of the Mn_3AgN film in figure 5-9 (d) appears to be most degraded. The porous nature mentioned in the topography is very clearly visible in the side profile as well. For films with higher content of Cu (X=0.6 and 1) the side profile looks more intact. It gives the impression that the upper layer acts like a protective layer for the underlying, thereby protecting from further degradation. It is presumed that the film is being attacked by the Oxygen present in the air when moved between different regions within the tube furnace. The images in figure 5-9 (d) to (f) also suggest that the increment in overall thickness and thickness of the upper layer also depends upon the composition of the film, tabulated in table 5-4. The Mn_3AgN film increases in overall thickness more than 150 nm to 694 nm of which 201 nm is the upper layer. Cu rich films (X=0.6 and 1) show comparatively much lower increases in thickness. The $Mn_3Ag_{0.45}Cu_{0.55}N$ increases by 55 nm to an overall thickness of 558 nm, of which the upper layer constitutes 107 nm. The pure Mn_3CuN film (X=1) only shows a moderate increment of 17 nm to form a 533 nm thick film, of which 89nm is clearly visible as the upper layer. If the upper layer is assumed to be rich in oxides then the higher thickness of the upper layer for Mn_3AgN films compared to Mn_3CuN films, ties very well with the presence of pronounced manganese oxide peaks in the XRD spectrums for Ag rich $Mn_3Ag_{(1-X)}Cu_{(X)}N$ (figure 5-7 (a)-(f)). It can be reasoned that the presence of Ag because of its higher surface activity makes the Mn_3AgCuN structure less stable so that at higher temperature the cubic structure disintegrates into its individual components. Transition metals then migrates to sub surface, leaving Mn available for oxidation. This is supported by the SIMS depth profile performed further on.

Table 5-4 Table of film thickness as grown and post heat treatment for value of X.

Sample no	As grown (nm)	After heat treatment at 325ºC (nm)	
		Upper layer	Total thickness
1 (X=0)	546	201	694
4 (X=0.6)	503	107	558
6 (X=1)	516	89	533

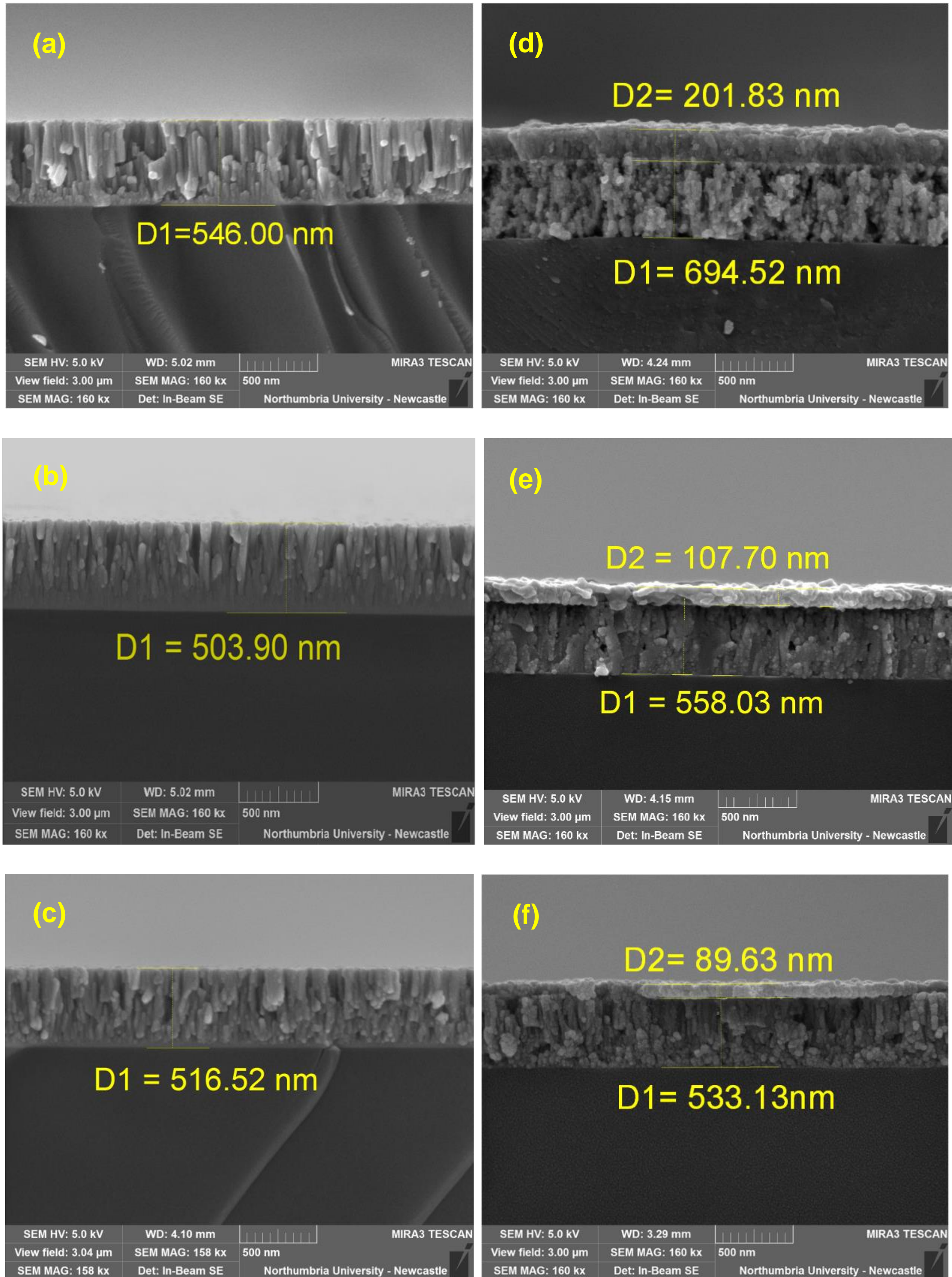

Fig 5-9 SEM images showing the cross section of $Mn_3Ag_{(1-X)}Cu_{(X)}N$ with X = 0, 0.6 and 1 as grown (a) (b) and (c) and after heat treatment at 325ºC (d) (e) and (f) respectively.

The thickness of the upper layer is not only dependent on the composition of the film. Figure 5-10 (a) (b) and (c) shows the side profile imaging of Mn_3CuN samples

after heat treating at 300, 350 and 375^{0}C respectively. After heat treatment at 300^{0}C the upper layer is observed to be only 56 nm thick, which increases to 89 nm when heat treated at 325^{0}C, as seen in figure 5-9 (f). For 350^{0}C of heat treatment, there is a drastic increase in the upper layer thickness to 157 nm and after heat treatment at 375^{0}C this layer thickness increases to 175 nm. The drastic increase in upper layer thickness at 350^{0}C correlates very well with the trends observed in sheet resistance variation and XRD. If the upper layer is an oxide of Manganese or the transition metal (Ag/Cu), the increase in sheet resistance is expected. For heat treatment up to 325^{0}C, the increment in sheet resistance because of this layer can be presumed as being compensated or even overcome by the crystallization and defect healing, which appears as a reduction in sheet resistance. However, after 350^{0}C the effect of crystallization is not strong enough to overcome the sheet resistance increment produced by the thicker upper layer, which could be primarily oxides

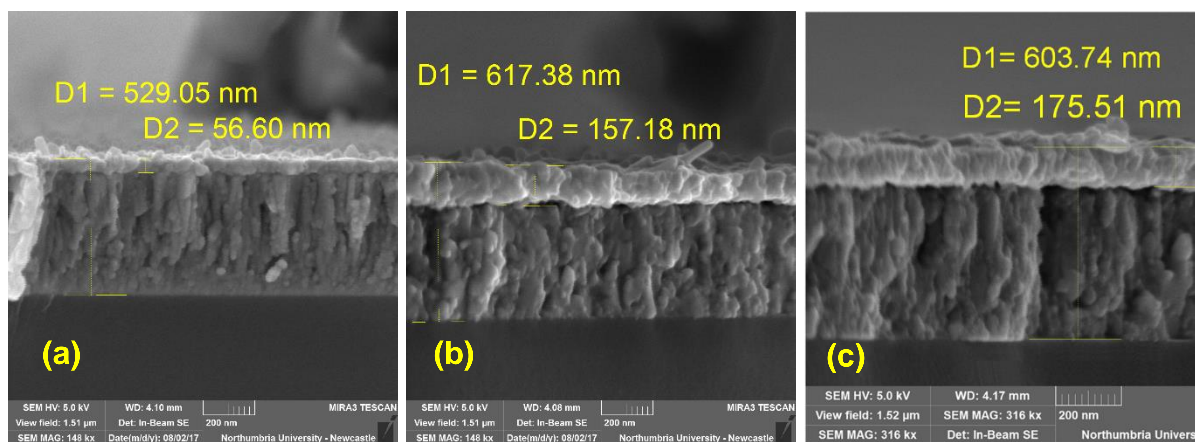

Fig 5-10 SEM images showing the cross section of $Mn_3Ag_{(1-X)}Cu_{(X)}N$ with X=1 after heat treatment at (a) 300^{0}C (b) 350^{0}C and (c) 375^{0}C .

The general EDX analyses the composition of the film within the whole interaction volume where the electron beam interacts with the surface, which is generally 500 nm of thickness. This is not suitable for application where composition analysis of much smaller and specific sections of films is required, like the upper layer of the films shown in figure 5-10. For these purposes, two other techniques could be used: SIMS (Secondary ion mass spectroscopy) or Low voltage cross section EDX. SIMS as explained in section 3.1.4, is a destructive technique, which bombards accelerated ions onto the film surface, and then detects the particles ejected out.

In this way, it creates a depth profile of each element in the film. Figure 5-11 (a) to (d) shows the depth profile for Mn^+, Cu^+, N_2^+ and O_2^- ions from SIMS analysis of Mn_3CuN films (Composition 6) before and after heat treatment at 325ºC. For the as grown film, represented by the blue line, it can be seen that the concentration of Mn, Cu and N_2 ions are very consistent throughout the film thickness. Time 0 sec indicates the start point on the surface of the film and the sharp drop in the element concentration represents the interface between the film and the glass substrate. The film appears to be around 2300 seconds thick. Although quantitative analysis is not a strength of SIMS, it is evident that the intensity of Cu and N are equal as expected and that for Mn is almost three orders higher. This is in agreement with the general EDX result of the Mn_3CuN films.

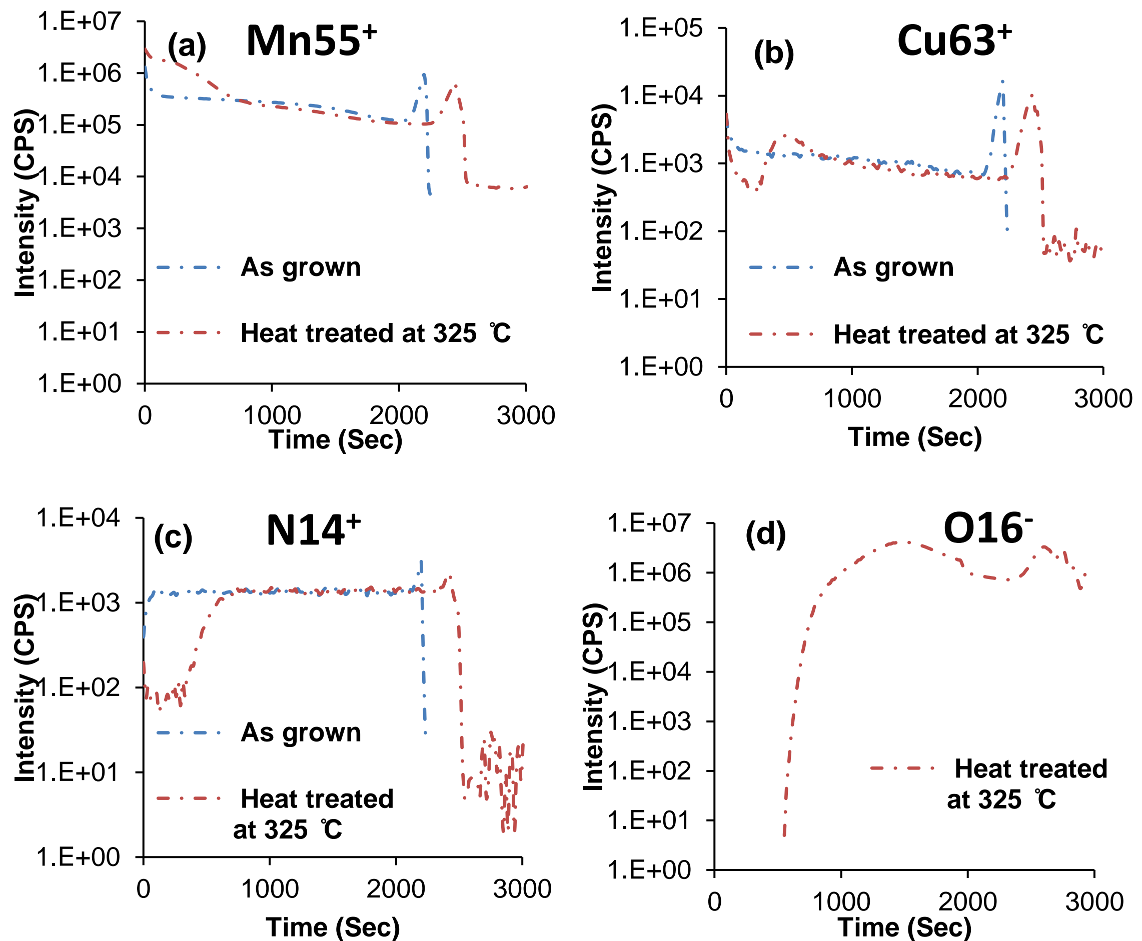

Fig 5-11 Graphs showing elemental depth profile of (a) Mn^+(b) Cu^+ (c) N^+ and (d)O^- ions in Mn_3CuN films (X=1.0) before and after heat treatment at 325ºC .

After heat treatment, films are seen to be 500 seconds thicker (represented by red lines for each element), suggesting a grain growth, which is again in agreement with the SEM images studied earlier. By comparing the two curves for Manganese, it can be seen that there is a migration of Mn ions towards the film surface post heat treatment for roughly 500 seconds. This corresponds very well with the approximate 500 seconds for which the Copper and Nitrogen ions withdraw from the upper layer to lower layers. The first 500 seconds for a 3000-second thick film roughly translates to 16.6% of the total thickness being the upper layer. With this expectation, for a 550 nm thick Mn_3CuN film nearly 91 nm should be upper layer, which matches very well with the SEM images. Therefore, from comparing SIMS and SEM data, it can be said that the upper layer seen in SEM images are richer in Mn ions as Cu and N_2 ions move lower into the film. It is not a surprise as Cu with a density of 8.96 gcm^{-3} could easily sink below Mn ions, which only has a density of 7.43 gcm^{-3}. However, in figure 5-11 (d) the absence of Oxygen in the upper layer of approximately 500 seconds is very surprising and contradictory to the XRD results. SIMS identifies the ions based upon their atomic mass unit (a.m.u), therefore while looking for specific species of elements, if their molecules are ejected out, SIMS can miss them because the combined a.m.u of the molecules not matching with the individual a.m.u`s of either of the species. The presence of Oxygen in the lower layers could be explained as to be coming from the Al_2O_3 (Alumina) substrate. Because of uneven nature of alumina substrate thin film deposited on these substrate are extremely thin at certain place (as shown in Figure 5-12) and could be eroded much faster to reach the substrate layer beneath thereby registering presence of oxygen in the lower layers.

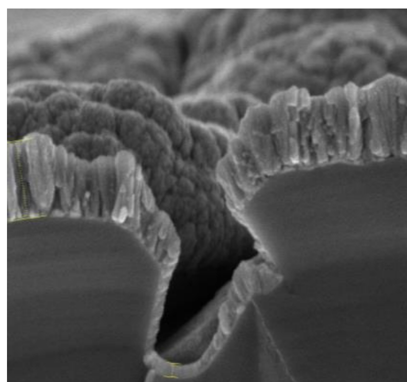

Fig 5-12 Cross section image showing thin deposition of film in the valley between two alumina grain responsible for detection of O- in the SIMS

To confirm the chemical composition low voltage EDX has to be performed on the side profiles of samples, which can pick up the oxygen even if bonded in oxide form but without picking up from substrate layer. Low voltage side profile EDX was performed across the various sites on the side profile image of as-grown and heat treated sample 6, as shown in figure 5-13. The EDX results from these sites are presented in table 5-5. From table 5-5, it can be clearly seen that the as-grown film follows the composition very uniformly throughout the depth of the sample. The decrease in the copper and nitrogen content also agrees very well with the SIMS result. However, unlike the SIMS result, the upper layer is seen to be very rich in oxygen, which is also supported by the presence of manganese oxide peaks on the XRD spectrum.

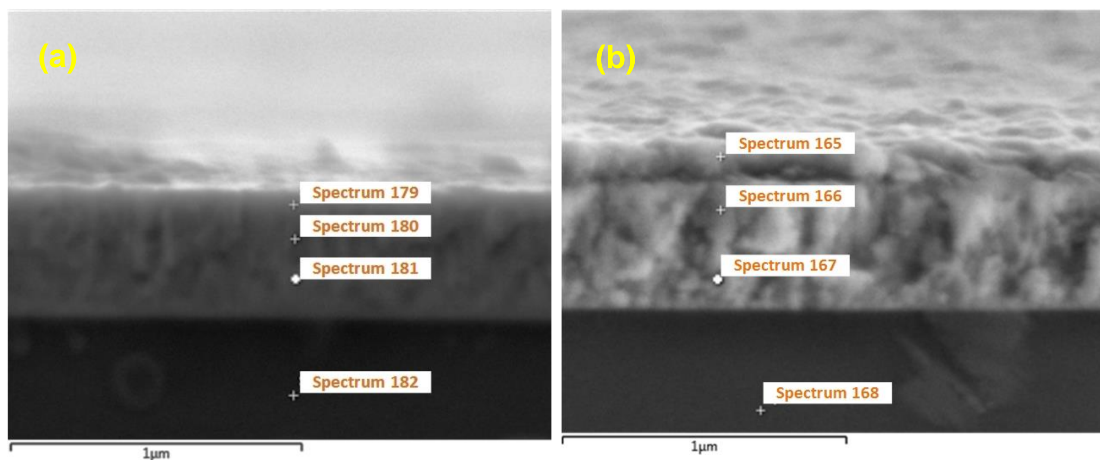

Fig 5-13 Sites at the side profile image of Mn_3CuN films for EDX analysis of (a) as-grown (b) heat treated at 325ºC .

To summarize, from XRD it can be concluded that manganese oxide peaks arise more prominently for Ag rich antiperovskite films. SEM images show the development of a secondary layer after heat treatment and its thickness depends heavily on the composition of the film and on the heat treatment temperature. SIMS proves that Manganese ions move towards the surface during heat treatment while side profile EDX concludes that the upper layer is rich in oxygen as well.

Table 5-5 Table showing composition from cross section of Mn_3CuN films as-grown and after heat treatment at 325ºC .

Spectrum Label: As grown		Mn	Cu	N	O	Si	Total
Spectrum 179	AP layer	60.46	19.88	19.66			100
Spectrum 180		60.66	20.03	19.31			100
Spectrum 181		60.84	19.26	19.9			100
Spectrum 182	substrate				63.98	36.02	100
Heat treated		**Mn**	**Cu**	**N**	**O**	**Si**	**Total**
Spectrum 165	Upper layer	47.85	0.61	2.31	49.23		100
Spectrum 166	AP layer	54.65	19.71	18.65	6.99		100
Spectrum 167		56.1	22.09	18.66	3.16		100
Spectrum 168	substrate				67.38	32.62	100

Second stage of heat treatment:

The role of the first stage of heat treatment is to tune the TCR value closer to zero. The second stage of heat treatment was performed to improve the stability of the performance-tuned resistors. Five samples from each of the 6 compositions were first heat treated at 325ºC in a closed N_2 environment for 3 hours and then stabilization heat treated at 260ºC in open air for 16 hours. Figure 5-14 shows the values of sheet resistance observed before and after performing stabilization heat treatment. Most of the compositions show 5 to 10% change in resistance after stabilization treatment in open-air environment. Whereas, sample sets with X=0.2 and X=0.6 showed comparatively high percentages of resistance change of 17.9 and 27.9% respectively.

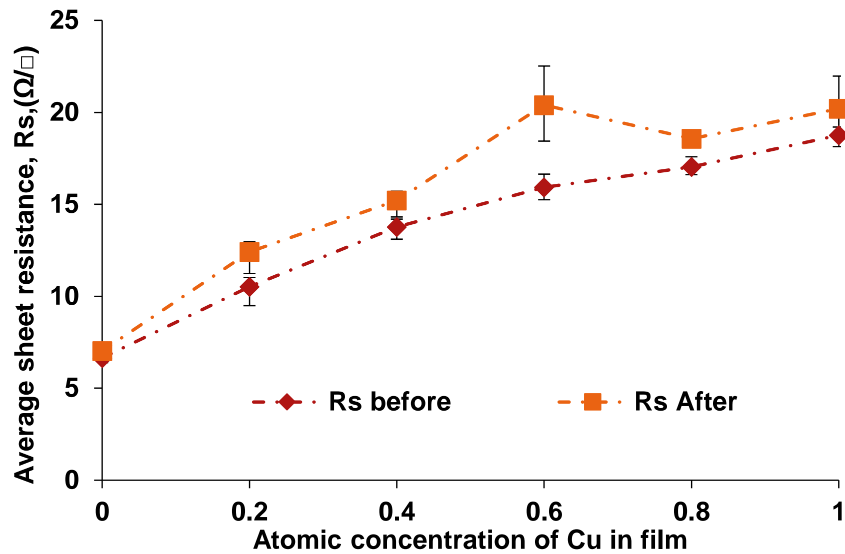

Fig 5-14 Graph of sheet resistance values before and after introducing second stage of heat treatment.

The total percentage change in resistance observed after the dry heat stability test for 168 hours is shown in the figure 5-15 below. With increasing concentration of Cu in the $Mn_3Ag_{(1-X)}Cu_{(X)}N$ film, the stability figure improves considerably. For the Mn_3AgN film (X=0) the average stability figure observed is 13.97% after 1 week with quite wide error bars and none of the samples in the composition showed better values than 12.34%. However, with a mere 0.2 atomic % increment in Cu concentration, the stability figure almost improves by a factor of 2 to 7.98%, and with each successive increments of 0.2 Cu concentration, the stability figure improves to 5.48, 3.39, and 2.57% respectively. For films without any Ag or Mn_3CuN films, the average stability figure falls below 1% to a value of 0.85% with the best figure seen of 0.67%. The improvement in the stability figure to 0.85% for the Mn_3CuN samples with stabilization heat treatment stage introduced, is very clear when compared to the stability figure measured for Mn_3CuN films without stabilization heat treatment stage, where the best stability figure registered was at 11.3% (section 4.3.5).

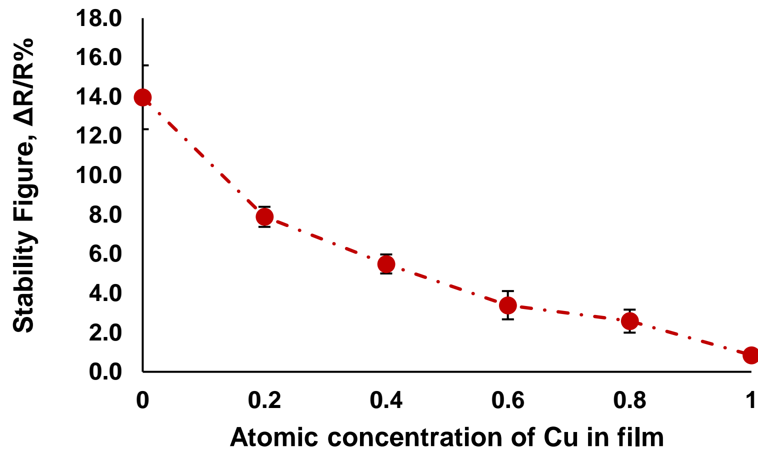

Fig 5-15 Graph of percentage change in resistance for six composition of $Mn_3Ag_{(1-X)}Cu_{(X)}N$ ternary films with increasing Cu dopant concentration

The dry heat stability test conducted on the samples clearly shows the beneficial effect of stabilization heat treatment. Even though the samples were subjected to two stages of heat treatment and 1 week of dry heat stability test, the electrical parameters were not measured as-grown or after the first stage of heat treatment. So far, none of the sample set has been subjected to the entire process stages with all the electrical parameters measured after each stage. In order to study the combined effect of all the process stages run sequentially, on the electrical parameters of ternary films, 9 samples each from composition 1, 4 and 6 (X=0, 0.6 and 1) were first measured for as grown electrical properties. Then they were heat treated in flowing N_2 environment for 3 hours at 325^oC, and after this, their heat treated electrical parameters were measured. Later these same films were subjected to 16 hours of stabilization heat treatment at 260^oC in open-air environment. Electrical parameters were once again measured after stabilization heat treatment and then these films were subjected to 1 week of dry heat stability test at 155^oC for 168 hours with electrical resistance measured every 24 hours. After 1 week, the electrical parameters were measured once again to finish the process.

Figure 5-16(a) shows change in the sheet resistance at each key stage for the compositions of $Mn_3Ag_{(1-X)}Cu_{(X)}N$ with x = 0, 0.6 and 1. For the Mn_3AgN films, the average sheet resistance value of 9.02 Ω/□ decreases by 1.7% to 8.86 Ω/□ after

the first heat treatment stage and thereafter increases by 4.6% to 9.27 Ω/□ after the stabilization heat treatment. After one week at 155ºC this film changes its resistance value by 13.14%. The copper rich film of $Mn_3Ag_{(1-X)}Cu_{(X)}N$ with x = 0.6, decreases 6% from its as-grown sheet resistance of 17.87 Ω/□ to 16.70 Ω/□. During the stabilization heat treatment, the sheet resistance of this film increases dramatically to 27.90 Ω/□, increasing by 67%. However, during the 1 week of dry heat test this film only increases its sheet resistance by 7.7% comparatively better than Mn_3AgN films. Most stable of the group are the Mn_3CuN films, which decrease by 1.5% after the heat treatment stage from 19.18 Ω/□ to 18.88 Ω/□. During the stabilization heat treatment in open air this film changes its resistance value by 10.4% to 21.08 Ω/□. During 1 week of dry heat stability test, this film only changes it sheet resistance by a tiny percentage of 0.55% to 21.20 Ω/□.

Similar to sheet resistance, TCR values were measured before and after each of the process stages. The variation of TCR for three compositions of $Mn_3Ag_{(1-X)}Cu_{(X)}N$ with x = 0, 0.6 and 1 are shown in figure 5-16 (b). After the first stage of heat treatment, the Mn_3AgN films shift their average TCR value from -240.6 ppm/ºC to -19.6 ppm/ºC but after stabilization heat treatment in air this average TCR value shoots up to +88.8 ppm/ºC and thereafter remains fairly constant after 1 week of dry heat stability test. The $Mn_3Ag_{(1-X)}Cu_{(X)}N$ with X=0.6 shifts its TCR value from -312.4 ppm/ºC to -51.2 ppm/ºC which quickly rises to 74.1 ppm/ºC after stabilization treatment. After 1 week at 155ºC for the dry heat stability test, this set of films register an improvement in TCR value to + 68.21 ppm/ºC. Mn_3CuN that registered the most negative as-grown TCR of -327.0 ppm/ºC shifts to -21.0 ppm/ºC after the first stage of heat treatment. After the stabilization heat treatment stage, this value moderately increases to +19.8 ppm/ºC. After 1 week at 155ºC this set of films moves closer to the zero TCR line by registering an average TCR value of +14.25 ppm/ºC.

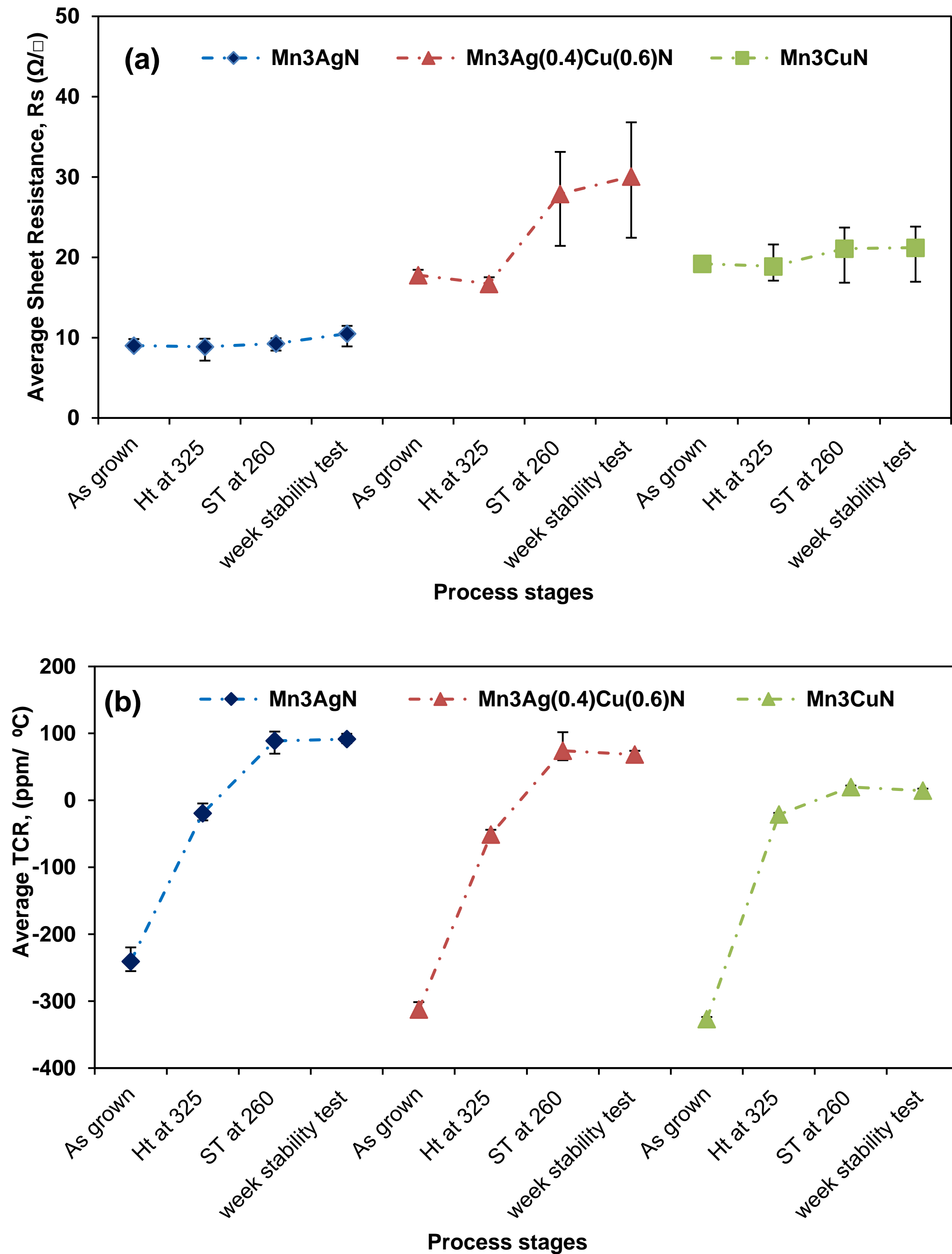

Fig 5-16 Graph showing variation in (a) Sheet resistance (b) TCR values of three composition of $Mn_3Ag_{(1-X)}Cu_{(X)}N$ with X=0,0.6 and 1, with each process stage

Figure 5-17 (a) to (c) shows the side profile imaging carried out on films of $Mn_3Ag_{(1-X)}Cu_{(X)}N$ on alumina substrates with X= 0, 0.6 and 1, to visualize the effect of sequential process run on film morphology. Mn_3AgN films which had registered a total thickness of 694 nm with 201 nm of upper oxide layer after the first heat treatment stage increases to 755 nm with 281 nm of upper oxide layer after all

process stages are run in sequence, figure 5-17 (a). $Mn_3Ag_{0.4}Cu_XN$ appears to be the sample most adversely affected when process stages are run in sequence as it shows a tripling of the upper oxide layer thickness from 107 nm to 307 nm in figure 5-17 (b) when the total thickness of the film only increases from 558 nm to 629 nm. Again, the Mn_3CuN sample set shows the best stability in film morphology as the increment in film upper oxide layer from 89 nm to 93 nm is barely noticeable when compared to the overall film increase from 533 nm to 561 nm, which is due to grain growth and additional oxide layer on the upper layer.

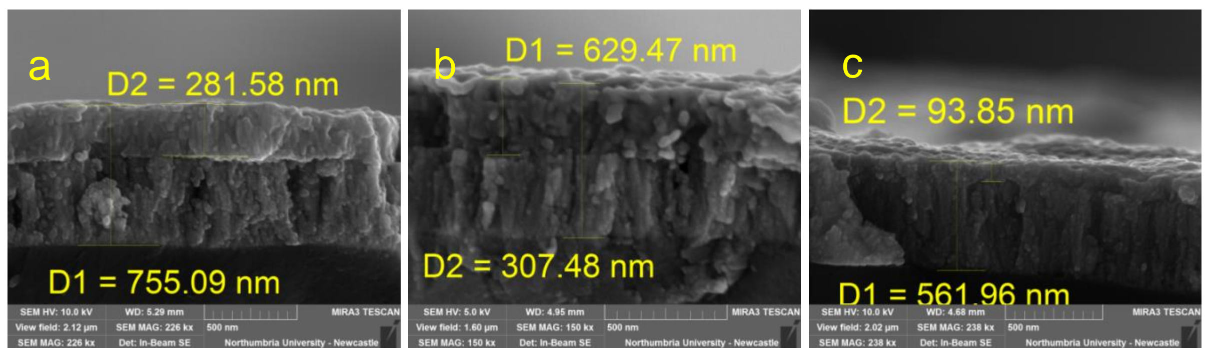

Fig 5-17 Cross section image of upper layer after two stages of heat treatment and dry heat stability test on $Mn_3Ag_{(1-X)}Cu_{(X)}N$ with X= (a) 0 (b) 0.6 and (c) 1

Table 5-6 compares the electrical performance results achieved when each process stage was run on separate chip resistor sample sets in an isolated fashion to when every process stage was performed sequentially on the same chip resistor sample sets. The table presents results for composition 7 (Mn_3CuN) samples (similar comparison for Mn_3AgN and $Mn_3Ag_{0.4}Cu_{0.6}N$ are presented in the appendix 2). The process run parameters experimented so far are the exact repetition of the industrial fabrication cycle (up to step 5) described in section 2.5. Therefore, sequentially running every process stage on the same thin film sample can be considered as a mock up for the real industrial fabrication cycle as well. The electrical performance results are highly comparable between both modes of process runs and this combined with least variation in morphology, as seen in side profile imaging, suggests that the Mn_3CuN material system has the potential to survive the industrial process run without much deviation from the prototype results achieved thus far.

Table 5-6 Table of electrical performance from process run in isolated mode and sequential mode on chips from composition 6.

Mn_3CuN	Process run type	As-grown	After Heat treatment	After stabilization treatment	After stability test
Rs (Ω/□)	Isolated	21.94	18.90	20.19	20.37
	Sequential	19.18	18.85	21.08	21.20
TCR (ppm/ºC)	Isolated	-351	-25	Not measured	Not
	Sequential	-327	-21	19	14
Stability (ΔR/R%)	Isolated	N/A			0.85
	Sequential				0.57

5.4 Summary

This chapter explored the possibility of further improving the performance of the Mn_3AgN antiperovskite structure by partially substituting it with Cu and proves that extremely low TCR values are possible with the ternary composition of $Mn_3Ag_{(1-X)}Cu_{(X)}N$. It also investigates the optimum heat treatment conditions required to attain the best possible electrical properties.

Six compositions of ternary films were developed by gradually increasing the Cu dopant factor X in $Mn_3Ag_{(1-X)}Cu_{(X)}N$ films. The as-grown electrical sheet resistance increases from 7.01 Ω/□ to 21.95Ω/□ with gradual increase of Cu in the film. For the same compositions, as-grown TCR values were found to become progressively more negative from -233 ppm/ºC, observed for 100% Ag films, to -351.5 ppm/ºC for 100% Cu films. As grown films were observed to have some degree of crystallinity. This was observed for the set of samples where all three targets were running in co-sputtering mode, which raised the temperature inside the chamber. Films with 100% Cu were seen to be amorphous in the as grown state. The sheet resistance of all the compositions showed a decrease in value when heat-treated up to 325ºC and thereafter started increasing sharply. This trend is observed to fit very well with that observed for the thickness of the upper oxide layer, which increases at a much faster rate above 325ºC. The upper layer being primarily

Manganese oxide is mainly responsible for the increase in the sheet resistance. The heat-treated TCR value also starts to move in a positive direction with increasing heat treatment temperature. Most of the compositions achieve a near zero TCR value after treatment at 325°C. The lowest average TCR value of -4.66 ppm/^{o}C is observed for $Mn_3Ag_{(0.4)}Cu_{(0.6)}N$ when heat treated at 350°C. Introduction of a secondary stage of heat treatment is realised to bring a considerable improvement in the stability figure for Mn_3CuN films. For films, which were not stabilization treated, a massive 11.32% change in electrical resistance was seen after 1 week of stability test. This figure reduced to just 0.8% after stabilization treatment of the films. No major changes were observed between the results when films were subjected to isolated process stages and when subjected sequentially to every process stage together. This upholds the suitability of Mn_3CuN material system for commercial application where the film will have to survive all of the fabrication process stages.

CHAPTER 6 Process Tuning and Commercial fabrication feasibility

6.1 Introduction

In chapter 4, the effect of substrate temperature and N_2 flow rate on Mn-AgN and Mn-CuN films were studied in order to achieve the lowest TCR value possible, and in chapter 5, an attempt was made to further reduce the low TCR value observed for Mn_3AgN by partially doping with Cu. Although, extremely low TCR values of -4.6 ppm/ºC were observed for the $Mn_3Ag_{0.4}Cu_{0.6}N$ composition, stability of this particular composition was not as good as that observed for Mn_3CuN. Therefore, Mn_3CuN films were selected to perform heat treatment optimization to identify conditions most suitable to preserve the best electrical properties.

In addition to substrate temperature explored in chapter 4, deposition pressure is observed to have a significant effect on electrical properties of thin films [153].These two factors form the key variable parameters of the structure zone model of thin films presented by J.A. Thornton in 1988, a well-established model in thin film grain development [154]. Figure 6-1 presents the schematic representation of the structure zone model by Thornton. The entire model is divided into four zones: Zone I, Zone T, Zone II and finally Zone III according to argon pressure (mtorr) and ratio of substrate temperature T to melting temperature Tm.

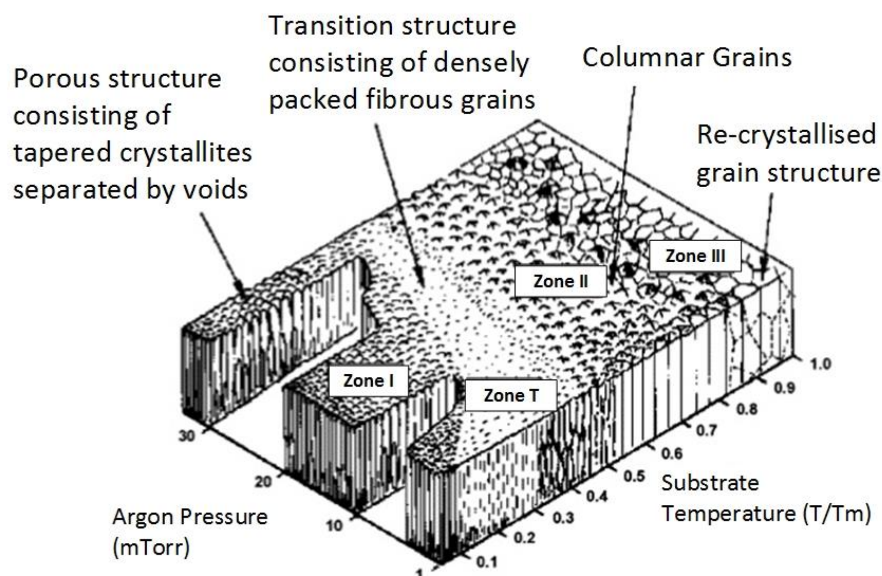

Fig 6-1 Schematic representation of the structure zone model by Thornton depicting four zones based upon temperature [155]

When species arrive at the substrate for deposition, they collate around surface irregularities like scratches, steps, dust/impurities, also known as nucleation sites. Zone I is observed for sputter deposition carried at low substrate temperature, when incoming species do not receive sufficient energy from the substrate to overcome the nucleation site. Because of preferential collation around the surface irregularities, films deposited in this zone of substrate temperature and pressure have a porous structure. Zone T is observed when the energy provided from the substrate temperature is sufficient to help incoming species to move away from these nucleation sites thereby form into a fibrous structure with well-defined boundaries. Zone II is observed for high substrate temperature depositions where energy from the substrate enables incoming species to diffuse into a columnar structure with dense boundaries. Finally, in Zone III, high temperature from the substrate causes bulk diffusion of the film, leading to grain growth and recrystallization [156].

While exploring the effects of substrate temperature, in-situ crystallization has been observed for samples deposited at high temperatures. However, other than this, no positive effects of substrate temperature were observed on the antiperovskite films. In chapter 4, N_2 flow rate was varied to study the material system, but at that time, the overall working pressure of system was kept constant at 3 μbar by changing the Ar flow rate accordingly. Work done by Lee et al. (1988) shows that the microstructure of TbFeCo films changes from smooth and featureless to having a high density of micro-voids with increasing sputtering pressure [157]. Similarly work done by Gunnarssan et al. (2016), observed that the shape of Titanium oxide nanocrystals change from spherical to cubical to "cauliflower like" with increase in pressure [158]. H Yuan and D.E. Laughlin (2010) based on their observations on Ru +TiO_2, the microstructure changed from percolated to granular with increasing working pressure [159].

Another important parameter related to heat treatment, not studied thus far, is the environment in which heat treatment is carried out. In chapter 4 the heat treatment temperature and duration was narrowed down to a range of 300 to 350ºC and 3 hours and in chapter 5 it was seen that a second stage of heat treatment improves

the stability figure of Mn_3CuN films significantly. Previously in section 5.2.2, it was seen that, while moving samples from the hot zone to the cold zone within the tube furnace, the Oxygen from the surrounding environment gets into the tube and comes into contact with the deposited films, which are at high temperature, thereby oxidising them. This could be the cause of the rapid increase in sheet resistance at heat treatment temperatures above 350^oC. Therefore, the question arises if the electrical performance parameters could be improved by isolating the samples from the external environment for the duration of heat treatment.

6.2 Experimental

The main objective of experiments performed in the further sections is to explore the scope of performance tuning possible for Mn_3CuN thin film resistive material, by varying the working pressure in the deposition chamber. Optimization of heat treatment conditions were performed by studying the electrical and physical characteristics of the Mn_3CuN samples heat-treated under environment having a varying amount of Oxygen content. This chapter then proceeds to investigate the effect of laser trimming, which is the next stage of TFR fabrication after stabilization heat treatment, on Mn_3CuN films. This will help to understand the suitability of this material system on an industrial fabrication scale.

6.2.1 Effect of varying working pressure

The depositions of Mn_3CuN films in chapter 4 and 5 were performed at a constant working pressure of 3 µbar. This was achieved by keeping total gas flow into the chamber at a constant value of 30 sccm. For the increase in N_2 flow rate from 2 to 6 sccm, the Argon flow rate was decreased from 30 to 24 sccm. And then it was observed that at an Argon to N_2 ratio of 25:5, the antiperovskite structure of Mn_3CuN could be realised. This translates to a partial Nitrogen pressure of 16.6%

Now the deposition pressure or working pressure is determined by the total amount of gas present in the chamber during deposition. In order to study the effect of deposition pressure on the electrical properties of Mn_3CuN films, three sets of

depositions were carried out as shown in table 6-1. The first sample set, TC 627 is deposited at 3 µbar, achieved by a total gas flow of 30 sccm as a reference point for the next data points. The maximum gas flow possible on the mass flow controller for Ar is 50 sccm. When a higher volume of gas is allowed in the chamber, the plasma plume is densely populated with Ar and N_2 ions, which present higher resistance to target species travelling towards substrate and allow more time for Nitrogen species to react. Therefore, lower Nitrogen partial pressure was found sufficient to maintain the chemical composition of the thin film. The highest working pressure of 5 µbar was realised by adjusting the Ar flow rate to 45 sccm and N_2 flow rate to 7 sccm giving a total gas flow of 52 sccm. It was not possible to strike and sustain plasma on the target for total gas flow below 15 sccm. Therefore, the lowest working pressure possible was 2 µbar, realised by 24 sccm of gas in the chamber (20 sccm of Ar and 4 sccm of N_2).

Table 6-1 Table showing Argon and N_2 flow rates for Mn_3CuN depositions at varying pressures.

Deposition No.	Ar flow (sccm)	N_2 flow (sccm)	Total gas (sccm)	Working pressure (µbar)	Partial N_2%	Time (minutes)
TC 637	20	4	24	2	16.6	90
TC 627	25	5	30	3	16.6	90
TC 635	45	7	52	5	14.0	90

6.2.2 Heat treatment optimisation

To obtain the best heat treatment environment, ternary samples were subjected to 4 cases of heat treatment combinations. The first stage of heat treatment was varied over two levels. The first case is the same as before, in which the seal of the tube furnace is broken after 3 hours at 325ºC, in order to move the samples to a rapid cooling zone. This introduced Oxygen into the tube while the samples were still at high temperature, thereby leading to a higher rate of oxidation. In the second case, samples were left to cool overnight in the flowing Nitrogen environment,

thereby minimizing the exposure to ambient Oxygen while at higher temperature. The tube furnace was set to start cooling down after 3 hours at 325ºC.

The second stage of heat treatment or stabilization heat treatment was also varied over two levels. For the first level, samples were stabilized in an open-air environment exposing samples to maximum Oxygen content in air for 16 hours at 260ºC. For the second level, samples were stabilized in a closed tube furnace with flowing Nitrogen to minimise the presence of Oxygen, at 260ºC for 16 hours. In total, this led to four sets of heat treatment condition as shown in table 6-2. Four separate sets consisting of 5 chip resistors from the Mn_3CuN sample set, were subjected to each of the four heat treatment conditions.

Table 6-2 Table of heat treatment conditions for ternary films.

TCR tuning heat treatment (325ºC for 3 hours)	Stabilization heat treatment (260ºC for 16 hours)	Case No.
Seal broken to rapidly cool samples in N_2	Stabilization in Open air	1
	Stabilization in sealed N_2 environment	2
Samples cooled overnight in flowing N_2	Stabilization in Open air	3
	Stabilization in sealed N_2 environment	4

6.2.3 Commercial fabrication cycle feasibility study

Deposition and heat treatment processes are among the most important fabrication stages for thin film resistors. Now from section 5.3.2, it is observed that Mn_3CuN films can pass through the combined effect of these process stages while maintaining a low TCR value of 14 ppm/ºC as well as a good stability value of 0.57%. However, as explained in section 1.6 and section 2.5, the next most important step, which bears foremost effect on electrical properties of thin film resistor, is the laser trimming process. In order to consider Mn_3CuN as a suitable candidate for the thin film resistor industry, its ability to maintain desirable electrical properties after laser trimming will have to be determined.

To study the effect of the entire process cycle, Mn_3CuN films were deposited on a standard industrial size 1206 substrate plate using university facilities and then processed on TT Electronics resistor fabrication line. 1206 substrate package has resistor circuits of 3 mm by 1.5 mm (0.012 inch by 0.006 inch) size, figure 6-2 (a) (detailed dimensions provided in the appendix 1). After deposition, the mask protecting the conductor pads was rinsed off using Alpha 2110, a cleaning concentrate intended for removal of resin mask from PCBs. The substrate plate was then heat-treated at 325ºC for 3 hours in a closed N_2 environment and later stabilized at 260ºC in open air for 16 hours. Resistor circuits on this plate were then laser trimmed in a serpentine pattern, using a LASERTEK TF3050 type green laser, as seen in figure 6-2(b). The laser trimming was performed to increase the resistance value of each circuit from an initial value of 35Ω to the required value of 3KΩ, with the laser parameters set to the specification as shown in table 6-3. Thereafter a secondary stabilization heat treatment was performed at 240ºC for 16 hours in air followed by a second stage of trimming. Sheet resistance and TCR were measured for 9 resistor circuits across the plate (as shown by red dots in figure 6-2 (a)), using the AEMIC AE-1155D and AE-162E, high speed resistance checker system from AEMIC corporation.

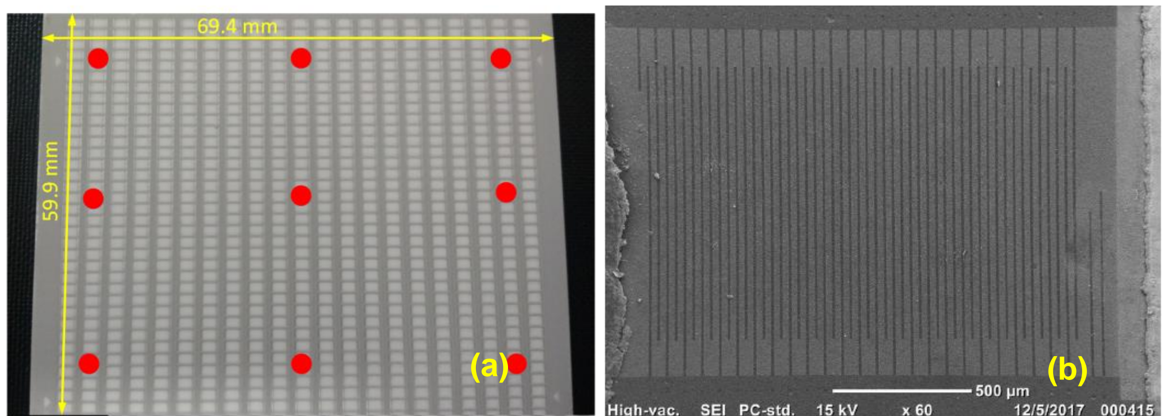

Fig 6-2 (a) Standard 1206 industrial package (b) standard serpentine trimming pattern on a single 1206 circuit.

Table 6-3 Table of Laser trimming specification for Mn_3CuN films on 1206 plate.

Trimming Parameters	Trimming Parameters	
	1st stage	**2nd stage**
PV (Pre trim value)	35R	35R
Final trim Value	3K	3K
Laser power	0.45W	0.45W
Max No. cuts	25	2
Spacing between (mm)	0.06 mm	0.06mm
Length of cut	85%	85%
First trim offset	-2%	-2%
Pulse Density (pulse/mm)	600	600
Speed (mm/sec)	60	60
Q- Rate	36	36

6.3 Result and discussion

6.3.1 Effect of varying working pressure

Chemical composition and thickness

As in previous chapters, film samples were analysed for composition using EDX at five different sites and then composition values were averaged. A section of glass substrates was covered with kapton tape during deposition and later five sites from this section were measured using the profilometer to determine the thickness of the deposited film. The averaged thickness and composition values of Mn:Cu:N for films deposited at three deposition pressures are as shown in table 6-4.

The average composition value for Mn:Cu:N for all the deposition pressures remained close to the required 60:20:20 at.% ratio. The composition of N_2 in the film was seen to vary across samples, which could be attributed to the adjustments in gas flows made to achieve the required varying working pressures. It was also noticed that the composition of Mn varies directly in relation to N_2 in the film.

Throughout the range, it was observed that the amount of Copper in the samples stays constant at 20%. Whereas, thickness appears to change without any correlation to working pressure. The lowest thickness of 437 nm is achieved for films grown at 3 µbar, followed by films deposited at 2 µbar (460nm) and then films deposited at 5 µbar at 498nm. Effect of working pressure on film thickness is not very clear as there are contradictory claims about increasing film thickness with increasing working pressure [160] and vice versa [161]. Nonetheless, both composition and thickness are within the comparable limits to the samples studied in the previous chapters, to carry forward the experiments planned in section 6.2

Table 6-4 Table of thickness and composition for Mn_3CuN films at varying pressures.

Sample No	Deposition pressure (µbar)	Composition	Atomic % of Mn:Cu:N	Film Thickness (nm)
1	2	Mn_3CuN	59:20:21	460
2	3	Mn_3CuN	58:20:22	437
3	5	Mn_3CuN	61:20:19	498

Electrical properties

Average electrical sheet resistance for 10 samples from each of the three batches deposited at varying deposition pressure is shown in figure 6-3. The sheet resistance of the Mn_3CuN films was observed to increase with increase in the deposition pressure. Films deposited at 2 µbar record the lowest as grown sheet resistance of 17.70 Ω/□, which increases to 18.48 Ω/□ when deposited at 3 µbar, while films deposited at 5 µbar show the highest as grown sheet resistance of 27.33 Ω/□. This increase in the sheet resistance for the same material system could be explained by the increased porosity of the films when deposited at higher deposition pressure. K.Eufinger et al (2006) observed a 5 to 25% increase in porosity of TiO_2 thin films, when the deposition Ar pressure was increased from 0.5 to 2.5 Pa [162]. This led to considerable change in photocatalytic activity of TiO_2 thin films. With decrease in working pressure, the sputtered particles experience less scattering on their travel towards the substrate, which results in increased energy of the particles when they reach the growing film at the substrate and leads

to densification of the film [163]. This porous nature of the film acts like a void hindering the transport of charge carrier and thereby increasing the electrical resistance.

The characteristic reduction in sheet resistance observed after the initial heat treatment stage because of defect healing and crystallization, is observed for the films deposited at lower deposition pressures of 2 and 3 μbar. The average sheet resistance values reduce to 16.42 Ω/□ and 17.47 Ω/□ respectively for 2 and 3 μbar. On the other hand, for films deposited at higher working pressure of 5 μbar only a few circuits show this reduction in sheet resistance, while most of the resistor circuits show an increase in their sheet resistance after the first stage of heat treatment, indicated by the large error bar, as seen in figure 6-3. The average sheet resistance value for this set of films increases to 27.36 Ω/□. This could again be associated to the porous nature of the films at higher deposition pressure. Annealing is known to cause densification of porous films [162]. Therefore, for the films which show a reduction in sheet resistance, it could be expected that densification caused by annealing helps the crystallization and defect healing effects to reduce sheet resistance. Whereas, it is logical for these effects to be ineffective in reducing sheet resistance, if densification from annealing is not strong enough to reduce porosity of the film sufficiently. Therefore, these two arguments could help us to infer that while films deposited at higher working pressure are porous in nature, the porosity is not uniform throughout the deposition area, at least not at the deposition pressure of 5 μbar. Progressing to the stabilization heat treatment stage, the characteristic increase in the sheet resistance indicative of oxidation of the top layer in open air, is clearly present for all the samples deposited. The closing value for the three samples stands at 21.83, 22.22, and 34.21 Ω/□ for films deposited at 2, 3 and 5 μbar respectively. Error bar for films deposited at 5 μbar remain far wider than films deposited at lower deposition pressures.

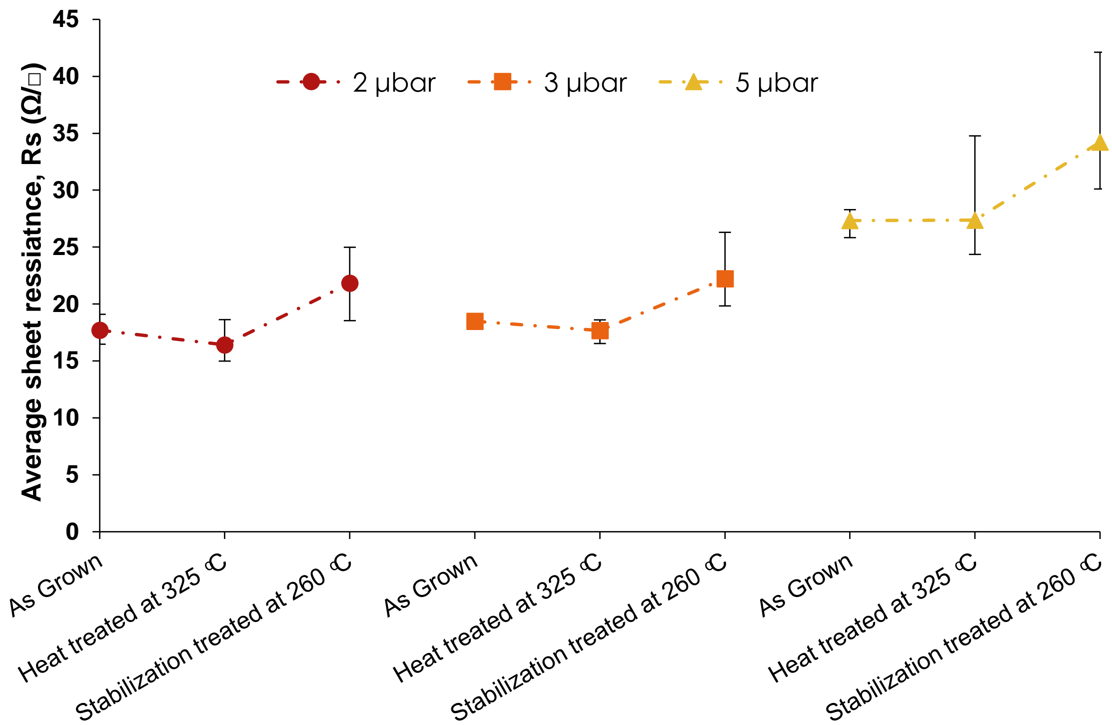

Fig 6-3 Graph showing variation in R_s of Mn_3CuN samples deposited under varying pressure, with heat treatment stages.

TCR values measured for 10 resistor circuits each from samples deposited at varying pressure is shown in figure 6-4 (a). TCR measurements were made as grown, after the heat treatment stage and after the stabilization heat treatment stage. The result for as grown TCR is observed to become more negative with increasing deposition pressure. The films deposited at 2 μbar register a TCR of -335 ppm/^{0}C with films deposited at 3 μbar registering a slightly more negative value of -340 ppm/^{0}C which becomes -378 ppm/^{0}C for films deposited at 5 μbar. Voids in the porous films are represented by increased barrier height, which confines charge carriers within grains and thereby increases the resistance of the films [164]. Therefore, it is reasonable to think that films deposited at higher pressure having porous structure will exhibit TCR values which are more negative. After each stage of heat treatment, TCR shifts in a positive direction. The films deposited at 2 μbar register an average TCR value of -6 ppm/^{0}C after the stabilization treatment stage. The shifts into the positive region become more pronounced with increasing deposition pressure. The films deposited at 3 μbar register a closing TCR value of 15 ppm/^{0}C while films deposited at 5 μbar close at 37 ppm/^{0}C. Inokuma at al. (1985) experimented with adding oxides of various transitional

metals together with RuO_2 to control the TCR value of in printed resistors and observed that oxides of most of the transition metals reduce or shift the TCR in the negative direction [165]. However, they observed that addition of Copper and Cobalt oxides shifted TCR in the positive direction. It could be inferred that the porous nature of films deposited at higher deposition pressure, exposed comparatively larger amounts of Cu within Mn_3CuN to oxidation during the heat treatment stages. Thereby increasing the content of Copper oxide within the film, which in turn aids the shift of TCR in the positive direction.

Figure 6-4 (b) shows the stability figure achieved for three samples of Mn_3CuN at different deposition pressure after the dry heat stability test for 1 week at 155ºC. The stability figure for the films deposited at higher deposition pressure of 5 μbar is observed to be worse compared to the films grown at lower deposition pressures of 2 and 3 μbar. The films deposited at 5 μbar had an average stability figure of 2.38% change in resistance over a course of 168 hours when kept at 155ºC. Samples among this set reported stability figures no better than 2.03% and no worse than 2.62%. However, for the same test the films deposited at 2 μbar registered an average figure of 0.74% with worst and best figures of 0.97 and 0.57% respectively. The films deposited at 3 μbar finished slightly higher at 0.76% average stability figure with worst and best values at 0.86 and 0.68% respectively. This trend is thought to be a result of the porous structure of films at higher temperature, making them more susceptible to impurity inclusion and higher degree of oxidation at higher temperature.

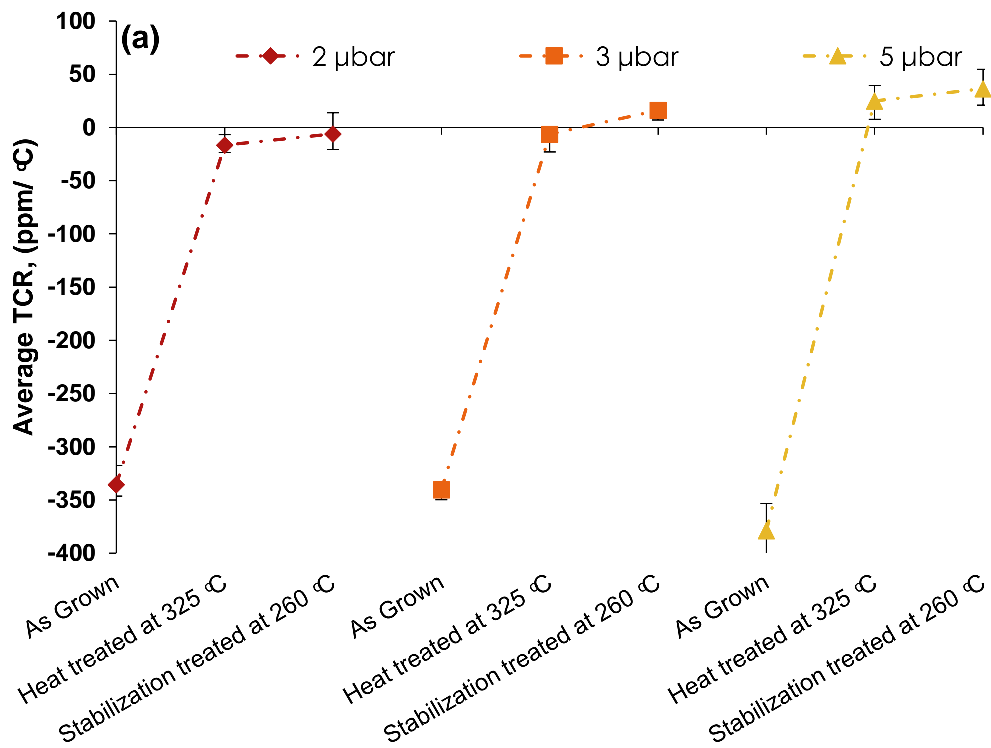

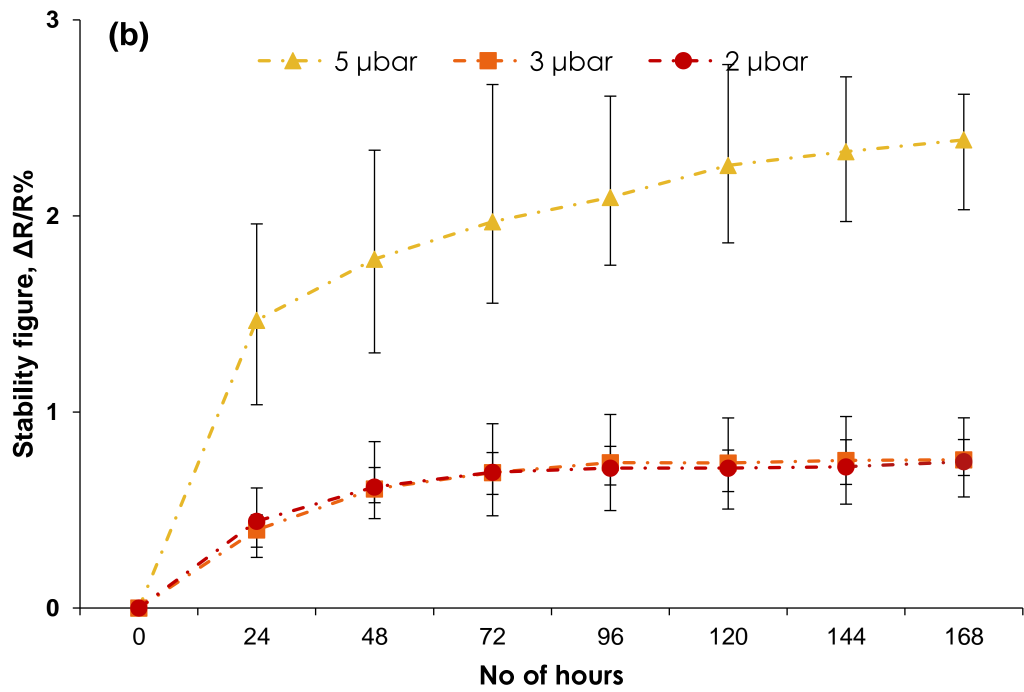

Fig 6-4 Graph for Mn_3CuN films deposited at varying pressure showing (a) TCR values (b) percentage change in resistance.

Structural and morphological analysis

XRD spectrum for Mn_3CuN samples at various stages of heat treatment can help to visualize the development of an oxide structure for films deposited at varying deposition pressure. Figure 6-5 (a) shows the XRD spectrum for Mn_3CuN films grown at three varying deposition pressures of 2, 3 and 5 μbar. There exists a sharp contrast between the films deposited varying deposition pressures. Films grown at lower deposition pressure of 2 and 3 μbar show a higher degree of crystallinity with preferential crystal orientation along the [200] plane with peaks at 46.66^{o} and 46.64^{o} respectively. There is a drastic reduction in peak intensity when deposition pressure increases from 2 to 3 μbar. While for films deposited at 5 μbar the peak completely disappears. Increased gap between the film features are known to decrease the intensity of the crystalline peaks during XRD analysis [166]. Therefore, it could be assumed that films deposited at 5 μbar, because of their porous nature, register a drastic decrease in their peak intensities. No additional peaks were observed for any of the deposition set.

Figure 6-5 (b) shows the XRD spectrum for the three sets of films after subjection to the initial heat treatment stage. For films deposited at higher pressure of 5 μbar, after initial heat treatment a small protrusion can be observed around the [200] central peak of the antiperovskite structure. This supports the idea that the antiperovskite structure was existing for these films in as-grown state as well, but because of higher porosity, peak intensity could not be detected. However, heat treatment of these samples results in grain growth and in turn densification of the film, leading to peak detection. For films at lower deposition pressure, intensity of the central peak increases, indicating growth of grain size, coupled with the appearance of peaks around 40.8^{o}, characteristic of Manganese oxides [152]. Appearance and intensities of the MnO peak remains comparable for all the films irrespective of deposition pressure. From previous chapters, it could be expected that upper layers of the as grown film react with Oxygen present and form Manganese oxide as an additional layer on top of the film. Crystallization and defect healing aids the sheet resistance reduction, while porosity and oxide formation increases sheet resistance, therefore, the sheet resistance value seen after the first stage of heat treatment is resultant of dominant effects. The crystal structure

of samples after the stabilization stage of heat treatment is shown in figure 6-5 (c). It can be again observed that the central peak at 46.64^o, representing the antiperovskite structure, sharpens further. The peak at 40.8^o also grows in intensity indicating more oxidation of the film when exposed to open air at high stabilizing temperature of 260°C. No other peaks are observed which could indicate degradation of the existing structure in any manner. Therefore, it is reasonable to say that the antiperovskite structure can maintain a stable crystal structure for process temperatures up to 325°C.

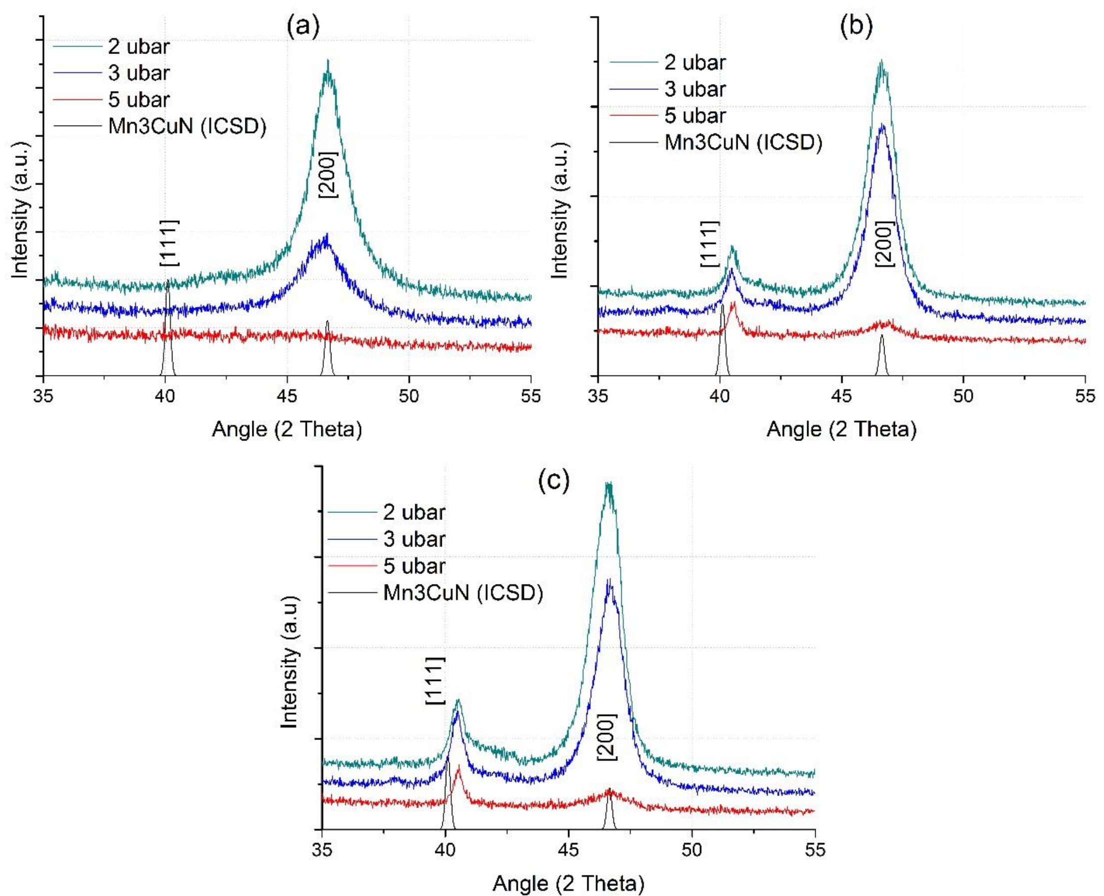

Fig 6-5 XRD spectrum for Mn_3CuN films deposited at varying pressures (a) as grown (b) heat treated at 325°C (c) stabilization treated at 260°C.

Table 6-5 presents the FWHM and corresponding grain size calculated for films grown at each deposition pressure after two stages of heat treatment. Films grown at 5 µbar don't have strong enough XRD peaks to calculate grain size. Films deposited at 3 µbar are calculated to have an average grain size of 12 nm and then is a clear increase of 7 nm for films deposited at the lowest deposition pressure of

2 μbar to 19nm. After the stabilization stage of heat treatment the final average grain size is calculated to be around 27.1 and 25.0 nm for films grown at 2 and 3 μbar respectively.

Table 6-5 Table of FWHM and crystallite grain size for Mn_3CuN samples deposited at varying pressure.

Deposition pressure (μbar)	Process stage	FWHM (º radians)	Mean Grain Size (nm)
2	As-Grown	0.031	19.431
	Heat treated at 325ºC	0.023	25.140
	Stabilization treated at 260ºC	0.025	27.527
3	As-Grown	0.046	12.475
	Heat treated at 325ºC	0.024	24.400
	Stabilization treated at 260ºC	0.025	25.082

These values can be confirmed by analyzing a topology image of the sample surface. Topology image taken from the SEM gives very clear visualization of the sample surface but the software lacks the capability to perform accurate grain size estimation. On the other hand, the AFM data could be easily resolved to find average grain size by using Gwyddion software (as seen in figure 6-6 (a)). The surface of only as grown samples deposited at 2, 3 and 5 μbar were mapped using the AFM tip and processed in Gwyddion 2.50.

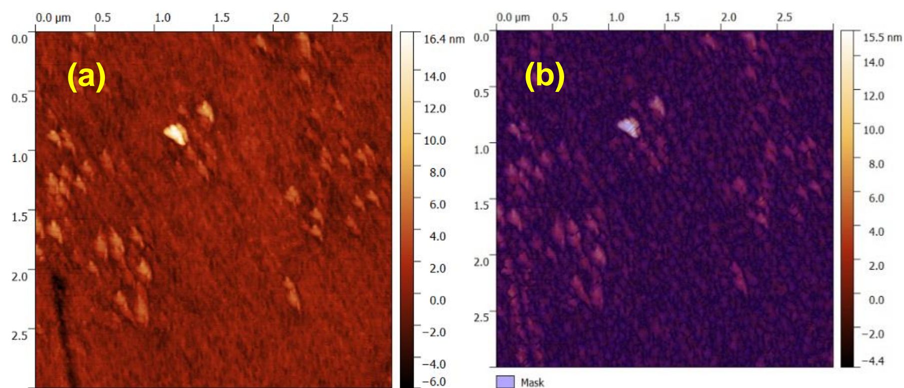

Fig 6-6 (a) Original AFM images of as grown Mn_3CuN films (b) Grain boundary mask generated by segmentation algorithm.

The grain boundaries were marked using a segmentation algorithm. By default, the algorithm maps the valleys in an AFM image and fully segments the pixels into motifs, which are grouped to match with underlying grains. The algorithm extends the capability to map the mask onto the real image by adjusting a Gaussian smoothing filter, gradient and curvature of the mask [167]. Then the inbuilt program measures the average area of the total number of grains detected in this way. The figures in 6-6 (a) and (b) show the match achieved between a real AFM image and a grain detection mask using the segmentation algorithm. Table 6-6 compares the average grain size achieved using Scherer's formula on XRD spectrum peaks and by using computational analysis of the segmented mask on the AFM image. It can be seen that both the tables are a very close match and therefore it could be reasonable to believe that the average grain size achieved by XRD on the heat treated samples are also reliable and accurate. With the best mask match possible, the 5 µbar sample grain size were measured to be 9.8nm, therefore it could be expected that realistic size will be still finer than 9.8nm. Heat treated samples would have their Ap grains covered by the upper oxide layer.

Table 6-6 Table comparing calculated crystallite grain size for as grown Mn_3CuN film using AFM and SEM technique.

Deposition pressure (µbar)	Process stage	Mean grain size (nm)	
		Using XRD	Using AFM
2	As-Grown	19.431	20.3
3	As-Grown	12.475	13.4
5	As-Grown	--	<9.8

The change in the surface topology of the films can be clearly seen in figure 6-7(a) to (i), by comparing the AFM images taken for films deposited at three sets of deposition pressure, as-grown and after each stage of heat treatment. Each AFM image is a square of 3 µm by 3 µm taken on the same glass substrate after each stage of heat treatment.

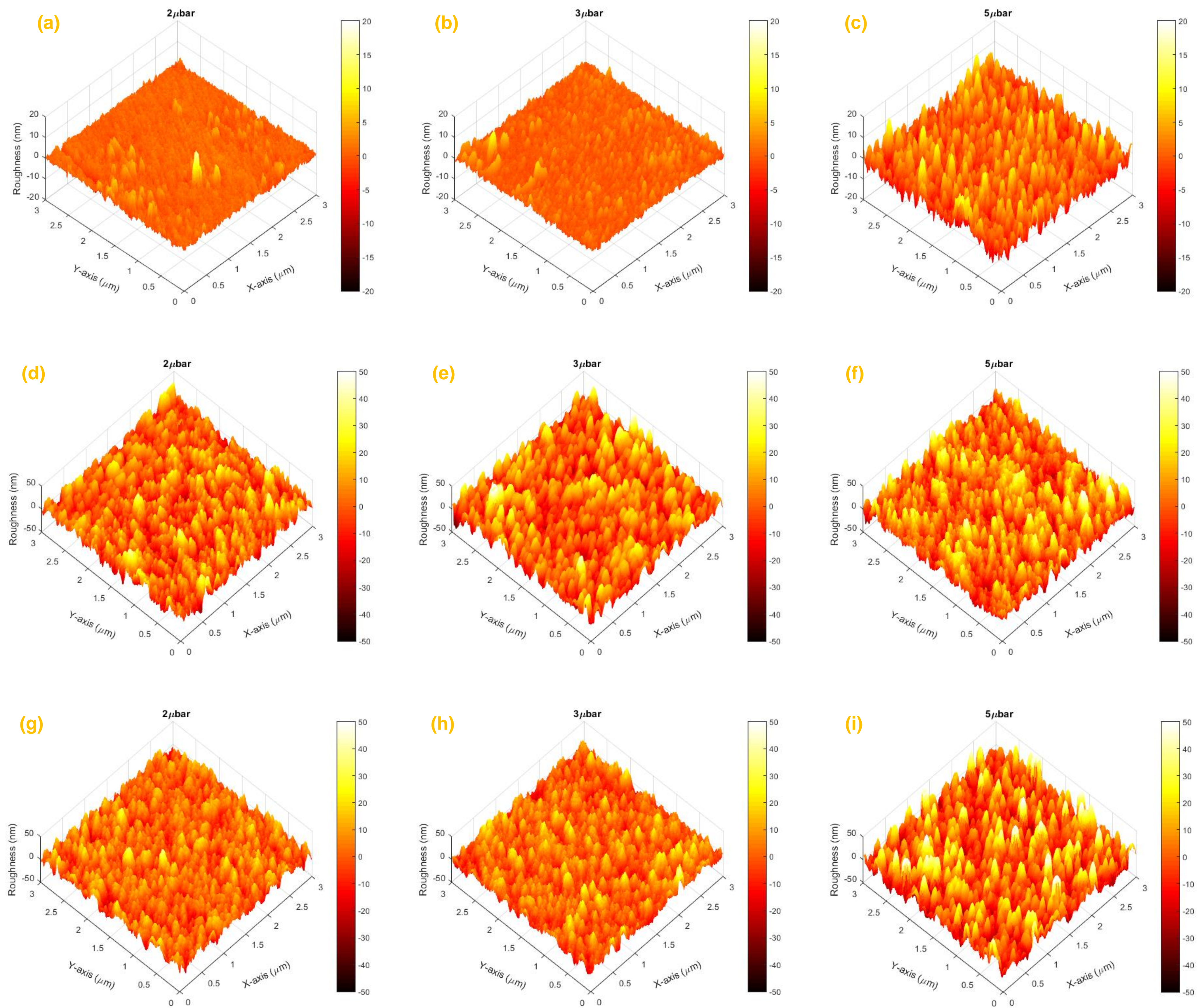

Fig 6-7 AFM image of Mn_3CuN films deposited at 2, 3 and 5 μbar respectively (a-c) as-grown (d-f) heat treated at 325ºC (g-i) stabilization treated at 260ºC.

The films deposited at 2 μbar are clearly much denser, and with increasing deposition pressure the film appears to get porous, showing very high crests and troughs for the films deposited at 5 μbar. This lends support to the effect of film porosity on electrical properties discussed above. From XRD spectrums and AFM grain size calculation, grains of films deposited at 5 μbar are expected to be below 9.8 nm in size. Therefore, the larger sized structures observed in figure 6-7 (c), are expected to be islands of 50-100 nm, formed by clustering together of smaller Mn_3CuN grains, which are still disjointed from the other similar islands nearby.

Heat treatment leads to formation of a rough layer on the top surface of films, which are known to be oxides of Manganese observed as a peak around 40.8^0 in the XRD spectrums in figure 6-5. Since the upper layer is of Manganese oxide, no attempts were made to measure the grain size of heat-treated film using AFM image to compare with XRD data. After the first stage of heat treatment, the surface look identical for all the three films. After the stabilization stage of heat treatment the topography becomes similar to the as grown film, with films deposited at 2 μbar having a more densely packed surface compared to films deposited at 5 μbar, which is again observed to be very porous. The porosity difference on the surface can be clearly seen in the AFM images; however, the formation of oxide layer hinders the observation of the underlying layer after heat treatment. The cross sections of the samples were analyzed using the SEM to observe the effect of deposition pressure on the layer formation after the stabilization treatment stage.

Cross sectional images of films deposited at varying deposition pressures are compared in figure 6-8 (a) to (c). The very first thing which can be observed is that, irrespective of deposition pressure, all the layer thicknesses are very similar for all three sets of films. After two stages of heat treatment, the final film thickness lies in the range of 503 to 512 nm for all of the films. Along with overall thickness, the thickness of the upper layer is also very much comparable, lying between 119 to 130 nm for all the deposition pressures. Therefore, it can be reasonable to say that the deposition pressure has no effect on the final thickness of the film. From previous chapters, starting composition and the following heat treatment conditions are known to have a major effect on this property of the film.

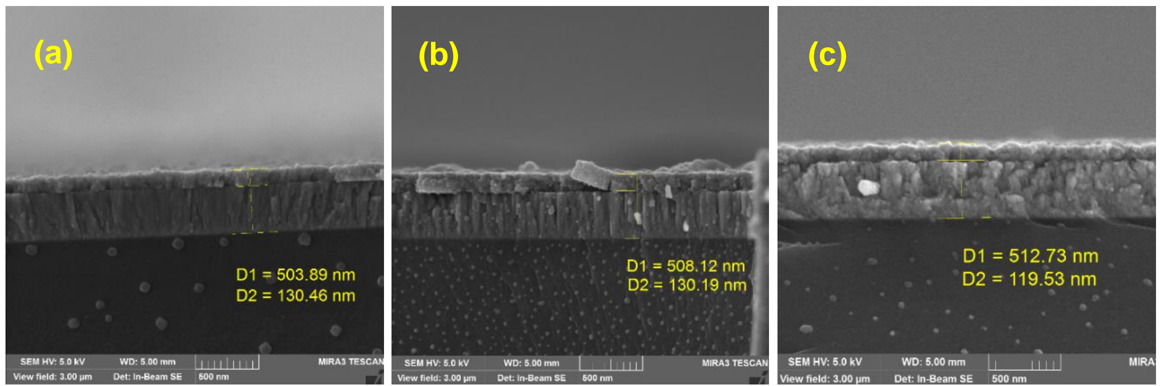

Fig 6-8 Cross section images of Mn_3CuN films (a)2 µbar (b)3 µbar and (c)5 µbar.

The existence of porosity can be visualized faintly in figure 6-8 (a) to (c). Films deposited at lower deposition pressure of 2 µbar are seen to be very densely packed that even the columns are not distinguishable, whereas for the films deposited at 3 µbar the column boundaries could be seen. The side profile image of films deposited at 5 µbar shows a deviation from a columnar structure with frequent gaps in between the individual islands. The higher porosity observed in as-grown film has decreased as the film undergoes densification during each of the two stages of heat treatment, but is still more visible compared to films at lower deposition pressures.

In order to analyze if varying deposition pressure brings any difference in the chemical composition of the final film, EDX analysis was carried out on cross sections of films grown at varying deposition pressure. Figures 6-9 shows the sites at which EDX analysis was carried out for films deposited at various pressure. An additional site, from the glass portion of the cross section was analyzed for each film to provide a reference. At this site, Si and O_2 were the main constituents, roughly in 2:1 atomic ratio, indicating SiO_2 along with traces of Na, Ca, and Mg as expected in soda lime glass. For each deposition pressure, two sites were measured from the antiperovskite layer while one site was measured from the upper layer. The EDX data from the analysis is presented in table 6-7.

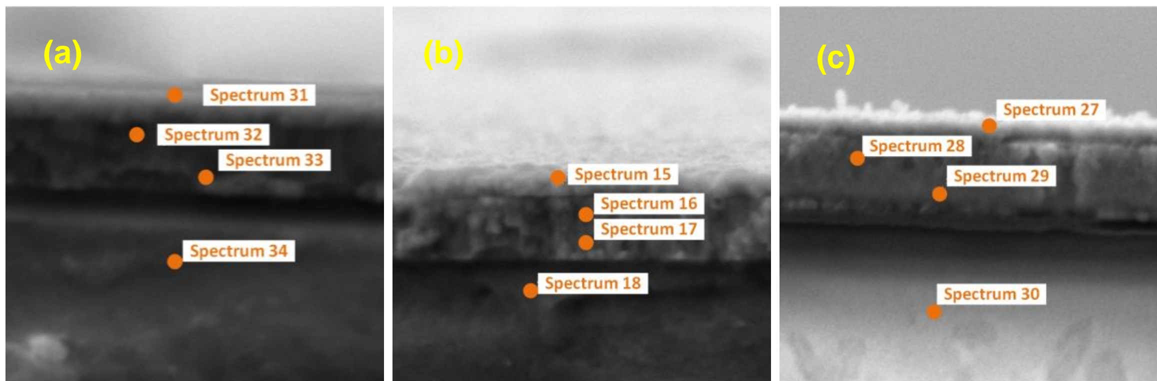

Fig 6-9 Cross section image of showing sites of EDX measurement for films deposited at (a) 2 µbar (b) 3 µbar (c) 5 µbar

A very clear trend visible in this table is the correlation between the content of Copper in the upper layer and the deposition pressure. For the films deposited at 2 µbar, no Copper is observed in the upper layer, which increases to 1.19 at% of Copper when deposited at 3 µbar. This figure increases steeply to a value of 20.74 at% for films deposited at 5 µbar. This steep rise could be a result of a porous structure at higher deposition pressure, which exposes the Copper to the Oxygen environment thereby forming Copper oxide. This observation ties in very well with the previously made estimation that the presence of Copper oxide might be responsible for shifting the TCR value in positive direction for the films deposited at higher pressure after heat treatment.

With the increasing porosity at higher deposition pressure, the protection provided by the upper layer also appears to be less effective, as more Oxygen content is found in the antiperovskite layer for films deposited at higher pressure. This definitely supports the fact that depositing antiperovskite at lower pressure is more beneficial, as it exposes less of the Copper to the surrounding environment keeping the positive migration in check. Moreover; the lesser the porosity of the film, the better is the protection offered to the underlying antiperovskite structure. Electrical properties could be enhanced for the antiperovskite structure by optimizing the deposition pressure.

Table 6-7 EDX analysis of films deposited at varying deposition pressure

Deposition pressure	Spectrum Label	N	O	Si	Mn	Cu	Total
2 µbar	Upper layer	--	54.6	--	45.4	--	100
	Antiperovskite layer	19.77	4.11	0.84	56.05	19.23	100
3 µbar	Upper layer	--	48.83	0.38	49.6	1.19	100
	Antiperovskite layer	17.09	8.29	--	53.01	21.62	100
5 µbar	Upper layer	--	48.71	1.87	28.68	20.74	100
	Antiperovskite layer	13.57	25.04	--	47.05	14.34	100

6.3.2 Heat treatment optimisation

It has been shown in section 5.3.2 that the layer found on top the film after heat treatment is primarily an oxide of Manganese and that its thickness is affected by the composition of the original film and heat treatment temperature. For the Mn_3CuN sample set, it was understood to act like a protective layer preventing the underlying layer from further attack from the Oxygen environment. So far, heat treatments were performed in a closed flowing N_2 environment for 3 hours, after which the seal of the tube was opened to move the samples to a cooling zone. Then stabilization treatment was performed in an open tube furnace for 16 hours. In order to optimise the heat treatment condition, four separate sets of 5 samples, each from composition no 6 (X= 1), were subjected to four cases of heat treatment conditions as shown in table 6-8. Breaking the seal to move the samples into the cooling zone lets in Oxygen rich air while the samples are still at high temperature; therefore, this heat treatment level is identified as Open HT. In the second case, samples were left to cool overnight in the same flowing N_2 condition, switching off the heater source after 3 hours, this heat treatment condition is identified as Closed HT. Similarly, for stabilization treatment, samples stabilized for 16 hours in open air are identified as Open ST and the ones stabilized in closed flowing N_2 are identified as Closed ST.

Table 6-8 Table of heat treatment optimization cases and case ID for each case.

TCR tuning heat treatment (HT)	**Stabilization heat treatment (ST)**	**Case ID**
Seal broken to rapidly cool samples (Open HT)	Stabilization in Open air (Open ST)	Case 1 (Open HT/Open ST)
	Stabilization in sealed N_2 environment (Closed ST)	Case2 (Open HT/Closed ST)
Samples cooled overnight in flowing N_2 (Closed HT)	Stabilization in Open air (Open ST)	Case3 (Closed HT/Open ST)
	Stabilization in sealed N_2 environment (Closed ST)	Case 4 (Closed HT/Closed ST)

Figure 6-10 shows the average sheet resistance of three samples sets after subjection to four heat treatment conditions. After the first stage of heat treatment, the sheet resistance values for samples which were left in closed N_2 conditions (Case 3 and Case 4) were observed to be lower (17.20 and 17.11 Ω/□ respectively) than those for samples which were heat treated in open HT condition (Case 1 and 2 at 18.85 and 19.24 Ω/□ respectively). Samples under open HT condition are exposed to ambient air, while still at higher temperature, when the seal is opened to move the samples to a cooler region; therefore, they are more prone to oxidization, which led to increase in their sheet resistance.

Similarly, samples which were stabilization treated in open air environment (Case 1 and 3) recorded higher increases from their heat treated sheet resistance values (21.08 and 20.19 Ω/□ respectively) than those stabilized in closed N_2 conditions (Case 2 and 4 at 19.53 and 17.43 Ω/□ respectively). These observations support that exposure to Oxygen leads to an increase in the sheet resistance value of the thin films. This is also observed when comparing the sheet resistance values of case 2 and 3, after stabilization treatment. Samples under case 2, after the first stage of heat treatment show higher sheet resistance than samples under case 3 (19.24 compared to 17.20 Ω/□), but when subjected to a prolonged duration under reversed conditions, samples under case 3 surpass the sheet resistance value of samples under case 2 (19.43 compared to 20.19 Ω/□).

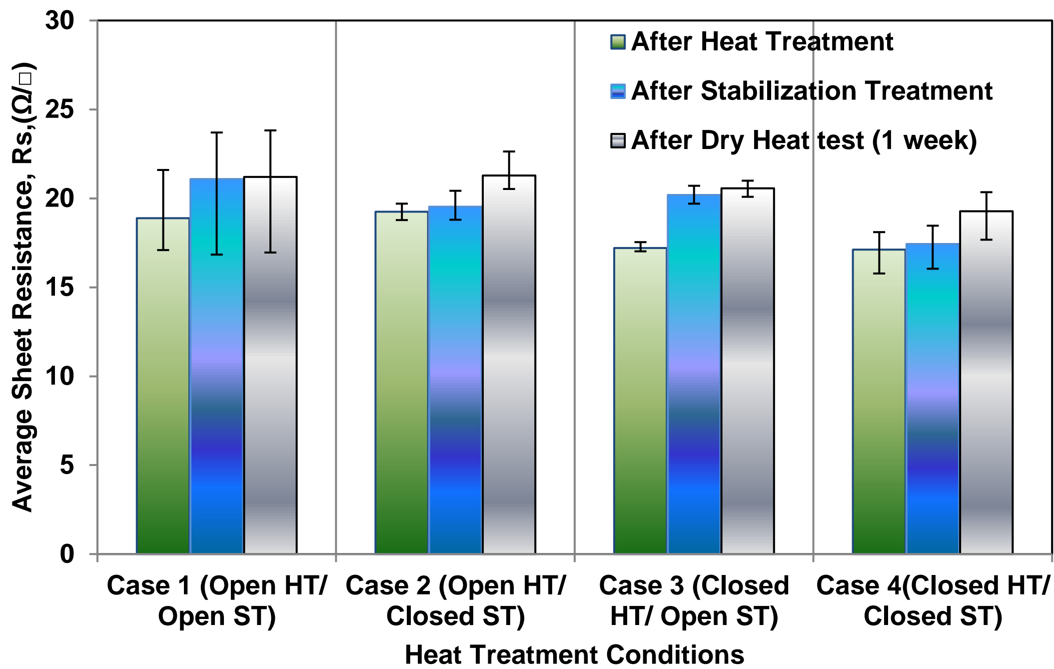

Fig 6-10 Bar chart of Rs values for four heat treatment cases.

However, after 1 week of dry heat stability test, the least change in sheet resistance value is observed for samples which had more frequent exposure to Oxygen. Samples under case 1, which encountered Oxygen during both the stages of heat treatment, only showed a minor increment from 21.08 Ω/□ to 21.20 Ω/□ after 1 week. Then comes the samples under case 3, which were not exposed to Oxygen during the first stage of heat treatment but stabilization treatment for this set of samples was also performed under open-air condition. The sheet resistance for this film increased from 20.19 to 20.56 Ω/□ after 1 week at 155°C. The set of samples for which stabilization treatment was performed in closed N_2 environment showed higher increase in sheet resistance value after the stability test. The sheet resistance value for samples under case 2 increase from 19.53 to 21.28 Ω/□ whereas for the samples under case 4 the sheet resistance value increased from 17.43 to 19.27 Ω/□.

The effect of heat treatment optimization conditions on the stability of these films can be better represented by plotting the percentage change in the sheet resistance after 1 week at 155°C, as seen in figure 6-11. The best stability figure of 0.57% is achieved for samples under case 1 followed by samples under case 3,

which registered an average 1.93% change in sheet resistance value after 1 week of stability test. The stability figure of 0.57% for an unprotected resistive film is much closer to standard manufacturing values of the thin film resistor industry. Samples under case 2 and case 4 showed 10.23 and 10.44% change in resistance value after 1 week, which are not suitable by a great margin for the thin film resistor industry.

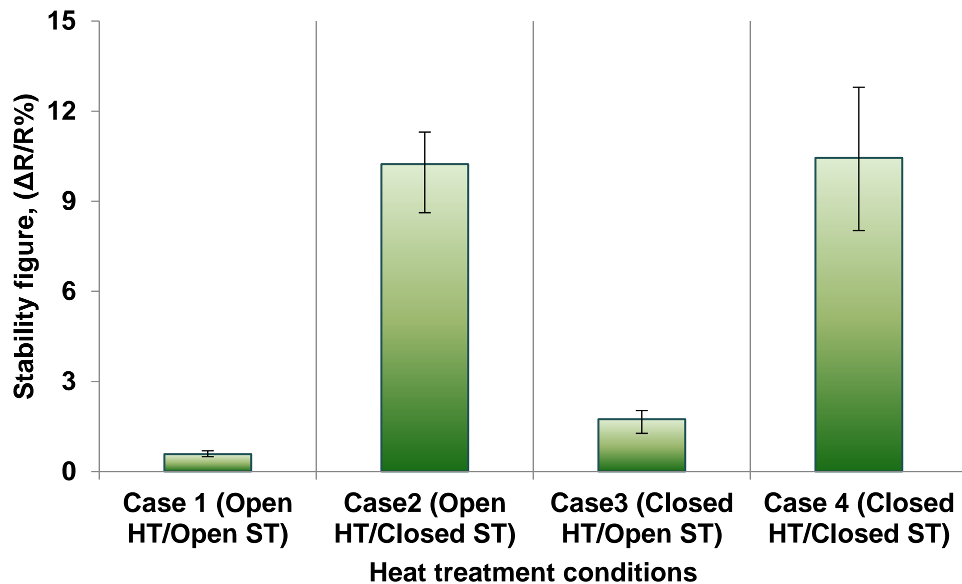

Fig 6-11 Bar chart of electrical stability value for four heat treatment cases.

Figure 6-12 shows the average TCR value measured for each sample case after each stage of heat treatment. The film with least exposure to Oxygen in case 4 reports a negative value of TCR even after stabilization heat treatment. Even though the average value of TCR is a negative figure of -13.3 ppm/^{0}C, samples under this case reported a large variation in the TCR value among the group creating a very wide error bar even reaching into the positive region of the graph. The most favorable value of TCR is seen for samples under case 2, which showed an average TCR value of 1.93 ppm/^{0}C. The majority of films in this group have a negative TCR under -5 ppm/^{0}C but because of one circuit with high TCR (11 ppm/^{0}C) the overall average rises up with a wide error bar. This is a very favorable result but when compared with figure 6-11, this set of samples are seen to have one of the worst stability figures. As the films in this set are not exposed to Oxygen

environment, the TCR value after stabilization treatment does not change much from its heat-treated value. However, when these films are exposed to the external environment, the electrical resistance value shifts by a great margin. For the next two sets of films, Case 1 and Case 3, the average TCR values recorded are +19.85 ppm/ºC and +13.07 ppm/ºC respectively. Both these sets of samples change from their heat-treated value by a good 40 ppm/ºC, which could be attributed to their exposure to the external environment. However, these sets of samples retain much better stability figures as seen in figure 6-11

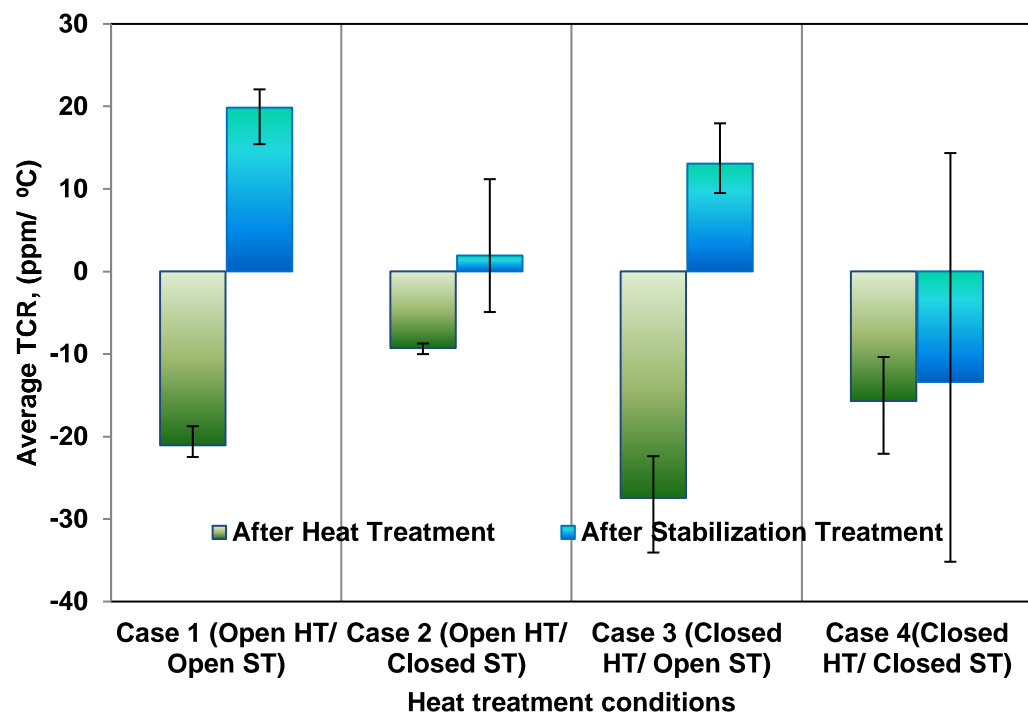

Fig 6-12 Bar chart of TCR values for four heat treatment cases

In order to analyze the effect of heat treatment optimization on the topology and chemical composition of the films, side profile imaging and EDX are performed on all the four sets of samples. Only alumina circuits were subjected to the varying heat treatment conditions hence results are based upon tests conducted on these substrates. Figure 6-13 shows the side profile images of Mn_3CuN after subjection to the four heat treatment conditions. The curvature observed for figure 6-13 (a) and (d) are from the alumina grain and film is just following the curvature of alumina grian. The overall thickness of the films remain similar between 523 to 563 nm.

However, the striking difference is that for samples under case 1 and 3, the upper oxide layer is seen to be thicker around 112- 114 nm whereas samples under case 2 and 4 are observed to have a thinner oxide layer of 73-75 nm. The stabilization stage is the common factor between these groups. Case 1 and 3 are stabilized in open-air environment whereas samples under case 2 and 4 were stabilized in closed flowing N_2 environment. From figures 6-11 and 6-12 similar trends could be seen for stability figures and TCR values as well. Therefore, by comparing these three data sets, it is possible to relate a thicker oxide layer with a positive TCR and better stability for case 1 and 3, which were stabilized for 16 hours in open-air environment. On the other hand, poor stability and negative TCR of samples treated under case 2 and 4 could be attributed to a thinner oxide flayer formed on the surface of these films, which offers less protection from outer environment.

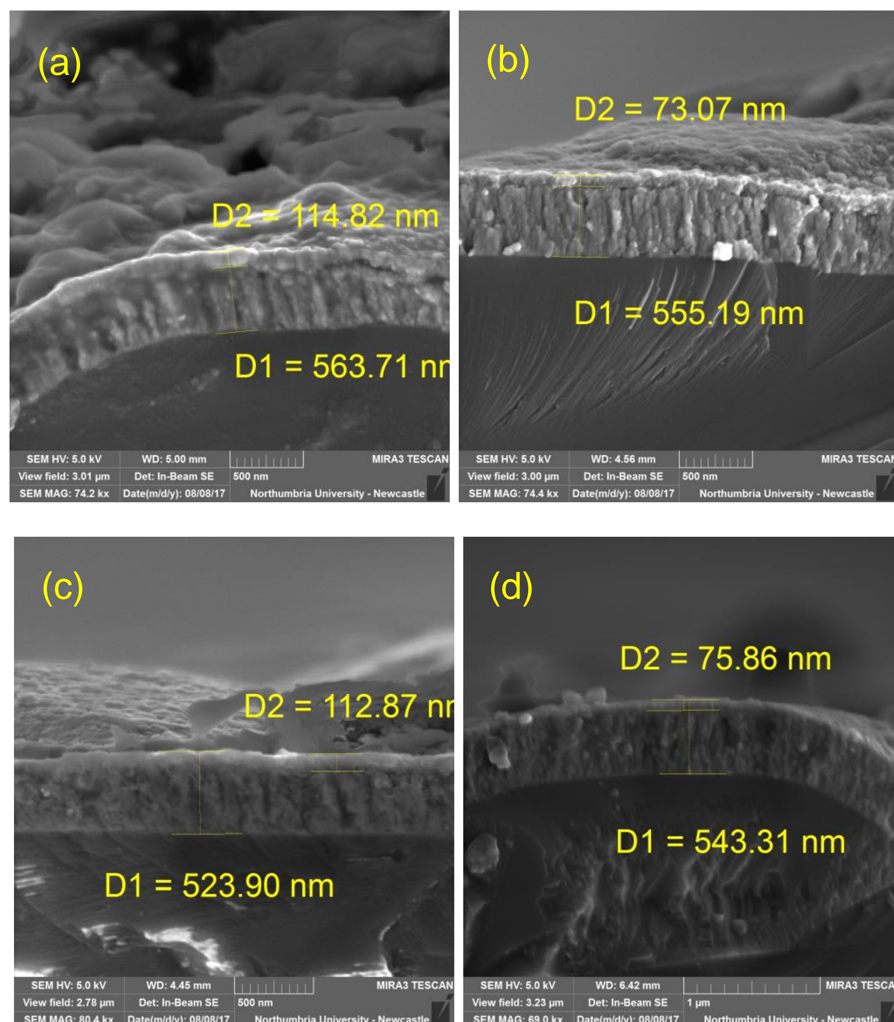

Fig 6-13 Cross section images of upper oxide layer on Mn_3CuN film after heat treatment under (a) Case 1 (b) Case 2 (c) Case 3 (c) Case 4.

Table 6-9 presents the chemical composition of the upper oxide layer under the four different heat treatment conditions. Samples under case 4 maintain the closest chemical composition to the original antiperovskite composition, even after the stabilization stage of heat treatment and are observed to have the lowest Oxygen content of the lot. Therefore, when subjected to 1 week of dry heat stability test, the upper layers of samples under this case are attacked more vigorously by the ambient Oxygen leading to a larger change in resistance value. Samples under case 2 have comparatively higher concentration of Oxygen but the improvement in the stability value for this set of samples is not evident. Whereas samples under case 1 and 4 appear to have reached saturation level for Oxygen in the upper layer, thereby, providing better protection for the underlying layer against attack from ambient Oxygen, hence the better stability. Therefore, it could be said that by choosing proper heat treatment environment for Mn_3CuN thin films, electrical properties of this material system could be fine-tuned to make it suitable for the thin film resistor industry. Still it needs to be seen if these properties would survive the fabrication process stages.

Table 6-9 Table of elemental composition for upper oxide layer for each heat treatment conditions.

Heat treatment condition	Atomic % elemental composition				
	Mn	Cu	N	O	Total
Case 1- Open HT - Open ST	39.71	1.95	0.7	57.64	100
Case 2- Open HT -Closed ST	44.19	3.31	1.84	50.67	100
Case 3- Closed HT -Open ST	40.27	2.07	0	57.66	100
Case 4- Closed HT -Closed ST	48.22	16.95	11.23	23.6	100

6.3.3 Commercial fabrication cycle feasibility study

As explained in section 6.2.3, 1206 alumina substrate plates deposited at the University facility with Mn_3CuN, were processed at TT electronics thin film resistor fabrication facility to check the repeatability of these properties in a real world fabrication scenario. The average sheet resistance value measured for nine resistor circuit across the 1206 plate is as shown in figure 6-14. Sheet resistance

value is presented after each process stage. As grown sheet resistance of 15.02Ω/□ only increases to 16.65 Ω/□ after the second stage of stabilization heat treatment, which is as expected because of increased contact with the Oxygen rich environment causing oxidation of the film surface. Laser trimming removes the resistive material from the substrate in a selective pattern, which presents hindrance to the existing current travelling path and forces it to take a longer route. This is manifested as an increased resistance value. For resistors with dimensions as in the 1206 plate, this final resistance value of 3 KΩ translates to a required final sheet resistance of 1500 Ω/□. After the first round of laser trimming, the sheet resistance value rises sharply to 1.39 kΩ/□. The laser trimming process is set to achieve a final resistance value of 3 KΩ. After another set of stabilization treatment and laser trimming this value increased to 1.47 kΩ/□, further closer to the required target. While the average value remains fairly constant after laser trimming, the error bars become quite wide indicating a large variation of the resistance values of the individually trimmed resistor circuits.

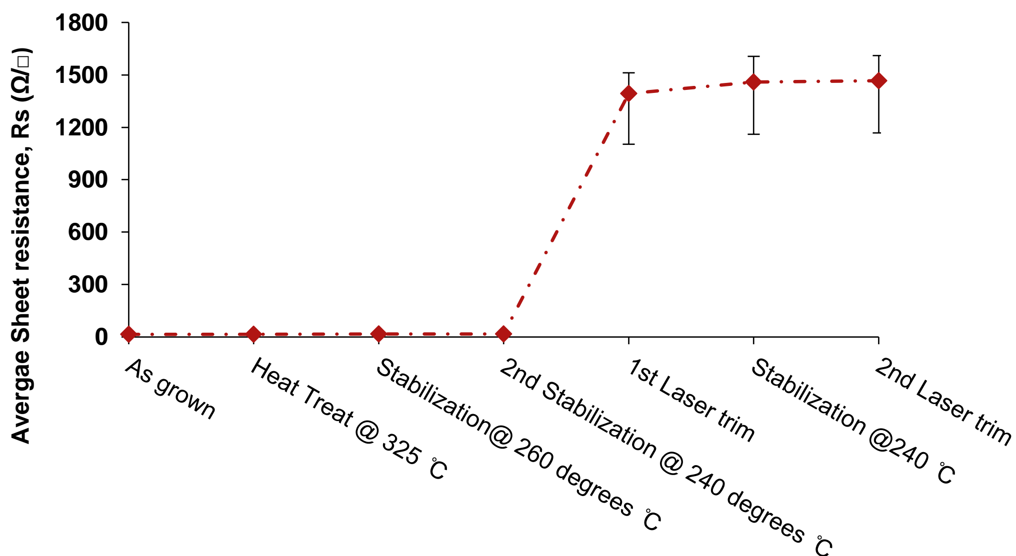

Fig 6-14 Graph of sheet resistance variation in 1206 samples at various fabrication process stage

The graph in figure 6-15, shows the variation in the average TCR value measured from 9 circuits across the 1206 plate after performing each key stage of fabrication. The average value of as grown TCR value is seen to be -355 ppm/^{0}C, which is in

line with those seen before for as grown Mn_3CuN films. This value rises steeply to a near zero TCR of -22 ppm/^oC after initial heat treatment and maintains this value after stabilization heat treatments. After the first laser trimming stage, there is a small dip in the TCR value to -39 ppm/^oC because of freshly exposed underlying layer of resistive layer after laser trimming. However, it is regained to -21 ppm/^oC after subsequent stabilization and improves to -19 ppm/ ^oC after second laser trimming. The flat nature of the TCR curve indicates the stability of TCR value for Mn_3CuN films when processed using the commercial fabrication process.

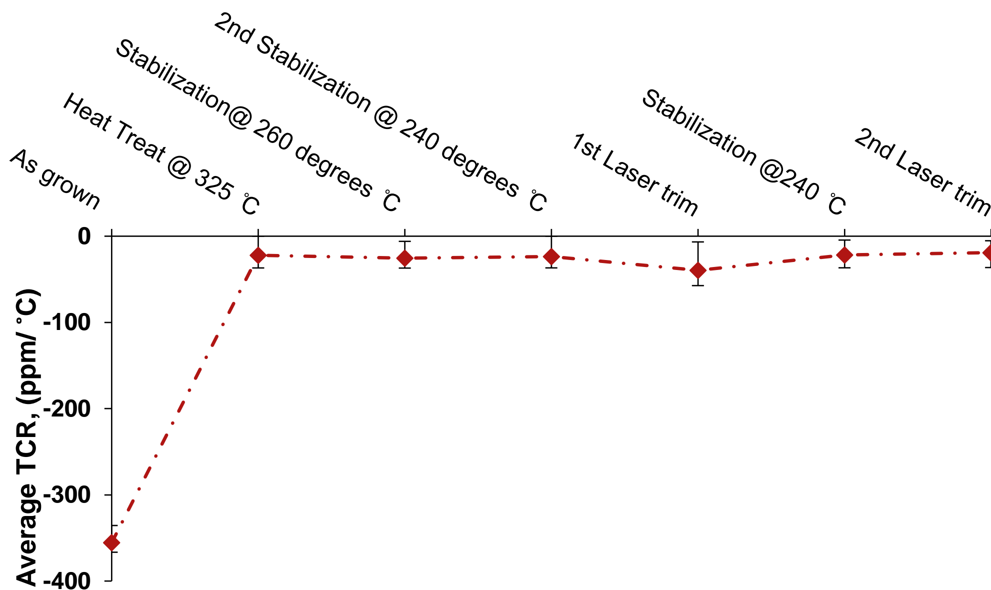

Fig 6-15 Graph of TCR variation in 1206 samples at various fabrication stages

The only fabrication process stage after second laser trim, which could affect the electrical properties of resistor material, is the encapsulation stage, indicated as step 9 in figure 2-7. This stage is known to preserve the stability figure of the films by coating them in a molten resin coating to protect them from the external environment. It was not possible to get clearance from TT Electronics facility, to coat the university developed prototypes with encapsulation, therefore the effect of the fabrication process could only be studied up to the stage before i.e. second laser trim stage. According to TT Electronics, encapsulation of the resistor film is performed at around 200^oC, which is well below the temperature at which stabilization heat treatment is performed (260^oC), therefore, will not bring change in the electrical properties of films. However, it would be worthy to perform

encapsulation in future to enhance the stability figure by protecting the resistive film from external elements.

6.4 Summary

Deposition pressure is noticed to have a pronounced effect on the morphological features of the Mn_3CuN thin films. Films deposited at higher deposition pressure of 5 μbar are observed to have higher degree of porosity, which leads to an increase in the sheet resistance and negative TCR values when compared to the films deposited at lower deposition pressure. Films deposited at lower deposition pressure of 2 μbar showed better stability figures around 0.75% compared to average stability figures of 2.38% for films deposited at higher deposition pressure. It is therefore recommended that the fabrication of thin film resistors be carried at lower deposition pressure to develop components with better stability figures.

From the heat treatment optimization run, it was observed that the most favorable electrical properties are sustained when heat treatment is performed in a controlled closed flowing N_2 environment, followed by a stabilization treatment in open air. The advantage of stabilization treatment in open air is that it helps in development of an upper oxide layer of sufficient thickness to offer protection to the underlying film from the surrounding environment and thereby improves the stability performance. The best electrical parameters thus far are a sheet resistance of 21.20 Ω/□ and TCR value of +19.85 ppm/^{o}C along with a stability figure of 0.57% achieved for Mn_3CuN films heat-treated in closed N_2 environment for 3 hours at 325°C followed by a stabilization heat treatment in open air for 16 hours at 260°C.

By running the Mn_3CuN films through commercial TFR fabrication process stages, it was seen that this material system is capable of maintaining the low TCR value of -19 ppm/^{o}C throughout all the process stages and therefore the Mn_3CuN could be readily incorporated into commercial fabrication cycle. Encapsulation stage was not performed for lack of clearance from company but as this stage is performed at temperature much lower than temperature at which films are stabilized this stage will not affect electrical properties.

CHAPTER 7 Conclusions and Recommendations for Future Work

7.1 Conclusions

This work has investigated in detail the suitability of Mn based antiperovskite as a potential material system for thin film resistor fabrication. Continuous research has been carried out to improve the electrical properties of existing TFR materials but very limited works explore the possibility of developing a novel material with inherent low TCR nature. A review of existing literature concluded that the family of Mn based antiperovskite structures exhibit many interesting properties and extremely low TCR is one among them. However, suitability of this material system for thin film resistor fabrication, in terms of its electrical stability and potential to survive the fabrication process stages had not been studied to date.

Initial trial runs confirmed the capability of university facilities to deposit and characterize Mn based antiperovskite material by simultaneously co-sputtering Mn, Ag and Cu targets. While Manganese in bulk is known to have positive TCR values, the results obtained from these initial samples confirmed that negative TCR as low as -67 ppm/^oC could be readily achieved on thin films of Mn deposited together with Cu/Ag in a reactive N_2 environment, and tuned closer to zero by subsequent heat treatment.

Next, the Mn_3AgN and Mn_3CuN antiperovskite structures were successfully realized by controlling the partial Nitrogen pressure within the chamber at 10 and 16.66% respectively. Both types of antiperovskite had very negative values for as-grown TCR, lying between -180 to -355 ppm/^oC. Though after 3 hours of heat treatment between 300 and 350^oC in flowing N_2, these values were tuned closer to the zero line at +47 ppm/^oC and +21 ppm/^oC for Mn_3AgN and Mn_3CuN respectively. The substrate temperature was also found to aid shifting of TCR in the positive direction. Nevertheless, it was not as effective as post deposition heat treatment, hence it was maintained at room temperature for all further experiments. Grain growth, defect healing, crystallization and growth of the upper oxide layer were found to be key factors affecting the development of electrical properties. However, one major concern with binary films was that they were found to have unacceptably

high values of stability when tested at 155°C for 1 week, faring no better than 11% for either of the two compositions.

By partial substitution of Cu in Mn_3AgN, ternary antiperovskite structures were realized and average TCR values as low as -4.6 ppm/^{o}C were successfully achieved for a composition of $Mn_3Ag_{(0.4)}Cu_{(0.6)}N$ when heat treated at 350°C. Though these ternary structures reported extremely low TCR values, stability figures could not be improved to a value better than 11%, even with additional stabilization in air. On the other hand for Mn_3CuN films, introduction of additional stabilization treatment in air was observed to significantly improve the stability figure from 11.3% to just 0.8%, while maintaining an average TCR value of 14ppm/^{o}C. It was noticed that during heat treatment, Manganese in the film has a tendency to migrate to the upper layer and create Manganese oxide, which offers a protection to underlying layers from further oxidation and stabilizes the electrical resistance value of the films.

Exploring the effect of deposition pressure on Mn_3CuN films, revealed that lower deposition pressure results in densely packed films, which yield better electrical properties in terms of lower TCR and better stability. The lowest average TCR value of -6 ppm/^{o}C was achieved for films deposited at 2 µbar, with a stability figure of 0.75%. By performing the initial treatment in N_2 and stabilization treatment in open air, the stability figure for Mn_3CuN films could be slightly improved to a value of 0.57%, but this offset the TCR value to +19 ppm/^{o}C. By subjecting the Mn_3CuN films deposited on 1206 plates, to an industrial fabrication process cycle it could be successfully verified that Mn_3CuN antiperovskite can survive the TFR fabrication cycle, while maintaining an appreciable TCR value of -19ppm/^{o}C.

Overall, the objectives set out for this project have been achieved and the study has been successful in its novel approach to investigate Mn based Antiperovskite structures as a candidate for the fabrication of thin film resistor components. Experiments and results from this work justify the findings of the literature review, that binary and ternary forms of $Mn_3Ag_{(x)}Cu_{(1-X)}N$ have TCR values extremely close

to zero. This is first time that the ternary composition of $Mn_3Ag_{(0.4)}Cu_{(0.6)}N$ in its thin film form has successfully demonstrated average TCR values lower than 5 ppm/ºC. While, the best compromise between TCR and stability was achieved for Mn_3CuN, with TCR values still below ± 20 ppm/ºC and stability values better than 0.6%. The thin films were also capable of withstanding the commercial fabrication cycle while maintaining these outstanding electrical properties. This work takes the very first step in developing thin film resistors using the antiperovskite material system and was successful in attracting the attention of a market leading international electronic component manufacturer to consider Mn based antiperovskites as an alternative for NiCr and TaN thin film resistor products.

7.2 Recommendations for future work

For the realisation of antiperovskite on a commercial TFR fabrication scale, its TCR value will need to be pushed closer to zero while improving the stability values even lower than 0.57%. This would require participation from the industry as well as academia, to pool in dedicated resources and intellect to develop this concept further into a commercially viable and environmentally sustainable product.

From the discussions made in previous chapters, it would be of interest to conduct further investigation to study the:

- Effect of replacing the transition metals

  In chapter 2, it was mentioned that there are many families of antiperovskite materials which exhibit extremely low TCR properties. Replacing all the three sites of the Mn_3AX structure, partially or entirely, could be experimented with other elements. Published work documents low TCR for compositions where Ni and Sn replaced Cu, or where Mn sites were replaced with Cobalt or Carbon replaced N_2 sites [54]. While many models exist for the low TCR nature of antiperovskite, it is of higher importance to develop further research work especially into theoretical calculations to explain the low TCR nature of antiperovskite nitrides.

- Effect of extended deposition parameter ranges

  As discussed in chapter 6, performing deposition at lower deposition pressure is expected to improve the electrical characteristics because of the higher density of films formed at these pressures. However, because of mass flow controller limitations and the design of the deposition plant used in this study, it was not possible to explore pressure ranges lower than 2 μbar. Similarly, elevated substrate temperature up to 130ºC was found to aid the shift of TCR in the positive direction. However, due to limitation of the heater element within the deposition chamber, temperature ranges above this value could not be explored further to see if as-grown TCR could be shifted close to zero without an additional heat treatment stage. Therefore, it will be worthy to explore the effects of lower deposition pressure and higher substrate temperature ranges on the structural and electrical properties of Mn based antiperovskite materials

- Sputtering from a composite target

  In this work, the magnetrons were loaded with individual targets of Mn, Ag or Cu to develop binary or ternary forms of Mn_3AgCuN, by controlling the power levels on each target and the amount of reactive Nitrogen in the chamber. Due to the time and funding constraints, this work could not explore the benefits of sputter depositing these thin film structures from a composite target made of stoichiometric composition of Mn:Ag/Cu:N. It is an area worthy of further investigation to attain better control over the chemical composition of the film, thereby keeping it constant within and across individual deposition cycles.

- Developing fully functional test resistors

  Mn_3CuN films researched in this work were tested on the industrial fabrication process only up to the second stage of laser trimming. However, the encapsulation stage, which occurs later in the process stage, coats the resistive film in a resin compound, providing protection from the external environment during stability tests. Therefore, it will be worthy to develop a fully functional batch of test resistors using the industry fabrication cycle and then perform the full set of commercial and environmental testing to further assess the suitability of Mn based antiperovskite nitrides for the thin film resistor industry.

References:

1. Marsten, J. (1962). "Resistors-A Survey of the Evolution of the Field." Proceedings of the IRE 920-924.
2. Zandman, F., P.-R. Simon and J. Szwarc (2001). Resistor theory and technology. New Jersey Scitech Publishing Inc.
3. Liu, X., G. J. Ma, G. Sun, Y. P. Duan and S. H. Liu (2011). "Effect of deposition and annealing temperature on mechanical properties of TaN film." Applied Surface Science 258(3): 1033-1037.
4. Malmros, A., K. Andersson and N. Rorsman (2012). "Combined TiN and TaN temperature compensated thin film resistors." Thin Solid Films 520(6): 2162-2165.
5. Khor, C. W., C. Leung and O. L. Neel (2012). Reliability Analysis of CrSi Thin Film Resistors. Physical and Failure Analysis of Integrated Circuits (IPFA). Singapore IEEE. 19th: 1 – 4
6. Park, K.-W., S.-G. Hur, J.-K. Ahn, N.-J. Seong and S.-G. Yoon (2010). "High resistivity thin film resistor grown using CrB2-Si-SiC materials by radio frequency magnetron sputtering." IEEE transactions on electron devices 57(No.6): 1475-1480.
7. Lane, C. H. (June 1973). Nichrome resistor properties and reliability. New York, Rome Air development center, Griffiss Air force base, New York.
8. Satrapinski, A. F., A. M. Savin, S. Novikov and O. M. Hahtela (2009). "NiCr Based Thin Film Cryo Resistors." IEEE TRANSACTIONS ON INSTRUMENTATION AND MEASUREMENT 58(4): 1206-1210.
9. Satrapinski, A. F., A. M. Savin, S. Novikov and O. M. Hahtela (2008). "Experimental study of Evanohm thin film resistors at subkelvin temperatures." Measurement Science and Technology 19(5): 1-5.
10. Danışman, M. and N. Cansever (2010). "Effect of Cr content on mechanical and electrical properties of Ni–Cr thin films." Journal of Alloys and Compounds 493(1-2): 649-653.
11. Lifei, L., Z. Wenjin, F. Xianzhu, S. Rong and D. Ruxu (2013). "Optimization of sputtering parameters for Ni–Cr alloy deposition on Copper foil as embedded thin film resistor." Surface and Coatings Technology 218: 80-86.
12. Lifei, L., Z. Wenjin, F. Xianzhu, S. Rong and D. Ruxu (2012). "Annealing effect on the electrical properties and microstructure of embedded Ni–Cr thin film resistor." Journal of Alloys and Compounds 538: 125-130.
13. Yong, K., K. Nam-Hoon, C. Gwang-Pyo, L. Woo-Sun, S. Yong-Jin and P. Jinseong (2005). "Structural and surface properties of NiCr thin films prepared by DC magnetron sputtering under variation of annealing conditions." Microelectronic Engineering 82(3-4): 314-320.
14. D.Nachrodt, U. Paschen, A. T. Have and H. Vogt (2008). "Ti/Ni(80%)Cr(20%) thin-film resistors with a nearly zero temperature coefficient of resistance for integration in standard CMOS process." IEEE ELECTRON DEVICE LETTERS VOL. 29(NO. 3): 212-214.
15. Seema, V., H. P.Vyas, K. Muraleedharan and V. D. Vankar (2006). "Ni–Cr thin film resistor fabrication for GaAs monolithic microwave integrated circuits." Thin Solid Films 514(1-2): 52-57.

16. Yan, J. W. and J. C. Zhou (2007). "Optimising of strain sensitivity and electric characteristics of Ni–Cr thin film fabricated by magnetron sputtering." Materials Science and Technology 23(2): 195-202.

17. Lai, L., R. Sun, X. Fu and R. Du (2012). Influence of segregation and diffusion behavior on electrical properties of embedded Ni- Cr thin film resistor. International Conference on Electronic Packaging Technology & High Density Packaging.

18. W. Briickner, J. S., S. Baunack, W. Pitschke, Th. Knuthb (1995). "Resistance behaviour and interdiffusion of layered CuNi-NiCr films." Thin Solid Films 258: 236-246.

19. Maissel, L. I. and R. Glang (1970). Handbook of thin film technology. United States of America, Mc-Graw Hill, Inc.

20. Sinclair, I. (2001). Passive Components for circuit design Oxford, Newnes An imprint of Butterworth-Heinemann.

21. Gorham, D. and J. Wood (1985). Electronic Materials and Devices - Block 1, Resistors, Resistivity and Wafers,. Milton Keynes, the Open University.

22. Precision thin film technology, VMN-PL0020-1008. Malvern, PA 19355, United States, Vishay Intertechnology, Inc.

23. Major Advancements in the Protection of Thin Film Nichrome-Based Resistors with Specialized Passivation Methods (SPM). Technical Note by Vishay Thin Film. 25-Feb-2008.

24. Drift Calculation for Thin Film Resistors, . Technical Note by VISHAY INTERTECHNOLOGY, INC. 12 april 2013.

25. Collins, F. M., W. A. Anderson and E. M. Ma (1999). "Thin film resistors - historical development." Wiley Encyclopedia of Electrical and Electronics Engineering. : 125-133.

26. Precision Thin Film Chip Resistor PFC series, (2017). Technical note by TT Electronics PLC. 05 2013.

27. Elshabini-Riad, A. and F. D.Barlow (1998). Thin film technology handbook. United states of America, McGraw Hill

28. B.K.Jones and G. P. Zhigal'skii (2003). The physical properties of thin metal films. London, Taylor and Francis.

29. Wu, F., A. W. McLaurin, K. E. Henson, D. G. Managhan and S. L. Thomasson (1998). "The effects of the process parameters on the electrical and microstructure characteristics of the CrSi thin resistor ®lms: part I." Thin Solid Films 332: 418-422.

30. Application and Design of thin film resistors. Document no. 61083, 01-Dec 2004. Technical note by Vishay Electro films, France

31. Bluhm, T. (30 October 2013). Application Note: Using Laser trimmable resistors. Document no: 28893. Vishay Beyschlag.

32. Birkett, M. and R. Penlington (2012). "Laser Trimming of CuAlMo Thin-Film Resistors: Effect of Laser Processing Parameters." Journal of Electronic Materials 41(8): 2169-2177.

33. TNPW-Thin film resistor. Application note by Vishay Intertechnology, Inc.

34. Birkett, M. (2009). Optimisation of the performance characteristics of Cu-Al-Mo thin film resistors. Doctor of Philosophy, University of Northumbria

35. Diletti, H., J. R.Noser and G. J. Sele (1985). "Polyimide Protection of Thin Film Chip Resistors." Microelectronics International 2(4): 28-31.

36. THIN FILM CIRCUITS -Fixed resistors Application Note, Issue 2. TT Electronics

37. H. Khajezadeh and A. S. Rose (1975). Reliability evaluation of hermetic integrated circuit. Reliability Physics Symposium, Las Vegas, NV, USA, USA, IEEE.

38. Fisher, J. S. and P. M. Hall (1971). "Termination Materials for Thin FilmR esistors." PROCEEDINGS OF THE IEEE 59(10): 1468-1473.

39. Cole, M., L. Hedlund, G. Hutt, T. Kiraly, L. Klein, S. Nickel, P. Singh and T. Tofil (2010). Harsh environement impact on resistor reliability. SMTA International, Hopewell Junction, NY, IBM Corporation.

40. Seung-Kyu, L., N. Seong-Hun, P. Eun-Mi, K. Jin-Soo and S. Su-Jeong (2012). "Electrical and structural properties of a Co-sputtered SiO2-Pt composite thin film for an embedded resistor." Journal of the Korean Physical Society 61(7): 1056-1059.

41. Duy, C. N., K. Dong-Jin, K. Byoung-Don, K. C. Soo and Y. Soon-Gil (2007). "Characterizations of high resistivity TiNxOy thin films for applications in thin film resistors." Microelectronics Reliability 47(4-5): 752-754.

42. Yamadera, H. (2008). "Granular Films for Use as Thin-Film Resistors." Journal of Electronic Materials 37(7): 1020-1023.

43. Kwon, S.-H., S.-W. Kang and K.-H. Kim (2008). "Controlling the temperature coefficient of resistance and resistivity in RuO2–TiO2 thin films by the intermixing ratios between RuO2and TiO2." Applied Physics Letters 92(18): 181903.

44. In-Soo, P., P. Se-Young, J. Geun-Hee, N. Suok-Min and S. Su-Jeong (2008). "Fabrication of Ta3N5–Ag nanocomposite thin films with high resistivity and near-zero temperature coefficient of resistance." Thin Solid Films 516(16): 5409-5413.

45. NOVENTIN®Data sheets // Isabellenhütte Heusler GmbH & Co. KG, 01 April 2016.

46. MANGANIN® // 7Data sheets // Isabellenhütte Heusler GMBH & co. KG, 29 March 2014.

47. ZERANIN® 30 // 7Data sheets //. Isabellenhütte Heusler GmbH & Co. KG., 29 March 2014.

48. V.J.Hammond, D.R.Gray and G.V.Planer (1968). "New thin film cermet resistor." Microelectronics and reliability 7(4): 287.

49. Olumekor, L. and J. Benyon (1977). "Reliability of pure Mn and Mn/MgF2 cermet thin film resistors. ." Thin Solid Films 44: 2.

50. Shivprasad, S. M., M.A.Angadi and L.A.Udachan (1980). "Temperature coefficient of resistance of thin Manganese film" Thin Solid Films 71: L1-L4.

51. Angadi, M. A. and S. M. Shivprasad (1984). "A new material for fabrication of thin film resistor " Journal of material science letters 3(8): 739-742.

52. Ammar, A. H. (1996). "Electrical transport properties of Manganese thin films." ELSEVIER Physica B 225: 132 136.

53. Misti, S.N., et al., *Effect of Abrasive Machining on the Electrical Properties Cu86Mn12Ni(2) Alloy Shunts.* Materials (Basel), 2017. **10**(8).

54. Peng, T., W. Bo-Sen and S. Yu-Ping (2013). "Mn-based antiperovskite functional materials: Review of research." Chinese Physics B 22(6): 067501.

55. Goldschmidt, V. M. (1926). "Die Gesetze der Krystallochemie." Naturwissenschaften 14(21): 477-485.

56. Johnsson, M. and P. Lemmens (2008). "Perovskites and thin films-crystallography and chemistry." J Phys Condens Matter 20(26): 264001.

57. Roth, R. S. (1957). "Classification of Perovskite and Other AB03-Type Compounds." Journal of Research of the National Bureau of Standards 58(2): 75-89.

58. Bilal, M., S. Jalali-Asadabadi, A. Rashid and A. Iftikhar (2015). "Electronic Properties of Antiperovskite Materials from State-of-the-Art Density Functional Theory." Journal of Chemistry 2015: 1-11.

59. Petrović, M., V. Chellappan, and S. Ramakrishna, *Perovskites: Solar cells & engineering applications – materials and device developments.* Solar Energy, 2015. **122**: p. 678-699.

60. Zuo, C., et al., *Advances in Perovskite Solar Cells.* Adv Sci (Weinh), 2016. **3**(7): p. 1500324.

61. Ball, J., et al., *The New Solar System*. March 2017, Stanford's Steyer-Taylor Center: Stanford.

62. Morral, F. R. (1934). "The constitution of iron rich Fe-Al-C alloys." Journal Iron and Steel institute London 130 419-430.

63. Wang, C., K. Takenaka, L. Li and Y. Sun (2013). "Lattice and Magnetic and Electronic Transport Properties in Antiperovskite M3AX Compounds." Advances in Condensed Matter Physics." 2013.

64. He, T., O. Huang, A. P. Ramirez, Y. Wang, K. A. Regan, N. Rogado, M. A. Hayward, M. K. Haas, J. S. Slusky, K. Inumara, H. W. Zandbergen, N. P. Ong and R. J. Cava (2001). "Superconductivity in the non-oxide perovskite MgCNi3." Nature 411(6833): 54-56.

65. Bing, H., D. Cheng, Y. Lihong, C. Xiaochao, G. Linhui, M. Libin and S. Youguo (2013). "CuNNi3: a new nitride superconductor with antiperovskite structure." Superconductor Science and Technology 26(12): 125015.

66. Wu, S. Q., Z. F. Hou and Z. Z. Zhu (2009). "Elastic properties and electronic structures of CdCNi3: A comparative study with MgCNi3." Solid State Sciences 11(1): 251-258.

67. Olabi, A. G. and A. Grunwald (2008). "Design and application of magnetostrictive materials." Materials & Design 29(2): 469-483.

68. Shibayama, T. and K. Takenaka (2011). "Giant magnetostriction in antiperovskite Mn3CuN." Journal of Applied Physics 109(7): 07A928.

69. Shimizu, T., T. Shibayama, K. Asano and K. Takenaka (2012). "Giant magnetostriction in tetragonally distorted antiperovskite Manganese nitrides." Journal of Applied Physics 111(7): 07A903.

70. Gómez, J. R., R. F. Garcia, A. D. M. Catoira and M. R. Gómez (2013). "Magnetocaloric effect: A review of the thermodynamic cycles in magnetic refrigeration." Renewable and Sustainable Energy Reviews 17: 74-82.

71. Ming-Hui, Y., L. H. Lewis and A. R. Moodenbaugh (2003). "Large magnetic entropy change in the metallic antiperovskite Mn[sub 3]GaC." Journal of Applied Physics 93(12): 10128.

72. Lin, S., B. S. Wang, J. C. Lin, L. Zhang, X. B. Hu, Y. N. Huang, W. J. Lu, B. C. Zhao, P. Tong, W. H. Song and Y. P. Sun (2011). "Composition dependent-magnetocaloric effect and low room-temperature coefficient of resistivity study of iron-based antiperovskite compounds Sn1−xGaxCFe3 ($0 \le x \le 1.0$)." Applied Physics Letters 99(17): 172503.

73. Evans, J. S. O. (1999). "Negative thermal expansion materials." The Royal Society of Chemistry: 3317–3326.

74. Takenaka, K. and H. Takagi (2005). "Giant negative thermal expansion in Ge-doped anti-perovskite Manganese nitrides." Applied Physics Letters 87(26): 261902.

75. Hamada, T. and K. Takenaka (2011). "Giant negative thermal expansion in antiperovskite Manganese nitrides." Journal of Applied Physics 109(7): 07E309.

76. Moritomo, Y., A. Asamitsu, H. Kuwahara and Y. Tokura (1996). "Giant magnetoresistance of Manganese oxides with a layered perovskite structure." Nature 380(6570): 141-144.

77. Shirai, M., Y. Ohata, N. Suzuki and K. Motizuki (1993). Electronic Structure and Ferromagnetic-Antiferromagnetic Transition in Cubic Perovskite-type Compound Mn3GaC. 9th intl conf. Ternary and multinary compounds, , Yokohama, Japan, Jpn. J. Appl. Phys.

78. Wang, B. S., C. C. Li, J. C. Lin, S. Lin, P. Tong, X. B. Zhu, B. C. Zhao, W. J. Lu, Z. R. Yang, W. H. Song, J. M. Dai and Y. P. Sun (2010). "Metastability across the antiferromagnetic-ferromagnetic intermediate phase transition and enhanced giant magnetoresistance in Zn-doped antiperovskite compounds Ga[sub 1−x]Zn[sub x]CMn[sub 3]." Applied Physics Letters 97(14): 142505.

79. Takenaka, K., A. Ozawa, T. Shibayama, N. Kaneko, T. Oe and C. Urano (2011). "Extremely low temperature coefficient of resistance in antiperovskite Mn3Ag[1−x]Cu [x]N." Applied Physics Letters 98(2): 022103.

80. E.O.Chi, W.S.Kim and N.H.Hur (2001). "nearly zero temperature coefficient of resistiivty in antiperovskite compound CuNMn3." Solid state communication 120: 307-310.

81. Ying, S., G. Yanfeng, L. Jun, W. Cong, W. Xia, S. Clastin and Y. Kazunari (2014). "The Unusual Resistivity Behavior and Correlated Magnetic Properties of Antiperovskite Mn3Ag[1−x]M[x]N (M = Sn, Zn) Compounds." Science of Advanced Materials 6(7): 1394-1398.

82. Ying, S., W. Cong, N. Yuanyuan, C. Lihua, W. Yongchun and N. Man (2010). "Investigation of antiperovskite Mn3CuNx film prepared by DC reactive magnetron sputtering." Materials Research Bulletin 45(9): 1230-1233.

83. Yuanyuan, N., W. Cong, S. Ying, C. Lihua, N. Man, J. Nian and W. Jian-ping (2011). "Structure and properties of ternary Manganese nitride Mn3CuNy thin films fabricated by facing target magnetron sputtering." Materials Research Bulletin 46(7): 1022-1027.

84. Masahiro, A., T. Koshi and I. Hiroshi (2013). "Sputter deposition and characterization of Mn3CuN thin films." Journal of Alloys and Compounds 577: S314-S317.

85. Ying, S., W. Cong, C. Lihua, W. Yongchun, N. Man and L. Fusheng (2010). "Low temperature coefficient of resistivity induced by magnetic transition and lattice contraction in Mn3NiN compound." Scripta Materialia 62(9): 686-689.

86. Yuanyuan, N., W. Cong, C. Lihua, D. Lei, Y. Jun, X. Yafei, X. Wanfeng and C. Xiaolong (2011). "Preparation and properties of antiperovskite Mn3NiN thin film." Materials Letters 65(23-24): 3447-3449.

87. Oe, T., C. Urano, M. Hadano, A. Ozawa, K. Takenaka and N. Kaneko (2012). Antiperovskite compound standard resistor. Precision Electromagnetic Measurements (CPEM), 2012 Conference on.

88. Oe, T., C. Urano, M. Hadano, A. Ozawa, K. Takenaka and N.-h. Kaneko (2013). "Optimization ofMn3Ag1−xCuxN Antiperovskite Compound Fabrication for Resistance Standard." IEEE TRANSACTIONS ON INSTRUMENTATION AND MEASUREMENT 62 (6): 4.

89. Lei, D., W. Cong, C. Lihua, Y. Jun, N. Yuanyuan, H. Qingzhen and C. Xiaolong (2011). "Near zero temperature coefficient of resistivity in antiperovskite Mn3Ni1−xCuxN." Applied Physics Letters 99(25): 251905.

90. Lu, N. P., T. Xu, Z. X. Cao and A. L. Ji (2016). "Ternary Mn3NMn1−xAgxcompound films of nearly constant electrical resistivity and their magnetic transport behaviour." Journal of Physics D: Applied Physics 49(4): 045308.

91. Gennes, P. G. D. and J. Friedel (1958). "Anomalies de résistivité dans certains métaux magníques." Journal of Physics and Chemistry of Solids 4(1): 71-77.

92. Cote, P. J. and L. V. Meisel (1978). "Origin of Saturation Effects in Electron Transport." Physical Review Letters 40(24): 1586-1589.

93. Gunnarsson, O., M. Calandra and J. E. Han (2003). "Saturation of electrical resistivity." Reviews of Modern Physics 75(4): 1085-1099.

94. "Precision thin film nichrome chip resistor. PCF series data sheet, March 2015."

95. Cheng, H. Y., Y. C. Chen, C. L. Li, P. J. Li, M. P. Houng and C. F. Yang (2016). "Developments of the Physical and Electrical Properties of NiCr and NiCrSi Single-Layer and Bi-Layer Nano-Scale Thin-Film Resistors." Nanomaterials (Basel) 6(3).

96. Water Insoluble nitride Thin Film Precision Chip Resistors: WIN Series, 2017. Technical note by TT Electronics plc.

97. Nishat, A., L. Junqing, L. C. Gyu, K. B. Heun and A. Faheem (2014). "Effects of Nitrogen Content on the Phase and Resistivity of TaN Thin Films Deposited by Electron Beam Evaporation." Jom 66(9): 1893-1899.

98. Bielicka, A., I. Bojanowska and A. Wiśniewski (2005). "Review Two Faces of Chromium - Pollutant and Bioelement." Polish Journal of Environmental Studies 14(1): 5-10.

99. Oe, T., C. Urano, N.-H. Kaneko, H. Eisaki, Y. Yoshida, A. Yamamoto and K. Takenaka (2014). "Antiperovskite Manganese nitride Standard Resistor." IEEE TRANSACTIONS ON INSTRUMENTATION AND MEASUREMENT: 5.

100. Oe, T., C. Urano, N. Kaneko, M. Hadano and K. Takenaka (2013). "Standard-resistor compounds with adjustable operating temperature." Applied Physics Letters 103(17): 173518.

101. Janesch, J. (2013) "Two-Wire vs. Four-Wire Resistance Measurements: Which Configuration Makes Sense for Your Application?", 1-2.

102. Poon, C. Y. and B. Bhushan (1995). "Comparison of surface roughness measurements by stylus profiler, AFM and non-contact optical profiler " Wear 190 76-88

103. "Optical Profilometry." http://www.nanoscience.com/technology/optical-profiler-technology/ Retrieved 13/04/2017, 2017.

104. Jaturunruangsri, S. (2014). Evaluation of Material Surface Profiling Methods: Contact versus Non-contact. Master of Philosophy, Brunel University London.

105. Joseph, G. (1981). Scanning electron microscopy and X-ray microanalysis : a text for biologists, materials scientists, and geologists. New York.

106. Grahame, L. (1987). Scanning electron microscopy and x-ray microanalysis. Chichester, published on behalf of ACOL by Wiley.

107. "Signals emitted from different parts of the interaction volume, Wikipedia page, https://en.wikipedia.org/wiki/Scanning_electron_microscope."

108. Nermut, M. V. and D. H. Kay (1967). "Techniques for Electron Microscopy (2nd edition). 560 S., 218 Abb., 18 Tab. Oxford 1965: Blackwell Scientific Publications 84 s." Zeitschrift für allgemeine Mikrobiologie 7(2): 169-170.

109. Zemel, J. N. (1979). Nondestructive evaluation of semiconductor materials and devices NATO advanced study institutes series. Series B, Physics v. 46, New York, Plenum Press.

110. Francisco, L. F. (2012). Secondary Ion Mass Spectrometry (SIMS): principles and applications. Capítol del llibre: Handbook of instrumental techniques for materials, chemical and biosciences research,, Centres Científics i Tecnològics. Universitat de Barcelona. Part I. Materials technologies (MT), MT.10, : 14 p.

111. Infinitfocus, F. V., Alicona Yearly magazine (2010/2011). 4-13.

112. Gerard, O. and D. M. Jordi (2012). Atomic force microscopy: probing the nanoworld. Handbook of instrumental techniques for materials, chemical and biosciences research. Barcelona, Centres Científics i Tecnològics. Universitat de Barcelona. MT.7, : 10 p.

113. Walter, B.-O. (1995). Crystallography. Berlin Springer-Verlag Berlin Heidelberg.

114. Paresh, N. (2009). The development of cuIn1-xALSe2 thin films for use in photovoltaic solar cells, University of Northumbria at, Newcastle.

115. Gregory, S. G. (2011). X-ray crystallography. Basingstoke, Basingstoke : Palgrave Macmillan.

116. http://icsd.cds.rsc.org/search/basic.xhtml

117. Dyos, G. T. and T. Farrell (1992). Electrical Resistivity Handbook. Stevenage, United Kingdom, Peter Peregrinus.

118. Kulkarni, A. K. and L. C. Chang (1997). "Electrical and structural characteristics of chromium thin films deposited on glass and alumina substrates." Thin Solid Films 301: 17-22.

119. Neugebauer, C. A. (1962). The temperature coefficient of ressitance in ultrathin evaporated metal films (investigation of metal thin film formation and structure). Schenectady, New York.

120. Das, A., C. Grabbe and R. Hufnagel (2008). complexities in the deposition of thin film resistor CARTS 2008- symposium for passive electronic components, Newport Beach, California, USA, Curran Associates, Inc.

121. Lai L., R. S., Xianzhu Fu , Ruxu Du (2012). Influence of segregation and diffusion behavior on electrical properties of embedded Ni- Cr thin film resistor. International Conference on Electronic Packaging Technology & High Density Packaging.

122. Au, C. L., W. A. Anderson, D. A. Schmitz, J. C. Flassayer and F. M. Collins (1990). "Stability of tantalum nitride thin film resistors." Journal of Materials Research 5(06): 1224-1232.

123. Nakamura, M., M. Fujimori and Y. Nishimura (1973). "Improvement of Tantalum nitride Resistor Film Stability Through Analysis on Plateau Phenomena." Japanese Journal of Applied Physics 12(1): 30.

124. Yoshitake, M., T. Yotsuya and S. Ogawa (1991). "Effects of Nitrogen Pressure and RF Power on the Properties of Reactive Magnetron Sputtered Zr-N Films and an Application to a Thermistor." Japanese Journal of Applied Physics.

125. Toku, H., R. S. Pessoa, H. S. Maciel, M. Massi and U. A. Mengui (2010). "Influence of process parameters on the growth of pure-phase anatase and rutile TiO2 thin films deposited by low temperature reactive magnetron sputtering." Brazilian Journal of Physics 40: 340-343.

126. Anjana, A., Y. K. Takahashi, M. Yoshio and K. Hono (2008). "Effect of base pressure on the structure and magnetic properties of FePt thin films." Journal of Magnetism and Magnetic Materials 320(3-4): 250-256.

127. Radhakrishnan, K., N. G. Ing and R. Gopalakrishnan (1999). "Reactive sputter deposition and characterization of tantalum nitride thin films." Materials Science and Engineering B 57: 224–227.

128. Nie, H. B., S. Y. Xu, S. J. Wang, L. P. You, Z. Yang, C. K. Ong, J. Li and T. Y. F. Liew (2001). "Structural and electrical properties of tantalum nitride thin films fabricated by using reactive radio-frequency magnetron sputtering." Applied Physics A Materials Science & Processing 73(2): 229-236.

129. Riekkinen, T., J. Molarius, T. Laurila, A. Nurmela, I. Suni and J. K. Kivilahti (2002). "R eactive sputter deposition and properties of Ta N thin films." Microelectronic Engineering 64: 289–297.

130. Marcela, M. and M. A. Q. Lopez (2016). "Stable temperature coefficient of resistance in TiSiON thin film resistors deposited by magnetron co-sputtering." Current Applied Physics 16(11): 1484-1490.

131. Kang, S. M., S. G. Yoon, S. J. Suh and D. H. Yoon (2008). "Control of electrical resistivity of TaN thin films by reactive sputtering for embedded passive resistors." Thin Solid Films 516(11): 3568-3571.

132. Jahanbakhsh, M., S. Zahra and N. Hossein (2012). "Effect of substrate temperature and film thickness on the characteristics of silver thin films deposited by DC magnetron sputtering." The European Physical Journal Applied Physics 60(2): 20301.

133. Zhou, Y. M., Z. Xie, H. N. Xiao, P. F. Hu and J. He (2009). "Effects of deposition parameters on tantalum films deposited by direct current magnetron sputtering." Journal of Vacuum Science & Technology A: Vacuum, Surfaces, and Films 27(1): 109-113.

134. Hur, S., D. Kim, B. Kang and S. Yoon (2004). "Effect of the deposition temperature on temperature coefficient of resistance in CuNi thin film resistors." Journal of Vacuum Science & Technology B: Microelectronics and Nanometer Structures Processing, Measurement, and Phenomena 22(6): 2698-2701.

135. Cuong, N. D., N. M. Phuong, D.-J. Kim, B.-D. Kang, C.-S. Kim and S.-G. Yoon (2006). "Effect of annealing temperature on structural and electrical properties of tantalum nitride thin film resistors deposited on SiO2⁄Si substrates by dc sputtering technique." Journal of Vacuum Science & Technology B: Microelectronics and Nanometer Structures Processing, Measurement, and Phenomena 24(2): 682-685.

136. Cheng, H.-Y., Y.-C. Chen, P.-J. Li, C.-F. Yang and H.-H. Huang (2015). "Effect of Annealing Process on the Properties of Ni(55%)Cr(40%)Si(5%) Thin-Film Resistors." Materials 8: 6752–6760.

137. Shen, H. and R. Ramanathan (2006). "Fabrication of a low resistivity tantalum nitride thin film." Microelectronic Engineering 83(2): 206-212.

138. Sonoda, S., J. H. Won, H. Yagi, A. Hatta, T. Ito and A. Hiraki (1997). "Effect of Nitrogen incorporation on electrical properties of boron-doped diamond films." Applied Physics Letters 70(19): 2574-2576.

139. Lee, Y., W. Tsai and J. Maa (2001). "Effects of substrate temperature on the film characteristics and gas-sensing properties of Copper phthalocyanine films." Applied Surface Science 173: 352-361.

140. Meng, L. and M. P. DosSantos (1998). "Properties of indium tin oxide films prepared by rf reactive magnetron sputtering at different substrate temperature." Thin Solid Films 322: 56-62.

141. EnGang, F., Z. DaMing, Z. Gong, Y. WeiFang and Z. Ming (2003). "Substrate temperature dependence of the properties of ZAO thin films deposited by magnetron sputtering." Applied Surface Science 217(1-4): 88-94.

142. Nisha, M., S. Anusha, A. Aldrin, R. Manoj and M. K. Jayaraj (2005). "Effect of substrate temperature on the growth of ITO thin films." Applied Surface Science 252(5): 1430-1435.

143. Jih-Fen, L., H. Okimura and J. O. Brittain (1990). "The electrical resistance of the group IV transition metal monocarbides and mononitrides in the temperature range 20–1000°C." Materials Science and Engineering: A 123(1): 129-140.

144. Banakh, O., P. E. Schmid, R. Sanjine and F. Le´vy (2002). "Electrical and optical properties of TiOx thin films deposited by reactive magnetron sputtering." Surface and Coatings Technology 151-152: 272-275.

145. Jie, T., H. Rongjin, W. Wei, L. Wen, Z. Yuqiang, L. Shaopeng, H. Yemao, H. Chuanjun and L. Laifeng (2015). "Broad negative thermal expansion operation-temperature window in antiperovskite Manganese nitride with small crystallites." Nano Research: 1-6.

146. Product Family: 40 Watt RF Chip Power Resistor Part Number Series: CFN2525 Series, N.M. Thin Film Technology Corp. / 1980 Commerce Drive, MN 56003 (USA) / (507) 625-8445 / www.thin-film.com, Editor.

147. Precision Thin Film Nichrome Chip Resistors : PCF Series. Technical note by TT Electronics plc 2016.

148. Raj, P. M., K. P. Murali, S. Gandhi, R. Tummala, K. Slenes and N. Berg (2012). Integration of precision resistors and capacitors with near-zero temperature coefficients in Silicon and organic packages. 2012 IEEE 62nd Electronic Components and Technology Conference.

149. Fu, B. and L. Gao (2006). "Tantalum nitride/Copper nanocomposite with zero temperature coefficient of resistance." Scripta Materialia 55(6): 521-524.

150. Lin, J. C., B. S. Wang, P. Tong, S. Lin, W. J. Lu, X. B. Zhu, Z. R. Yang, W. H. Song, J. M. Dai and Y. P. Sun (2011). "Tunable temperature coefficient of resistivity in C- and Co-doped CuNMn3." Scripta Materialia 65(5): 452-455.

151. Ruben, S. (1985). Hnadbook of the elements. La Salle, Illinois, USA, Open Courth Publishing Company.

152. Kim, J., H. Song, E. K. Kim, S. Lee and Y. Shon (2008). "Electrical Properties of Zn(Mn,Co)O Films Grown by Pulsed Laser Deposition Method." ECS Transactions 16(12): 27-31.

153. Zhao, H., et al., *Surface activity of antiperovskite manganese nitrides.* Journal of Materials Research, 2013: p. 1-7.

154. Shenjiang, W., C. Hang, D. Xiaoping and L. Zhengjun (2016). "Effect of deposition power and pressure on rate deposition and resistivity of titanium thin films grown by DC magnetron sputtering." Spectroscopy Letters 49(8): 514-519.

155. Thornton, J. A. (1988). Structure-Zone Models Of Thin Films. 31st Annual Technical Symposium on Optical and Optoelectronic Applied Sciences and Engineering, SPIE.

156. Charpentier, C., P. Prod'homme, I. Maurin, M. Chaigneau and P. R. Cabarrocas (2012). "X-Ray diffraction and Raman spectroscopy for a better understanding of ZnO:Al growth process." EPJ Photovoltaics 2: 25002.

157. Mukherjee, S. and D. Gall (2013). "Structure zone model for extreme shadowing conditions." Thin Solid Films 527: 158-163.

158. Lee, J. W., H. P. D. Shieh, M. H. Kryder and D. E. Laughlin (1988). "The effects of deposition conditions on microstructure and magnetic properties of TbFeCo." Journal of Applied Physics 63(8): 3624-3626.

159. Rickard, G., P. Iris, B. Robert, B. Nils and H. Ulf (2016). "The influence of pressure and gas flow on size and morphology of titanium oxide nanoparticles synthesized by hollow cathode sputtering." Journal of Applied Physics 120(4): 044308.

160. Yuan, H. and D. E. Laughlin (2010). "Experimental Study of Structural Zone Model for Composite Thin Films in Magnetic Recording Media Application." Processing of Nanoparticle Materials and Nanostructured Films 223: 161-168.

161. Zheng, W. T., H. Sjöström, I. Ivanov, K. Z. Xing, E. Broitman, W. R. Salaneck, J. E. Greene and J. E. Sundgren (1996). "Reactive magnetron sputter deposited CNx: Effects of N2 pressure and growth temperature on film composition, bonding, and microstructure." Journal of Vacuum Science & Technology A: Vacuum, Surfaces, and Films 14(5): 2696-2701.

162. Wang, C., B. L. Cheng, S. Y. Wang, H. B. Lu, Y. L. Zhou, Z. H. Chen and G. Z. Yang (2005). "Effects of Oxygen pressure on lattice parameter, orientation, surface morphology and deposition rate of (Ba0.02Sr0.98)TiO3 thin films grown on MgO substrate by pulsed laser deposition." Thin Solid Films 485(1): 82-89.

163. Eufinger, K., D. Poelman, H. Poelman, R. Gryse and G. B. Marin (2007). "Effect of microstructure and crystallinity on the photocatalytic activity of TiO2 thin films deposited by dc magnetron sputtering." Journal of Physics D: Applied Physics 40(17): 5232-5238.

164. Mahieu, S., P. Ghekiere, D. Depla and R. D. Gryse (2006). "Biaxial alignment in sputter deposited thin films." THIN SOLID FILMS 515(4): 1229-1249.

165. Arun, P. and A. G. Vedeshwar (2003). "Influence of grain size on the electrical properties of Sb2Te3 polycrystalline films." Materials Research Bulletin 38(15): 1929-1938.

166. Inokuma, T. and Y. Taketa (1985). "CONTROL OF ELECTRICAL PROPERTIES OF RtlO2 THICK FILM RESISTORS." Active and Passive Electronic Components 12: 155-166.

167. Rahul, S., J. Kihun, Y. Hyunuk, Y. Seongil, G. Thothadri, H. Sung-Hwan and A. Heejoon (2011). "Chemical synthesis and electrochemical analysis of nickel cobaltite nanostructures for supercapacitor applications." Journal of Alloys and Compounds 509(23): 6677-6682.

168. Vincent, L. and P. Soille (1991). "Watersheds in Digital Spaces: An Efficient Algorithm Based on Immersion Simulations " IEEE TRANSACTIONS ON PATTERN ANALYSIS AND MACHINE INTELLIGENCE 13(6): 583-598.

Appendix 1- Substrate Dimension Diagrams

University designed substrate:

The CAD drawing of the substrate plate designed for use within university is shown in the image below.

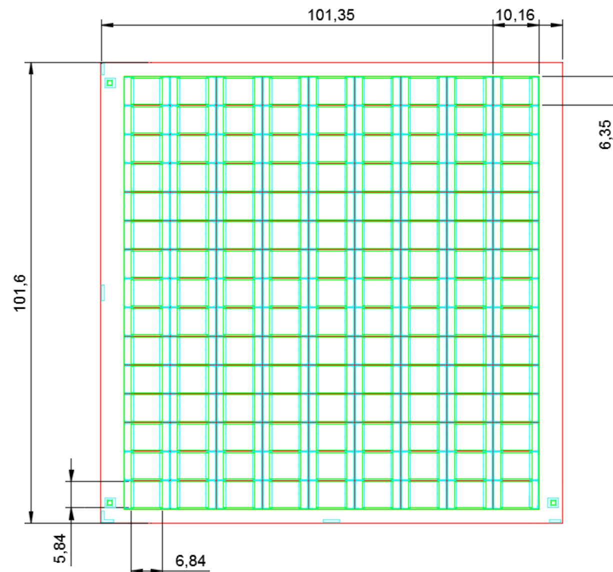

Substrate parameter	Value
Plate dimension	101.6 mm by 101.35 mm
Chip dimension	10.16 mm by 6.35 mm
Ressitive film dimension	6.84 mm by 5.84 mm
No of coloumns	9
No. Of Rows	15
Total number of chips in one plate	135
Substrate material	96% alumina (Al_2O_3)
Conductor pad material	Ag
Conductor pad dimension	6.05 mm by 2.01 mm

From table, it can be seen that each resistor circuit has a resistive element deposited in a rectangle of 6.84 by 5.84mm. So by equation 1.9,

Number of squares in university designed alumina substrate

$$n = \frac{L}{W} = \frac{6.84}{5.84} = 1.17$$

1206 substrate plate

The CAD drawing of the 1206 substrate plate commonly used within Thin film resistor fabrication industry is shown in the image below (courtesy of TT Electronics, Bedlington).

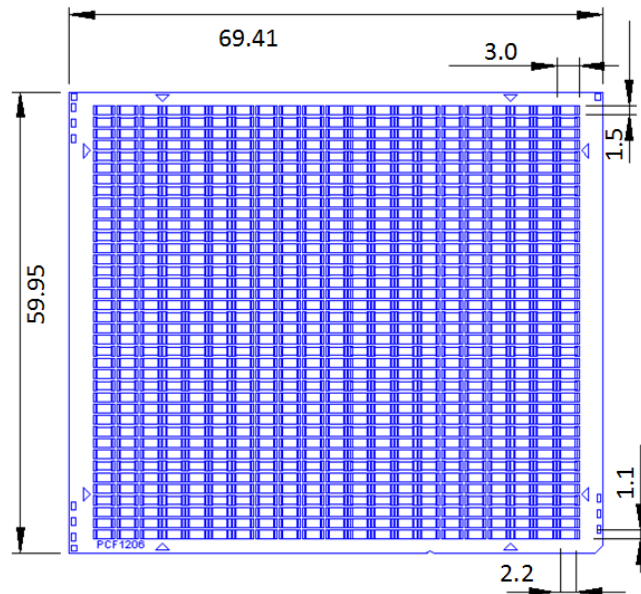

Substrate parameter	Value
Plate dimension	69.41 mm by 59.95 mm
Chip dimension	3 mm by 1.5 mm
Ressitive film dimension	2.2 mm by 1.1 mm
No of coloumns	21
No. Of Rows	38
Total number of chips in one plate	798
Substrate material	96% alumina (Al_2O_3)
Conductor pad material	Ag
Conductor pad dimension	1.2 mm by 0.45 mm

From table, it can be seen that each resistor circuit has a resistive element deposited in a rectangle of 2.2 mm by 1.1 mm. So by equation 1.9,

Number of squares in 1206 industrial alumina substrate

$$n = \frac{L}{W} = \frac{2.2}{1.1} = 2$$

Appendix 2: Result comparison from isolated and sequential process run

In chapter 5, a comparison was drawn between the electrical performance results achieved on chip resistors from Mn_3CuN sample set, when subjected to process run, with each stage running individually and sequentially. The table below compares the results from Mn_3AgN and $Mn_3Ag_{0.4}Cu_{0.6}N$, set of film, Chips from Mn_3AgN and $Mn_3Ag_{(0.4)}Cu_{(0.6)}N$ set also show a close match between both sets of runs. For Mn_3AgN, TCR values are within better tolerance limit when compared to Mn_3CuN films and stability value shows no improvement better than 13.1% in either of runs. On the other hand, for $Mn_3Ag_{(0.4)}Cu_{(0.6)}N$ set of films the stability value deteriorates from 3.4% to 7.4%, when process stages are run back to back.

Table 1: Mn_3AgN		**As-grown**	**After Heat treatment**	**After stabilization treatment**	**After 1 week stability test**
Rs (Ω/□)	Isolated	7.01	6.60	7.02	8.01
	sequential	9.02	8.86	9.27	10.49
TCR (ppm/ºC	Isolated	-233	-18	Not measured	Not measured
	sequential	-240	-19	88	91
Stability (ΔR/R%)	Isolated	N/A			13.97
	sequential				13.14

Table 2: $Mn_3Ag_{(0.4)}Cu_{(0.6)}N$		**As-grown**	**After Heat**	**After stabilization treatment**	**After 1 week stability test**
Rs (Ω/□)	Isolated	17.29	17.05	20.39	21.09
	sequential	17.78	16.20	27.90	30.06
TCR (ppm/ºC	Isolated	-317	-41	Not measured	Not measured
	sequential	-312	-51	74	68
Stability (ΔR/R%	Isolated	N/A			3.4
	sequential				7.4

---X---